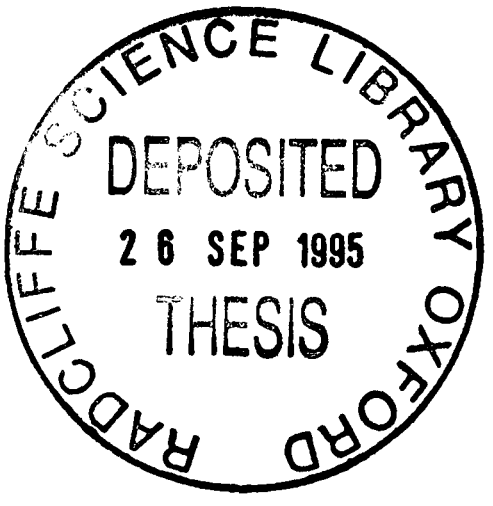
# Extrinsic and radiation induced point defects in diamond

Owain David Tucker

A thesis submitted for the degree of Doctor of Philosophy
at the University of Oxford

Merton College
Oxford




Trinity Term
1995

## Abstract

### Extrinsic and radiation induced point defects in diamond

A thesis submitted for the degree of
Doctor of Philosophy in the University of Oxford

O.D.Tucker,
Merton College, Oxford
Trinity Term, 1995

Methods for measuring Electron Nuclear Double Resonance (ENDOR) from optically created paramagnetic states in diamond have been developed. These were used in conjunction with conventional Electron Paramagnetic Resonance (EPR) and ENDOR measurements to investigate extrinsic and radiation induced point defects in natural and synthetic diamond.

ENDOR has unambiguously identified the ionized di-nitrogen (or A) centre as two identical nitrogen atoms in neighbouring substitutional sites. The nitrogen hyperfine and quadrupole parameters for the defect have been accurately measured. Molecular orbital theory calculations showed the unpaired electron to be almost 100% localized in the antibonding orbital between the nitrogen atoms. The N–N bond has extended to 1.86 Å. The $^{13}C$ ligand hyperfine interaction with six equivalent nearest neighbours was measured. The centre is created by photons of $E > 3.0$ eV, either by ionization of the A-centre, or by electron capture in $[N–N]^{2+}$. It decays logarithmically with respect to time, with a temperature independent rate below 50K indicating electron tunnelling through barriers of random width.

The first ENDOR measurements on an optically excited state in diamond have been made. These identified the $^5A_2$ excited state of the neutral vacancy in radiation damaged natural diamond. The measured hyperfine interactions with nearest and next-nearest neighbour $^{13}C$ ligand atoms showed the defect symmetry to be $T_d$. The unusual EPR line shape has been explained, and reasons for the non-Boltzmann population distribution within the spin manifold are suggested. The decay lifetime on removal of illumination has been measured.

A combination of low temperatures and high frequency EPR has been applied to the W11–W14, and R1 radiation damage defects in neutron irradiated type Ib diamond. Boltzmann depopulation between the spin sublevels allowed measurement of the sign of the fine structure interaction and the determination of the effective spins. The W11 centre was identified as an excited state, and explanations for the unusual depopulation behaviour of the W14 centre were presented. This is the first time this technique has been applied to diamond.

Intrinsic radiation damage defects in a 50% $^{13}C$ enriched type IIa synthetic diamond were examined and the R1 defect was shown to be optically active.

# Acknowledgements

I would like to thank my supervisors, Dr Mark Newton and Dr Michael Baker for their direction and patience during this thesis, and for their critical reading of the manuscript.

I would also like to thank:

Dr Lee's Professors of Experimental Philosophy, Professor Llewellyn-Smith and Professor Cowley, for extending the facilities of the Clarendon Laboratory.

The staff of the Clarendon Laboratory for their help with the experimental aspects of the work.

Professor John Weil for encouragement and many useful discussions.

The members of my research group, Andrew Cox, James Pfeffer, Daniel Talbot-Ponsonby, and Daniel Twitchen for help and companionship. A special thank you must be given to Daniel Twitchen for reading the manuscript.

Andrew Ward for Christian fellowship and many squash and weights sessions.

My friends from South Africa, Martin Müller, Ian Stewart and John Chiang, who though now scattered around the globe have given me support and encouragement.

Dr Robert Caveney and De Beers Industrial Diamond Division for financial support.

The Institute of Physics, Merton College, the Scott Fund, Oxford Lasers and De Beers Industrial Diamond Division for providing funding for the attendance of conferences.

Heartfelt thanks must be given to:

Carol Thompson who has given me support over the last few years, and who has tirelessly read many versions of the manuscript.

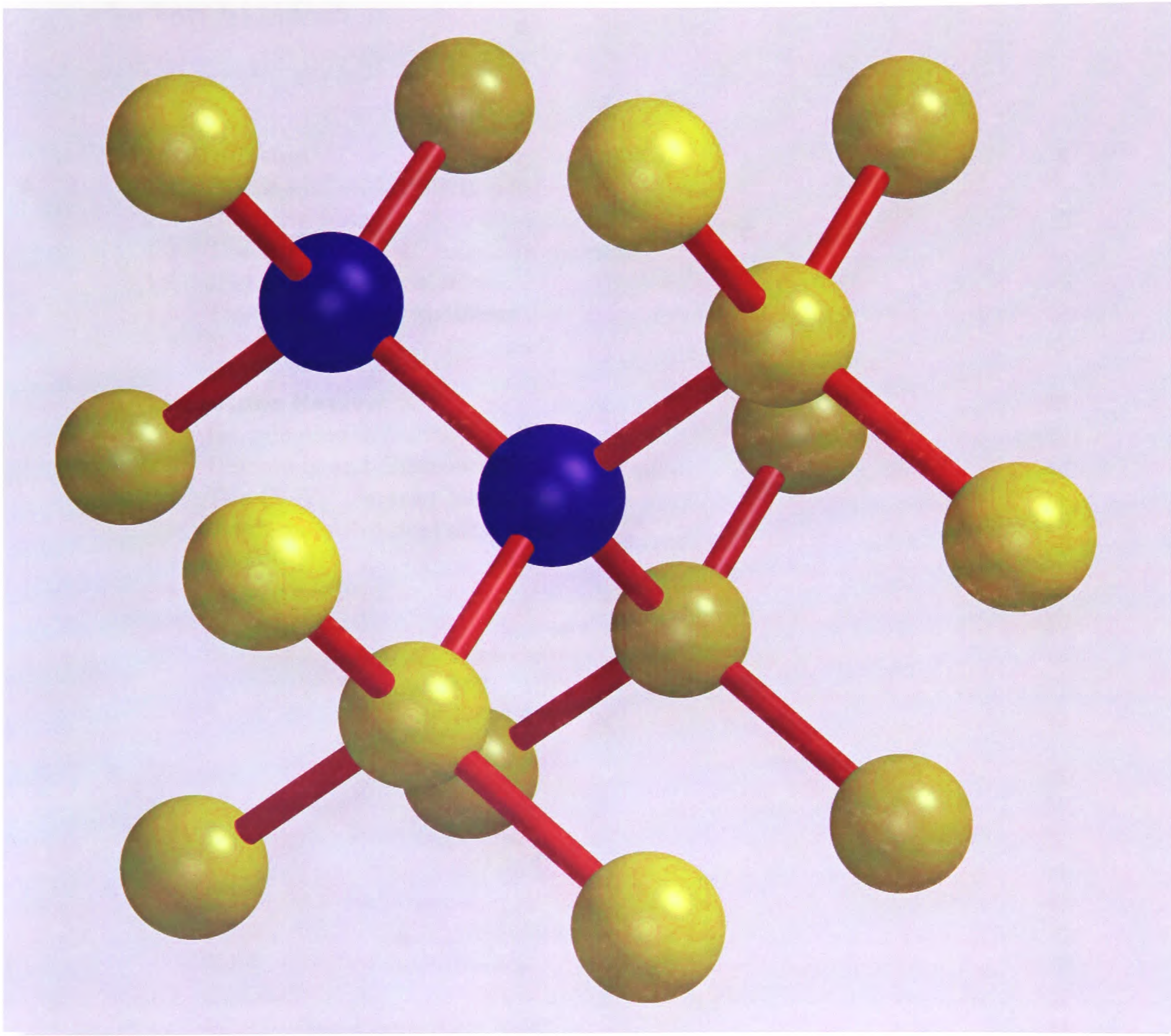
My parents for long distance support, encouragement, and the occasional Christmas Cake mailed from South Africa!

God, without whose support and blessings I would never be able to do anything.

"O Diamond! Diamond!
thou little knowest the mischief done!"

Sir Isaac Newton

To my parents



# Contents


**1 Introduction** **1**
- 1.1 Diamonds: an historical perspective . . . 1
- 1.2 Diamond today . . . 2
- 1.3 The study of point defects in diamond . . . 4
- 1.4 Diamond classification . . . 6
- 1.5 The structure of this thesis . . . 6
- 1.6 Notation . . . 7

**2 Literature Review** **10**
- 2.1 Introduction . . . 10
- 2.2 Diamonds and Diamond Physics . . . 10
- 2.3 The $[N–V]^-$ centre (W15) . . . 11
- 2.4 Single substitutional nitrogen - $[N–C]^0$ . . . 15
- 2.5 Nickel . . . 17
- 2.6 Boron . . . 18
- 2.7 Phosphorus . . . 19
- 2.8 General radiation damage centres . . . 19
  - 2.8.1 R3, R14 and R15 . . . 19
  - 2.8.2 NIRIM-3 and NIRIM-4 . . . 19

**3 Theory** **21**
- 3.1 Introduction . . . 21
- 3.2 Description of spin systems . . . 21
  - 3.2.1 Electron spin and EPR . . . 21
  - 3.2.2 Full Hamiltonian . . . 23
  - 3.2.3 Electron-Electron interactions . . . 24
  - 3.2.4 Nuclear contributions . . . 29
- 3.3 ENDOR . . . 31
  - 3.3.1 Continuous wave ENDOR . . . 34
- 3.4 Physical interpretation of parameters . . . 36
  - 3.4.1 Linear combination of atomic orbitals . . . 36
  - 3.4.2 Bond angles and extensions . . . 40
- 3.5 Simulation of spectra . . . 42
  - 3.5.1 Lattice symmetry . . . 42

3.5.2 Transition probabilities and calculation of intensities . . . . . 45

**4 Experimental methods** **47**
4.1 Introduction . . . . . 47
4.2 Q-band . . . . . 48
4.2.1 Description of spectrometer . . . . . 48
4.3 X-band . . . . . 50
4.3.1 Description of original bridge . . . . . 50
4.3.2 Changes to the microwave circuit . . . . . 50
4.3.3 Modifications to detection circuit . . . . . 52
4.3.4 Magnetic field and EPR signal measurement . . . . . 53
4.3.5 Optical illumination . . . . . 56
4.3.6 Time resolved measurements . . . . . 61
4.3.7 Cryogenics . . . . . 66
4.3.8 ENDOR I - Clarendon-built cavity . . . . . 69
4.3.9 ENDOR II - Bruker cavity . . . . . 70
4.4 Software . . . . . 73
4.4.1 Data collection I - EPR . . . . . 73
4.4.2 Data collection II - Time resolved . . . . . 75
4.4.3 Signal processing . . . . . 75
4.4.4 Spectrum manipulation . . . . . 77
4.4.5 Spectrum fitting and simulation . . . . . 79
4.5 Optical measurements . . . . . 80
4.6 Concentration measurement . . . . . 80

**5 $[N–N]^+$ centre** **83**
5.1 Introduction . . . . . 83
5.2 Background . . . . . 83
5.2.1 The optical A–centre, measurements . . . . . 83
5.2.2 The optical A–centre, theory . . . . . 86
5.3 Previous measurements on the $[N–N]^+$ centre . . . . . 88
5.4 The experiment . . . . . 90
5.4.1 Characterization of the sample . . . . . 90
5.4.2 Experimental details . . . . . 93
5.5 Measurements . . . . . 94
5.5.1 Nitrogen ENDOR . . . . . 94
5.5.2 EPR measurement of $^{15}N$ and $^{13}C$ hyperfine structure . . . . . 98
5.5.3 EPR saturation effects . . . . . 103
5.5.4 Lifetime of the $[N–N]^+$ centre . . . . . 105
5.5.5 Excitation energy dependence . . . . . 108
5.5.6 Distribution of $[N–N]^+$ centres created by illumination . . . . 109
5.5.7 The $[N–N]^+$ centre in powdered diamond . . . . . 109
5.6 Discussion . . . . . 111
5.6.1 Hyperfine interaction . . . . . 111

5.6.2 Determination of bond angles and bond lengths . . . . . 114
5.6.3 Overlap . . . . . 114
5.6.4 The $^{14}$N quadrupole interaction . . . . . 120
5.6.5 The various ionization states of the [N–N] species . . . . . 125
5.7 Conclusion . . . . . 128

**6 The Vacancy** **130**
6.1 Introduction . . . . . 130
6.2 Background . . . . . 131
6.2.1 Formation of vacancies: radiation damage . . . . . 132
6.2.2 The neutral vacancy: GR1 or $[V]^0$ . . . . . 132
6.2.3 The negative vacancy: ND1 or $[V]^-$ . . . . . 137
6.3 The sample . . . . . 138
6.4 Optical absorption measurements . . . . . 139
6.5 EPR measurements . . . . . 141
6.5.1 EPR spectra in principal directions . . . . . 143
6.5.2 Saturation behaviour . . . . . 144
6.5.3 Angular variation . . . . . 146
6.5.4 Concentrations . . . . . 147
6.5.5 Temperature dependence . . . . . 149
6.5.6 Dependence of $[N–C]^0$, $[V]^-$ & $[V]^*$ EPR on incident photon energy . . . . . 149
6.5.7 Lifetimes, quenching, and recovery . . . . . 151
6.6 ENDOR measurements . . . . . 156
6.6.1 $^{13}$C nearest neighbour ENDOR . . . . . 156
6.6.2 $^{13}$C next-nearest neighbour ENDOR . . . . . 158
6.7 Fitting . . . . . 158
6.7.1 $^{13}$C nearest neighbours: $[V]^*_{10}$ . . . . . 158
6.7.2 $^{13}$C next-nearest neighbours: $[V]^*_{01}$ . . . . . 159
6.7.3 Additional crystal field terms for $S$=2 . . . . . 160
6.8 Discussion . . . . . 160
6.8.1 Identification of the $^5A_2$ excited state of the neutral vacancy, $[V]^*$ 160
6.8.2 Line shapes I - second order hyperfine interaction . . . . . 161
6.8.3 Line shapes II - selective population of levels . . . . . 165
6.8.4 The electronic $g$-shift . . . . . 165
6.8.5 The unpaired electron and relaxation . . . . . 166
6.8.6 Temperature dependence . . . . . 167
6.8.7 Lifetime and excitation energy dependence . . . . . 168
6.9 Conclusions . . . . . 171
6.10 Further work . . . . . 171

**7 W11–W14** **173**
7.1 Introduction . . . . . 173
7.2 Previous work on W11–W14 . . . . . 174
7.3 Methods of effective spin determination . . . . . 177
7.3.1 $S$=1 and $S$=$\frac{3}{2}$ energy levels . . . . . 178
7.3.2 Half and third field transitions . . . . . 182
7.3.3 Thermally populated excited states . . . . . 184
7.4 The sample . . . . . 185
7.5 Experimental techniques . . . . . 185
7.6 Results and Discussion . . . . . 186
7.6.1 Spin Hamiltonian parameters and the spectrum . . . . . 186
7.6.2 Depopulation measurements . . . . . 188
7.6.3 Half and third field transitions . . . . . 191
7.6.4 General discussion . . . . . 193
7.7 Conclusion . . . . . 196
7.8 Further work . . . . . 196

**8 Isotopically enriched diamond** **198**
8.1 Introduction . . . . . 198
8.2 Isotopically pure and enriched diamond . . . . . 198
8.3 Previous work . . . . . 199
8.4 Results and Discussion . . . . . 203
8.4.1 The sample . . . . . 203
8.4.2 $[V]^-$ . . . . . 211
8.4.3 R1 . . . . . 215
8.4.4 ENDOR . . . . . 218
8.5 Conclusions . . . . . 219

**A W11–W14 depopulation curves** **221**

**Bibliography** **223**

# List of Figures


1.1 Diamond classification . . . . . 6

3.1 Energy levels for a system with hyperfine and quadrupole interactions 33
3.2 Relaxation paths in a four level system . . . . . 35
3.3 Model $C_{3v}$ defect used for bond-extension calculations . . . . . 41

4.1 Schematic of Q-band bridge . . . . . 48
4.2 Detail of Q-band EPR cavity . . . . . 49
4.3 Schematic of original X-band bridge . . . . . 51
4.4 Comparison of noise levels from Gunn diode and phase locked oscillator 51
4.5 Illumination of the sample using liquid and quartz light guides. . . . . 57
4.6 High pressure Hg lamp spectrum when passed through the Jarrell Ash monochromator . . . . . 60
4.7 Xe and Hg bulbs . . . . . 61
4.8 Control system for time resolved measurement . . . . . 63
4.9 Experimental assembly for time resolved measurements . . . . . 64
4.10 Shape or rf pulse . . . . . 65
4.11 Fastest measurable transient response . . . . . 65
4.12 $TM_{110}$ ENDOR cavity . . . . . 69
4.13 Powder ENDOR in diamond . . . . . 70
4.14 Micro-ENDOR coil and sample mount/light guide . . . . . 71

5.1 Model of the A centre . . . . . 85
5.2 EPR spectrum showing the $[N–N]^+$, $[N–C]^0$, $[N_3V]^0$ and W21 centres 91
5.3 Saturation curve for the $[N–N]^+$ centre . . . . . 92
5.4 Infrared absorption spectrum of the $[N–N]^+$ sample . . . . . 93
5.5 uv/visible absorption of $[N–N]^+$ sample . . . . . 94
5.6 EPR and ENDOR transitions in the $[N–C]^0$ system . . . . . 95
5.7 Cross relaxation in the $[N–C]^0$ system . . . . . 96
5.8 Typical ENDOR spectrum from the $[N–N]^+$ system . . . . . 96
5.9 Simulated and experimental EPR spectra for $[N–N]^+$ centre . . . . . 99
5.10 $^{13}C$ hyperfine structure on the $^{15}N$ transition . . . . . 99
5.11 Diamond lattice showing C–neighbour positions for $[N–N]^+$. . . . . 100
5.12 $^{13}C$ hyperfine structure in the $[N–N]^+$ centre . . . . . 101
5.13 Effect of light intensity on $[N–N]^+$ and $[N–C]^0$ . . . . . 103

5.14 Enhancement of the $[N–N]^+$ EPR signal . . . . . 104
5.15 Temperature dependence of $[N–N]^+$ EPR signal decay . . . . . 106
5.16 Logarithmic temperature dependence of $[N–N]^+$ EPR signal decay . . 107
5.17 Wavelength dependence of the $[N–N]^+$ and $[N–C]^0$ centres . . . . . 109
5.18 Simulation of $[N–N]^+$, $[N–C]^0$ and O1 powder spectra . . . . . 110
5.19 Powder spectra showing the $[N–N]^+$ centre . . . . . 111
5.20 C–C overlap as a function of bond extension . . . . . 117
5.21 N–C overlap as a function of bond extension . . . . . 118
5.22 N–N overlap as a function of bond extension . . . . . 119
5.23 $[N–N]^+$ antibonding orbital . . . . . 120
5.24 Fraction of the unpaired electron population vs quadrupole interaction for substitutional nitrogen containing defects . . . . . 122

6.1 Infrared absorption spectra for $[V]^*$ sample . . . . . 141
6.2 uv/visible absorption spectra for $[V]^*$ sample . . . . . 142
6.3 $[V]^*$ EPR spectra before and during illumination . . . . . 143
6.4 $[V]^-$ spectrum with B‖(100) . . . . . 144
6.5 Central region of the $[V]^*$ spectrum . . . . . 145
6.6 $[V]^*_{10}$ EPR saturation curve . . . . . 145
6.7 Angular variation of $[V]^*$ EPR in (110) plane. . . . . 146
6.8 Effect of uv light on central region of the $[V]^*$ spectrum . . . . . 148
6.9 Angular variation for $[V]^*_{10}$ in (111) plane . . . . . 148
6.10 Temperature dependence of $[V]^*_{10}$ between 300K and 5.5K . . . . . 149
6.11 Temperature independence of $[V]^*$ below 100K . . . . . 150
6.12 Intensity of the $[V]^*$ centre as a function of incident photon energy . . 150
6.13 Decay, recovery and enhancement of $[V]^-$ at 5K . . . . . 152
6.14 Decay, recovery and enhancement of $[V]^-$ at room temperature . . . . 153
6.15 Decay, and recovery of $[V]^*$ at 5K . . . . . 154
6.16 Decay, and recovery of $[V]^*$ at room temperature . . . . . 154
6.17 Decay, and recovery of $[V]^-$ at 5.0K . . . . . 155
6.18 $^{13}C$ ENDOR from the $[V]^*_{10}$ centre. . . . . 156
6.19 $^{13}C$ ENDOR from the $[V]^*_{10}$ centre. . . . . 157
6.20 Contributions to the $[V]^*_{10}$ line shape . . . . . 162
6.21 $[V]^*_{10}$ simulation . . . . . 164
6.22 $[V]^*_{10}$ EPR intensity as a function of line width . . . . . 167

7.1 $S$=1 and $S$=$\frac{3}{2}$ energy levels. . . . . 178
7.2 Effect of partition function on intensity ratio . . . . . 183
7.3 Half and third field transitions. . . . . 183
7.4 Q-band experimental spectrum showing W11,W12,W13,W14 and R1 186
7.5 Simulated spectra for W13 . . . . . 187
7.6 Thermal depopulation of the W11 excited state . . . . . 188
7.7 Depopulation of W-centres at low temperature . . . . . 189
7.8 Determination of the effective spin of the W-centres . . . . . 190

7.9 Half and third field transitions at X-band . . . . . 192
7.10 Effect of singlet on depopulation . . . . . 194

8.1 Infrared absorption of synthetic 50% $^{13}C$ sample before irradiation . . 204
8.2 uv/visible absorption of synthetic 50% $^{13}C$ sample before irradiation . 204
8.3 uv/visible absorption of synthetic 50% $^{13}C$ sample after irradiation . 207
8.4 Room temperature EPR of synthetic 50% $^{13}C$ sample after irradiation 208
8.5 Structure of $[V]^-$ showing nearest neighbours . . . . . 212
8.6 Nearest neighbour $^{13}C$ hyperfine splittings in $[V]^-$ . . . . . 213
8.7 Simulated and experimental spectra for $[V]^-$ with 50% $^{13}C$ . . . . . 213
8.8 Population inversion of R1 system under illumination . . . . . 216
8.9 Quantitative effect of light on the R1 defect . . . . . 217

A.1 Determination of the effective spin of the W-centres . . . . . 222

# List of Tables


1.1 Names of defects . . . . . 9

2.1 Calculated values for $[N–N]^+$ bond extensions . . . . . 17

4.1 Light source switching times . . . . . 65

5.1 Experimental and calculated values for A–centre vibrational frequencies 87
5.2 $^{14}N$ hyperfine and quadrupole parameters for $[N–N]^+$, measured at 5K 98
5.3 Probabilities and ratios for one $^{13}C$ and various numbers of neighbours 102
5.4 Hyperfine, quadrupole and wavefunction parameters for $[N–N]^+$ and $[N–C]^0$ . . . . . 112
5.5 Displacements of the nitrogen and carbon atoms in $[N–N]^+$ and $[N–C]^0$ 113
5.6 Values for the effective atomic number $Z^*$ . . . . . 116
5.7 Calculated values for $\bar{\eta}_i^2$ and $\zeta^2$ . . . . . 119

6.1 $^{13}C$ hyperfine parameters for $[V]^-$ and $[V]^*$ . . . . . 159

7.1 Hamiltonian parameters for W11–W14 . . . . . 176
7.2 Methods of effective spin determination . . . . . 177

8.1 Large synthetic diamonds . . . . . 200
8.2 Tabulated parameters for R1 and R2 . . . . . 200
8.3 R1 $^{13}C$ hyperfine parameters . . . . . 201
8.4 Additional lines possibly associated with R1 . . . . . 201
8.5 Probability for $^{13}C$ in nearest neighbour positions around the vacancy 212

# List of Plates


I Bruker cavity ENDOR system and time resolved illumination . . . . 67
II Natural IaB sample . . . . . 140
III Unirradiated 50% $^{13}C$ enriched sample . . . . . 205
IV Irradiated 50% $^{13}C$ enriched sample . . . . . 209
V Slice through irradiated 50% $^{13}C$ enriched sample . . . . . 210

# Chapter 1

# Introduction

## 1.1 Diamonds: an historical perspective

Diamonds have been known to man since antiquity, having been discovered 2700 years ago in India by the Dravidians [1]. The word "diamond" derives from the Greek *adamas* (ἀδάμας) which literally means "unvanquished"[1] and was called 'indomita vis' (unconquorable force) by Pliny [2], but this was generally the name given to iron or an iron alloy. However, it is thought that Ovid may have intended it to mean diamond when using it in the second half of the first century BC [1].

That the Romans knew of diamond is evidenced by Manilius's [3] reference to them in AD 16, and Pliny the Elder, writing of six varieties in AD 100, who opinioned that "it is the most valuable of gems known only to kings" [4]. These diamonds entered the Roman Empire from India via Persia, Egypt and Greece. Later Roman writers hinted at the source of the crystals describing "Indian rivers yielding up diamonds from their sands", indicating that diamonds were originally found in alluvial deposits.

The first modern account is given by the French traveller and merchant, Jean Baptiste Tavernier writing in 1684, who documents large numbers of diggers in the Kollur gorge of the Krishina river in the south of the kingdom of Golconda,[2] India. Tavernier is responsible for bringing many famous diamonds to Europe, including the

[1] See footnote b. p.208 reference [2].

[2] Now part of the State of Hyderabad.

Blue Tavernier from the Kollur mine, from which it is thought that the infamous Hope diamond was cut [1].

In 1725 alluvial deposits were discovered in the Minas Geraes region of Brazil which became the main source of supply in the eighteenth century and the first half of the nineteenth century until succeeded by South Africa [1, 5]. In 1866 the rush to South Africa began, with the discovery of alluvial diamond near the Orange River, but it was another 45 years before the first "pipe mine", Koffiefontein, was discovered, with the famous Kimberley mine starting one year later [1, 5]. In these mines the source of the alluvial diamonds had been found, in extinct volcanic pipes filled with weathered "yellow ground" and deeper unweathered "blue ground", dotted with diamonds. The Kimberley mine was worked until 1914, and when it closed it was over 3500 feet deep, and 25 million tons of ground had been removed yielding just over 3 tons of diamond.

Today natural diamonds are primarily found in Australia, Zaire, Botswana, Russia, South Africa, Namibia and Brazil, and the worldwide annual diamond production in 1994 was around 101 million carats[3] or 20.2 tonnes [5]. Natural diamond is, however, no longer the only source of diamond. In 1953 high-temperature high-pressure synthesis of diamond was achieved,[4] in the early 1960's shock synthesis of diamond was reported, and in the late 1960's the first diamond was deposited from the vapour phase (see p.13 [6], and §8.2 for single crystal synthesis).

## 1.2 Diamond today

The past five years have seen a resurgence in interest in the study of diamond. This has been catalysed by the demanding needs of the electronics industry and by the industrial production of thin film or chemical vapour deposition (CVD) diamond. The quality of single crystal synthetic diamond has increased to the extent that it is possible to grow gem stones which are only distinguishable from natural specimens

[3] A carat is equivalent to 0.2 g.

[4] This was not reported, and the first reported synthesis was in 1955 by General Electric, see [6] p.12.

by their lack of flaws.[5]

While the most valuable industrial application of diamond is probably still in the exploitation of its hardness, new applications are becoming more important. Some of these, along with general references, are listed below:

- Thermal management: increasing use in the telecommunications industry as heat conductors, rapidly removing heat from laser diodes and repeaters to be dissipated in conventional heat sinks [7, 8, 9].

- Optical windows: as pure diamond is transparent across most of the visible spectrum and much of the infrared, and it is chemically inert and scratch resistant, it is the ideal candidate for optical windows in harsh environments. Its most exotic use in this capacity was as a window on an infrared spectrometer on the Pioneer Venus large space probe. Here the window withstood a pressure of 90 atmospheres and a 450°C mixture of sulphuric acid and $CO_2$, while probing the Venusian atmosphere. An industrial application is as a window for online monitoring of the reactor vessels used in plastics manufacture. The military is also interested in the use of diamond to protect infrared sensors on missiles, planes and tanks [7, 10].

- Radiation detectors: when diamond is correctly doped it can be used either as a static radiation dose recorder (where it is exposed and later analyzed using its thermoluminescence spectrum) or as a dynamic recorder in medical applications. At the other end of the scale it has been proposed to use doped diamond as a radiation detector on particle accelerators [7, 11, 12, 13].

- Semiconductors: A number of diamond semiconducting devices which include cold cathode electron emitters, opto-electronic switches, microwave filters, and $p$–$n$ diodes have been made from CVD diamond. This technology is still in its infancy, but progress in the fabrication of such devices is continuing, aided by the development of CVD technology [14, 7, 15].

[5]This is true if the synthetic gem has been cut from a single growth sector, otherwise the growth sector dependence can give them away.

- Surgical: The high strength of the diamond lattice makes it possible to polish diamond blades to extreme sharpness while maintaining their strength. The fine blades are used in applications such as eye surgery, and they have the added advantage of remaining constantly sharp. The high resistance to wear is also used in other precision applications, such as the machining of contact lenses and telescope mirrors [7].

## 1.3 The study of point defects in diamond

The properties of diamond are affected, or even produced, by point defects within the lattice, making the study of these defects of paramount importance to further industrial exploitation. The nature of diamond as the archetypal covalent solid makes its study of additional value as a test of theoretical models; where the description of defects within a lattice is one of the most trying problems.

A parallel may be drawn between silicon and diamond since, before silicon could be employed to make the well characterized and reliable devices of today, years of study were spent understanding the behaviour of point defects, otherwise termed dopants.[6] In contrast to silicon, where the main study technique was magnetic resonance (EPR and ENDOR), diamond has received most attention through optical techniques[7] which have been used to classify gems since antiquity. There is therefore a huge body of optical data on diamonds.

Optical techniques are sensitive, and are often experimentally simple. Interpretation is however complex. Uniaxial stress measurements yield the symmetry of defects in the crystal, and thermoluminescence gives important information on traps and donors, but a major problem is encountered in the identification of the defect nuclei involved. Workers are forced to recourse to isotopic substitution and complex annealing experiments, and of course the only time isotopic substitution may take place is during growth. Paramagnetic resonance spectroscopy, via the ENDOR mechanism

[6]See Bridges [16] for a recent tabulation of many defects in silicon, and for further references.
[7]See, for example [17].

(§3.3 and §3.3.1), solves the problem of identification as it facilitates direct recognition of defect nuclei by measuring the nuclear $g$-factor. Paramagnetic resonance, however relies upon the presence of a paramagnetic electron, generally in the ground state.

Combination of the optical and magnetic resonance techniques is obviously desirable as optical excitation can provide unpaired electrons, extending the scope of magnetic resonance experiments, providing direct identification of constituent nuclei, yielding information about electronic and spin energy levels within a system, and linking EPR and optical defects.

This thesis concentrates on two fronts, the study of point defects in diamond using predominantly EPR and ENDOR, and the development of combined optical and Electron Nuclear Double Resonance techniques; applying them to the study of diamond for the first time. Using the combined techniques ENDOR was performed on:

- The ionized state of the most common optical defect in natural diamond, the A-centre.
- An excited state of the most common radiation damage defect, the neutral vacancy. This was the first excited state ENDOR to be performed in diamond.

Preliminary EPR measurements were also made on:

- Irradiated $^{13}C$ isotopically enriched synthetic diamond, targeted at intrinsic radiation damage defects.
- Neutron irradiated synthetic diamond. Here low temperatures were combined with high microwave frequencies to generate a significant Boltzmann depopulation between spin sublevels. The population difference was used for the determination of the sign of the fine structure constants, and the effective spins of a number of radiation damage defects. This was the first time this technique had been applied to diamond.

## 1.4 Diamond classification

The classification scheme for diamond has been developed over many years, with the original *type* classification being introduced by Robertson *et al.* in 1934 [18]. It is based mainly on the defect-induced one-phonon optical absorption [19] and is summarized in Figure 1.1.

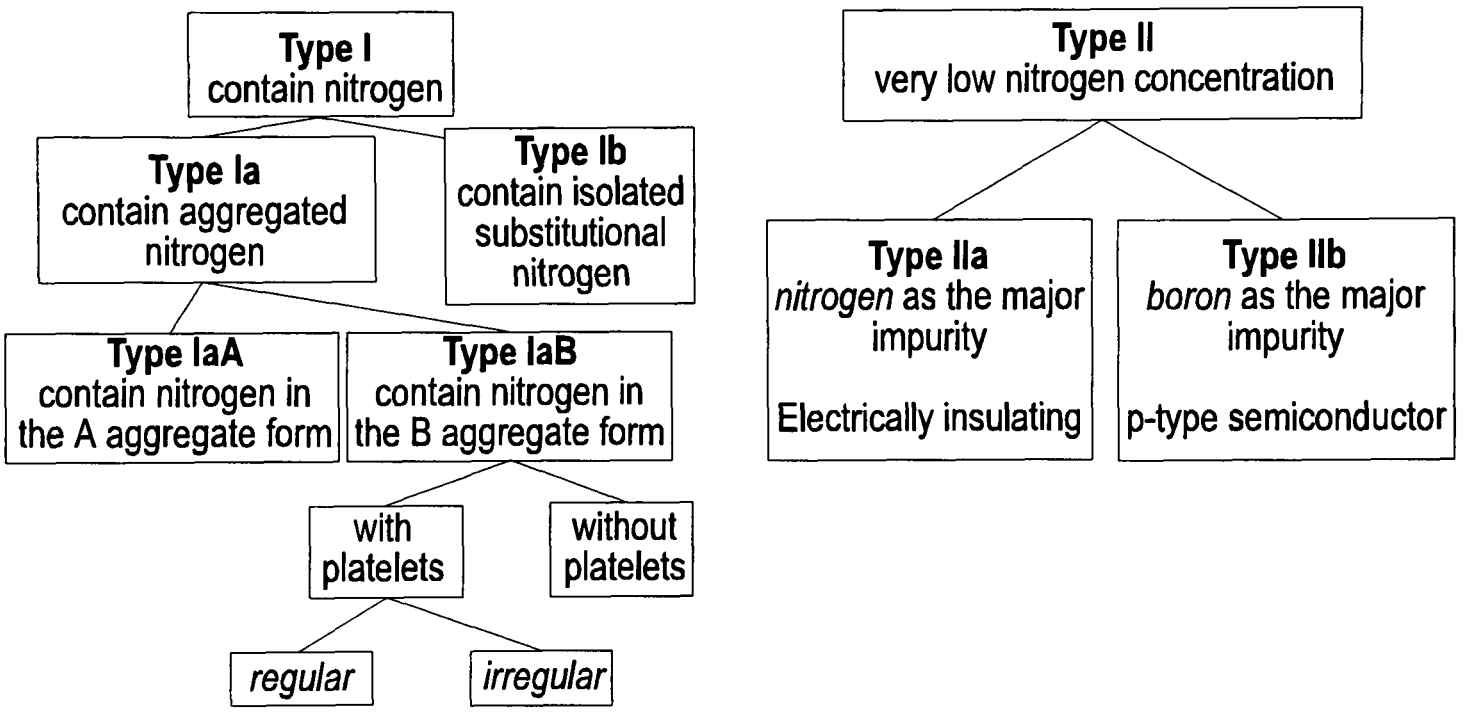



Figure 1.1: The classification scheme for diamond, after Collins [19]. *regular* denotes that the intensity of the B′ peak (at 1365 $cm^{-1}$) correlates with that of the B spectrum, while *irregular* indicates the opposite (see [19]).

With the advent of CVD diamond it is necessary to recognize that the polycrystalline films produced may not fall neatly into single-crystal classes. The differences occur during growth when substrate material, graphite, and dangling bonds are incorporated into the structure. CVD diamond is not examined in this thesis, but Davies [17] provides a comprehensive summary of the characteristics and growth of this material.

## 1.5 The structure of this thesis

The thesis consists of three introductory chapters and five experimental chapters.

- The introduction provides a brief view of diamond, its classification, and the reason for its study. It also defines the notation conventions used throughout, and provides a comparison between the different nomenclatures for the principal defects studied.

- The Literature Review in Chapter 2 examines the study of defects in diamond, concentrating on paramagnetic defects and theoretical calculations. Discussion of defects which have been studied in this thesis has been left to the chapters wherein they are treated.

- A brief theoretical introduction to magnetic resonance spectroscopy in given in Chapter 3, before explaining the effective spin Hamiltonian terms needed in this work. A discussion of the simulation of EPR spectra is presented, including the treatment of different ligand isotopes.

- The experimental work (Chapter 4) is introduced with a description of the spectrometers used and of developmental work performed on the microwave and electronic circuits, the optical system, the magnetic field metering, and the data acquisition and data processing software.

- The experimental results are presented in four chapters, starting with the ionized di-nitrogen centre (Chapter 5), then the excited state of the neutral vacancy (Chapter 6). These are followed by shorter chapters detailing introductory studies of the W11–W14 radiation damage centres (Chapter 7), and of intrinsic defects in isotopically enriched synthetic diamond (Chapter 8).

## 1.6 Notation

### Defect names

A number of notational conventions are used in the literature when discussing optical and magnetic resonance measurements. In EPR the convention has been to use the first letter of the institution followed by a number, for example: O1 denotes the

first defect found at the University of Oxford, while W24 is the 24$^{th}$ identified at the University of the Witwatersrand. Optical systems have two labelling methods: a system can be labelled by the energy or wavelength of the zero phonon line (in nanometres, angstroms or wavenumbers); or it can be labelled according to production method, for example the GR1 defect is General Radiation damage defect number one.

This thesis discusses optical and magnetic resonance defects. Confusion can occur in cases such as the P2 EPR centre which is also the N3 optical centre (which is not related to the N3 EPR centre). For this reason, a structurally derived notation has been adopted where possible. In this notation, substitutional defects are indicated by the perturbed atoms, for example: the P1 defect is a single substitutional nitrogen, but the defect has undergone a trigonal distortion to produce an unique carbon atom. It is therefore denoted by $[N–C]^0$. The superscript identifies the charge state. The P2 (optical N3) defect is thought to be three nitrogen atoms surrounding a vacancy and is denoted by $[N_3V]^0$. The conventions employed can be stated as:

- substitutional atoms are denoted by their atomic label, eg. [N]
- interstitials have the subscript $i$, eg. $C_i$
- the vacancy is denoted by [V]
- the superscript denotes the charge state of the defect
- subscript numbers have been used to indicate neighbouring ligand sites surrounding the vacancy (as described in Table 1.1)
- a superscript * denotes an excited state

**Other notation**

- Group theoretical notation follows the Schoenfleis system, thus the tetratrahedral group is $T_d$. Representations follow the A B E T notation, for example $^5A_2$ is an orbital singlet (of even parity) with $2S+1=5$ spin projections. It is the second (hence antisymmetric under reflection) A representation in the group. The full labelling convention is given in Appendix 10 of Atkins [20].

Table 1.1: Names of the major defects discussed in this work, giving the structural, EPR, and optical notation. A full tabulation of diamond defects, and the known relations between optical and EPR defects, is given by Bridges *et al.* [16].

| Structural | EPR | Optical | Comments |
|---|---|---|---|
| $[N\text{–}C]^0$ | P1 | — | Single substitutional nitrogen. |
| $[N_3V]^0$ | P2 | N3 | Three nitrogen atoms surrounding a vacancy. |
| $[N\text{–}N]^0$ | — | A-centre | Two adjacent substitutional nitrogen atoms. |
| $[N\text{–}N]^+$ | W24 | — | Ionized di-nitrogen centre, also $[N\text{–}N]^-$, $[N\text{–}N]^{2+}$. |
| $[V]^0$ | — | GR1 | Neutral vacancy. |
| $[V]^-$ | ND1 | ND1 | Also Baldwin S1 EPR centre, negative vacancy. |
| $[V]^*$ | *none* | — | Only structurally derived EPR notation, excited state of the vacancy. Disregards ligand hyperfine interactions (see next entry). |
| $[V]^*_{10}$ | *none* | — | The subscripts denote 1 nearest neighbour $^{13}C$ atom, and 0 next-nearest neighbour $^{13}C$ atoms in this case. |
| ? | R1 | — | Radiation damage induced EPR centre, no structure known. |
| ? | R2 | 1.685 eV | Radiation damage induced EPR centre, associated with 1.68 eV ZPL seen in optical absorption. |
| ? | O1 | — | Modelled as ⟨100⟩ Frenkel pair ($C_i$+V), in neutral charge state. Possible correlation with cathodoluminescence ZPL's at 511.5 nm and 509 nm. |

| | |
|---|---|
| — | indicates the absence of an identified EPR or optical defect |
| ? | indicates that the structure is unknown |
| *none* | indicates that there is no EPR notation for the defect |

This table is also included on the back cover.

- Vectors have been denoted by bold lettering, eg. $\mathbf{B}$, rank 2 tensors (and pseudo tensors) by bold and underline, eg. $\underline{\mathbf{A}}$, and operators by a circumflex, eg. $\hat{\mathbf{S}}$. Vector operators are bold, scalars are not. Rotation matrices have not been emphasized but are self evident in their use, eg. $R^{-1}\underline{\mathbf{A}}R$.

- Energy levels in spin manifolds have been labelled with 1,2,3,... in order of decreasing energy unless otherwise stated.

- The names of computer programs have been *italicized.*

- In figures the units (au) denote "arbitrary units".

# Chapter 2

# Literature Review

## 2.1 Introduction

In this section no attempt will be made to review diamond physics in its entirety. With the exception of §2.2 and §2.3 the review will concentrate on publications which have appeared since the reviews of Cox and Newton [21, 22] or that were not covered in their theses.

## 2.2 Diamonds and Diamond Physics

The field of Diamond physics has been extensively reviewed by Field [23, 24] in two editions: *The Properties of Diamond* and *The Properties of Natural and Synthetic Diamond*, and by Wilks and Wilks [6] in *The Properties and Applications of Diamond.* Both works detail the growth, classification, properties and applications of diamond, with the latter covering applications in more detail.

Two books of interest to the reader wanting to place Diamonds in an historical context are *Diamonds* [1] and *The Diamond Diggers* [25]. The authors present an historical overview of diamond discovery starting 2700 years ago, they also describe the beginnings of a company whose name is inextricably entwined with diamonds today – De Beers. In addition to the history, [1] reviews methods of extraction, prospecting and cutting, up to 1970.

References [6], [23] and [24] give many details on defects in diamond, spread through over one thousand pages. This information has recently been collated in an IEEE "datareview" publication: *Properties and growth of diamond* [17]. The work consists of separate articles covering topics ranging from the bulk properties of diamond, through radiation damage to CVD and high temperature, high pressure synthesis. Tables summarizing the properties of optical and EPR defects are given along with extensive references, making this a recommended source if one is hunting for papers on specific defects. As this thesis concentrates on magnetic resonance measurements, no attempt will be made to review the optical work on diamond extensively and the reader is referred to [17] for a detailed study. However, selected reports which have direct relevance to the work herein will be mentioned. Moving to the EPR and ENDOR in diamond, the theses of Newton [22] and Cox [21] present detailed surveys of the field at their time of publication. Newton covers the P1, P2, W21, and N1 centres in his review, whilst reporting on original work on the OK1, N3, W7, N2 and N4 centres. Cox brings Newton's review on the W21 centre up to date and reviews the W24, W15, W11 to W14, H2 and H3, O1, R5, vacancy centres (GR1 and ND1), Ni-Vacancy and Ni centres. He presents original work on the N2, P1 and N1 defects in single crystals, and also his initial study of CVD films.

## 2.3 The $[N–V]^-$ centre (W15)

The $[N–V]^-$ centre[1] is one of the most studied centres in diamond, and is of particular interest because of its optical and EPR activity. It will therefore be examined in detail, as many of the measurements have relevance to the $[N–N]^+$, R1 and $[V]^*$centres examined in this thesis.

The $[N–V]^-$ optical centre was isolated in 1965 by du Preez [26], where it was named the 1.945 eV (640 nm) band. du Preez gave the necessary conditions for

[1]The negative sign is assumed as i) $[N–V]^0$ would have a spin of $\frac{1}{2}$ or $\frac{3}{2}$, ii) $[N–V]^+$ and $[N–V]^-$ would allow $S$=1, but as the diamond contains the $[N–C]^0$ donor a negative state is more likely. The charge state has not been mentioned in any of the references cited here.

observation of the band[2] showing that it occurred in radiation damaged type Ib diamond when annealed at temperatures over 900K.

In 1971 Clark and Norris [28] showed, using polarized luminescence measurements, that the symmetry of the centre was limited to trigonal, monoclinic I or rhombic I. In 1974 Davies [29] reported the temperature dependence of the 1.945 eV absorption band showing that the transition probability for the zero-phonon transition decreased with increasing temperature according to theory based on a totally symmetric electron phonon coupling. Davies followed this work performing uniaxial stress measurements showing the transition to be between an $^1$A (ground) state and an E (excited) state of a trigonal centre [27]. Annealing experiments suggested the centre to be either a substitutional nitrogen atom plus an interstitial nitrogen atom, or a substitutional nitrogen atom, plus a vacancy. He also showed that differences between the absorption and luminescence bands correlated with the double minimum vibrational potential of the [N–V]$^-$ model. Davies commented that further verification of the defect model was not possible using optical techniques and that EPR might be the next step.

In 1977 Loubser and van Wyk [30] observed a triplet state with ⟨111⟩ axial symmetry, $g = 2.0028 \pm 0.0003$ and $D = (960 \pm 2) \times 10^{-2} \text{cm}^{-1}$ (287.8±0.6 MHz). The triplet state was optically excited and the Hamiltonian parameters were consistent with an [N–V]$^-$ model. They observed:

- a nitrogen hyperfine interaction;
- a population inversion with the high field EPR lines being in emission;
- that the intensities of the EPR lines exhibited a polarization dependence;
- and that it was possible to trace roughly the absorption spectrum of [N–V]$^-$ by plotting the EPR intensity as a function of illuminating wavelength.

They proposed that, as the optical transitions were between singlet states, the population of the excited state producing the EPR was caused by an intersystem coupling

[2] According to reference [27].

between the singlet and triplet state. This was caused by the relaxation of selection rules brought about by the mixing effect of the spin orbit interaction.

Further work by Collins [31], measuring the decay time of the luminescence between 77K and 700K, did not contradict the Loubser model, however, persistent spectral hole burning spectroscopy [32] showed the presence of side holes which suggested the existence of undiscovered splittings in the excited E state. Reddy and Manson [33] examined this effect, finding antiholes at $\pm 2.88$ GHz on either side of the zero-phonon line (ZPL), which coincided with the frequency obtained in EPR for zero field splitting of a meta-stable $^3$A state. They also performed magnetic-circular dichroism measurements and re-classified the system as having a $^3$A ground state and $^3$E excited state for the 638 nm (1.945 eV) ZPL. These measurements identified the EPR as occurring in the ground triplet state with no intersystem coupling necessary.

Additional evidence that the [N–V]$^-$ centre was a ground state was produced using optical detection of spin coherence [34]. The authors also obtained information on the spin dynamics of the system, and produced evidence for spin diffusion caused by magnetic dipole-dipole couplings which flipped electron and nuclear spins at nitrogen nuclei in the crystal. Redman [35] finally proved the ground state nature in 1991, observing unpolarized EPR without illumination. The Curie-law behaviour of the susceptibility ruled out all but a metastable triplet state with $\Delta E < 8.6$ meV. Redman also showed the existence of a metastable $^1$A state lying between the $^3$E and $^3$A states. This provided a possible explanation for the spin polarization of the ground state: a spin dependent interaction selectively transfers electrons to the long-lived $^1$A state, thereby leaving a polarization in the ground $^3$A and excited $^3$E states.

Much work has been performed on the cross relaxation (CR) of the [N–V]$^-$ defect. It has been shown that CR occurs between [N–V]$^-$ states aligned parallel to the applied Zeeman field and [N–V]$^-$ centres with other axes. CR has also been observed between [N–V]$^-$ centres and [N–C]$^0$ centres [35, 36, 37, 38, 39, 40]. Additional work has been performed on the energy levels of the system, with Redman [41] characterizing the energies and relaxation processes of the lowest seven. The excited state dynamics were studied using a two-beam coupling method based on acousto-optic

modulation [42]. The results yielded the fundamental decay constants for the centre. The $^3$E state was found to decay rapidly in $13.3 \pm 0.2$ ns, while the intersystem crossing from the $^1$A state to the ground state ($\tau$=265 ms) and the spin-lattice relaxation between the $^3$A ground state components ($\tau$=1.17 ms) were extremely slow. Evidence was found for strong excited state absorption from the $^1$A metastable level, possibly to the conduction band. If this is the case it places the $^1$A state within 1.945 eV of the conduction band.

The [N–V]$^-$ centre has been used as a test bed for the new measurement technique of *Raman Heterodyne Detected Magnetic Resonance* [43]. The technique has been used to investigate the level anticrossing in the $^3$A ground state, to measure the hyperfine interaction with the $^{14}$N nucleus [44, 45, 46], and to measure the nuclear dipole moment and homogeneous NMR line width. The centre has also been used in new measurements aimed at resolving inhomogenously broadened transitions, where it has been shown that Autler-Townes interactions can be resolved in the time domain by performing a modified spin echo experiment [47].

Further work on optical hole burning measurements is reported in references [48] and [49]. Strain in the centre was reported in [48] where strain induced splittings of the $^3$A ground state were observed in the optically detected magnetic resonance (ODMR) spectrum, and an internal strain induced lifting of the orbital degeneracy in the excited $^3$E state was observed.

Recently Wei *et al.* used the system in its role as a two level optical system to investigate the effect of strongly driving the ZPL transition and using a weak probe for analysis [50]. The aim was to use this rather clean two level optical system to test the theoretical results predicting its behaviour.

Hanzawa *et al.* [51] have measured the Zeeman effect on the zero-phonon line of the [N–V]$^-$ centre in synthetic diamond. They performed the experiment at 150 T and 77K and found absorption peak energies for the circularly polarized light $\sigma^+$ and $\sigma^-$ to be shifted oppositely and non-linearly as a function of the magnetic field for $\mathbf{B} \| \langle 100 \rangle$ in the Faraday configuration. They measured a Zeeman splitting of 2.2 meV at 100 T which implied a $g$-value of 0.22 for the excited state. The deviation from the

expected value of 1.00 [51] was attributed to the quenching of the angular momentum.

A theoretical study of nitrogen-vacancy complexes has been performed by Mainwood [52]. She used a semi-empirical molecular-orbital technique incorporating Car-Parinello molecular dynamics to investigate the structure and properties of the $[N–V]^-$ complexes. She showed that it is energetically favourable for vacancies to be trapped at nitrogen. The activation energy for the vacancy was found to be 2.4 eV – in close agreement with experiment. She also investigated the mechanics for nitrogen aggregation.

## 2.4 Single substitutional nitrogen - $[N–C]^0$

Substitutional nitrogen was the first impurity in diamond to be positively identified using EPR [53], coming to light soon after Kaiser et al. [54, 55] showed that nitrogen was a common impurity in natural samples. The nitrogen atom forms four hybrid bonds with its neighbouring carbon atoms. The unpaired electron resides in an anti-bonding orbital directed along one of the bonds, and is localized in the carbon atom. The N–C bond extension is approximately 30% and the centre has trigonal symmetry ($C_{3v}$) with the threefold axis along $\langle 111 \rangle$ [56].

Cox [21] has extensively reviewed both optical and magnetic resonance measurements made on the $[N–C]^0$ centre,[3] and theoretical work in describing these. He subsequently presents original high resolution ENDOR measurements of the $^{14}N$ hyperfine and quadrupole interactions, the $^{15}N$ hyperfine interaction, and ligand $^{13}C$ hyperfine interactions. A cross relaxation enhancement effect between the $[N–C]^0$ centres and $[Ni]_s^-$ defects enabled measurement of ENDOR from the $^{13}C$ ligand atoms. These centres also provided cross relaxation paths between the various $[N–C]^0$ spin sublevels, complicating the ENDOR interpretation by relaxing the spin selectivity of the technique, videlicet: when the Zeeman field was set to excite a specific EPR resonance, ENDOR lines were observed not only between spin levels associated with that EPR line, but also between spin levels associated with other EPR lines in the de-

[3] Also called the P1 centre, see Table 1.1.

fect. His $^{15}$N measurements show a previously unreported hyperfine anomaly caused by the difference in the zero-point vibration amplitudes of the two isotopes. All the ENDOR measurements are of a higher precision than previously reported and have facilitated more accurate calculation of the bond extensions, angles, and the electron distribution [57].

Recent work on high quality synthetic type IIa diamonds has led to a re-evaluation of the $g$-tensor for the [N–C]$^0$ centre [58]. Isotopically pure (99.95:0.005::$^{12}$C:$^{13}$C) samples with nitrogen concentrations of $\sim$100 ppb. were used. As the samples were free from strain and had little $^{13}$C or $^{14}$N dipolar broadening, the peak-to-peak line width was 4 $\mu$T. This facilitated highly accurate measurement of the line position as a function of applied magnetic field direction. Using this an anisotropy of the $g$-tensor was measured: $g_\perp - g_{||} = 0.0001 \pm 0.00003$. The authors, however made a mistake in the analysis neglecting to include the effect of the hyperfine interaction on the central ($m_N = 0$) transition. Inclusion of this term reduces the estimate to 0.00003(1) [59]. They confirmed the $\langle 111 \rangle$ symmetry to better than 0.5°.

The incorporation of [N–C]$^0$ into the lattice has been investigated theoretically using a number of calculation techniques which are discussed by Stoneham [60]. Predicted bond extensions and calculation methods (along with references) are summarized in Table 2.1. The initial calculations confirmed the model for a $\langle 111 \rangle$ distortion with the N–C bond extended with respect to the C–C bond and the C relaxing to a greater extent [61, 62], however they predicted that the relaxation was produced by a large static Jahn-Teller distortion. *Ab initio* calculations of Briddon and Jones, and Kajihara *at al.*, have shown that the ground state is $^2$A$_1$, an orbital singlet, thus ruling out the possibility of a Jahn-Teller interaction. The distortion is therefore a consequence of the covalent bonding and the incorporation of the charge in the antibonding orbital between the nitrogen and unique carbon (see Table 2.1 for references).

Lang *et al.* [71] have examined the dilatation of synthetic type Ib diamond by substitutional nitrogen. Using sequences of high-Bragg-angle double-crystal X-ray topographs to measure the lattice parameter differences between the growth sectors

Table 2.1: Calculated values for $[N–N]^+$ bond extensions

| Author(s) | Year(s) | Clust. | Ext.(%) | Calculation method |
|---|---|---|---|---|
| Messmer *et al.* [61, 62] | 1970/3 | 35 | 26,26.2 | LCAO-Extended Hückel |
| Mainwood [63] | 1979 | 47–68 | 5–10 | CNDO–MO |
| Briddon *et al.* [64, 65, 66] | 1991/2/3 | 86 | 28 | *ab initio* LDF |
| Kajihara *et al.* [67, 68] | 1991/3 | 64 | 25 | *ab initio* Car Parinello |
| Cunha *et al.* [69] | 1993 | 5 | 42 | *ab initio* Hartree-Fock |
| Anderson *et al.* [70] | 1993 | 71–84 | stretch | ASED–MO |
| Mainwood [52] | 1994 | 69–74 | 24–25 | CNDO–MO combined with Car Parinello dynamics |

| | |
|---|---|
| LCAO | Linear combination of atomic orbitals |
| LDF | Local density functional theory |
| CNDO-MO | Complete neglect of differential overlap molecular orbital |
| ASED-MO | Atom superposition and electron delocalization molecular orbital |

they found that the effective volume of a single, randomly substituted nitrogen atom was 1.41±0.06 times that of the carbon atom replaced. They used this to place a lower limit of 30% on the N–C bond extension.

The binding energies for substitutional N, Li, P, and for interstitial Li, have been calculated [70]. It was found that N and Li could enter the lattice but that it was energetically unfavourable for P. N was once again found to be a deep donor. The similarity between the core exciton and the nitrogen donor $[N–C]^0$ has been examined in reference [72], while the exciton itself has been measured in reference [73].

Finally, new work has been performed on the relationship between the infra red absorption and $[N–C]^0$ concentration [74].

## 2.5 Nickel

In 1993 Cox [21] reviewed studies on nickel as an impurity in diamond. He commented on the desaturating effect of Ni on the $[N–C]^0$ system. Additional Ni related optical and EPR defects have been reported in the last two years. Samples with a low nitrogen concentration were synthesized and new ZPL structure between 1.2 eV and 1.25 eV was observed. These lines showed strong polarization effects, analogous

to the 1.4 eV ZPL, and they were confined to the {111} growth sectors of diamond. They are proposed to result from a different charge structure of the 1.40 eV nickel system [75]. An annealing study of nickel point defects has been carried out and produced a correlation between the diminution of the 1.883 eV and 2.51 eV systems and the creation of a new structure giving a rich golden-yellow colour to the samples [76]. Further EPR work has recently been performed allowing the identification of numerous nickel and nickel-nitrogen defects [77, 78]. As ENDOR has yet to be performed in these NE1–NE7 defects, the models presented in references [77, 78] are not unequivocal. Unidentified centres, possibly associated with nickel, have recently been reported by Isoya *et al.* [79]. These are the NIRIM-5 centre having trigonal symmetry and observed in boron doped crystals grown from Ni solvent; and the NIRIM-6 and NIRIM-7 centres observed in crystals grown from an Ni-Ti solvent. NIRIM-5 has $g$-values similar to those observed in transition metals with $g_{||}$=4.0 and $g_{\perp}$=$\sim$0.

A recent theoretical study by Lowther [80] has investigated the optical features corresponding to different charge states of nickel in diamond. A multiplet structure for each of the charge states was deduced and shown to be consistent with the experimental results. It was suggested that interstitial nickel would have a transition metal character, while substitutional nickel would display characteristics similar to a positively charged vacancy [80].

## 2.6 Boron

The electronic properties of boron in diamond have been extensively studied and are reviewed in [81]. It has been shown that it behaves as a hydrogenic acceptor with an ionization energy of 0.368 eV [19]. Optical absorption and luminescence measurements are reviewed in reference [19]. No boron related EPR centres have been incontravertably identified, although the NL1 and W36 centres [82, 83, 84] have been tentatively associated with boron.

Recent studies have included cathodoluminescence of diamond films where resolved donor-acceptor pair-recombination was noted. Likely candidates for the pairs

were the nitrogen donor and boron acceptor [85]. An *ab initio* study of substitutional boron has been performed using local-density-functional theory and the vibrational modes have been calculated [86]. The bonds to the first nearest neighbours of the boron were found to increase in length by 3%.

See §2.8.2 for a description of the NIRIM-4 EPR centre [79] which exhibits hyperfine interactions with the 80.2% abundant $I=\frac{3}{2}$ $^{11}$B nucleus.

## 2.7 Phosphorus

The first observation of phosphorus in diamond has been reported by Samsonenko *et al.* in synthetic high-temperature high-pressure grits [87].

## 2.8 General radiation damage centres

### 2.8.1 R3, R14 and R15

Two new radiation damage centres have been found in type Ia and IIa diamond [88]. The centres have effective spins of one and were observed after electron-irradiation and have been labelled R14 and R15. Further work on the R3 damage centre has also been reported [88]. It was noted that the centres are produced after irradiation, which creates vacancies and interstitials, but anneal out below the temperature at which the vacancy becomes mobile. The centres have therefore been associated with the carbon interstitial.

### 2.8.2 NIRIM-3 and NIRIM-4

Two centres have been observed in boron doped (type IIb) crystals grown using Ni or Co solvents after irradiation [79]. NIRIM-3 was observed after electron irradiation at room temperature (3 MeV, total fluence $4\times10^{17}$ to $3\times10^{18}$ cm$^{-2}$), or $H^+$ implantation at room temperature (10 MeV, total fluence 1 to $9\times10^{15}$ cm$^{-2}$). The defect had an effective spin of one half, trigonal symmetry, and $g$-values of $g_{||}$=2.0009 and $g_{\perp}$=2.0024

at 4K. $^{13}$C satellites were observed corresponding to an approximately axially symmetric interaction along [111] with principal values of $A_{||}$=1.17 mT and $A_{\perp}$=0.75 mT at 4K. The spin density on each nearest neighbour carbon atom was calculated to be 0.05 (16% 2*s* character, 84% 2*p* character). The symmetry of the centre agrees with the model of the positively charged vacancy, however the electron has a greater delocalization than would be expected [79]. NIRIM-4 was observed after electron irradiation,[4] and had orthorhombic ($C_{3v}$) symmetry and $S=\frac{3}{2}$. It exhibited hyperfine interactions with the 80.2% abundant $^{11}$B $I=\frac{3}{2}$ nucleus. This was the first time that the hyperfine interaction with the boron nucleus had been observed for point defects in diamond. It was suggested that the NIRIM-4 centre was a boron-vacancy complex. The *g*-values measured were $g_1$=2.0050||[100], $g_2$=2.0042||[011], $g_3$=2.0059||[0$\bar{1}$1]. The boron hyperfine interaction measured was $A_1$=1.16 mT, $A_2$=1.52 mT, $A_3$=0.90 mT with the same principal axes as the *g*-matrix.

[4]No dose given.

# Chapter 3

# Theory

## 3.1 Introduction

In this chapter theoretical aspects relevant to the understanding and interpretation of the experimental measurements will be discussed. Where a theoretical treatment has specific relevance to only one experimental section it has been discussed therein.

## 3.2 Description of spin systems

### 3.2.1 Electron spin and EPR

The first observation of the intrinsic angular momentum of the electron was in the experiments of Stern and Gerlach in 1921–22, though this was not recognized as the cause of the results until Goudsmit and Uhlenbeck postulated its existence in 1925 [89, 89, 90]. The intrinsic angular momentum of the electron, its spin, is represented by the operator $\hat{\mathbf{S}}$ and is related to the magnetic moment operator by:

$$\hat{\boldsymbol{\mu}} = \frac{e\hbar}{2m_e c} g_e \hat{\mathbf{S}} \tag{3.1}$$

where $\frac{e\hbar}{2m_e c} = \mu_B$ the Bohr magneton. $g_e = 2.0023...$ is a constant. The value of 2 is derived from relativistic quantum mechanics and the .0023... correction emanates from the electron *Zitterbewegung* described by Quantum Electrodynamics.

In the absence of a magnetic field the electron spin states are degenerate, but this degeneracy is lifted in non zero fields. The system is described by the Hamiltonian:

$$\mathcal{H} = -\hat{\boldsymbol{\mu}} \cdot \mathbf{B} = -g_e \mu_B \hat{\mathbf{S}} \cdot \mathbf{B} \tag{3.2}$$

If the $z$-axis of the spin operator is chosen to coincide with the direction of the Zeeman field then the eigenstates are $|\pm\frac{1}{2}\rangle$ with energies of $E_\pm = \pm\frac{1}{2} g_e \mu_B B$. Exposure to an oscillating magnetic field $\mathbf{B}_1$ will introduce a time dependent perturbation to the system and induce transitions between the eigenstates. The probability that the transition will occur depends on the polarization of the perturbing field and its frequency (as described in reference [91] p.98ff and, for a general EPR system in §3.5.2). A working condition for transitions to occur is:

$$h\nu = g_e \mu_B B \tag{3.3}$$

where $\nu$ is the frequency of the applied radiation.

In electron paramagnetic resonance spectroscopy, the degeneracy is usually lifted using magnetic fields of between 0.5 and 2 T, which places the photon energies in the microwave region. In equation 3.3 there are two external variables, the microwave frequency and the magnetic field. Experimentally it is simpler to produce constant frequency microwaves and to vary the magnetic field. The sample is normally placed in a critically coupled microwave resonant cavity to enhance sensitivity, the magnetic field is varied, and the change in the microwave absorption is recorded. As the probabilities for induced emission and absorption are equal, no continuous absorption will be observed. However, there is generally a thermodynamic distribution[1] of population between the energy levels, with a greater number of spins in the lower levels, and this population difference is maintained by non-radiative relaxation paths produced by the interaction of the electron with the crystal lattice. The Hamiltonian in equation 3.2 is over-simplified as the electron is not isolated but is part of a solid-state system. A more complete Hamiltonian must therefore be considered.

[1] Discussed in §3.5.2.

### 3.2.2 Full Hamiltonian

In solid state systems, paramagnetic resonance occurs when unpaired electrons exist within the crystal lattice. Diamond is covalently bonded and these electrons will usually occupy hybrid atomic orbitals. When more than one electron is in the orbital, or in close proximity to an electron in another orbital, the electrons can interact (§3.2.3). The energy of the spin system would then be described by the interaction of each electron's spin and orbital angular momentum with:

- the applied magnetic field;
- any nuclei with non-zero spins;
- every other unpaired electron; and
- the crystal field.

Luckily the interaction between the unpaired electrons in a paramagnetic defect often allows the system to be viewed in terms of the Russell-Saunders or LS coupling scheme. This introduces the concept of the effective spin $S$ and, with certain approximations discussed in subsequent sections, it is possible to describe the EPR system using an *effective spin Hamiltonian*:

$$\mathcal{H} = \underbrace{\mu_B \hat{\mathbf{S}} \cdot \underline{\mathbf{g}} \cdot \mathbf{B}}_{1} + \underbrace{\hat{\mathbf{S}} \cdot \underline{\mathbf{D}} \cdot \hat{\mathbf{S}}}_{2} + \sum_j [\underbrace{\hat{\mathbf{S}} \cdot \underline{\mathbf{A}}_j \cdot \hat{\mathbf{I}}_j}_{3} - \underbrace{\mu_N g_{Nj} \hat{\mathbf{I}}_j \cdot \mathbf{B}}_{4} + \underbrace{\hat{\mathbf{I}}_j \cdot \underline{\mathbf{P}}_j \cdot \hat{\mathbf{I}}_j}_{5}] + \underbrace{\sum_{q,k} B_k^q O_k^q}_{6} + \cdots \tag{3.4}$$

Only those terms used in this thesis are given in equation 3.4. The terms labelled 1–6 are:

1. The electron Zeeman interaction where spin orbit coupling with excited states has been included by writing the $g$-factor as a matrix (§3.2.3).
2. Electron-electron interactions, described in §3.2.3.
3. The hyperfine interaction of the electrons with nuclei having non-zero nuclear spin (§3.2.4).

4. The nuclear Zeeman interaction (§3.2.4).

5. The interaction of each nucleus with the total electric field gradient at the nucleus, or nuclear quadrupole interaction. This occurs only for $I \geq 1$ (§3.2.4).

6. Higher order crystal field interactions. The $B_k^q$ are coefficients of the spin operators $O_k^q$. This was only applicable here for $k = 4$ and $q = 0, 4$ (see Chapter 6).

A full treatment of the effective spin Hamiltonian can be found in reference [91] while a short description of some of the contributions to the terms in equation 3.4 is given in the following sections.

### 3.2.3 Electron-Electron interactions

When a defect consists of more than one unpaired electron, the electrons interact with each other. There are numerous forms of interaction between the electrons [92] but in this work three types of electron-electron interaction were of importance, namely the exchange interaction, the magnetic dipolar interaction, and the interaction between the orbital angular momentum and the crystal field. Each interaction makes a contribution to the $D$-tensor in equation 3.4.

#### Exchange interaction

When two electrons are present at the same defect the direct overlap of the wave functions introduces an isotropic exchange interaction, but when the spin-orbit coupling energy is included this ceases to be a scalar and becomes anisotropic. For two electrons the exchange interaction can be represented as a tensorial coupling between the spins:

$$\mathcal{H}_{\text{ex}} = \hat{\mathbf{S}}_1 \cdot \underline{\mathbf{J}} \cdot \hat{\mathbf{S}}_2 \tag{3.5}$$

If it is assumed[2] that the $g$-matrices for the electrons have the same principal values and principal axes, that the axes coincide with those of the exchange interaction, that

[2]Following the treatment of Abragam and Bleaney, p.603 [91].

the $J$-tensor is symmetric, and the magnetic field is applied along a principal axis which will be denoted $\hat{\mathbf{z}}$, then the Hamiltonian for the pair of electrons ($i$ and $j$) is:

$$\mathcal{H} = g_z \mu_B B_z (\hat{S}_{iz} + \hat{S}_{jz}) + J_x \hat{S}_{ix} \hat{S}_{jx} + J_y \hat{S}_{iy} \hat{S}_{jy} + J_z \hat{S}_{iz} \hat{S}_{jz} \tag{3.6}$$

The basis used is composed of the functions $|m_i\, m_j\rangle$. The coupling produces combined eigenstates, consisting of three symmetric combinations and one antisymmetric combination. When the magnitude of the exchange interaction is large with respect to the Zeeman interaction, the states may be thought of as a triplet and a singlet respectively. As the perturbation Hamiltonian for magnetic resonance transitions is symmetric with respect to exchange of the two electrons, EPR transitions may only occur between states belonging to the triplet, and no singlet-triplet transitions are allowed. In this strong coupling case the Hamiltonian (equation 3.6) can be re-written in terms of the total spin projections, $T_\xi = (S_{i\xi} + S_{j\xi})$, $\xi = x, y, z$:

$$\mathcal{H} = g_z \mu_B B_z \hat{T}_z + \tfrac{1}{2}(J_x \hat{T}_x^2 + J_y \hat{T}_y^2 + J_z \hat{T}_z^2) - \tfrac{1}{4}(J_x + J_y + J_z) \tag{3.7}$$

Re-writing the exchange interaction as $J_x = J'_x + J$, where $J = \frac{1}{3}(J_x + J_y + J_z)$, and noting that the trace of the anisotropic part $\sum_{\xi=x}^{z} J'_\xi = 0$ the Hamiltonian becomes:

$$\mathcal{H} = g_z \mu_B B_z \hat{T}_z + \tfrac{1}{2}(J'_x \hat{T}_x^2 + J'_y \hat{T}_y^2 + J'_z \hat{T}_z^2) + \tfrac{1}{2} J \{T(T+1) - \tfrac{3}{2}\} \tag{3.8}$$

If the exchange is isotropic, then at zero field all the triplet levels have the same energy, $+\frac{J}{4}$, while the singlet has energy $-\frac{3}{4}J$. Examination of equation 3.8 reveals that in the isotropic case the exchange interaction has no effect upon the positions of the transitions within the triplet manifold. For this reason the isotropic exchange interaction is generally ignored when discussing EPR spectra. At low temperatures, where $kT \sim J$, Boltzmann depopulation can affect the intensities of the EPR transitions. If $J$ is positive the triplet state lies higher in energy than the singlet and can depopulate.[3] If the singlet lies higher than the triplet the intensity of the triplet

[3] As was the case with the W11 centre discussed in §7.6.2.

transitions will be proportionally larger than expected when compared to transitions of a purely ground state defect. Thus low temperature measurements can be used to determine the value of the isotropic exchange interaction.

The anisotropic portion of the exchange interaction lifts the zero field degeneracy within the triplet state in a manner analogous to the fine structure splitting. It can be included in the $D$-tensor by labelling $D_\xi = J'_\xi/2,\ \xi = x, y, z$. This contribution can have either a positive or negative sign in a solid state system.

If the exchange interaction is not large with respect to the Zeeman splitting the coupling scheme is incorrect and the system has to be represented by a Hamiltonian of the form:

$$\mathcal{H} = \mathcal{H}_1 + \mathcal{H}_2 + \mathcal{H}_{ss} \tag{3.9}$$

where $\mathcal{H}_1$ and $\mathcal{H}_2$ are effective spin Hamiltonians for the separate spins and may include hyperfine interactions, fine structure and other local spin-spin interactions, and $\mathcal{H}_{ss}$ represents the spin-spin interactions between the electrons within the two defects.[4]

### Magnetic dipolar interaction

This interaction originates from the classical interaction between two magnetic dipoles, $\hat{\boldsymbol{\mu}}_1$ and $\hat{\boldsymbol{\mu}}_2$. Replacement of the classical magnetic moment operators with the quantum mechanical spin operators yields the following magnetic dipolar interaction Hamiltonian:

$$\mathcal{H}_{dip} = \left(\frac{\mu_0}{4\pi}\right) g^2 \mu_B^2 \left[\frac{\hat{\mathbf{S}}_1 \cdot \hat{\mathbf{S}}_2}{r^3} - \frac{3\left(\hat{\mathbf{S}}_1 \cdot \mathbf{r}\right)\left(\hat{\mathbf{S}}_2 \cdot \mathbf{r}\right)}{r^5}\right] \tag{3.10}$$

where $\mathbf{r}$ is the vector joining the two spins. If the operators are expressed in terms of the total spin operator $\hat{\mathbf{S}} = \hat{\mathbf{S}}_1 + \hat{\mathbf{S}}_2$ and expanded, it can be shown that $\mathcal{H}_{dip}$ may

[4]This case is often encountered in chemical problems in which the systems are termed biradicals.

be written as:[5]

$$\begin{aligned}\mathcal{H}_{\text{dip}} &= \left(\frac{\mu_0}{4\pi}\right)\frac{1}{2}g^2\mu_B^2\left[\hat{S}_x,\hat{S}_y,\hat{S}_z\right]\begin{bmatrix}\left\langle\frac{r^2-3x^2}{r^5}\right\rangle & \left\langle-\frac{3xy}{r^5}\right\rangle & \left\langle-\frac{3xz}{r^5}\right\rangle\\ \left\langle-\frac{3xy}{r^5}\right\rangle & \left\langle\frac{r^2-3y^2}{r^5}\right\rangle & \left\langle-\frac{3yz}{r^5}\right\rangle\\ \left\langle-\frac{3xz}{r^5}\right\rangle & \left\langle-\frac{3yz}{r^5}\right\rangle & \left\langle\frac{r^2-3z^2}{r^5}\right\rangle\end{bmatrix}\begin{bmatrix}\hat{S}_x\\ \hat{S}_y\\ \hat{S}_z\end{bmatrix}\\ &= \hat{\mathbf{S}}\cdot\underline{\mathbf{D}}\cdot\hat{\mathbf{S}}\end{aligned} \tag{3.11}$$

where $\langle\rangle$ denotes the spatial average over the electronic wavefunction.

Defining $D$ and $E$ in the usual manner with respect to the diagonalized tensor:

$$\begin{aligned}D &= \frac{3}{2}D_z\\ E &= \frac{1}{2}(D_x - D_y)\end{aligned} \tag{3.12}$$

and taking the Zeeman field to be along the principal direction of the $D$-tensor, $D$ and $E$ may be written:

$$D = \left(\frac{\mu_0}{4\pi}\right)\frac{3}{4}g^2\mu_B^2\left\langle\frac{r^2-3z^2}{r^5}\right\rangle \tag{3.13}$$

$$E = \left(\frac{\mu_0}{4\pi}\right)\frac{3}{4}g^2\mu_B^2\left\langle\frac{y^2-x^2}{r^5}\right\rangle \tag{3.14}$$

If the spin-spin interaction is purely dipolar (ie. no fine structure or anisotropic exchange interaction) and $E$=0 the energy of the $|+1\rangle$, $|-1\rangle$ states will be $D$ greater than that of the $|0\rangle$ state at zero field.

### Spin-Orbit Interaction

Consider the Hamiltonian in the LS coupling scheme [94]:

$$\mathcal{H} = \mu_B\mathbf{B}\cdot\left(\hat{\mathbf{L}} + g_e\hat{\mathbf{S}}\right) + \xi\hat{\mathbf{L}}\cdot\hat{\mathbf{S}}, \tag{3.15}$$

[5] After p.226 reference [93].

where $\xi$ is an effective spin orbit constant, derived from the potential in which the electrons move. In a pure ground state the angular momentum is zero to first order[6] and the terms involving $\hat{\mathbf{L}}$ vanish. In reality, such states do not exist because components of the excited states are mixed into the ground state. If it is assumed that the interactions between states are small compared to those in the ground state then they may be treated as a perturbation. Writing the states as $|n, m_s\rangle$ (where $n$ is a label for the states, with $n$=0 denoting the ground state), perturbation theory applied to equation 3.15 yields:[7]

$$\begin{aligned} \mathsf{H}(m_s, m_s') &= \langle 0, m_s | \mu_B g_e B_z \hat{S}_z | 0, m_s' \rangle \\ &- \sum_n{}' \left[ \langle m_s | \mu_B \mathbf{B} + \xi \hat{\mathbf{S}} | m_s' \rangle \langle 0 | \hat{\mathbf{L}} | n \rangle \right] \cdot \left[ \frac{\langle n | \hat{\mathbf{L}} | 0 \rangle \langle m_s' | \mu_B \mathbf{B} + \xi \hat{\mathbf{S}} | m_s \rangle}{E_n - E_0} \right] \end{aligned} \tag{3.16}$$

where the Zeeman field has been applied along $\hat{\mathbf{z}}$ and the prime signifies summation over all $n \neq 0$. The orbital terms can be factored out and written as a tensor:

$$\Lambda_{ij} = -\sum_n{}' \frac{\langle 0 | \hat{\mathbf{L}}_i | n \rangle \langle n | \hat{\mathbf{L}}_j | 0 \rangle}{E_n - E_0} \tag{3.17}$$

where $i$ and $j$ are any of the cartesian coordinates. Substitution of equation 3.17 into 3.16 yields:

$$\mathsf{H}(m_s, m_s') = \langle 0, m_s | \mu_B^2 \mathbf{B} \cdot \underline{\mathbf{\Lambda}} \cdot \mathbf{B} + 2\xi \mu_B \mathbf{B} \cdot \underline{\mathbf{\Lambda}} \cdot \hat{\mathbf{S}} + \xi^2 \hat{\mathbf{S}} \cdot \underline{\mathbf{\Lambda}} \cdot \hat{\mathbf{S}} | 0, m_s' \rangle \tag{3.18}$$

The first term on the right hand side is a spin independent constant and hence does not affect the EPR spectrum. Regrouping finally produces:

$$\mathcal{H}_s = \mu_B \mathbf{B} \cdot \underline{\mathbf{g}} \cdot \hat{\mathbf{S}} + \hat{\mathbf{S}} \cdot \underline{\mathbf{D}} \cdot \hat{\mathbf{S}} \tag{3.19}$$

where:

$$\underline{\mathbf{g}} = g_e \underline{\mathbf{1}} + 2\xi \underline{\mathbf{\Lambda}} \tag{3.20}$$

[6]See reference [91] p.746.
[7]See reference [94] p.44.

$$\underline{\mathbf{D}} = \xi^2 \underline{\mathbf{\Lambda}} \tag{3.21}$$

Thus we have a third contribution to the familiar $D$-tensor. Note that the mixing of the excited states into the ground state removes the condition that the orbital angular momentum is zero, hence producing additional Zeeman interactions, as in the first term on the right in equation 3.15. These effects, and the derivation above, are discussed in detail by Abragam and Bleaney in Chapters 19 and 20 [91].

### 3.2.4 Nuclear contributions

Terms 3, 4 and 5 in equation 3.4 reflect the contribution of the nuclei to the spin system. The nuclear hyperfine interaction can be separated into an isotropic and anisotropic term. The isotropic interaction, also called the contact or Fermi interaction, depends on the unpaired electron density at the nucleus – which arises from the $s$ electrons – and is given by:

$$a = A_{\text{iso}} = A_s = \frac{2\mu_0}{3} g_e \mu_B g_N \mu_N |\Phi(0)|^2 \tag{3.22}$$

Values for $|\Phi(0)|^2$ have been determined for many atoms in the gas phase by optical and atomic beam spectroscopy, and also from *ab initio* calculations [95]. The main contribution to the anisotropic dipolar term is produced by the magnetic dipolar interaction between the nucleus and the electron. This is analogous to the dipolar interaction between two electrons given in equation 3.10 with $\hat{\mathbf{S}}_2$ replaced by $\hat{\mathbf{I}}$, $\mu_B$ by $\mu_N$ and $g$ with $g_N$. The treatment on page 26 can then be followed with $\underline{\mathbf{D}} = \underline{\mathbf{A}}_{\text{dip}}$. The hyperfine interaction can then be expressed as the sum of the isotropic and anisotropic portions:

$$\underline{\mathbf{A}} = A_{\text{iso}} \underline{\mathbf{1}} + \underline{\mathbf{A}}_{\text{dip}}. \tag{3.23}$$

Small contributions are made to the hyperfine interaction by polarization, correlation and relativistic effects. These are described in references [21] and [94].

When the hyperfine interaction is axial the number of free parameters reduces to

two. In the principal axis frame the tensor may be given by:

$$\underline{\mathbf{A}} = \begin{pmatrix} A_{\parallel} & 0 & 0 \\ 0 & A_{\perp} & 0 \\ 0 & 0 & A_{\perp} \end{pmatrix} \tag{3.24}$$

This can be separated simply into its isotropic and anisotropic parts, labelled $a$ and $b$ respectively:

$$a = \tfrac{1}{3}(A_{\parallel} + 2A_{\perp}) \tag{3.25}$$

$$b = \tfrac{1}{3}(A_{\parallel} - A_{\perp}) \tag{3.26}$$

$\underline{\mathbf{A}}$ can then also be written as:

$$\underline{\mathbf{A}} = a\underline{\mathbf{1}} + \begin{pmatrix} 2b & 0 & 0 \\ 0 & -b & 0 \\ 0 & 0 & -b \end{pmatrix} \tag{3.27}$$

The nuclear Zeeman interaction is useful as it provides a means of identifying a nucleus directly via its unique $g$-value. In term 4 of equation 3.4 the nuclear $g$-value was given as a scalar. This is not generally true as the electronic wave-function around the atom changes in response to the Zeeman field and produces the equivalent of paramagnetic shielding in NMR (see [91] p.167). This effect has not been observed in diamond therefore the nuclear $g$-value is treated as a scalar and has its atomic value. It is not possible to determine the nuclear $g$-value from EPR measurements of allowed, $\Delta m_s = 1$, transitions as these transitions conserve the nuclear spin quantum number and are independent of the interaction. It is, however, possible to measure this accurately when performing ENDOR experiments.

There is no first order effect from the nuclear electric quadrupole interaction (term 5 of equation 3.4) on the positions of the allowed EPR $\Delta m_s = 1, \Delta m_N = 0$ transitions.[8] There are second order effects giving rise to terms in $m_N$ which change the spacing of

[8]Here $m_N$ denotes the nuclear spin projection quantum number.

all hyperfine lines evenly, and on $m_N^3$ which change the spacings of the outer transitions more than the inner ones. The quadrupole interaction gives a pattern symmetrical about the centre, whereas second order hyperfine effects produce terms in $m_N^2$ and do not. A more important effect of the quadrupole interaction is that the off-diagonal elements give rise to transitions in which $\Delta m_N = \pm 1, \pm 2$ that would otherwise be forbidden. Using these second order effects quadrupole coupling parameters can be deduced from the EPR spectrum, but ENDOR again provides a means for the direct measurement of this effect and is more accurate.

## 3.3 ENDOR

In cases where there is a hyperfine interaction there is the possibility of making electron nuclear double resonance experiments.

ENDOR was first performed by George Feher in 1957 [96]. Feher was studying the EPR of electrons bound to donor atoms in silicon and was attempting to resolve the hyperfine interaction from the 5% abundant $I=\frac{1}{2}$ $^{29}$Si nuclei. Because of the size of the electron orbit it can couple to many $^{29}$Si nuclei, and the nuclei induce a whole range of hyperfine fields at the electron depending upon its position. This produces broadening of the resonance and limits resolution.

Feher recognized that each Si nucleus experienced the field of only one electron and that the resonances would therefore be sharp. The problem was that the nuclear spin concentrations were too low to perform NMR. He then devised an ingenious method of detecting the nuclear resonance by means of its effect on the electron spin resonance. It is accomplished by monitoring the intensity of an EPR transition while applying a variable frequency rf field (in general) normal to the Zeeman and microwave fields. When the rf frequency equals that required for an NMR transition, between the nuclear spin sublevels, the relaxation mechanism in the system is altered and a change in the intensity of the EPR signal is observed. This technique maintains the resolution but increases sensitivity and was termed *electron nuclear double resonance*

or ENDOR. The increased sensitivity of ENDOR over NMR stems from the following:[9]

- The energy of the EPR quantum is much larger than that of the NMR quantum, and much greater Boltzmann population differences are therefore possible for the more widely spaced energy levels.

- The rate of energy absorption is greater at microwave frequencies than at radio frequencies (see reference on p.372 of [97]).

- The nucleus sees the sum of the Zeeman field and the field induced by the electron at the nucleus which is typically of the order of $10^3$–$10^5$ mT. The additional field enables the nucleus to be more effective at altering the intensity of the EPR line during an ENDOR experiment. The effect is termed "enhancement".

In addition to its increased sensitivity to the hyperfine parameters, ENDOR allows:

- positive identification of the nuclei through measurement of the nuclear $g$-factor; and

- direct measurement of the interaction of the nucleus with the total electric field gradient at the nucleus ie. the quadrupole interaction.

The high selectivity of ENDOR can produce significantly simpler spectra than EPR and greatly aids in the interpretation of complicated spectra like that of the $[N_3V]^0$ centre [98].

For a system with $I \geq \frac{1}{2}$ having axial symmetry, and magnetic dipole and electric quadrupole hyperfine structure, the ENDOR quantum for the transition $m_N \leftrightarrow m_N{-}1$ to first order is:

$$|h\nu_N| = Am_s + \frac{A_\parallel A_\perp^2}{2AG}\left[m_s^2 - S(S+1)\right] - G_N + P(2m_N - 1) + \cdots \qquad (3.28)$$

where $G{=}g\mu_B B$ and the nuclear Zeeman interaction is $G_N{=}g_N\mu_N B$. If the principal axes of the $A$ and $P$-tensors are assumed to coincide and the Zeeman field is set

[9] According to Weil *et al.* p.372 [97].

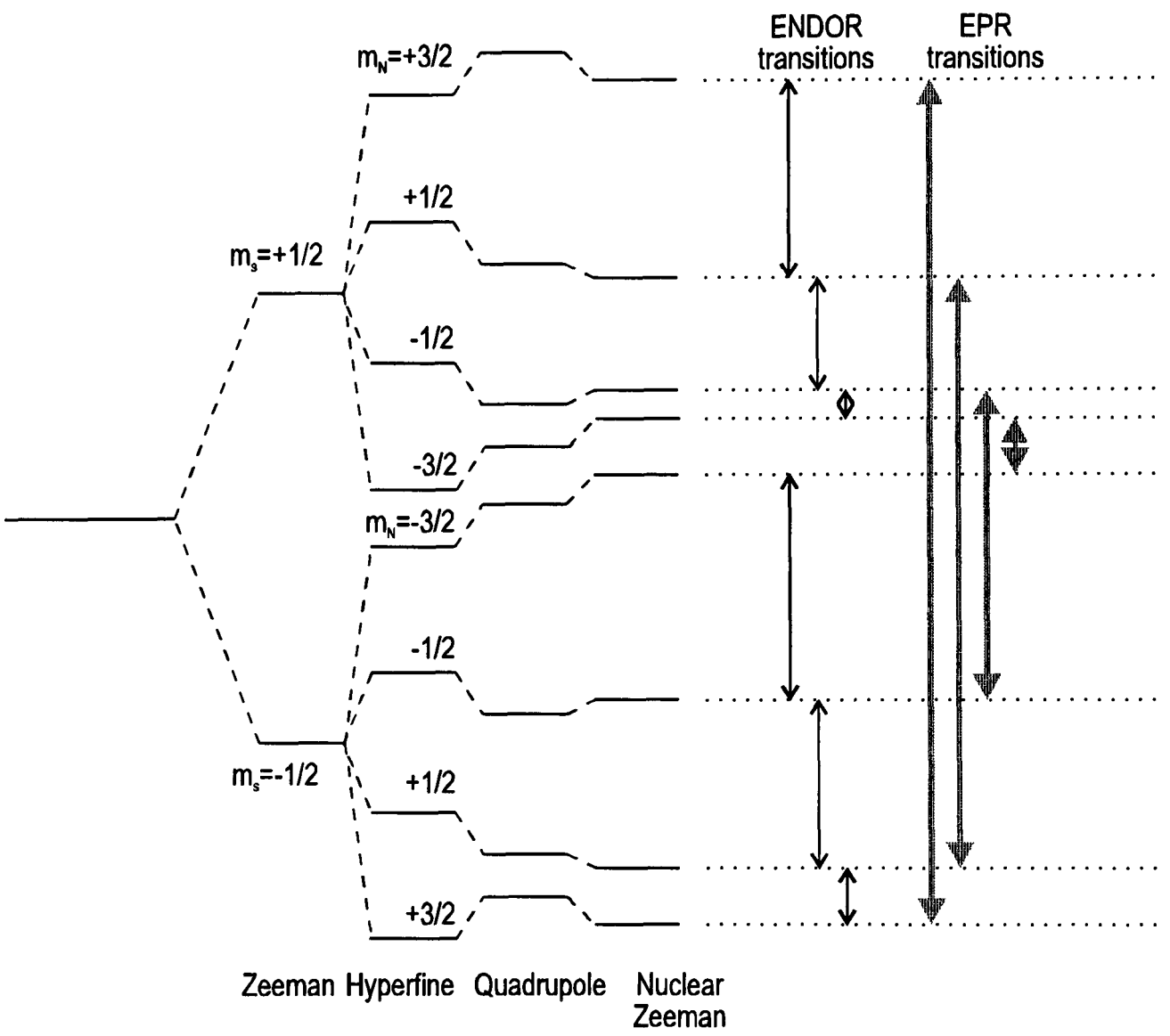



Figure 3.1: Schematic energy levels for a system with hyperfine and quadrupole interactions, showing the effect of applying successively the electronic Zeeman, the hyperfine, the quadrupole and finally the nuclear Zeeman interactions. The possible ENDOR and allowed EPR transitions are labelled.

parallel to $A_{||}$ then $A = A_{||}$ and $P = P_{||}$ (the general formula is given on p. 227 of [91]). The energy levels for the system are given in Figure 3.1 showing the effect of successively switching on the electronic Zeeman, the hyperfine, the quadrupole and finally the nuclear Zeeman interactions. The possible ENDOR and allowed EPR transitions are labelled. Examination of equation 3.28 and Figure 3.1 shows that the ENDOR transition depends on the nuclear hyperfine interaction, the nuclear Zeeman interaction, the effective electron spin, and the quadrupole interaction. The parameters, including the effective spin, can be extracted to a precision of a few kHz by measurement of the ENDOR transitions from a number of EPR lines and in different field directions.

### 3.3.1 Continuous wave ENDOR

ENDOR experiments rely on the detection of the change in the EPR signal produced by the modification of the spin population through the driving of a nuclear transition. If the change in the EPR signal intensity remains constant while the nuclear transition is pumped continuous wave ENDOR is possible. If, however, the EPR signal returns rapidly to its original value then only a transient response is measurable. Feher's original experiment [96] detected the transient response, however, all ENDOR measurements in this thesis employed continuous wave or steady state detection.[10] A brief outline of the basic ENDOR mechanism will be given below, while a detailed introduction is given by Abragam and Bleaney on p.243ff [91].

To examine the conditions and mechanisms for continuous wave ENDOR consider a simple four level system with $S = \frac{1}{2}$ and $I = \frac{1}{2}$. If the assumption is made that the hyperfine interaction is small compared to the electronic Zeeman interaction then the energy levels will look as in Figure 3.2. At thermal equilibrium the populations are approximately $1 \pm \delta_e/2$ for levels $m_s = \mp\frac{1}{2}$, where $\delta_e = g\mu_B B/kT = h\nu_e/kT$. The small population difference $\delta_N = g_N\mu_N B/kT = h\nu_N/kT$ has been ignored. $\nu_e$ and $\nu_N$ are the EPR and NMR transition frequencies. Four relaxation paths between the levels are considered, each with a characteristic relaxation time:

[10] Transient ENDOR responses are discussed on page 365 of [93].

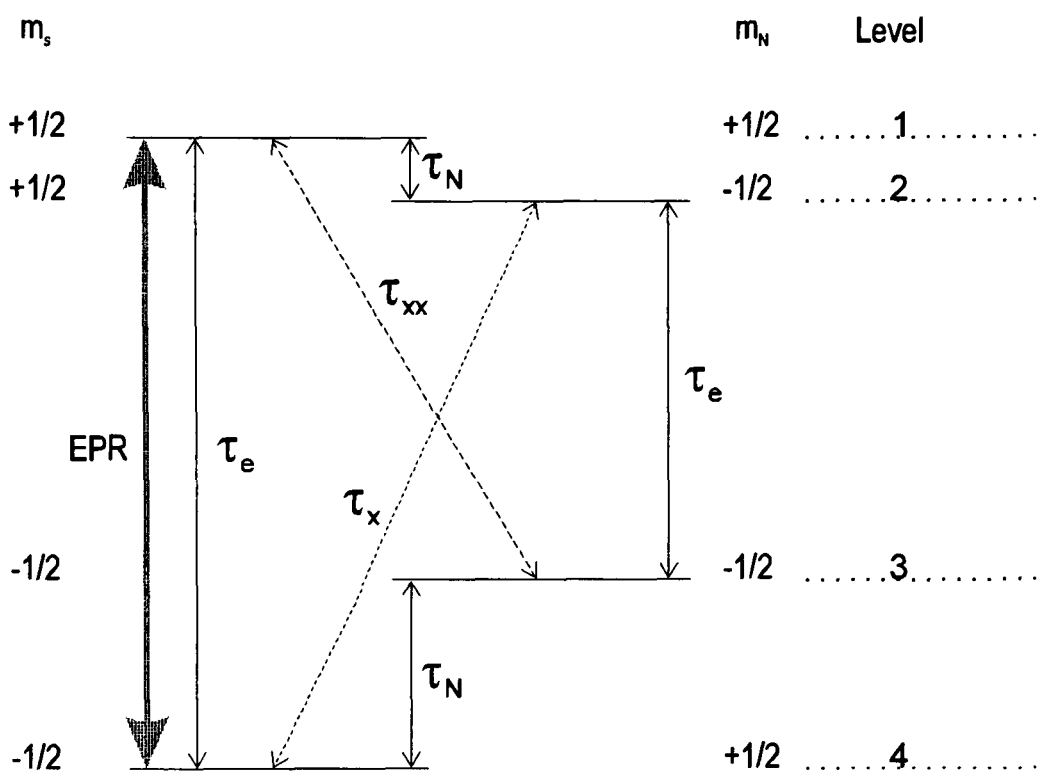



Figure 3.2: Four possible relaxation paths in a system with $S=\frac{1}{2}$ and $I=\frac{1}{2}$. When the labelled EPR transition is saturated ENDOR is observable from nuclear transitions between levels $1 \rightarrow 2$, and $3 \rightarrow 4$. In the absence of $\tau_{xx}$ only transitions between levels $1 \rightarrow 2$ would be seen.

- $\tau_e$, the electronic spin-lattice relaxation time;
- $\tau_N$, the nuclear spin-lattice relaxation time;
- $\tau_x$, spin flip-flop relaxation time, produced by transitions with $\Delta m_s + \Delta m_N = 0$.
- $\tau_{xx}$, spin flop-flop relaxation time, produced by transitions with $\Delta m_s + \Delta m_N = 2$.

In general $\tau_N >> \tau_x, \tau_{xx} > \tau_e$. When the EPR transition between levels 1 and 4 is saturated the populations of the two levels are equalized. The spins in the upper level can return to level 4 by:

i) following the direct vertical path, with rate $1/\tau_e$;

ii) the slower indirect path $1 \rightarrow 2 \rightarrow 4$, with a rate of $1/(\tau_N + \tau_x)$; or

iii) the other indirect path $1 \rightarrow 3 \rightarrow 4$, with a rate of $1/(\tau_N + \tau_{xx})$.

If an rf field which induces transitions at a rate much faster than $1/\tau_x$ is applied at the nuclear resonance frequency corresponding to transitions between levels 1 and

2, then $\tau_x$ becomes the dominating factor controlling return path ii) and the rate is reduced to $1/\tau_x$. Another relaxation path is therefore opened which can add to the direct path and reduce the saturation, thereby producing a change in the EPR signal. A change in the EPR response will also be observed when the rf field which induces transitions between levels 3 and 4 is applied, but in this case it is the flop-flop relaxation, $\tau_{xx}$, which contributes. As a different relaxation mechanism is involved the amplitude of the response at the two ENDOR frequencies need not be the same. In the work in this thesis additional relaxation paths were often observed (see §5.5.1) resulting in the detection of many nuclear transitions when saturating only one EPR transition.

## 3.4 Physical interpretation of parameters

### 3.4.1 Linear combination of atomic orbitals

Molecular orbital theory has been applied to the analysis of diamond in varying degrees of sophistication by a number of authors [99, 53, 100, 101, 102, 103].[11] It has been shown that it is possible to describe the structure of a defect and its electron distribution using simple Slater atomic orbitals [99, 53]. Although the molecular orbital treatment is simple, it compares well with complicated theoretical calculations. In fact, this simple approach is one of the few ways of relating hyperfine constants to theoretical models. This is because most cluster calculations suffer from their use of a basis of pseudo-wavefunctions which provide a poor representation of the actual wave function near the nucleus but the hyperfine interaction, by its very nature, relies heavily on the form of the wavefunction near the nucleus.

In this section, the molecular orbital approach to analyzing the hyperfine interaction will be described. The theory is applied in Chapters 5 and 6.

It is assumed that the unpaired-electron wavefunction can be constructed as a

[11] All the papers on this topic are too numerous to list here, however further references are given in Chapters 2, 5, 6, 7 and 8.

linear combination of atomic orbitals (LCAO) written as:

$$\Phi = \sum_i \eta_i \phi_i \tag{3.29}$$

where the summation is over various atoms on which the unpaired-electron probability density is non-zero. $\phi_i$, the atomic orbital on the $i^{\text{th}}$ site, was constructed from $2s$ and $2p$ hydrogenic orbitals for C or N atoms:

$$\phi_i = \alpha_i \Psi_{2s} + \beta_i \Psi_{2p} \tag{3.30}$$

Orthonormality of the wavefunctions $\phi_i$ and $\Phi$ requires that:

$$\alpha_i^2 + \beta_i^2 = 1 \tag{3.31}$$

$$\sum_i \eta_i^2 = 1 \tag{3.32}$$

The hyperfine coupling to a nucleus can be separated into an isotropic and a traceless part (see equation 3.27 and [104]):

$$\hat{\mathbf{S}} \cdot \underline{\mathbf{A}} \cdot \hat{\mathbf{I}} = A_s \hat{\mathbf{S}} \cdot \hat{\mathbf{I}} + \hat{\mathbf{S}} \cdot \underline{\mathbf{A}}_p \cdot \hat{\mathbf{I}} \tag{3.33}$$

The isotropic or contact term is given by:

$$A_s \hat{\mathbf{S}} \cdot \hat{\mathbf{I}} = \frac{2\mu_0}{3} g\, g_N \mu_B \mu_N \left|\Phi(0)\right|^2 \hat{\mathbf{S}} \cdot \hat{\mathbf{I}} \tag{3.34}$$

This requires a non-zero amplitude of the unpaired electron wave function at the nucleus, produced mainly by $s$-electron density. The anisotropic term is produced by the dipolar interaction between the unpaired electron and various nuclei as described in §3.2.4. When the dipolar hyperfine interaction is axially symmetric it is often assumed to arise from $2p$-electrons and the term becomes:

$$\hat{\mathbf{S}} \cdot \underline{\mathbf{A}}_p \cdot \hat{\mathbf{I}} = -\left(\frac{\mu_0}{4\pi}\right)(g\, g_N \mu_B \mu_N)\langle r_{2p}^{-3}\rangle(2\hat{S}_z\hat{I}_z - \hat{S}_x\hat{I}_x - \hat{S}_y\hat{I}_y) \tag{3.35}$$

In the simplest case, the hyperfine interaction my be treated as arising from the fraction of the unpaired electron orbiting the nucleus of interest, $i$ say. Then $|\Phi(0)|^2 = (\eta_i\alpha_i)^2 |\Psi_{2s}(0)|^2$ and $\langle r_{2p}^{-3}\rangle = (\eta_i\beta_i)^2\langle\Psi_{2p}|r^{-3}|\Psi_{2p}\rangle$. The constants $(\eta_i\alpha_i)^2$ and $(\eta_i\beta_i)^2$ can be obtained if the scalars $|\Psi(0)|^2$ and $\langle r_{2p}^{-3}\rangle$ are known. These are not known from experiment but have been calculated from Hartree-Fock-Slater atomic orbitals [95] for the free atom and are used to calculate $A_s^t$ and $A_p^t$ for 100% occupancy of the $2s$ and $2p$ orbital. Division of the measured hyperfine parameters by the theoretical values gives:

$$\frac{A_s}{A_s^t} = (\eta_i\alpha_i)^2 \tag{3.36}$$

$$\frac{A_p}{A_p^t} = (\eta_i\beta_i)^2 \tag{3.37}$$

Application of the normalization conditions (equations 3.31 and 3.32) gives the fraction of the unpaired electron appearing on atom $i$:

$$f_i \equiv \eta_i^2 \tag{3.38}$$

and the hybridization ratio:

$$\lambda_i \equiv (\beta_i/\alpha_i)^2 \tag{3.39}$$

The hybridization ratio can be used to estimate the bond angles using the assumption that the bonds formed by the hybridization of $p$ and $s$ orbitals on an atom are orthogonal to each other. Baker and Newton [104] caution that the estimate is crude and list the following factors that have been omitted:

1. The contribution to $A_s$ arising from the polarization of the core $s$-electrons by the unpaired $p$-electron which has the form:

$$A_s^c = \left(\frac{\mu_0}{4\pi}\right) g g_N \mu_B \mu_N \langle r_{2p}^{-3}\rangle c_p^2 K \tag{3.40}$$

   where $K \sim -0.1$ for fluorine atoms.

2. The anisotropic term has contributions from dipolar interactions with unpaired

electrons on other atoms. These are expected to be small owing to the $r^{-3}$ dependence of the dipolar interaction.

3. There are contributions through hyper-conjugation: when there is an enhancement in the coupling between an orbital containing the unpaired electron and an orbital on the nucleus responsible for the hyperfine coupling because of a correspondence in symmetry between the wavefunctions.

4. For distant nuclei there is both direct transfer and indirect transfer of spin polarization through intervening atoms.

In diamond it is often found that $\sum_i f_i$ is not quite unity. The omissions above have some effect, but the main contributions come from:

i) the accuracy of the atomic parameters used in the calculation;

ii) the possible omission of neighbouring atoms where some electron density might be present; and

iii) neglect of overlap in the normalization condition in equation 3.32.

Point ii) can be countered by measurement of ligand hyperfine interactions in $^{13}C$ isotopically enriched samples. The contribution from point iii) can be estimated. If it is assumed that the defect may be approximated by a homonuclear di-atomic *defect molecule* then the coefficients $\eta_i$ for the bonding and antibonding molecular orbitals are:[12]

$$\begin{aligned} \eta_1 &= \eta_2 = \frac{1}{\sqrt{2(1+S)}} \quad \text{bonding} \\ \eta_1 &= -\eta_2 = \frac{1}{\sqrt{2(1-S)}} \quad \text{antibonding} \end{aligned} \tag{3.41}$$

where $\mathcal{S}$ is the overlap integral:

$$\mathcal{S} = \langle \phi_1 | \phi_2 \rangle \tag{3.42}$$

Thus, if there were no overlap ($\mathcal{S}$=0) then $f_i = \eta_i^2 = 0.5$, while increasing the value of $\mathcal{S}$ will decrease $f_i$. The value of $\mathcal{S}$ depends on the hybridization ratio, the type

[12]See Atkins p.254 [20] for Schmidt orthogonalization.

of atom, the distance separating the atoms, and the choice of basis functions. Its dependence on these factors is investigated in Chapter 5 for the $[N–C]^0$ and $[N–N]^+$ defects and further discussion will be suspended until then.

### 3.4.2 Bond angles and extensions

Assuming that the hybridization ratios calculated from equation 3.39 are known for two neighbouring atoms it is possible to deduce the bond angles and extensions. In Figure 3.3 the atoms of interest are shown incorporated into the diamond lattice.[13] The defect in Figure 3.3 has $C_{3v}$ symmetry about the line joining $X$ and $Y$. To calculate the extension of the $X$–$Y$ bond relative to the normal C–C bond length, it is assumed that the six back bonding carbon atoms (see also the stippled atoms in Figure 5.11 page 100) are fixed in the undistorted diamond lattice positions and that the atoms $X$ and $Y$ are allowed to displace towards their basal planes. Following the discussion of Coulson [105] it is assumed that the orthogonality conditions are applicable and valid, such that the angles $\omega_{mn}$ between the $m^{\text{th}}$ and $n^{\text{th}}$ $sp$-hybridized orbitals on any atom are determined from the condition:

$$\lambda_m \lambda_n \cos\omega_{mn} + 1 = 0 \tag{3.43}$$

where $\lambda_m$ and $\lambda_n$ are the hybridization ratios for these orbitals (see §3.4.1). The $C_{3v}$ symmetry of the defect ensures that the angles $\theta_X$ ($\theta_Y$) and $\phi_X$ ($\phi_Y$) in Figure 3.3 are related by:

$$\cos\phi_{X,Y} = \frac{3\cos^2\theta_{X,Y} - 1}{2} \tag{3.44}$$

Hence it can be shown that from equations 3.43 and 3.44 that $\theta_X$ ($\theta_Y$) is given by:

$$\cos\theta_{X,Y} = -\frac{1}{\sqrt{3 + 2\lambda^2_{X,Y}}} \tag{3.45}$$

[13] $X$ and $Y$ here, could be considered to be the nitrogen and unique carbon of the $[N–C]^0$ centre, or the two nitrogens of the $[N–N]^+$ centre in Chapter 5.

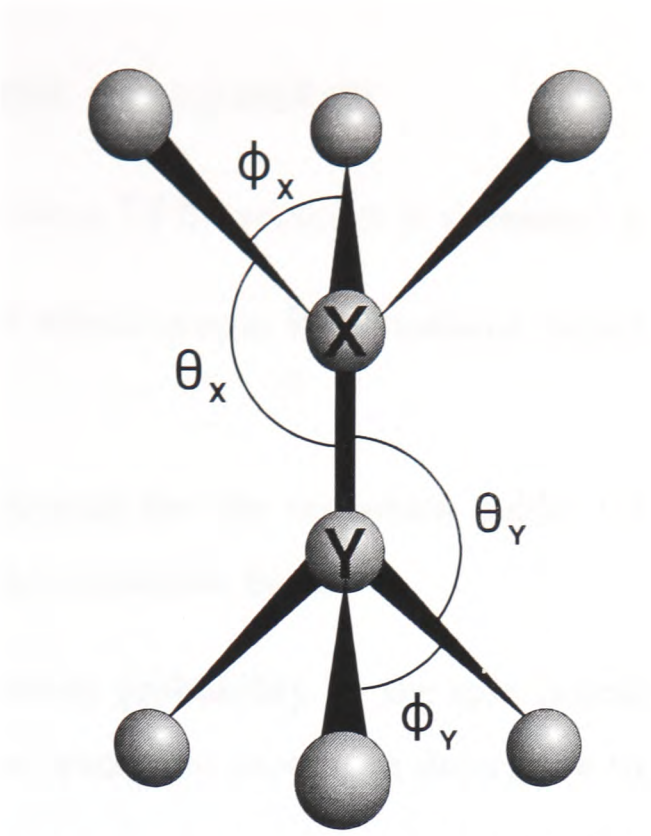



Figure 3.3: Model $C_{3v}$ defect used for bond-extension calculations.

where $\lambda_X$ ($\lambda_Y$) is the hybridization ratio for the unique orbital on atom $X$ ($Y$). The negative square root was chosen to place the angle in the second quadrant. Following simple geometrical considerations the displacement of $X$ or $Y$ towards their basal planes is calculated to be:

$$\Delta_{X,Y} = \frac{d}{3}\left[1 - \frac{2}{\sqrt{1+\lambda_{X,Y}^2}}\right] \tag{3.46}$$

where $d$ is the undistorted C–C bond length. The hybridization ratios can therefore be used to estimate bond angles and approximate bond extensions.

There is a caveat when using this method as the deduction of bond admixtures and angles depends upon the reliability of free atom calculations and their applicability to covalently bonded solids [103, 104]. Edwards and Fowler [106] have illustrated a case in $SiO_2$ where this method breaks down. Using self-consistent calculations on the E′ and $P_b$ centres they demonstrated that the molecular orbitals do not necessarily point towards the ligand, and that neutral-atom wavefunctions were not necessarily appropriate when considering defects in partially ionic materials. Diamond is, however, the archetypal covalent solid and neutral-atom wavefunctions have been widely applied with a high degree of success in the analysis of hyperfine coupling constants.

## 3.5 Simulation of spectra

When simulating field-swept EPR spectra it is necessary to:

1. Construct a set of effective spin Hamiltonians consistent with the lattice symmetry.

2. Solve each Hamiltonian for the transition fields, transition probabilities, and energy levels at the transition fields.

3. Weight each transition probability by the spin populations in the energy levels between which the transition occurs, to determine the intensity.

4. Convolute each transition with a shape function to account for the physical line shape and the effect of the spectrometer detection technique.

Each of these points is explored below.

### 3.5.1 Lattice symmetry

#### The diamond lattice

The diamond lattice has $T_d$ symmetry[14] and there are therefore twenty-four operations which transform the lattice back onto itself. The effect of the crystal symmetry on a defect introduced into the lattice is to incorporate it in twenty-four different orientations. Let us assume that the defect is paramagnetic, has a highly anisotropic $g$-tensor, spin of one half, and that it has no symmetry of its own (ie. $C_1$). When a magnetic field is applied it will therefore produce a spectrum consisting of a maximum of twenty-four lines. In general a defect has internal symmetry which renders its magnetic resonance spectrum invariant under some of the diamond rotations, hence reducing the number of lines in the spectrum. The effect of the inclusion of defects

[14]As magnetic resonance can not in general distinguish between $S_4$ and $C_4$, and $\sigma_d$ and $C_2'$, the group operations reduce to those of O and can be realized in the 3D matrix rotation representation (See reference [107],p.181). For simplicity the group will always be referred to as $T_d$ here.

of different symmetry on the magnetic resonance spectrum is explored by Cox who produces a very useful table summarizing this (reference [21] p.30).

When simulating a spectrum the diamond symmetry is reflected by rotating the interaction tensors of the effective spin Hamiltonian using the 3D rotation matrix representation of the $T_d$ group. For example, assume that the effective spin Hamiltonian is:

$$\mathcal{H} = g\mu_B \hat{\mathbf{S}} \cdot \mathbf{B} + \hat{\mathbf{S}} \cdot \underline{\mathbf{A}} \cdot \hat{\mathbf{I}}$$

then $\underline{\mathbf{A}}$ will be transformed as:

$$\underline{\mathbf{A}}' = R^{-1} \underline{\mathbf{A}} R \tag{3.47}$$

for all $R$ in the representation producing a set of 24 Hamiltonians. $g$ is not explicitly rotated above as it is isotropic. Each Hamiltonian produced must then be diagonalized for a specific Zeeman field direction and microwave frequency.

### Ligand hyperfine interactions

When some of the ligand atoms have nuclei with non-zero spin a hyperfine interaction is produced (see §3.2.4). This generally acts as a perturbation on the Hamiltonian producing a splitting of each resonance line. If there is more than one nearby atom with non-zero spin more than one interaction occurs and, upon simulation of this interaction, the following points must be considered:

1. The defect Hamiltonian must be constructed to account for all the ligand hyperfine interactions that occur.

2. The intensities of the interactions must be scaled according to the probabilities of occurrence of the isotope.

In diamond the $^{13}C$ isotope has a nuclear spin of $\frac{1}{2}$ and occurs in a natural abundance of 1.11%. The hyperfine interaction splits each energy level into two and produces a pair of satellite lines on either side of the main transition. Synthetic diamonds need not have the natural abundances if isotopically enriched starting material is employed in the synthesis process (see Chapter 8). Diamonds containing the $^{15}N$

isotope are of particular interest as the nuclear spin of $\frac{1}{2}$ does not permit nuclear quadrupole interactions. An example is given by the [N–V]$^-$ centre where it is difficult to interpret the spectra as the nitrogen quadrupole interaction is larger than the hyperfine interaction. Here spectroscopy of a $^{15}$N enriched sample would facilitate the deconvolution of these interactions.

Consider an intrinsic paramagnetic defect surrounded by four equivalent carbon sites. Most of the time there will be no hyperfine interactions, however, each site has a 1.11% chance of containing a $^{13}$C nucleus and hence producing a hyperfine interaction. Let the total number of atoms in the crystal be N and let M of them be $^{13}$C. As the sites are being treated as equivalent this is strictly a case of sampling without replacement, and the probability of obtaining $x$ $^{13}$C nuclei in a sample of $n$ equivalent nuclei is:

$$f(x) = \frac{\binom{M}{x}\binom{N-M}{n-x}}{\binom{N}{n}} \tag{3.48}$$

This is the hypergeometric distribution (reference [108] p.1208). In EPR the populations sampled are of the order of Avogadro's number, and the hypergeometric distribution reduces to the case of sampling with replacement:

$$f(x) = \binom{n}{x}\left(\frac{M}{N}\right)^x\left(1-\frac{M}{N}\right)^{n-x} \tag{3.49}$$

If we identify $p = \frac{M}{N}$ with the probability of having one $^{13}$C, and let $q = 1-p$ then the well known Binomial or Bernoulli distribution results:

$$f(x) = \binom{n}{x} p^x q^{n-x} \tag{3.50}$$

Thus equation 3.50 can be used to determine the probability of having zero, one, two, three or four $^{13}$C atoms in a set of four equivalent nearest neighbours. Once the probability of having $n$ neighbouring $^{13}$C atoms is known, the EPR intensities

for transitions corresponding to each configuration can be scaled according to the probability of obtaining that configuration.

When the hyperfine interaction reduces the symmetry from tetrahedral equation 3.50 still holds with respect to crystallographic sites, however, care must be taken when calculating the EPR intensities. Assume that a defect has tetrahedral crystallographic symmetry, with a $\langle 111 \rangle$ axial hyperfine interaction between the paramagnetic electrons and the $^{13}C$ ligand. Choose a cubic system of axes, placing the defect at the origin. The ligand atoms will then occupy the $(1,1,1)$, $(\overline{1},1,\overline{1})$, $(1,\overline{1},\overline{1})$, and $(\overline{1},\overline{1},1)$ sites. If the Zeeman field is directed along $\langle 100 \rangle$ the interaction will be equivalent for all four sites and the case discussed above will apply. If the field is placed along the $\langle 111 \rangle$ direction there will be one unique site $(1,1,1)$ and three equivalent sites making angles of 109.5° with the Zeeman field. The four-fold degeneracy on the transitions will therefore be lifted, leaving a threefold degenerate transition and a non-degenerate transition. The lines in the spectrum will occur in the ratio 3:1 for interaction with the $^{13}C$ isotope, while they will still be degenerate for the $^{12}C$ isotope. The total intensity, summing all the degenerate and non-degenerate transition intensities, must be scaled by the probability of the configuration occurring derived from the isotopic abundances.

### 3.5.2 Transition probabilities and calculation of intensities

The transition probability per unit time is calculated using the perturbation Hamiltonian:

$$\mathcal{H}_1 = -\hat{\boldsymbol{\mu}} \cdot \mathbf{B}_1(t) \tag{3.51}$$

and is performed automatically by the simulation program *EPR.FOR* [109]. For a discussion of the calculation of the transition probability per unit time, using time dependent perturbation theory for a system with $S{=}\frac{1}{2}$ and $\mathbf{B}_1 \perp \mathbf{B}_{\text{Zeeman}}$, see p.98ff of reference [91]. For this section it will be assumed that the transition probability per unit time between levels $i$ and $j$ has been calculated, and will be denoted by $\omega_{ij}$.

The intensity of an EPR transition depends on its transition probability and on

the population difference between the energy levels:

$$I_{ij} = \omega_{ij}(N_i - N_j) \tag{3.52}$$

Assume a system of $n$ energy levels, $\epsilon_i$, in thermodynamic equilibrium. Then:

$$I_{ij} = N\frac{\omega_{ij}}{\mathcal{Z}}(e^{\epsilon_i/kT} - e^{\epsilon_j/kT}) \tag{3.53}$$

with $\mathcal{Z}$ the canonical partition function, $k$ the Boltzmann constant, $T$ the absolute temperature, and $N$ the total number of spins in the ensemble.

Equation 3.53 illustrates that, for correct calculation of the intensity of a system, the probability for the occurrence of each transition must be divided by the partition function for the system. This result is of importance when generating mixed isotope spectra. Consider the case of the $[V]^-$ system (§8.4.2). The system has an effective spin of $\frac{3}{2}$ and therefore has four energy levels in the absence of any hyperfine couplings. When a nearest neighbour $^{13}C$ is introduced the interaction acts as a perturbation splitting each level into two, producing eight levels. When working at X-band the microwave quantum has an equivalent temperature of 0.43K, thus at room temperature $e^{h\nu/hT} \approx 1$ and the partition function for the bare system is $\sim 4$, while for the system with one $^{13}C$ atom it is $\sim 8$. To add the spectra correctly for zero and one $^{13}C$, the transition probabilities of the bare system must be divided by four, while those of the $^{13}C$ system must be divided by eight. In this specific case each spectrum must also be scaled in proportion to the isotopic abundances §3.5.1.The effect of the partition function at low temperatures on the observed spectrum is discussed in §7.3.1 and §6.8.2 examines the effect on the EPR spectrum when a non Boltzmann distribution of spin populations occurs.

# Chapter 4

# Experimental methods

## 4.1 Introduction

In this thesis the main spectroscopic techniques employed were those of electron paramagnetic resonance (EPR), and electron nuclear double resonance (ENDOR). These were combined with optical excitation allowing them to be performed on previously inaccessible systems. The main techniques were complemented by optical absorption spectroscopy. EPR measurements were performed at Q-band ($\nu \approx 33$ GHz) and X-band ($\nu \approx 9$ GHz). ENDOR and combined optical/magnetic resonance measurements, were performed using the X-band spectrometer. Each spectrometer will be discussed in turn on the following pages.

The basic construction of continuous wave EPR or ENDOR spectrometers has remained almost unchanged over the last twenty-five years, except for the introduction of microwave amplifiers and mixers. However, the quality and sensitivity of the microwave and electronic components used has increased greatly.

As the implementation of an EPR and ENDOR spectrometer is well documented [110], it will suffice to define briefly the instruments used, and then concentrate on additions and improvements made during this work. Attention will also be paid to some particular experimental problems and their resolution. A general introduction to EPR implementation is provided by Weil, Wertz and Bolton [97], while an in-depth treatise presenting a systematic study of each component in the bridge is given by

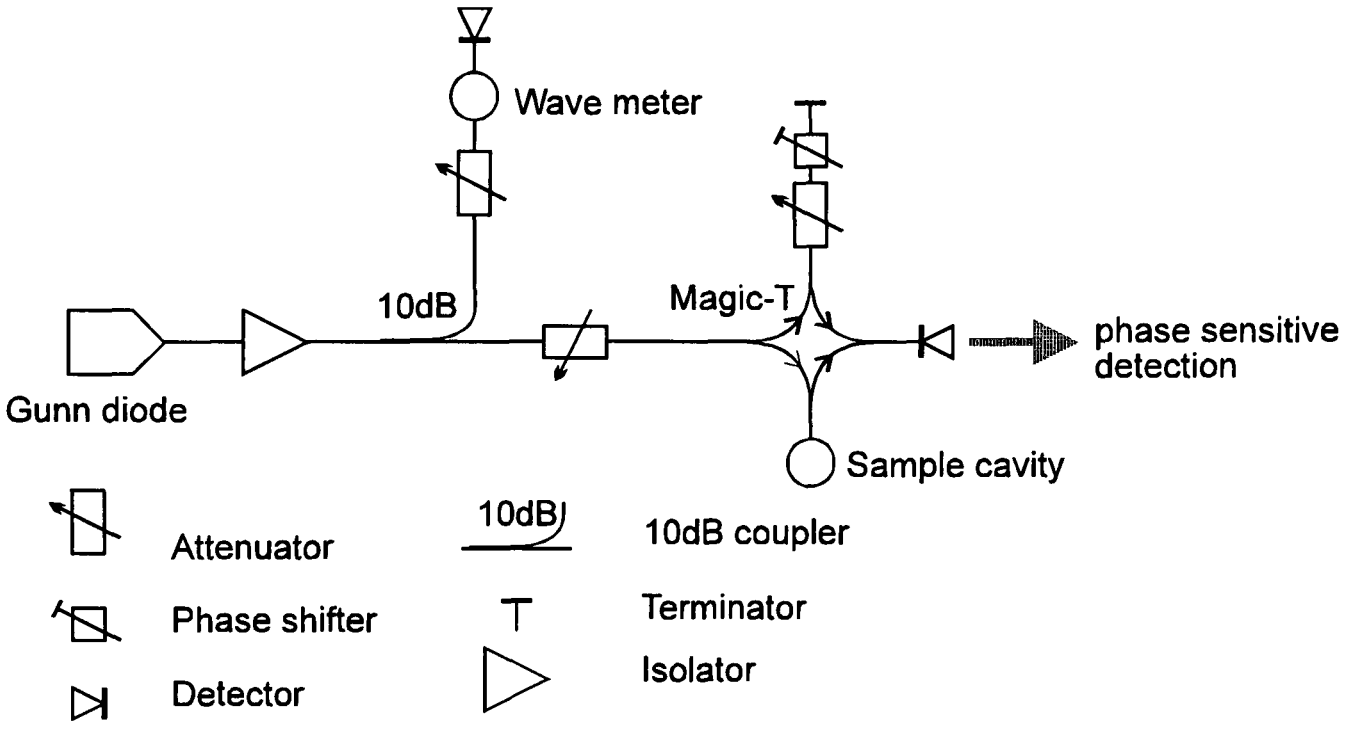



Figure 4.1: Schematic of the Q-band magic-T based bridge.

Poole [110].

## 4.2 Q-band

### 4.2.1 Description of spectrometer

The Q-band, magic-T based, homodyne spectrometer is depicted schematically in Figure 4.1. An almost identical device has been described in detail by O'Connell [111]. It was capable of working in absorption or dispersion mode, and of detecting either the first or second harmonic of the field modulated EPR signal. The $TE_{102}$ cylindrical cavity used is depicted in Figure 4.2.

The sample was cooled using a Clarendon-built immersion cryostat. This could be filled with liquid nitrogen giving a temperature of 77K, or liquid helium producing a temperature of 4.2K at atmospheric pressure, and temperatures between 1.5 and 4.2K when the vapour pressure was lowered by pumping with a large displacement rotary pump.[1] A continuous flow Oxford Instruments system[2] was employed to attain

[1] Edwards Speedivac high vacuum pump, single stage, model ISC 900.
[2] Oxford Instruments model CF200.

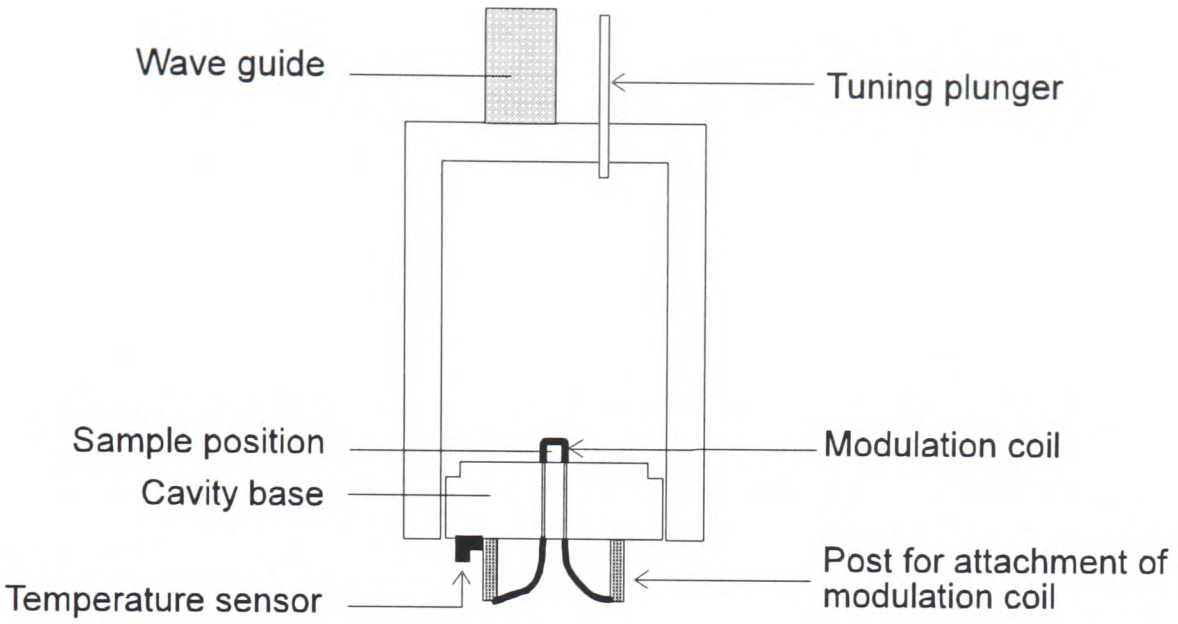



Figure 4.2: Detail of Q-band EPR cavity showing sample position, temperature sensor and modulation coil.

temperatures between 3.5K to 300K. A silicon diode[3] temperature sensor was used for the accurate temperature measurement required for the depopulation experiments in Chapter 7. When connected to a 10 $\mu$A current source the diode exhibited a well defined voltage change with temperature, measuring between 1K and 470K with a repeatability of 0.03K, and sensitivities between 60 mV/K at 4.2K and 2.2 mV/K at 300K. The voltage was measured using a six-figure volt meter.[4] The diodes are small ($2\times2\times1$ mm), accurate, inexpensive and easy to install. Their disadvantage is a sensitivity to magnetic fields, therefore, before measurement, both the static and modulating fields had to be switched off. The diode was calibrated by the Clarendon Laboratory Cryogenics Group. It was placed in contact with the brass base of the EPR cavity, which was in thermal contact with the sample (see Figure 4.2).

One cryogenic problem worthy of note is *drip*. This occurs when too much exchange gas is introduced into the EPR cavity and some of that gas condenses inside the cavity. The condensed helium drips from the roof of the cavity and produces spikes in the EPR spectrum. These spikes appear to follow a random pattern. Once identified, drip can generally be removed – even while cold – by pumping some of the

[3]Oxford Instruments model PD20004.
[4]Prema model 6001.

exchange gas out of the cavity.

The Q-band machine was plagued with a poor baseline. This was caused by pickup of stray modulation and its transmission to the phase sensitive detector. In an attempt to reduce stray 115 kHz fields, the modulation source[5] was moved away from the demodulation electronics and a triple shielded cable, grounded at the insert, was used to connect the source to the insert. In previous experiments the insert to the cryostat had been used as the return path for the modulation current. This was changed, and separate cables were used for the live and return. Some decrease in pickup was achieved.

## 4.3 X-band

### 4.3.1 Description of original bridge

The reference-arm bridge X-band spectrometer has been developed over a number of years [22, 21]. Figure 4.3 shows a schematic of the original microwave bridge with numbers indicating the points where the modifications, discussed in the following sections, were made.

### 4.3.2 Changes to the microwave circuit

The microwave circuit was improved by the replacement of the 3-port circulator and microwave amplifier (1 and 2 in Figure 4.3) with new models having better performance characteristics. The replacement circulator[6] had a band width of $\pm 0.5$ GHz centred around 9.5 GHz, a maximum insertion loss of 0.4 dB, and an interport isolation of between 25 and 28 dB. The amplifier[7] had a noise level of 1.37 dB and a gain of 29.8 at 9.5 GHz. The inclusion of a low noise, high gain microwave amplifier effectively eliminates detector noise,[8] however, there is an enhanced sensitivity to source

[5]Clarendon Electronics Workshop EW824.
[6]Quasar Microwave Technology model QWC18-9-5-30.
[7]Miteq model AFS-08501160-16-108-4.
[8]A discussion of the use of microwave amplifiers is given in references [112, 113, 114, 115].

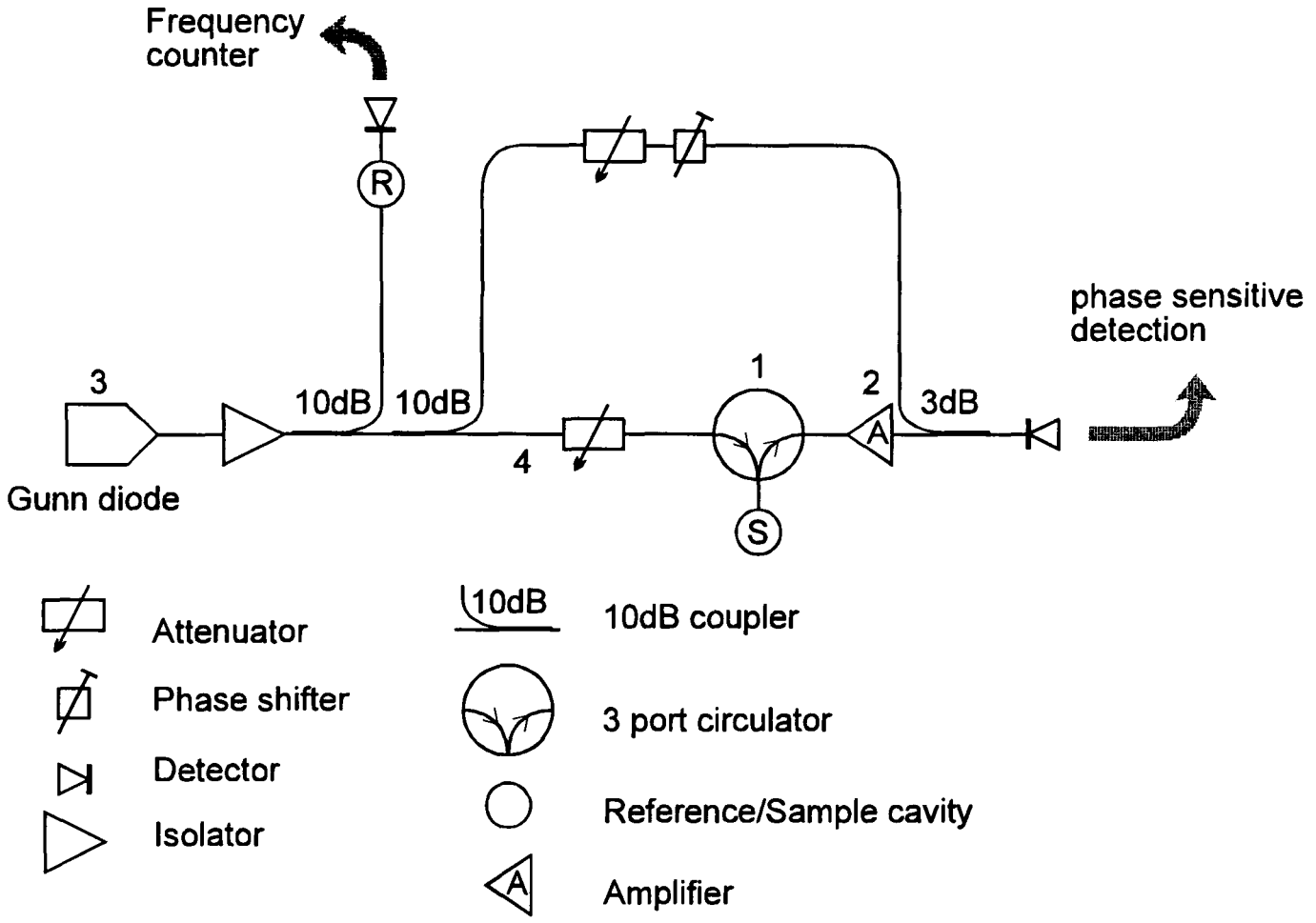



Figure 4.3: Schematic of the X-band bridge.

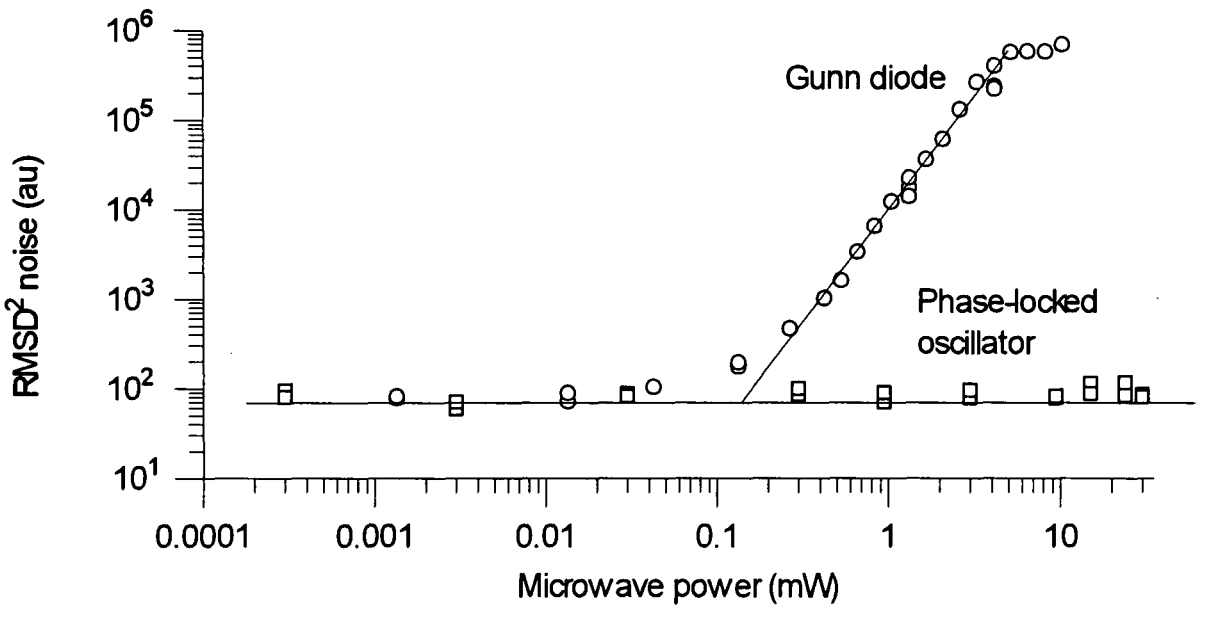



Figure 4.4: Comparison of noise levels from Gunn diode and phase locked oscillator using the Bruker cavity. The RMSD noise was calculated by fitting a straight line to a portion of spectrum showing no EPR signals. The difference between the fitted line and the experimental data, at each point, was squared, averaged, and the square root was taken. The square of the RMSD noise is proportional to the power and hence plotting the log of this gives a value proportional to the noise power at 115 kHz. The same portion of the EPR spectrum was used for all measurements.

FM noise demodulated by the EPR cavity [112]. The Bruker $TE_{104}$ microwave cavity had high Q[9] (about 10000) and was therefore effective at demodulating source noise, with a large noise amplitude for all powers in dispersion mode, and for powers above 0.2 mW in absorption mode. The Gunn oscillator[10] (3 in Figure 4.3) was replaced with a low phase noise phase locked oscillator.[11] This achieves low noise levels by filtering its output through a high Q-cavity and had a noise level of 120 dBc/Hz[12] at 100 kHz from the centre frequency, compared to a typical value of around 90 dBc/Hz for a Gunn diode. The noise levels for the Gunn diode and phase locked oscillator are compared Figure 4.4. Source noise becomes important at 0.3 mW for the Gunn diode, while it is still not visible at 30 mW (full power) for the phase locked oscillator.

The reduction in source noise allowed EPR and ENDOR experiments to be performed with the bridge tuned to dispersion mode. All the ENDOR measurements in Chapter 5 were performed while running in dispersion mode. The sensitivity of the bridge was increased by the modifications and a second attenuator was added (in position 4 in Figure 4.3). Using this configuration, spectra have been measured with less than 9 nW incident microwave intensity at the cavity.

### 4.3.3 Modifications to detection circuit

The detection circuit was upgraded with the replacement of the Clarendon Electronics Workshop phase sensitive detectors (PSD's) with commercial models from Princetown Applied Electronics. ENDOR decoding is performed using an EG&G model 5207 lock-in amplifier, while EPR detection is performed by an EG&G 5209 lock-in amplifier. The EPR replacement is recent and was only used in experiments on the vacancy (Chapter 6). The new PSD's have greater signal filtering and noise rejection capabilities, are less prone to pickup from the mains, have a greater dynamic range, and can be controlled by a computer. The model 5209 can generate TTL pulses and has built in 16 bit A–D converters. In the future this facility will supplant the

[9]Quality factor, see §4.3.9 for its definition.
[10]Alpha Industries model CME420BN, 150 mW, 9.40±0.2 GHz.
[11]Ferranti International, Cavity Oscillator model MCM/X22B/2705/1, 30 mW, 9350–9850 MHz.
[12]dBc denotes noise power with respect to the full power at the centre frequency.

PC-based A–D board on the X-band system, reducing sensitivity to PC-generated noise (see also §4.3.4).

### 4.3.4 Magnetic field and EPR signal measurement

The magnetic field was originally measured using Clarendon built Hall probes[13] calibrated with a Clarendon built NMR probe [116]. The signal from the Hall probe was read into the PC using a 16 bit A–D board[14] (the EPR signal was read using a 12 bit A–D board[15]). To reduce sensitivity to PC noise, picked up in the A–D conversion, the X-band Hall box was modified to give a zero to ten volts full scale swing, as opposed to a zero to one volt swing. Despite noise minimizing modifications, the use of the Hall probes placed serious limits on absolute accuracy and repeatability. When sweeping slowly at high resolutions the noise in the field measurement produced jagged, deformed EPR lines, because the noise amplitude was between 0.05 and 0.1 mT despite signal averaging, which was often comparable to, or larger than, the EPR line width. The Hall probe was therefore complemented by the addition of an NMR magnetometer.[16] This automatically tracks the magnetic field and can read to an accuracy of 0.1 $\mu$T. It also generates a 10 ms wide square ticker pulse at pre-set intervals, for example every 0.1 mT. Because of the slow read out time on the IEEE bus, the ticker was used as the main means of tracking the field. As the ticker pulse was short a Schmitt trigger/flip-flop combination was built[17] which changed state at each pulse. This relaxed the monitoring requirements placed upon the computer, reducing the frequency at which it had to pole the level of the ticker output, as it did not have to catch the narrow pulse.

At the same time as the magnetometer was installed, the 12 bit magnetic field controller was replaced with a 19 bit sweeper[18] able to produce 4 $\mu$T field increments. It was fully computer controlled, via the RS232 interface, and achieved the field sta-

[13]Clarendon Electronics analogue magnetometer EW845.
[14]See O'Connell, reference [111], p.15.
[15]Blue Chip Technology AIP-24.
[16]Bruker NMR Gauss Meter ER035M with ER088 PSU.
[17]Schmitt trigger built by D.F.Talbot-Ponsonby.
[18]Designed and built by Dr D.Smith of the electronics workshop.

bility needed to work with the Bruker proton probe. The home built 16 bit board and the 12 bit board were replaced with a commercial 16 bit board.[19] The board had multiple input channels and four binary output channels. A multiplexer[20] was introduced to improve isolation between the PC and the Hall magnetometer, as feedback from the PC caused the field reading to fluctuate rapidly. This was controlled from the 16 bit board's digital output lines and only one channel of the 16 bit A–D was used.

With the new control and monitoring system installed it was possible to choose between two modes of operation. For rapid scans the field changed too quickly for the NMR magnetometer to track, and the Hall probe was needed. For slow, high precision, scans the ticker was used to measure the field. When running in high precision mode the following methodology was used to read and control the magnetic field:

1. The field was ramped automatically to the start field using the Hall probe as a guide.

2. The start field was read into the computer from the NMR magnetometer via the IEEE bus.

3. The field was ramped at a pre-set rate and the NMR magnetometer ticks were registered.

4. The field sweep was terminated when the Hall probe field reached the stop value. The field was left to stabilize at this new value.

5. The final field was read using the NMR magnetometer.

The ticks were post-processed to yield the absolute field value at the NMR probe. The decoding is discussed in the computation section (§4.4). Using this method the field for the angular variation performed on the [V]* system was measured to an

[19]Strawberry Tree Mini 16.

[20]Martchwood technologies M410 multiplexer built into a case using a Lascar PSU206 power supply, supplied by Talisman Electronics, Reading.

absolute accuracy of better than 0.02 mT. Field resolution of the spectrometer is currently limited by the field sweeper, rather than the measurement system. Because the magnetic field is ramping, the limit in accuracy of field measurement is dictated by the speed at which the computer can register a tick generated by the NMR probe, with respect to the ramp rate. Therefore reducing the ramp rate, or increasing the computer sampling rate, increases the accuracy of the field measurement – until the 1 $\mu$T[21] limitation of the NMR probe is reached. The sweeper varied the field in steps of 4 $\mu$T, and thus placed the limitation on the resolution of spectral features because the individual field steps were visible on the EPR lines. A typical field sweep rate was 200 (on the sweeper register) with two signal averages for each collected data point. The limit on determination of the position of a tick in this case was 20 $\mu$T, when a 0.1 mT NMR tick spacing was used.

The absolute nature of proton resonance measurement, and its high accuracy, produced repeatable field measurement. It was therefore possible to signal average EPR spectra without any manual correction. In order to be able to add spectra, each spectrum must also be corrected for any change in the microwave frequency, as at X-band a change of 0.37 MHz produces a field offset of 0.1 mT in a system with $g$=2.0023. The frequency correction is only possible if all the systems producing spectral lines have similar $g$-values.

Knowledge of the field at the proton probe is the first step to determining an absolute $g$-value, however, the readings have to be corrected for the offset in field between the probe position and the sample position. It is possible to correct the offset if the sample contains a defect with an accurately known $g$-value and small line width, and the direction of the B-field with respect to the defect axes is known. This is probably the best method as the presence of the sample, which has a magnetic susceptibility, modifies the magnetic field at the defect. Another method of correction is the use of a $g$-marker, placed in the same position within the microwave cavity as the sample. Here care must be taken to match this sample to the one under investigation

[21]The highest resolution provided by the NMR probe was 0.1 $\mu$T, however, the long settling time required precluded its use when ramping the field.

to minimize discrepancies caused by the difference in susceptibility. Absolute field measurement at the sample are possible but fraught with problems and hence operose in their execution. Fortunately, in the experiments reported in this thesis it was possible to use a defect internal to the sample for field offset correction.

### 4.3.5 Optical illumination

#### Introduction

The development of the optical illumination system built upon work by Cox (unpublished). Cox attempted to observe optical effects using ultra-violet light from a *black light*. His attempts failed owing to low light intensity. In the light of his results, a more intense high pressure mercury vapour lamp and liquid light guide were purchased and a new system built. It was constructed in three phases, each prompted by the requirements of the experiment. The initial phase involved simple illumination with the lamp, with wavelength selection using glass or quartz absorption filters. The next phase involved the incorporation of a monochromator into the system and the development of equipment to measure relatively slow decays. The final phase involved a re-design of the optics to minimize loss, and the measurement of rapid decays. The phases can be identified with measurement chapters as follows: phase (i) – isotopically enriched diamond (Chapter 8); phase (ii) – $[N–N]^+$ centre (Chapter 5); phase (iii) – the vacancy (Chapter 6).

To perform combined optical and magnetic resonance experiments on diamond the following should be remembered:

1. The band gap of diamond is 5.4 eV (230 nm) and as defects are distributed through the whole gap much of the illumination needs to be near this energy. uv optics must therefore be used throughout.

2. As a rule, no metal must enter the microwave cavity, and dielectric loss must be kept to a minimum, to avoid degradation of the cavity $Q$.

3. Illumination must take place at temperatures ranging from 4 to 300K.

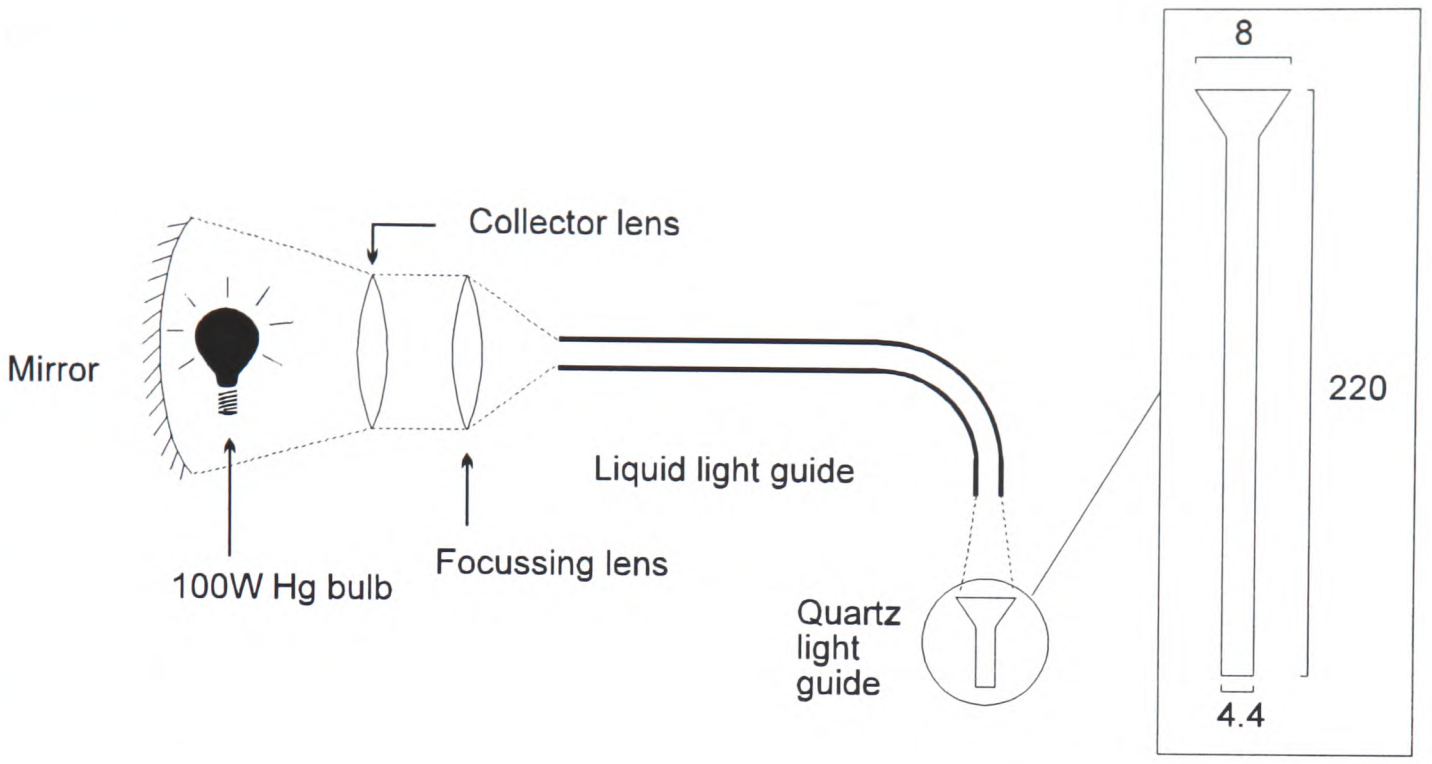



Figure 4.5: Illumination of the sample using liquid and quartz light guides. All lengths are in mm.

4. The light must be channelled into the microwave cavity which is sited in a large magnetic field.

### Illumination

Illumination was provided by a 100 W high pressure Hg lamp[22] which has a large output below 400 nm. Its spectrum is given in Figure 4.6. As can be seen the Hg lamp is ideal in its production of a large quantity of uv radiation, however, the spectrum is far from flat. A xenon[23] bulb was therefore purchased, and mounts were machined to allow its insertion into the lamp housing. The Xe spectrum is much smoother than the Hg spectrum at short wavelengths, but it produces less power at any given wavelength than the Hg lamp at the specific Hg wavelengths. The lamps were mounted in a lamp housing which had forced ventilation, a back reflecting mirror and an adjustable collecting lens.[24] The bulbs and lenses were uv-grade quartz.

Light was channelled into the microwave cavity using a spectrosil quartz light

[22]Osram HBO100/2.
[23]Osram XBO150.
[24]Spiers Robertson LH150 universal lamp housing, with Spectral Energy LPS 251 SR PSU.

guide. The sample was mounted on the lower end of the guide using araldite adhesive or high-vacuum grease. Care was taken to apply grease/glue round the edges of the sample only and to leave the largest area possible for unimpeded illumination. The light guide was fabricated by Mr S.Giles and the ends polished to an optical finish.[25] The rod was gripped just below the enlarged collecting surface by a mount which made vacuum seals with the rod and the cavity goniometer mount. The original mount was built by Andrew Cox. The light guide is depicted in Figure 4.5. In phases (i) and (ii), the light was focussed onto a liquid light guide[26] which channelled it into the magnet and hence to the spectrosil quartz light guide.

The Hg lamp was rated at 100 W of electrical power. At the focus of the beam, after the collecting and focussing lenses, and with the collecting lens close to the bulb for maximum collecting power, the integrated intensity over all wavelengths, was 2.0 W.[27] After the liquid light guide this had fallen to 600 mW, dropping finally to 200 mW after the quartz light guide. With 200 mW of light arriving in the cryogenics heating was bound to occur. This is discussed in Chapter 5. In future systems it is recommended that a water filter be used to remove infrared radiation and limit the heating effect.

In phase (iii), measurements were made on an excited state of the neutral vacancy in diamond ([V]*). This centre was short lived, and more difficult to create than the $[N–N]^+$ centre studied in phase (ii). As a result, the amount of light at the sample was the limiting factor. There were two ways of increasing the intensity at the sample: (a) use of a more powerful Hg source, and (b) removal of losses in the optics. It is in principle possible to run a 200 W Hg bulb from the power supply currently running the 100 W bulb,[28] however, the suppliers stated that under these conditions the PSU was more likely to fail and it was decided not to take the risk. It was therefore necessary to redesign the optics.

One of the largest losses in the optical system arose from the quartz light guide

---

[25] By Mr G.Reed.

[26] $\frac{1}{2}$m UVA liquid light guide supplied by Spiers Robertson.

[27] Measured using a Photon Control Model 11 Bolometer Power Meter, borrowed from Dr P.Baird, Atomic and Laser Physics.

[28] Spectral Energy LPS251SR.

which had an ~33% transmission integrated over the full Hg lamp spectrum. The light guide, however, could not be dispensed with or improved greatly as broad band (extending into the uv) anti-reflection coatings are not very efficient. Incorporation of the liquid light guide and necessary lenses into the system yielded a ~20% transmission. The light guide was therefore replaced with a quartz right-angled prism[29] which had a transmission of ~69% when incorporated into the configuration used. A jig (composed of hollow aluminium tubing and clamps) was constructed above the magnet to support the prism and focussing lens (see Plate I, page 67). The modification increased the power at the sample by a factor of 3.6. It is important to note that the above intensity measurements are integrated over the whole spectrum, and that the liquid light guide had a lower transmission in the infrared than the prism. Thus, the uv transmission for the light guide could be higher than the measurements indicate, however, it was observed that the EPR signal was larger after replacement of the light guide with the prism.

### Wavelength selection

In phase (i), wavelength selection was performed using film filters laminated between plates of glass or quartz. Diffraction filters with a 10 nm band pass, selected for the Hg wavelengths were also employed. The filters were placed before the liquid light guide. In phase (ii), the system was modified to accommodate a $\frac{1}{4}$m, high throughput, off-axis, Czerny-Turner monochromator.[30] The monochromator was placed after the focussing lens and an additional lens was used to re-focus the output light onto the liquid light guide. The monochromator was calibrated using the mercury spectrum [117] from the lamp by scanning the grating using a clock drive, while collecting the output light intensity with the bolometer detector.The calibration spectrum shown in Figure 4.6 revealed two problems. It showed (a) that the monochromator only worked between 300 and 600 nm (as specified on the grating) but outside these ranges light contamination from other wavelengths could occur, and (b) that most of the power

[29]Kindly lent by Dr C.D.Thompson, Atomic and Laser Physics.
[30]Jarrell-Ash model 82-410.

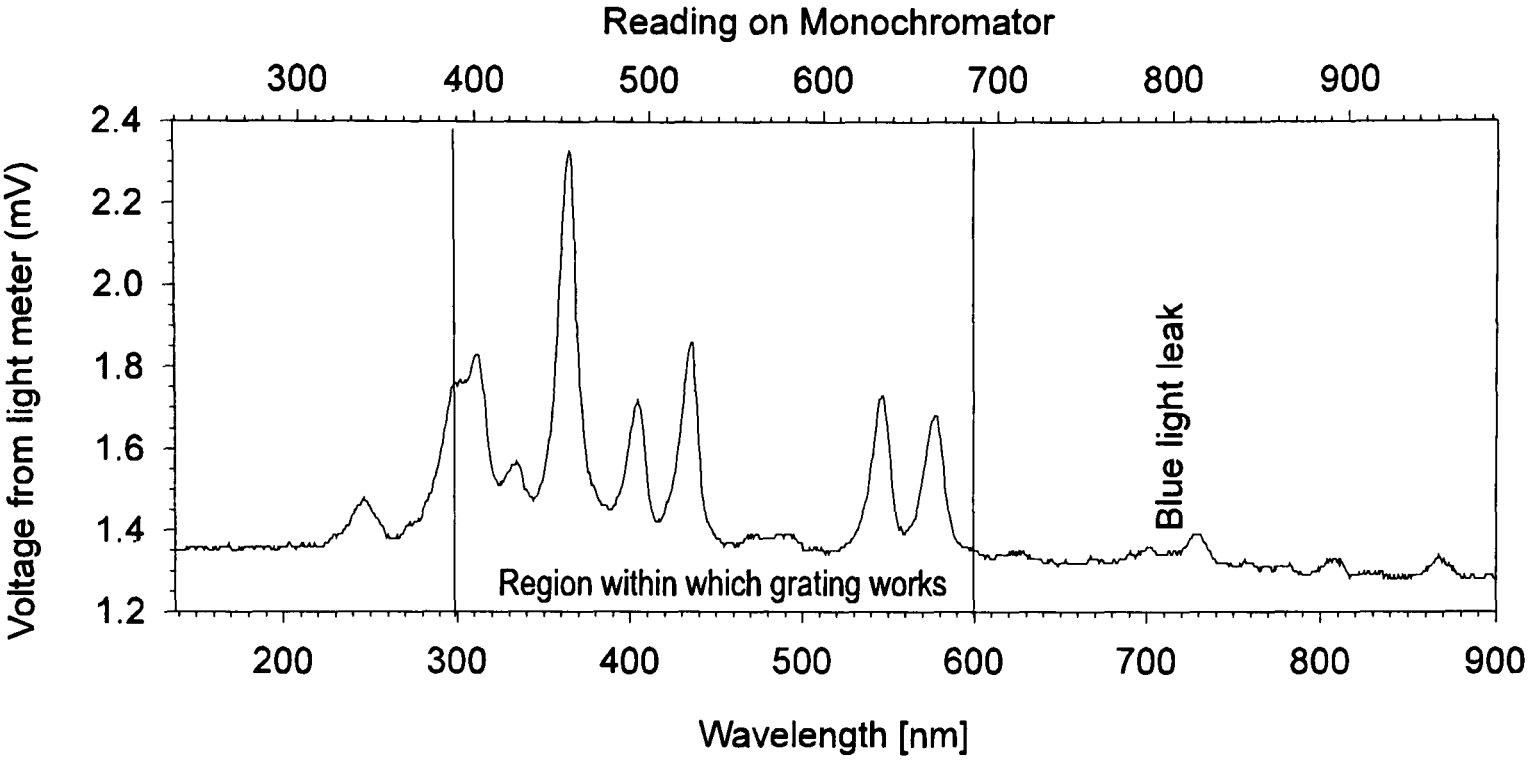



Figure 4.6: High pressure Hg lamp spectrum when passed through the Jarrell Ash monochromator. The slit resolution was set to 8 nm. The spectrum was calibrated using the major spectral features.

in the Hg spectrum was concentrated in lines of about 20 nm wide with large troughs in between (the slit width was set at 8 nm). The monochromator was used to make the wavelength selective measurements in Chapter 5, but these were only made at the peaks of the Hg spectrum. The EPR spectra were normalized for the differences in incident light intensity using the bolometer detector. This was placed after the liquid light guide and a quartz light guide identical to the one upon which the sample was mounted, and power measurements at the various light wavelengths were taken. An additional data point was added using a 3.5 mW, 670 nm diode laser.[31] The laser was focussed directly onto the spectrosil quartz light guide.

The Xe bulb was delivered after the completion of phase (ii) and could therefore not be used on the $[N–N]^+$ sample – it had by then been ground to powder! An attempt was made to use the Xe lamp on the $[V]^*$ system. A comparison of the full spectrum illumination using the Hg and Xe bulbs is presented in Figure 4.7 and reveals how the trade-off in intensity to obtain a smooth energy-spectrum did not succeed. Despite the extra 50 W of electrical power there was not enough intensity

[31] Borrowed from Dr C.Foot, Atomic and Laser Physics.

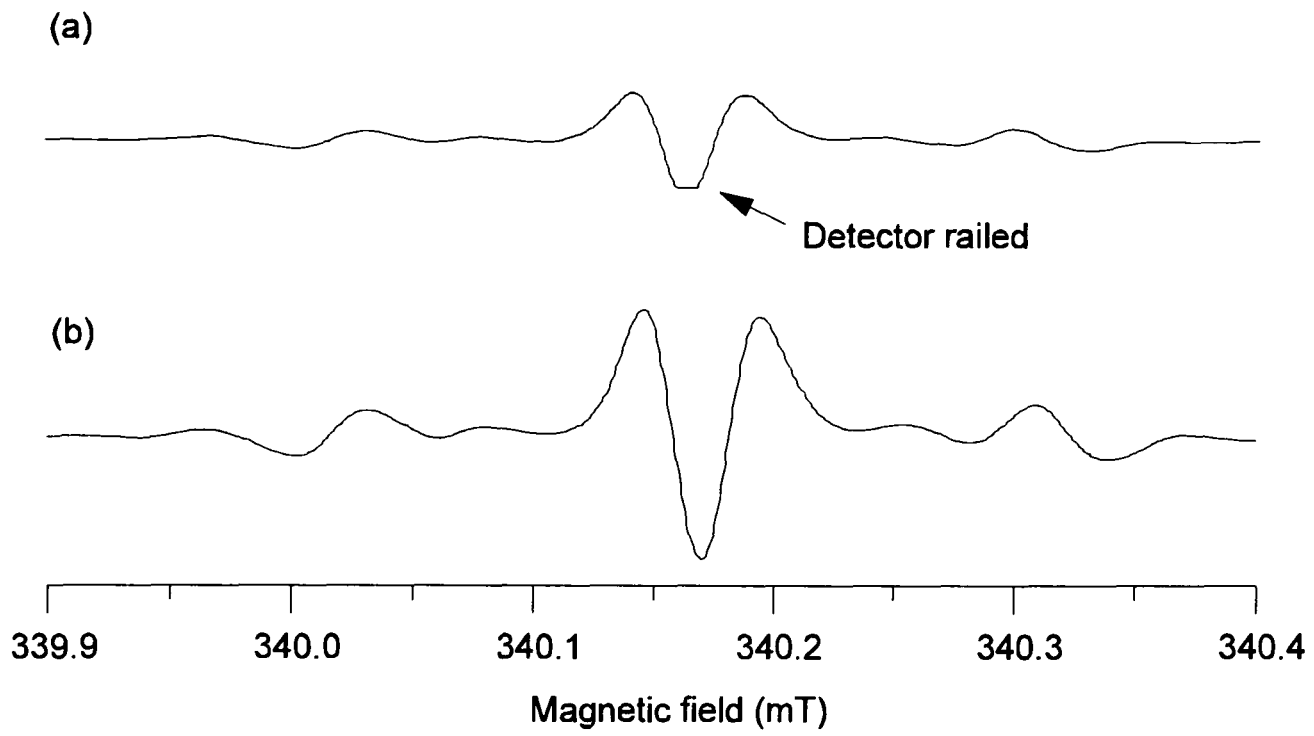



Figure 4.7: Comparison of the full spectrum excitation for (a) the Xe bulb and (b) the Hg bulb. The detector railed in trace (a) as the PSD amplification had been increased. The traces were corrected for the increased amplification.

to use the monochromator, and the EPR induced by the full energy spectrum of the lamp was much weaker than that produced by the Hg bulb (as $[V]^*$ was only created by uv light). The diffraction filters were as efficient as the monochromator at selecting the Hg peaks and were simpler to use, hence they were used in making the wavelength selective measurements during phase (iii).

### 4.3.6 Time resolved measurements

Time resolved measurements were first effected in phase (ii) on the $[N–N]^+$ centre. The lamp beam was interrupted by an electronic shutter.[32] The shutter was controlled from a 200 V power supply designed by the electronics workshop.[33] Upon application of a rising TTL edge, the PSU generated an initial voltage peak, followed by a constant lower voltage, and opened the shutter within 3 ms. The falling TTL edge switched the power off, closing the shutter. The input TTL level was generated by the 16 bit Strawberry Tree A–D card, however, it transpired that the output voltage was not quite large enough. A small inverting amplifier, powered from the multiplexer, was

[32]Melles Griot.

[33]Shutter Solenoid Drive, designed by Mr W.J.Siertsema and built by the Physics Electronics Workshop.

built to overcome this problem. The data collection software was re-written to capture single spectra, or multiple averaged scans, with respect to time and also allowed a variable delay time between scans. The new program, called *Spectime*, is described fully in §4.4.2. The fastest rate that *Spectime* could collect data was 1.4 ms/point. This experimental configuration is shown in Figure 4.8a.

In phase (iii), it was found that the decay times involved in the $[V]^*$ system were an order of magnitude shorter than in the case of $[N–N]^+$. The $\sim$3 ms shutter closing time and the slow data collection speed therefore limited resolution. By careful positioning of the shutter to use only a portion of the aperture, it was possible to decrease the closure time by about 0.5 ms. Optimization of the computer software produced a decrease in collection time of 50 $\mu$s/point, but the main log-jam was overhead produced by the A–D card driver software. This could be circumvented either/both by upgrading from the i286-based PC,[34] or by re-writing the collection software in C and using direct access libraries provided by the card manufacturer. Funding was not available for the upgrade of the computer nor a C compiler. An attempt to utilize another A–D board, which was directly addressable, failed owing to hardware problems. A digital storage adaptor[35] (DSA) was therefore connected to the computer and an oscilloscope, and used for data collection instead of the PC. The dynamic range of the DSA exceeded the system parameters by two orders of magnitude, however, its signal averaging was limited to 256 scans and the number of data points was limited to 512. Software was written to convert the DSA data format into an X–Y format with time as the X-axis. The DSA did not have the capability to control the shutter which was either controlled from the PC (Figure 4.8b), or from a square wave signal generator set to a frequency of a few mHz (Figure 4.8c). The DSA was externally triggered from the shutter control pulse.

A second shutter[36] with a 1 ms closure time, a chopper,[37] and a photodiode[38] were

---

[34]Viglen II.

[35]Thurlby DSA 524.

[36]Uniblitz LS21T2 shutter and D122 shutter driver, borrowed from Dr K.Zetie, Atomic and Laser Physics.

[37]Borrowed from Dr C.D.Thompson, Atomic and Laser Physics.

[38]Borrowed from Dr R.B.Warrington, Atomic and Laser Physics.

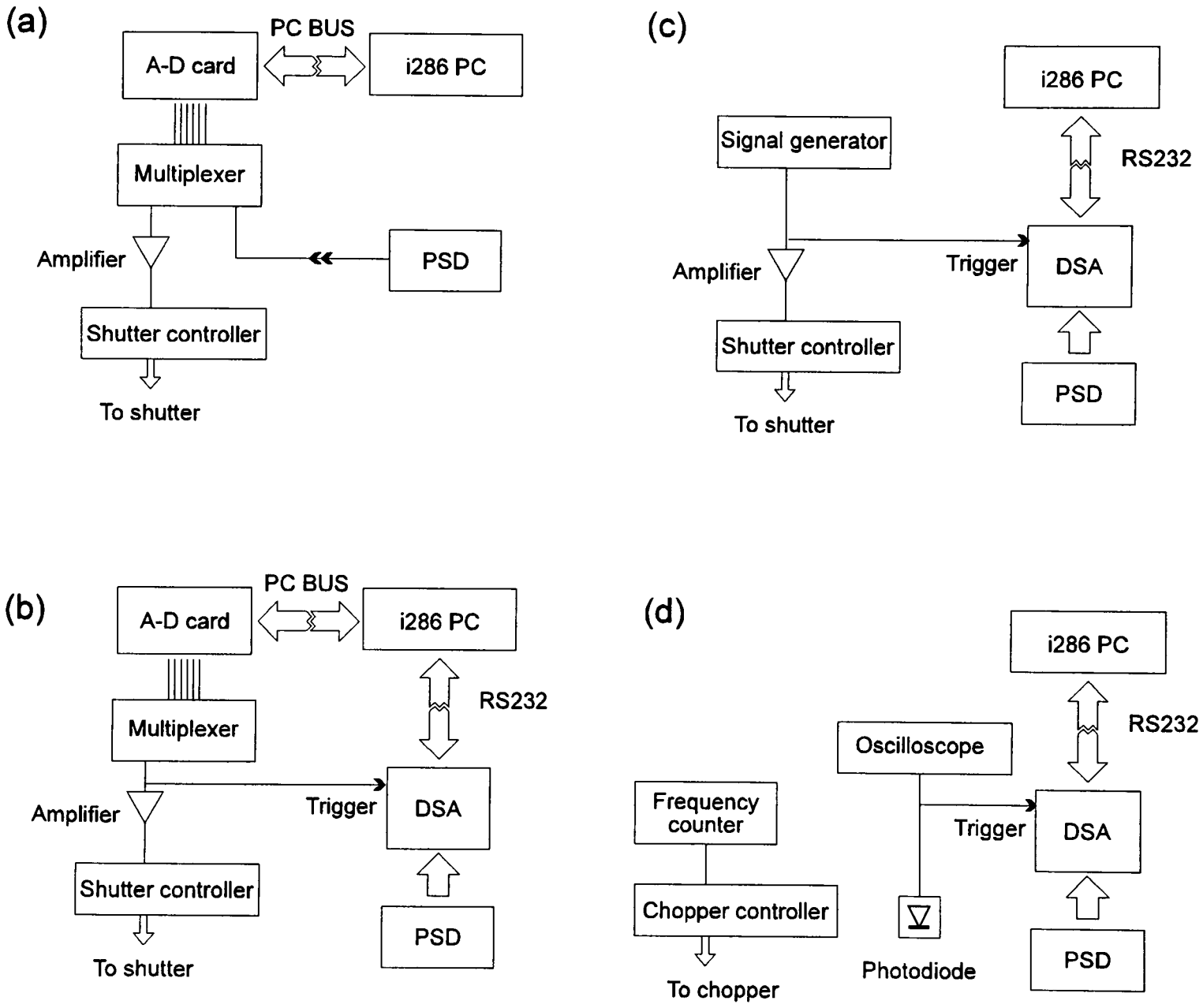



Figure 4.8: Control systems for time resolved measurement (see text for details).

borrowed, and the system response time, using each shutter, and the chopper, was investigated. The experimental configuration using the chopper is shown in Figures 4.8d and 4.9. First the diode rise and fall time was characterized using a HeNe laser and the chopper equipped with a high frequency wheel. The chopper wheel was then replaced by one with only two holes and the rise and fall times were measured as a function of chopper frequency, using the laser and Hg lamp. The Hg lamp had a 5 mm beam width as opposed to 1 mm for the laser. The response time was also measured using the two shutters. The response times are listed in Table 4.1.

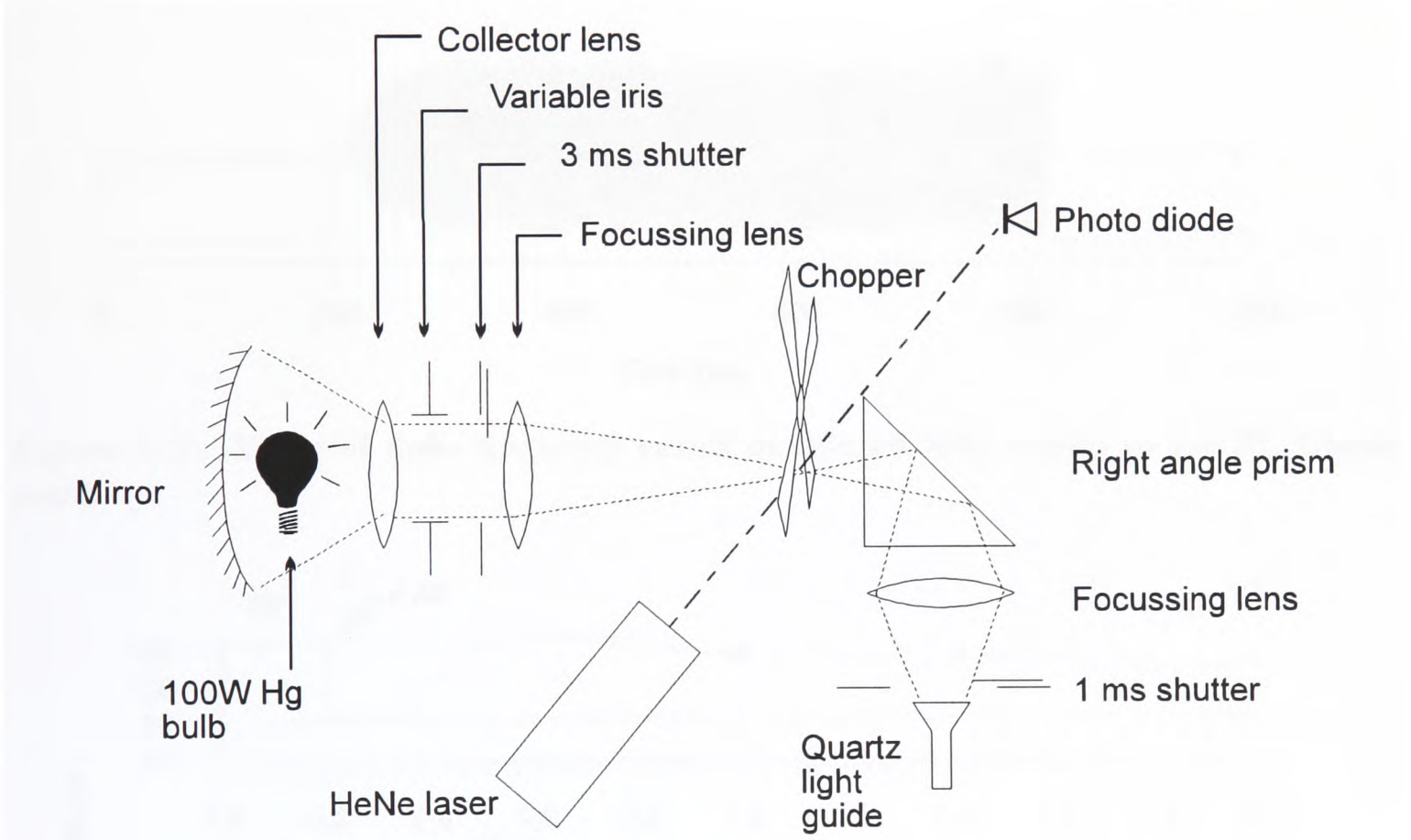



Figure 4.9: Schematic showing the experimental arrangement used when making time resolved measurements.

The measurement of the illumination switching times revealed the following.

- For decays of $\geq 20$ ms the Melles Griot shutter sufficed.
- For decays of $10 \rightarrow 20$ ms the Uniblitz shutter sufficed.
- For decays of 300 $\mu$s$\rightarrow 10$ ms the chopper needed to be used at top speed.

The time response of the detection system was then tested using the rapid quenching and recovery of the [V]* system produced by the application of a radio frequency

Table 4.1: Light source switching times

| Device | HeNe laser | Hg Lamp |
|---|---|---|
| Chopper, 30Hz | 500 $\mu$s | 5 ms |
| Chopper, 67Hz | 200 $\mu$s | 2 ms |
| Chopper, 120Hz | 100 $\mu$s | 1 ms |
| Chopper, 211Hz | 50 $\mu$s | 0.5 ms |
| Melles Griot Shutter | | 2.3 ms |
| Uniblitz shutter | | 1.4 ms |

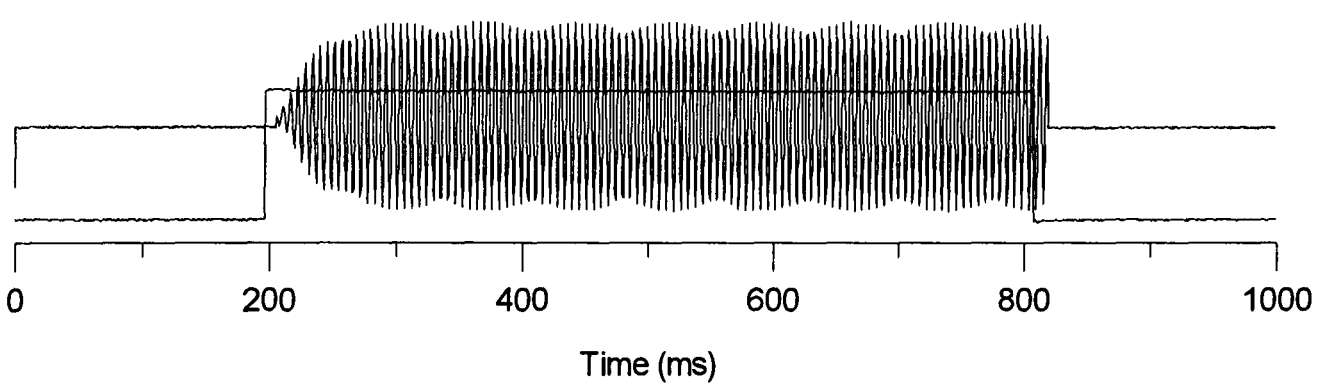



Figure 4.10: Shape of radio frequency switch on and off with respect to the PC trigger pulse.

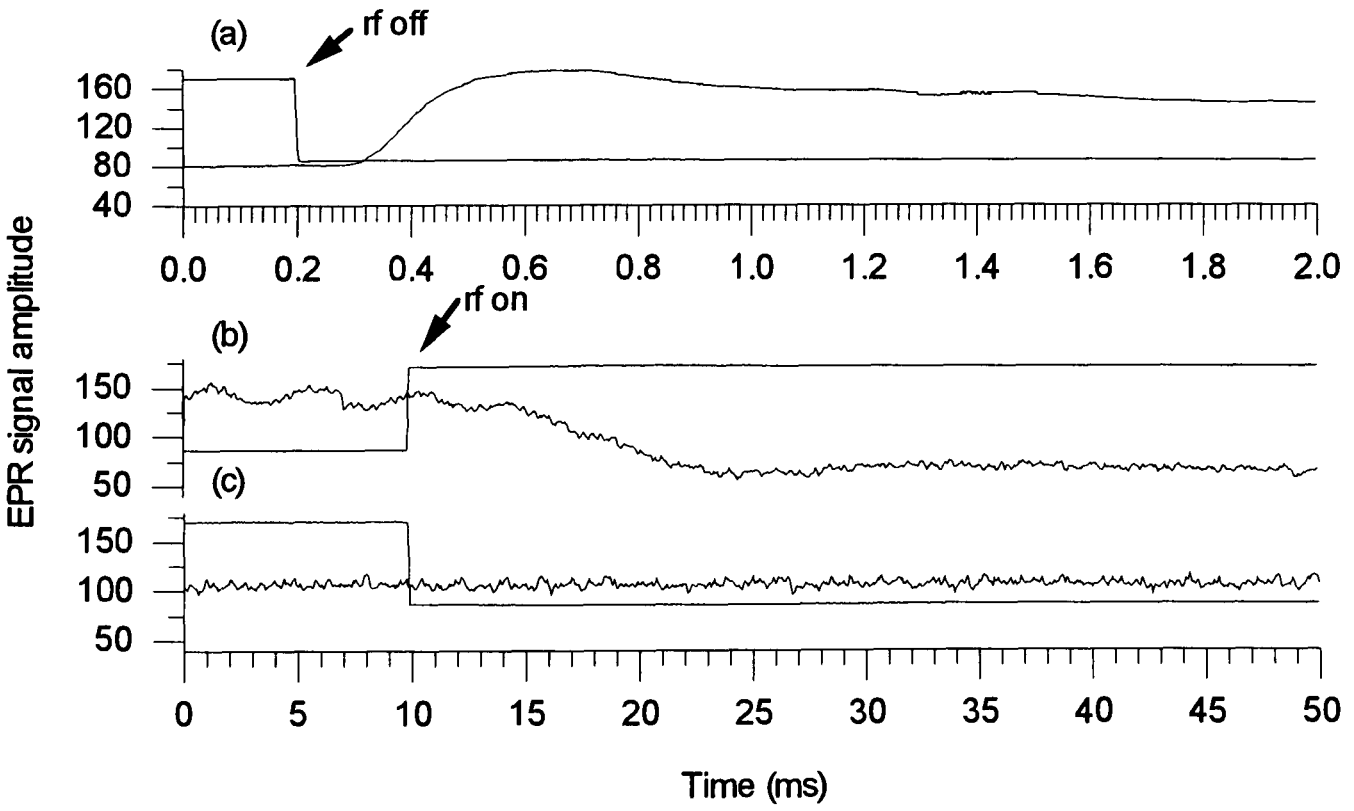



Figure 4.11: Fastest transient response measurable. (a) rf off, note the change in axis scale which also samples a different noise regime. (b) rf on, compare the gradual fall with the slow rf switch on in Figure 4.10. Zeeman field set to low field [V]* EPR resonance. (c) rf off, but not on [V]* EPR resonance.

at 3.65 MHz. The shape of the rf pulse is shown in Figure 4.10. The rf was produced by a signal generator[39] which was toggled on and off using specially written software on the PC, communicating via the IEEE bus. The program set the signal generator, then sent a trigger pulse to the DSA after a delay of 161 ms to compensate for inherent lag in the response of the signal generator. Notice in Figure 4.10, that the switch on is gradual but the switch off fast. The [V]* response to the rf is shown in Figure 4.11. The step function is the trigger pulse, the falling edge corresponding to rf off. The switch on time is slow as expected, but the switch off occurs in around 200 $\mu$s. Trace (c), where the spectrometer was tuned away from the [V]* resonance, shows that the effect does occur in the EPR cavity. The results show that the detection system could measure responses of $\sim$200 $\mu$s and above. This was consistent with the shortest time constant on the EG&G 5209 PSD of 200 $\mu$s and the 115 kHz modulation. To eliminate deconvolution problems, the shortest reliable time was judged to be 400 $\mu$s. When using the chopper wheel the trigger pulse was produced using a HeNe laser and photodiode with the laser passing through the light beam where it was chopped. Figure 4.9 shows a schematic of the experimental arrangement used for collecting time resolved data. Plate I shows the goniometer head, the ENDOR adaptor, the liquid light guide, the prism and the chopper wheel.

### 4.3.7 Cryogenics

The X-band system was cooled by an Oxford Instruments ESR 900 cold finger. This is a continuous flow liquid helium based system and was described by Newton [22]. In many of the experiments described in this thesis, temperature stability over time periods ranging from a second to twelve hours was vital as:

(i) the impedance of the cavity changed with the amount of helium gas present, and its temperature;

(ii) the susceptibility of the sample was temperature dependent; and

[39]Marconi Signal Generator 2022, also used for ENDOR.

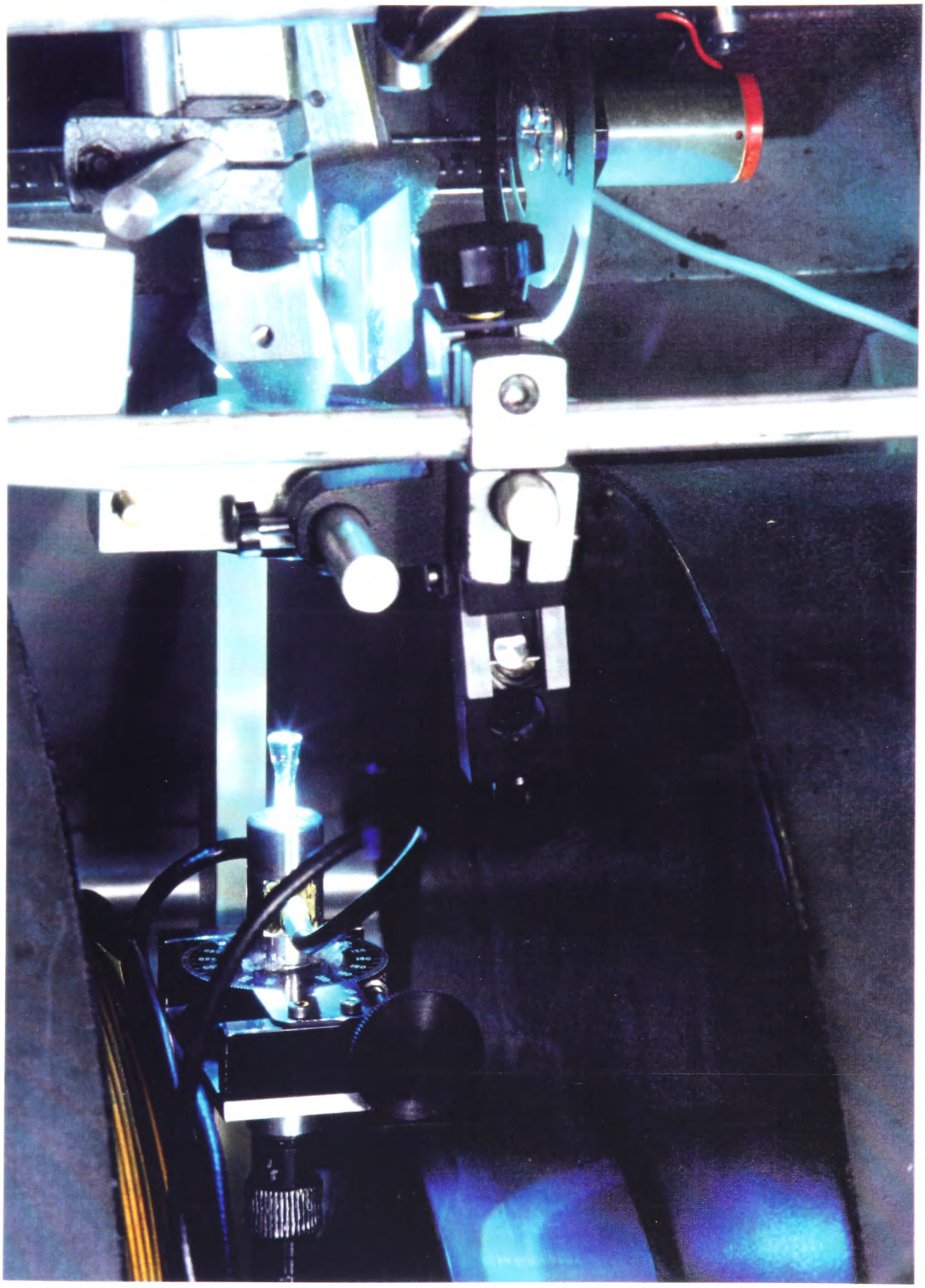


Plate I: Bruker cavity ENDOR system, showing the ENDOR adaptor on the goniometer which also holds the spectrosil quartz light guide. The prism and chopper wheel are also shown. The Uniblitz shutter has been removed from between the prism and the light guide for clarity. The photodiode was used in conjunction with the HeNe laser to trigger from the chopper wheel.

(iii) the relaxation mechanisms within the sample were often temperature dependent.

The maintenance of a steady temperature was one of the most significant problems encountered. Temperature fluctuations were generally caused by constrictions or heat leaks within the helium transfer siphons. In addition a siphon with a cold touch onto its helium capillary has a tendency to block, necessitating the removal of the siphon, warming to room temperature, flushing with gaseous helium, and re-insertion into the helium dewar and cryostat. This was a time consuming process which wasted two to three litres of liquid helium. The temperature stability problem was also exacerbated by the need to run at flow rates of 1.5 to 2 litres/hour, as opposed to 0.5 to 1 litres/hour specified by the manufacturer, because of a slow vacuum leak in the cryostat.

The temperature stability problems were minimized by continuous pumping on the siphon and the cryostat using a diffusion pump and liquid nitrogen cold trap. A number of siphons were tried, and returned repeatedly to the manufacturer for repair. The problem was finally solved by the purchase of a new siphon.[40] This was capable of operating with liquid nitrogen in addition to liquid helium as it had a larger capillary. The cryostat was reconditioned and upgraded to work with the new siphon. The upgrade occurred two months before the completion of the experimental portion of this thesis. The new system was therefore only used in the final work on the $[V]^*$ centre. It was found to have temperature stability of better than 0.1K. The increased stability was produced by the inclusion of a large thermal mass in the cryostat, which also increased the cool-down time from ten minutes to half an hour. Owing to the larger capillary it was possible to flood the cryostat with liquid helium. This produced rapid temperature fluctuations of one to two kelvin, and caused dangerous pressure rises when the heater coil was turned on and the liquid evaporated. The flooding effect also occurred in the Q-band continuous flow system, with the rapid boil off sometimes blowing the safety valve: a rubber bung which would hit the ceiling, accompanied by a very loud bang!

[40]Oxford Instruments GFS 600 transfer tube, with 1.2 m leg.

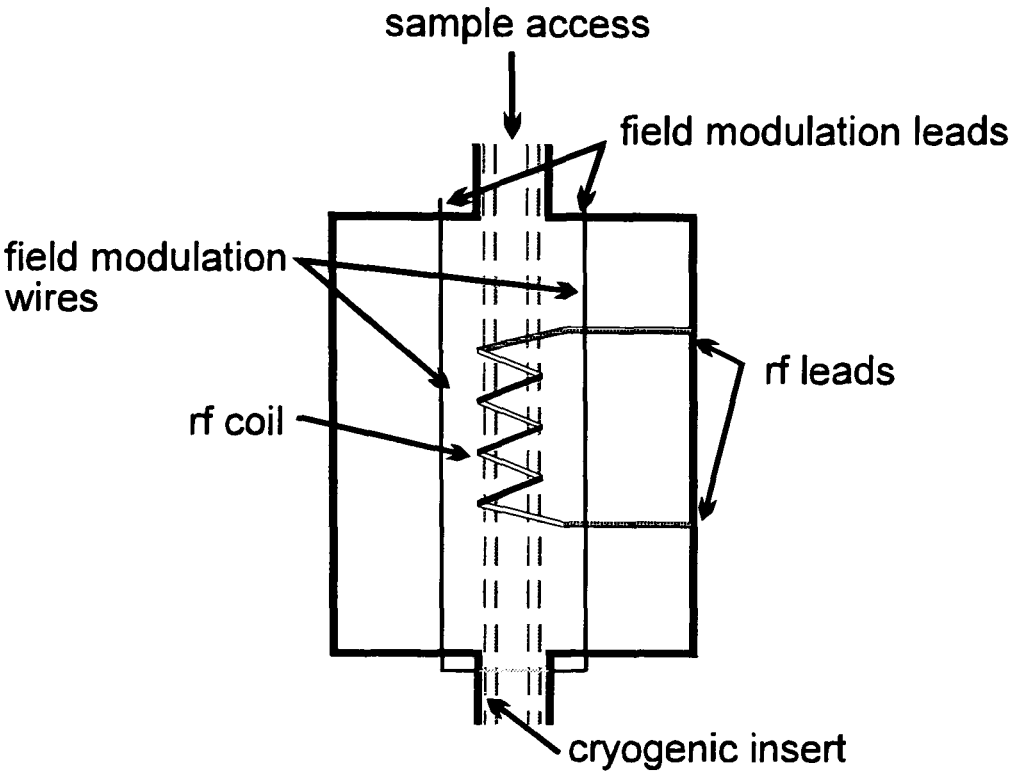



Figure 4.12: $TM_{110}$ ENDOR cavity, showing the position of the field modulation wires.

### 4.3.8 ENDOR I - Clarendon-built cavity

The ENDOR experiments detailed in Chapter 5 were performed on the spectrometer described by Cox *et al.* [118], and Cox [21]. The cavity worked in a $TM_{110}$ mode and is shown in Figure 4.12. Two problems plagued experiments: i) the cavity coupling varied with the amplitude of the 115 kHz field modulation, ii) there was a large 115 kHz background signal reaching the detector, often swamping it.

The field modulation is produced by two vertical wires placed in the nodal plane of the E-field as shown in Figure 4.12. It was initially assumed that slack in these wires was causing the change in coupling, and earth loops were producing the background. The wires were repeatedly tightened and re-threaded, using various metals, to prevent them moving in the Zeeman field and coupling to the microwave field. The problem remained constant and it was finally discovered that the loops of wire at the top of the cavity, where the leads were soldered to a BNC jack for connection to the 115 kHz source, were coupling to the magnetic field and vibrating. Both problems were solved by gluing the coils to the top of the cavity, minimizing the length of the wires.

The solution of the base line problem enabled broad ENDOR lines to be examined and facilitated the measurement of P1 powder ENDOR in diamond. The P1 powder ENDOR spectrum is shown in Figure 4.13, along with a simulated spectrum. This is

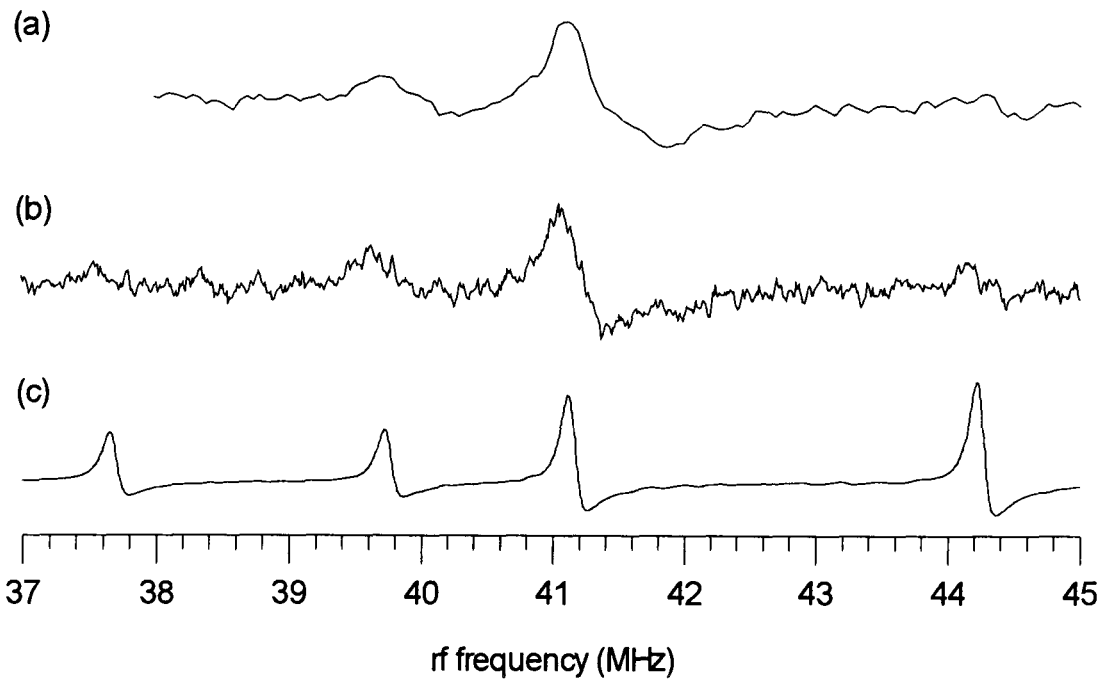



Figure 4.13: First powder ENDOR reported in diamond. The measurements were made on [N–C]$^0$centre (a) Experimental spectrum 21 scans; (b) Single scan; (c) Simulation, sitting on the central line assuming that all NMR transitions are visible. Collected at X-band at 5K.

the first time that powder ENDOR has been reported in diamond.

### 4.3.9 ENDOR II - Bruker cavity

The ENDOR experiments in Chapter 6 were performed using a new assembly the construction of which was motivated by the need for greater sensitivity. The $Q$ of the ENDOR cavity described above was about 3000, while the $Q$ of the Bruker EPR cavity is 10000. The quality factor, $Q$, of a resonator may be defined as:

$$Q = \frac{\omega_0}{\Delta\omega} \tag{4.1}$$

where $\omega_0$ is the resonance frequency and $\Delta\omega$ the half width at half height of the resonance. $Q$ can also be expressed as:[41]

$$2\pi \times \frac{\text{maximum microwave energy stored in the cavity}}{\text{energy dissipated per cycle}} \tag{4.2}$$

[41]See p.459 [93].

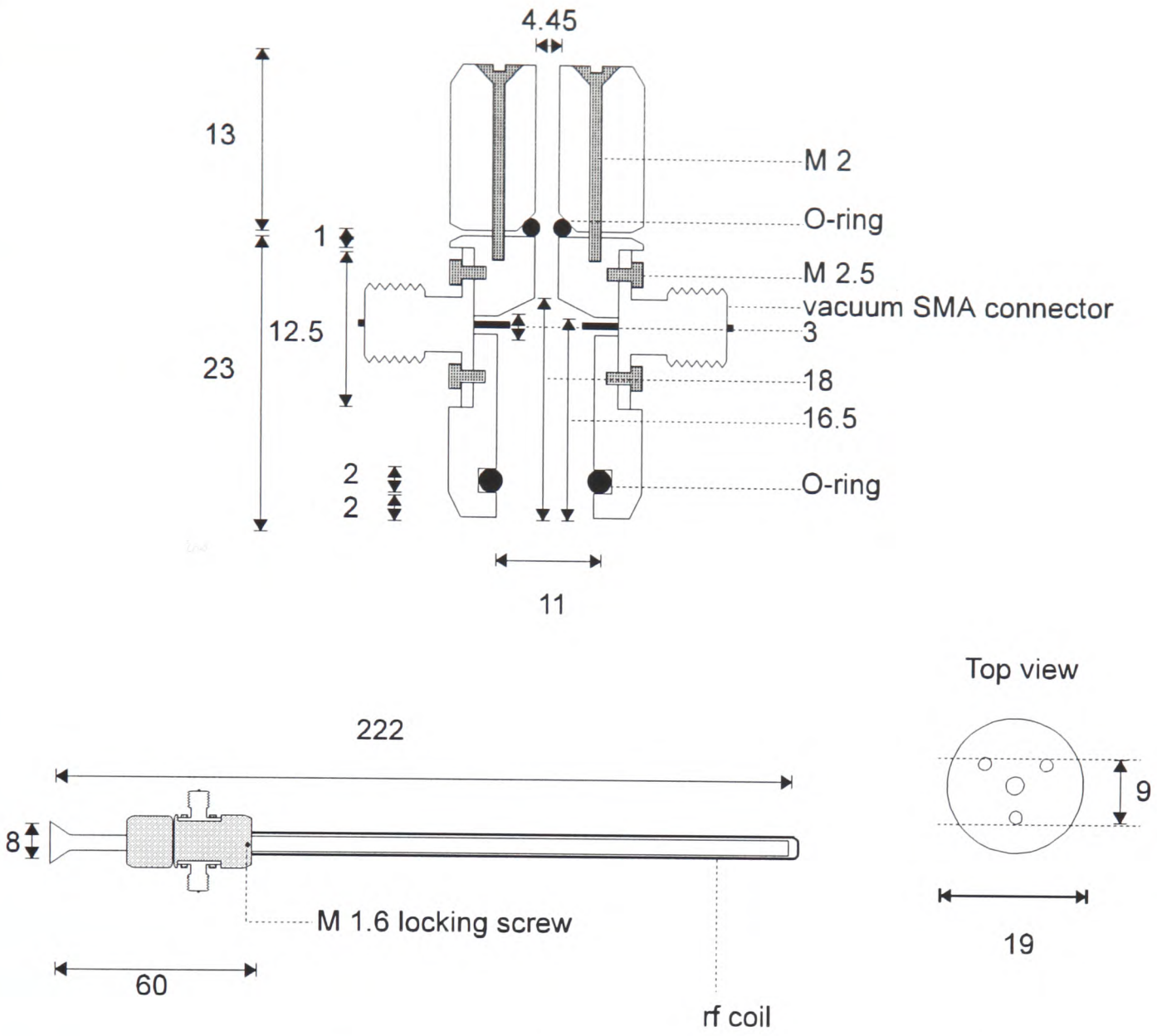



Figure 4.14: Micro-ENDOR coil and sample mount/light guide for the Bruker EPR cavity. Lengths in mm.

and is thus a measure of the loss of the cavity and, simplistically, a measure of its sensitivity to small "losses" in the sample. As diamond is a system with low losses, increasing the $Q$ of the resonator increases the sensitivity of the spectrometer.

To measure ENDOR in the Bruker EPR cavity a simple hair coil was inserted into it. The coil formed an integral part of the sample holder and light guide. The coil and rod are shown in Figure 4.14 and the sample holder is shown mounted on the goniometer in Plate I. The rf input and output connections were made through vacuum-tight SMA connectors, and the sample rod was inserted through an O-ring seal at the top. The cavity and cryostat could be used without modification. The coil

was connected in series with a 50 Ω broad band load,[42] and powered by a 100 W rf amplifier.[43] The matching load functioned to reduce reflected power which otherwise induced an unusable ENDOR base-line.

For $TE_{102}$ and $TE_{104}$ rectangular modes, the long leads of the ENDOR coil[44] (Figure 4.14) were perpendicular to the microwave E-field and positioned in or close to the nodal plane. By making the loop longer than the cavity, its base could be positioned outside the cavity, but it was found that it was possible to have the coil carefully wound directly around the sample without degradation of the cavity $Q$. This served the second purpose of holding the sample onto the bottom of the rod permitting room temperature illumination which had previously failed as the light had heated the araldite adhesive causing the crystal to drop into the cryogenics. For ENDOR measurements the rf-coil should be positioned such that the rf-field is perpendicular to the static field. It was found that a carefully constructed loop, flattened into a rectangular shape, did not degrade the quality factor, even when rotated within the cavity. It was therefore possible to take EPR measurements while using the rf desaturation technique [119] at any field orientation. This greatly enhances the versatility of the EPR system.

In the sample arrangement shown in Figure 4.14 orientation of a single crystal sample with respect to the Zeeman field, while maintaining the rf-field perpendicular to the Zeeman field, was difficult as it necessitated removal of the sample from the cryostat and rotation of the crystal on the base of the rod. A new goniometer head has recently been completed, in which the sample is mounted on a central rod, while the rf-coil is run down an outer hollow tube. The sample is therefore free to be rotated without disturbing the rf-coil. This goniometer head was completed after the end of the experiments in this thesis.

The micro-ENDOR system had the following advantages:

1. The field modulation was in the cavity walls and hence did not affect the resonator.

[42]Toyometer model T-200 wide band dummy load.
[43]rf power amplifier model 3100LA, ENI (Electronic Navigation Industries).
[44]Cu wire OD 0.25 mm.

2. Larger field modulations were possible: 5 mT as opposed to 0.1 mT in the Clarendon-ENDOR cavity.

3. The sensitivity was much higher.

4. The cavity allowed dual sample access and it was therefore possible to compare the EPR intensity to a standard without removing the sample.

5. It allowed rapid-sweep rf enhancement of the EPR.

6. It allowed EPR and ENDOR to be performed without changing the cavity or removing the sample.

## 4.4 Software

The software written during this thesis was programmed in object-oriented Borland Pascal version 7.0.

### 4.4.1 Data collection I - EPR

The basic data collection software was written for a research machines 380Z computer system [120, 22] and was modified for the PC by O'Connell [111]. The EPR software allowed the computer to act as a chart recorder but stored the data on disk, while the ENDOR software facilitated the control of the Marconi rf generator and averaging of data.

When the new 16 bit data acquisition board (referred to in §4.3.4) was installed the EPR software was modified to support it, and large sections were re-written to make it more robust and to allow it to collect data for increasing and decreasing magnetic fields.

In 1994 eighty percent of the data collection program, *Spect12*, was re-written (and renamed *Spect12.1*) to enable the computer to:

1. Control the new 19 bit magnet sweeper and hence control the magnetic field automatically.

2. Read the Bruker NMR probe.

3. Read the microwave frequency counters.

4. Read the NMR probe ticker output.

5. Control the signal multiplexer used in conjunction with the new 16 bit A–D board.

Other capabilities added included:

1. Read and save a configuration file, allowing the program to remember the settings entered by the user.

2. Support different hardware configurations eg. different frequency counters.

3. Various modes of operation eg. ticker or high resolution, standard or Hall probe based, and manual or automatic field control.

4. Greater signal averaging ability.

5. Reading the initial and final microwave frequencies.

The program was also written to be easily upgradable when new hardware was added and has latent capabilities such as EPR signal averaging. A new file format, allowing more information to be stored along with the spectrum, was adopted. The magnetic field control subroutines, and the subroutines to read the microwave frequency were written by D.F.Talbot-Ponsonby. When the ability to collect magnetometer ticks was added it was found that the original program did not collect data at fixed intervals using the timer interrupt[45] as the interrupt service routine was disabled whenever the screen was being updated. This interrupt was re-instated, and the program then collected a constant number of data points between ticks, facilitating accurate postprocessing to extract the magnetic field. As the data collection computer was old and slow, reinstating the interrupts produced an aesthetic trade-off

[45]See O'Connell, [111].

with the screen updating and display re-scaling taking longer and repeatedly pausing while the processor collected data points.

The ENDOR program (see [111]) was not modified.

### 4.4.2 Data collection II - Time resolved

As mentioned in §4.3.6, the EPR data collection software (the old version, *Spect12*) was modified to facilitate the collection of time resolved data and the resulting program was called *Spectime*. The modifications included the addition of the capability to control the shutter solenoid drive, and the implementation of a rigid time base. *Spectime* was optimized either to collect data every $n$ ms, or to collect as fast as possible. In the former mode, $n$ was set by the user. The program then ran short "test" spectra, timing itself, and adjusting the number of signal averages per data point and an internal delay until the desired time per point was accurately matched. In this mode the data was displayed on the screen as it was collected, point by point. In the second mode of operation, highly optimized subroutines were used to communicate with the A–D cards at the fastest rate possible. The data collection was defined by: the total number of data points to collect, the number of averages per data point, the number of times to average spectra, and a delay between collecting each spectrum to allow the system to settle after re-setting the shutter. At the end of each scan the current average of all collected data was displayed on the screen, along with the average time taken per data point. In both modes the spectra were saved to disk, in two column format, as a function of time in milliseconds.

### 4.4.3 Signal processing

The use of the NMR ticks to measure the magnetic field necessitated post processing of the collected data to extract the field from the recorded ticks. When the ticker was first implemented the spectra were processed in a spread sheet, but this could take up to half an hour per spectrum. A processing algorithm was therefore developed and is given below:

1. Determine where the ticks occur as the PC measures the voltage of the Schmitt trigger/flip-flop. This voltage also decreased over time as the batteries powering the trigger circuit run down over a number of weeks.

2. Count the number of data points between each tick.

3. Determine the mode of the number of data points between each tick.

4. Divide the number of data points between ticks by the mode and round off, to account for missed ticks.

5. Use the start value, the number of points between ticks, and the number of actual ticks between flip-flop state changes to assign a field value to each data point.

The algorithm was tested on a number of data sets and found to work about ninety percent of the time, but it was upset by the following:

1. Spikes in the data.

2. The first tick coinciding with the first data point.

3. When there were too few intervals to enable the deduction of the correct mode value, or when the field had been swept too fast causing a greater number of ticks to be missed by the NMR probe than registered.

The problem of spikes of one point in duration was overcome by filtering the data. This could be done without affecting accuracy as the spikes were easily distinguished from the steps which indicate ticks. Implementation of the filtering increased the reliability to about ninety eight percent. Automatic detection of the second problem is possible but has not been implemented as it manifests itself as a 0.1 mT field offset of the spectrum and can be detected easily when the processed spectrum is compared with a spectrum created assuming a linear increase of field between the start NMR field and the end NMR field. The third problem is generally the fault of the experimentalist for not providing enough data, however, the programs written

based on the algorithm did provide an option for manual input of the mode when the statistics were bad.

The algorithm was encoded in two programs, a stand alone version called *Ticker*, and it was included as an option in the spectrum manipulation package *TestSpec* (§4.4.4). *Ticker* was capable of producing output formatted either as an experimental data file, but with the corrected field, or in a multiple column format for import into a spreadsheet. The second format was the option of last resort, and used when the ticker data was of too poor a quality to process automatically. It included all the information that the algorithm could deduce about the spectrum, and the first column could be set to display either the raw ticks, or the algorithm's estimate of the magnetic field.

No dump facility was provided when the algorithm was included into *TestSpec*, instead the spectrum produced by linear interpolation between the end points was generated automatically, along with the corrected ticker spectrum. The spectra were then overlayed to allow for manual detection of problems such as the 0.1 mT offset, or a jump in the field caused by unfiltered noise.

It would have been possible to include greater intelligence in the algorithm, however, the problems were easy to detect, and the time needed to write and check new code outweighed the benefits.

### 4.4.4 Spectrum manipulation

O'Connell [111] wrote a program *Asciiplot* for viewing the computer collected spectra. The program allowed base-line correction, differentiation, integration and possessed a data cursor. Its disadvantages were that it i) only worked on Hercules display adapters (or adapters emulating Hercules), and ii) only allowed manipulation of one spectrum at a time and placed a limit on the number of data points.

*Asciiplot* was modified to use heap, rather than stack, memory to remove the restriction on data points, but it would have been very difficult to upgrade to support modern display technology and increased functionality. A new package, *TestSpec*, was therefore developed to overcome some of the problems of *Asciiplot* and to adapt to

the new data collection software. *TestSpec* was constructed in two sections, the kernel in which all data processing is performed, and the front end, where the graphical user interface is implemented. It was originally planned to use Microsoft Windows™ as the front end, and the current interface was developed to test the program: hence the *Test* in the name. The kernel of the package has been written in the object-oriented paradigm rendering it easily modifiable and extensible. The use of object-oriented programming greatly simplified the development of what is now a ten thousand line package.

Some of *TestSpec's* capabilities are listed below:

1. Simultaneous viewing and manipulation of multiple spectra.

2. Processing of ticker spectra.

3. Spectrum addition or subtraction.

4. Comparison of spectra with other spectra for intensity determinations.

5. Importing and exporting to many data formats.

6. Conversion of randomly spaced X-data to evenly spaced X-data.

7. Easy reading of peak-peak heights.

8. Printing and plotting of spectra.

9. Stacking multiple spectra on the screen.

Point (6) is one of the most useful as it facilitates point (3) and, when combined with the absolute field measurements produced by the NMR probe, enables the averaging of EPR spectra. This is the first time that EPR spectrum averaging has been available as standard in this laboratory.

An important use of the object-oriented technique has been the definition of operations on a spectrum in terms of tools. That is, ancestor tools for manipulating spectra have been defined, then operations such as taking the derivative of a spectrum have been defined as descendants of these ancestor tools. This technique has

already paid off. When the program was written it did not support integration of spectra or base-line fitting, however, another member of the group[46] was able to use the tools to add these capabilities to the package, without having to expend time in interpreting or even viewing the majority of the ten thousand lines. The program is therefore extensible, one of the main goals of object-oriented programming. *Testspec* has greatly simplified the job of spectrum analysis and interpretation.

### 4.4.5 Spectrum fitting and simulation

Until a few years ago a specific program had to be written to extract spin Hamiltonian parameters from experimental spectra, for each system studied. Recently general programs have been written that can adapt themselves to different effective electron spins and nuclear spins. The program used in this thesis is *EPR.FOR* [109]. It performs an exact diagonalization of the effective spin Hamiltonian and can include high spin terms, such as octupolar crystal field effects, in addition to the more common parameters.

*EPR.FOR* was used for simulation of EPR spectra and energy levels, and for fitting EPR and ENDOR spectra. A companion program, *OutSpec*, was written to read *EPR.FOR* output files and convert them into spectra. The program had the following advantages over the standard *EPR.FOR* output spectra as it allowed:

- the combination of multiple spectra of different intensities;
- selection of separate transitions and allowed the phase of each spectral line to be set;
- each transition to be weighted by an input factor, enabling the Boltzmann equilibrium population distribution to be reflected in the spectra (see §7.6.2); and
- simulation of spectra of differing line widths and shapes without having to re-diagonalize the Hamiltonian, a process that could be time consuming.

[46] D.F.Talbot-Ponsonby.

## 4.5 Optical measurements

Optical absorption measurements were made at room, liquid nitrogen and liquid helium temperatures using a Perkin-Elmer Lambda 9 UV/VIS/NIR Spectrophotometer, and with a Perkin-Elmer Infrared Fourier Transform Spectrometer at room temperature. The quality of sample preparation was important when making infrared measurements as small amounts of grease in the sample would produce spurious absorptions. The samples were typically prepared for infrared measurements by boiling in a mixture of concentrated nitric and suphuric acid for half an hour, then washing in distilled water. When making infrared measurements it was important not to breathe nearby when the sample chamber was open as this would affect the water and carbon dioxide background. It was often necessary to purge the chamber with dry nitrogen for a few hours before and during measurements.

## 4.6 Concentration measurement

EPR is a sensitive technique, capable of detecting as few as $10^{12}$ spins in a sample. It is therefore attractive for use in concentration measurement. Two methods of determining absolute spin concentrations are used:

(i) Absolute measurement, involving calculation of the sensitivity of the system based on the microwave power, temperature, sample losses and other factors. This method is described by Wertz and Bolton [93] on p.462, but is seldom used owing to the number of errors that can occur in the calculation.

(ii) Relative measurement, by comparison with a sample having either a known defect concentration or an absolute number of spins. Some details of this are also described in [93] on p.462.

The second technique was employed in this thesis. The use of a standard allows the effect of spectrometer sensitivity to be eliminated. The experimental method used here for concentration determination is given below:

1. Measure the microwave saturation behaviour of the sample at the temperature at which measurements are to be made. This allows correction to be made for saturation effects.

2. Collect a spectrum at known microwave power, temperature, and field modulation.

3. Replace the sample with the reference sample, placed in the same position within the microwave cavity, and collect a spectrum at known microwave power, temperature and field modulation.

4. Return the sample to the original position and repeat step 2 to measure any unrepeatability in the measurement.

5. Integrate the two sample, and one reference, spectra to determine the intensity under the absorption lines. If first harmonic detection was used double integration will be necessary. When integrating, care must be taken to correct for base-line shifts produced by other defects in the sample.

6. It is often only possible to integrate over one of the EPR lines in the sample owing to overlapping spectra from other defects. The difference in intensity between the integrated single line and the whole spectrum is corrected using simulated line intensities (see §3.5).

7. Correct for differences in field modulation. The intensity of a line is proportional to the amplitude of the field modulation, hence the reference and the sample must be corrected for the ratio of the modulation amplitude to their respective line widths. This relation between intensity and field modulation was verified using pseudomodulation on a simulated Lorentzian line, and experimentally by integrating the same EPR transition collected at different field modulations.

8. The ratio of the corrected integrated intensities is multiplied by the defect concentration of the standard to yield the concentration in the sample.

The reference sample used here was a synthetic type Ib diamond with 220 ppm. $\pm 10\%$ isolated nitrogen as determined from infrared absorption measurements.

# Chapter 5

# $[N–N]^+$ centre

## 5.1 Introduction

This chapter details the first ENDOR experiment performed on an optically created state in diamond. The results relate the most common optical defect ($[N–N]^0$ or the A-centre) to a paramagnetic defect ($[N–N]^+$ or W24). It starts by outlining the optical measurements and theoretical calculations performed on the A-centre, and previous EPR measurements on the ionized A-centre. This is followed by a discussion of the results, the calculation of the defect parameters from the measured hyperfine coupling constants, and the confirmation of the model for the ionized A-centre. A discussion is given examining the contribution of the overlap of atomic orbitals to the calculation of defect parameters, and the dependence on the choice of basis wavefunctions. The relation between the measured quadrupole parameter and the fraction of unpaired electron density for a number of substitutional nitrogen defects is also examined.

## 5.2 Background

### 5.2.1 The optical A–centre, measurements

In 1934 Robertson, Fox and Martin [18] reported the existence of two types of diamond distinguished by their infrared absorption. In 1954 Sutherland *et al.* [121] put

diamond classification onto a more quantitative footing, coining the names "A" and "B" band, identifying infrared absorption modes at 1282, 1203, 1093 and 480 $cm^{-1}$ as belonging to the "A" band, and those at 1426, 1372, 1332, 1171, 1003, 780, 328 $cm^{-1}$ to the "B" band. Custers and Raal [122] examined the problem more closely, recognizing the fundamental absorption edge of diamond (which they placed at 5.6 eV) and the secondary edge at 3.7 eV. Later Sobolev, Lisoivan and Lenskaya [123] suggested that the majority of nitrogen in diamond was in $N_2$ type associations. Davies [124] studied the system, and the previous experiments, and produced a model based upon the following:

1. In all samples studied the A infrared band had the same form, and the position of the 30307 $cm^{-1}$ line was constant. This implied that the A–centre has a well defined molecular structure.

2. The splitting of the 30307 $cm^{-1}$ line at low stress was characteristic of an $A_1$ to $A_1$ transition at a trigonal centre, leading him to propose trigonal symmetry.

3. The absence of any EPR correlating with the A absorption implied that each A–centre should contain an even number of nitrogen atoms to facilitate electron pairing.

4. Electron microscopy performed by Evans [125] suggested that each A–centre contained fewer than eight nitrogen atoms.

5. Luminescence quenching measurements [126] and zero-phonon strain broadening studies [127] were consistent with two nitrogen atoms per centre.

6. Thermal conductivity data [128, 129] suggested 5–16 atoms per centre, however Davies discounted this as A–centres are not the only source of thermal resistance in diamond.

7. The X-ray lattice parameter and density of diamond have been shown to be a function of nitrogen in the A–centres [55, 130]. These results revealed that for each nitrogen atom present in the A–centre, one carbon atom had been removed

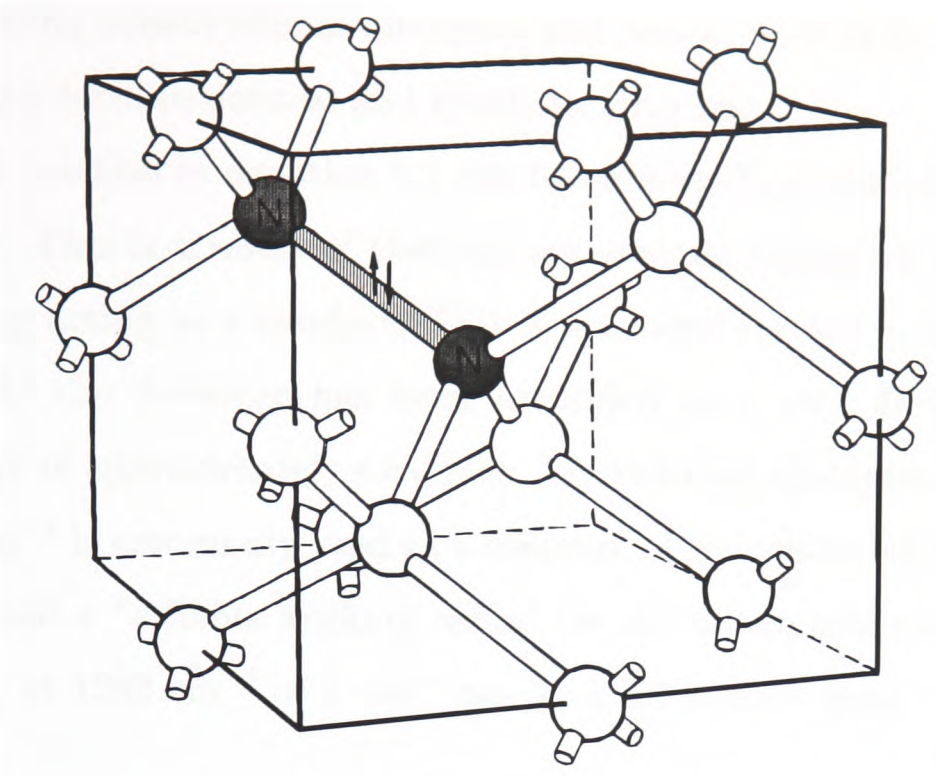


Figure 5.1: The model for the A–centre. The two electrons denoted by arrows are in an antibonding orbital between the nitrogen atoms.

from the diamond. In his argument Davies assumed these nitrogen atoms to be substitutional.

8. A radiation damage defect trapped at the A–centre produces the optical H3 centre. The results of annealing studies implied that the damage centre trapped by the A-centre is ND1 ($[V]^-$). Assumption of the $[V]^-$ model for the ND1 and $[N–N]^0$ for the A–centre reproduced the symmetry of the H3 centre.

9. EPR from an electron located in a C–N bond adjacent to a pair of substitutional nitrogen atoms had been identified [131].

Based on this evidence Davies proposed the model for the optical A–centre illustrated in Figure 5.1.

Annealing studies on type Ib and IaA/B diamond have shown that nitrogen in diamond undergoes the following reaction [132]:

$$[N–C]^0+[N–C]^0 \Longleftrightarrow \text{A–centre} \tag{5.1}$$

These studies have lent further support to the proposal that the A–centre is composed of two neighbouring substitutional nitrogens and hence, very importantly, show how such centres must form in natural and synthetic diamond.

The forward reaction in equation 5.1 can be enhanced by irradiation prior to heat treatment [132]. This is a result of the vacancy assisted migration of $[N–C]^0$ centres with the vacancy acting as a catalyst. This is discussed further in §5.2.2.

Electronically the A–centre has been identified as a very deep donor with an ionization energy of approximately 4 eV [19]. The infrared absorption of the A–centre peak at 1282 $cm^{-1}$ is commonly used as a measure of its concentration. Recent work [133] has produced a "reliable working value" for the absorption strength attributed to the A defect, at 1282 $cm^{-1}$ of 1 $cm^{-1}$ per $16.5 \pm 1$ atomic ppm..

### 5.2.2 The optical A–centre, theory

The A–centre was first discussed theoretically by Mainwood [63], however, the theoretical technique did not perform well and was all but dismissed within the paper. The first rigorous theoretical study was performed by Jones, Briddon and Öberg [65] and by Briddon and Jones [66], where a local-density-functional method was applied to a hydrogen-terminated eighty-six atom cluster. Two neighbouring central carbon atoms were replaced by nitrogen atoms and all atoms were allowed to relax. The nitrogen atoms were found to move away from each other normal to the planes of their carbon nearest neighbours, giving an N–N separation of 2.14 Å (38% extension) and a C–N separation of 1.46 Å (5% contraction). The trigonal symmetry of the defect was maintained. As the equilibrium bond length at 298K is 1.54 Å [23], relaxation of the back bonding carbon atoms is therefore not negligible and must be taken into account. The defect gave an occupied electronic energy level around midgap in accord with the measured ionization energy of about 4 eV [19] seen in type IaA diamonds. The positions of the atoms in the relaxed cluster were then used in a Green's function analysis to determine the vibrational frequencies of the system. The results (see Table 5.1) are in excellent agreement with the measured values lending further credence to the $[N–N]^0$ model for the A–centre.

Table 5.1: Experimental and calculated values for the vibrational frequencies of the A–centre.

| Experimental frequency ($cm^{-1}$) | Calculated frequency ($cm^{-1}$) | |
|---|---|---|
| | From maxima in density of states | Including matrix element effects |
| 480 | 524 | 543 |
| 1093 | 1061 | 1064 |
| 1203 | 1156 | 1182 |
| 1282 | 1290 | 1293 |

The next study by Cunha *et al.* [69] appeared a year later, but did not mention the Jones work. An eight carbon atom cluster, with two carbons replaced with nitrogen ($N_2C_6H_{18}$), was used. The calculations were made at the *ab initio* Hartree-Fock level within the molecular-cluster model. Relaxation was limited to the two nitrogen atoms. A displacement of each nitrogen atom in the $\langle 111 \rangle$ direction of 0.38 Å away from the other was found. This compares with the value of 0.30 Å calculated by Jones. Cunha *et al.* mention that the repulsion of the nitrogen atoms in the defect shows that formation should correspond to an unstable state. This comment will be discussed in conjunction with the succeeding paper. The authors then treated the defect in the positive state and found a broken symmetry corresponding to N and $N^+$ ions. They also calculated that the relaxation is limited to the charged nitrogen with it displacing by 0.42 Å. This contradicts the experimental evidence presented in this chapter and in [103]. No investigation into the effect of cluster size is mentioned, although Mainwood, using three clusters of 47, 59 and 68 carbons, found the relaxation of the N–C bond (which is also studied in her paper) to be strongly dependent on the cluster size [63].

Mainwood [52] has recently applied the *complete neglect of differential overlap* (CNDO) molecular-orbital method, incorporating Car-Parinello molecular dynamics. Her empirical parameters were derived to reproduce the band structure of pure diamond. The clusters comprised 69 and 74 atoms and the outer atoms consisted of $sp^3$ hybrids directed into the cluster to eliminate dangling bonds and problems associated with hydrogen termination of clusters. The calculations showed that the two neighbouring substitutional nitrogen atoms relaxed away from each other with an

elongation of 28% of the bond length. The N–C bond reduced by 4% in length. The total energy of this configuration was calculated to be 2 eV below that of two isolated substitutional nitrogen atoms. This is at odds with the assumptions of Cunha *et al.* [69]. The energy gain on aggregation of the nitrogen into pairs was caused by the lowering of the nitrogen donor level when occupied by the two excess electrons.

## 5.3 Previous measurements on the $[N–N]^+$ centre

In 1983 van Wyk and Loubser [134] reported EPR from a centre, found in gem-quality Cape Yellow diamonds, which was only observable upon illumination with ultraviolet light. Their analysis showed that an unpaired electron is in an orbital on two equivalent neighbouring substitutional nitrogen atoms. They fitted the system to the following effective spin Hamiltonian:

$$\mathcal{H} = g\mu_B \mathbf{B} \cdot \hat{\mathbf{S}} + \sum_{i=1}^{2} |A_{\|} \hat{S}_z \hat{I}_{z_i} + A_{\perp}(\hat{S}_x \hat{I}_{x_i} + \hat{S}_y \hat{I}_{y_i})| \tag{5.2}$$

where $g = 2.0025 \pm 0.0005$, $A_{\|} = 5.53 \pm 0.01$mT and $A_{\perp} = 2.89 \pm 0.01$mT. It was suggested that this centre is a derivative of the diamagnetic $[N–N]^0$ centre[1] and was labelled W24. As the model is confirmed in this work the notation $[N–N]^+$ will be used throughout. They observed a number of other features, listed below:

1. The $[N–N]^+$ centre was not observed in type IaB diamonds (ie. containing no $[N–N]^0$ centres).

2. The observed intensity of $[N–N]^+$ was usually larger in diamonds containing a smaller number of $[N–N]^0$ centres.

3. The concentration of $[N–N]^+$ created by illumination was larger in diamonds showing strong $[N_3V]^0$ luminescence. (This defect is also identified as the optical N3 centre and the EPR P2 centre as noted in Table 1.1.)

[1]The notation A–centre was used in the previous section as i) it concentrated on optical defects and ii) the determination of the model was being described. From henceforth the $[N–N]^0$ notation will be used for clarity.

4. In the majority of samples it was found that a high concentration of $[N–N]^+$ centres was created by illumination only when the concentration of $[N_3V]^0$ centres was more than thirty times that of $[N–C]^0$.

5. Light of wavelength shorter than 415(5) nm (3.0 eV) was required to produce $[N–N]^+$.

6. Two diamonds were cut into two portions each, so that the portions had different masses but faces of equal area. In each case the ratio of $[N–N]^+$ signals was larger than that of the $[N–C]^0$ signals and masses. This indicated that $[N–N]^+$ was not generated uniformly throughout the diamond.

7. The concentrations of $[N–N]^0$ and $[N_3V]^0$ centres are typically of the order of 0.1 atomic % and 0.001 atomic % respectively. This gave the probability of finding an $[N_3V]^0$ centre within one lattice spacing from an $[N–N]^0$ centre of $\sim 10^{-8}$. This corresponded to $10^{-6}$ atomic % and was of the order of the concentration of $[N–N]^+$ observed in the samples.

8. The lifetime of $[N–N]^+$ after extinction of the illumination was sample dependent, with rapid diminution generally occurring, but persistence of the order of minutes was observed in a few samples.

It should be noted that point 7 appears to be at odds with point 6. van Wyk and Loubser resolved the hyperfine interaction into isotropic and anisotropic parts $a$ and $b$ respectively (see equations 3.25 and 3.26 on p.30), with $a$=3.77 mT and $b$=0.88 mT. These values were used to calculate the $s$ and $p$ spin densities at the nitrogen nucleus which were found to be 0.06 and 0.044 respectively. This implied that each nitrogen accounts for 50% of the spin density excluding the possibility for involvement of another atom in the defect. They noted that the $p$:$s$ ratio indicated an extension of the N–N bond.

## 5.4 The experiment

### 5.4.1 Characterization of the sample

#### Choice of sample

Three samples that showed strong $[N_3V]^0$ luminescence when excited with 366 nm radiation were selected from a collection of natural Cape Yellow diamonds. The samples were cut and polished into cubes, with faces approximately parallel to the crystallographic planes {100} or {110}. $[N–N]^+$ centres were observed by EPR upon illumination with light of wavelength shorter than 415 nm and the concentrations of $[N–N]^+$, $[N–C]^0$ and $[N_3V]^0$ were similar in all three samples. The sample which was judged to give a marginally stronger signal was chosen for detailed study. This sample had one plane which was within 2° of a (100) plane and had dimensions of 2.00×2.00×2.08 mm. Two of the corners had cleaved along (111) planes.

#### Defect concentrations from EPR

The sample contained the $[N–N]^+$, $[N–C]^0$, $[N_3V]^0$ and W21 centres. The W21 centre, first observed by Loubser *et al.* [135], is thought to involve three nitrogen atoms in adjacent substitutional sites. Figure 5.2 shows the EPR spectrum of the sample with $\mathbf{B}\|\langle 100\rangle$. The concentration of W21 was too low for accurate measurement, however the concentration of the other defects was determined by comparison with a calibrated reference sample (see §4.6). The absolute concentrations of $[N–N]^+$, $[N–C]^0$, and $[N_3V]^0$ were 1, 4.5 and 190 ppm. respectively, with uncertainties of about 20%. It was found that it was easy to saturate the $[N–C]^0$ system and that the $[N–N]^+$ system reached its peak on the saturation/intensity curve at 20 dB attenuation (about 10 $\mu$W incident microwave power). The saturation curve is shown in Figure 5.3.

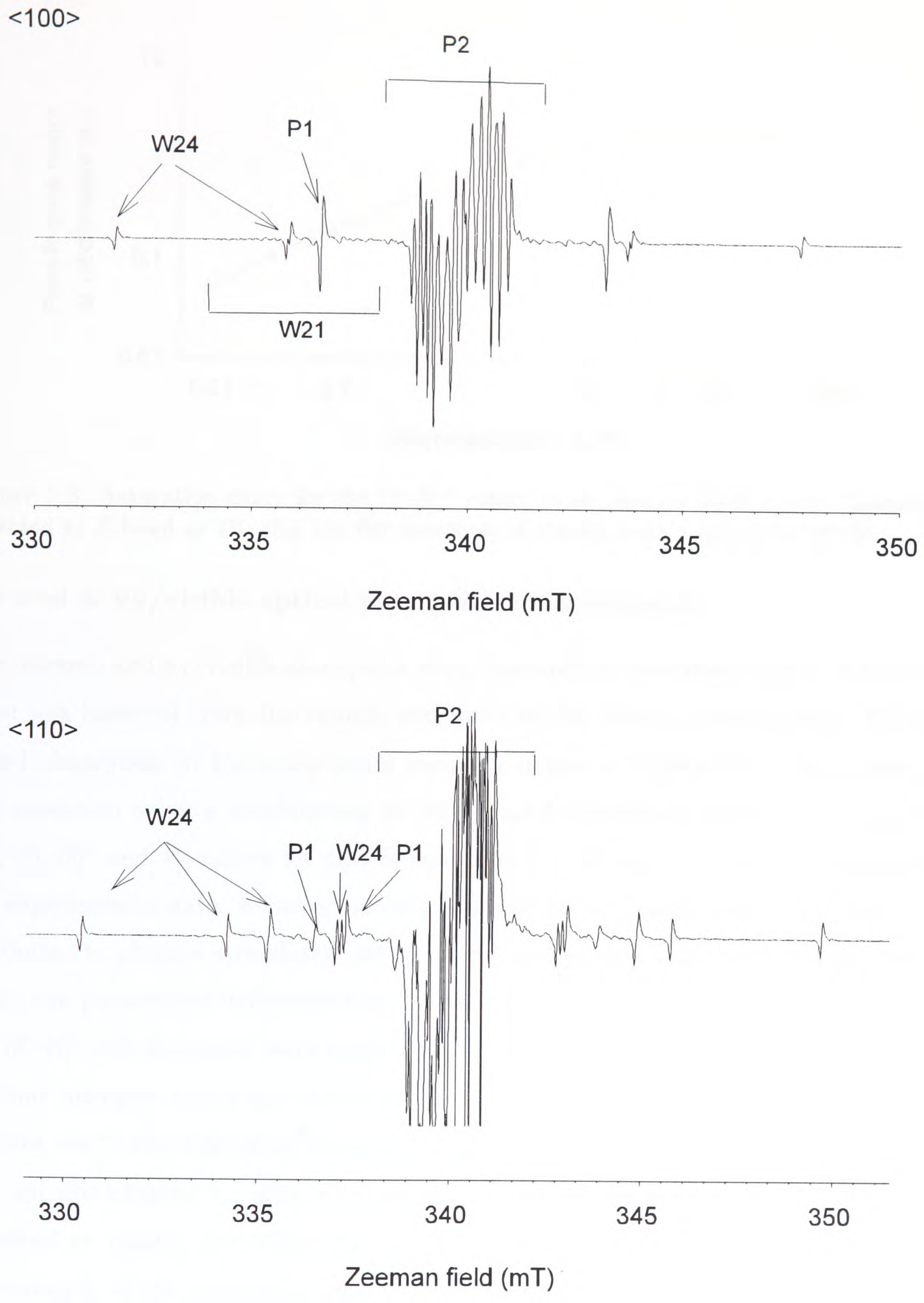



Figure 5.2: EPR spectrum showing the $[N–N]^+$, $[N–C]^0$, $[N_3V]^0$ and W21 centres. The spectrum was collected at X-band at 4K under ultraviolet illumination with $\mathbf{B}\|\langle 100\rangle$ and $\langle 110\rangle$.

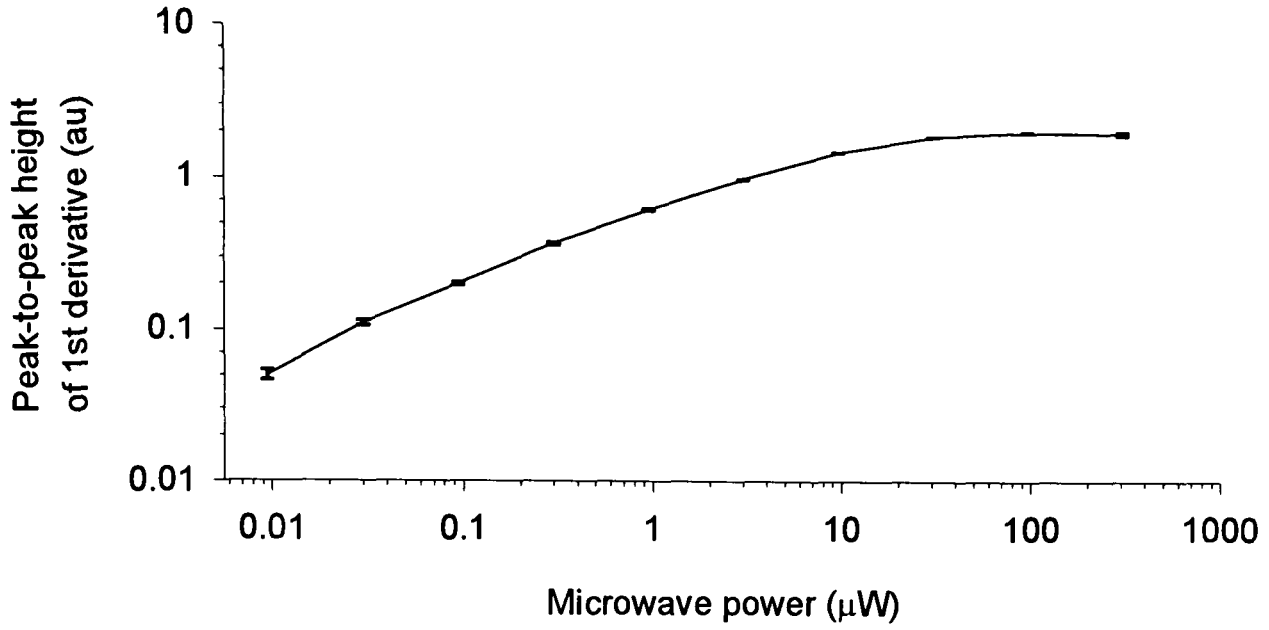



Figure 5.3: Saturation curve for the $[N–N]^+$ centre in the Bruker EPR cavity. Spectrum collected at X-band at 4K with the full spectrum of the Hg lamp running at 100 W.

## Infrared & uv/visible optical absorption measurements

The infrared and uv/visible absorption were measured as described in §4.5. A 0.4 mm plate was laser-cut from the sample and polished for these measurements. The infrared absorption in the one-phonon region is shown in Figure 5.4. Simulation of this spectrum using a combination of the infrared absorption spectra from the $[N–C]^0$, $[N–N]^0$ and B-centres (A and B components) did not satisfactorily reproduce the experimental data, however, inclusion of the D component [136, 137] (which is attributed to platelet stimulated lattice vibrational modes) improved the simulation. Using the parameters determined by Woods *et al.* [138, 139], the concentrations of the $[N–N]^0$ and B-centres were estimated as 150 and 750 ppm. respectively (assuming four nitrogen atoms per B centre). There is clearly a strong platelet peak (B′) at 1370 $cm^{-1}$ and additional structure near 1426 $cm^{-1}$ [137]. Following the notation usually adopted for infrared characterization of diamond [137], the sample was classified as *regular*, for which the intensity of the B′ peak is proportional to: (a) the strength of the absorption from the B nitrogen component; (b) the strength of the absorption due to the D component; and (c) the strength of the $[N_3V]^0$ optical absorption.

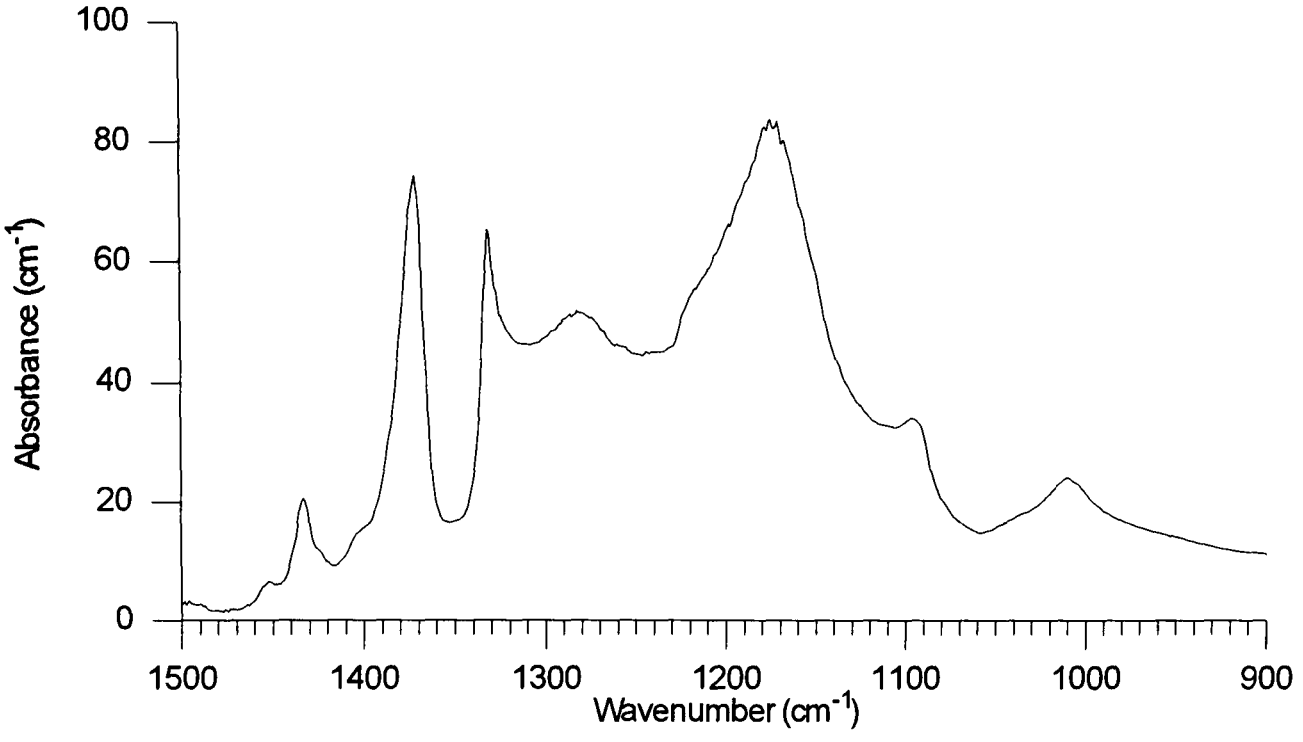



Figure 5.4: Infrared absorption spectrum, measured at 298K with a resolution of 1 $cm^{-1}$.

The room-temperature uv/visible absorption is shown in Figure 5.5. The $[N_3V]^0$ optical absorption between about 3.0 and 3.5 eV is clearly visible. The absorption increases slowly above 3.7 eV and the sample can be identified as type IaA.

### 5.4.2 Experimental details

As the $[N–N]^+$ centre is only visible under illumination, a system was developed to facilitate *in situ* illumination at 4K. This was achieved by mounting the sample at the end of a spectrosil quartz light guide which was then placed within the cold finger inside the Bruker EPR or Clarendon-built ENDOR cavities as described in §4.3.5.

The ENDOR measurements were made in the Clarendon-built cavity (§4.3.8) and the rapid sweep enhancement technique was used to relieve saturation at 5K [119]. The dispersion EPR signal was used as this gave a better response and saturated less easily. The ENDOR signals were detected using 115 kHz field modulation, frequency modulation of the radio frequency at 35 Hz, and double phase-sensitive detection. Frequency modulation at higher frequencies resulted in smaller ENDOR signals, indicating that the relaxation times governing the ENDOR response were long (of the order of tens of milliseconds).

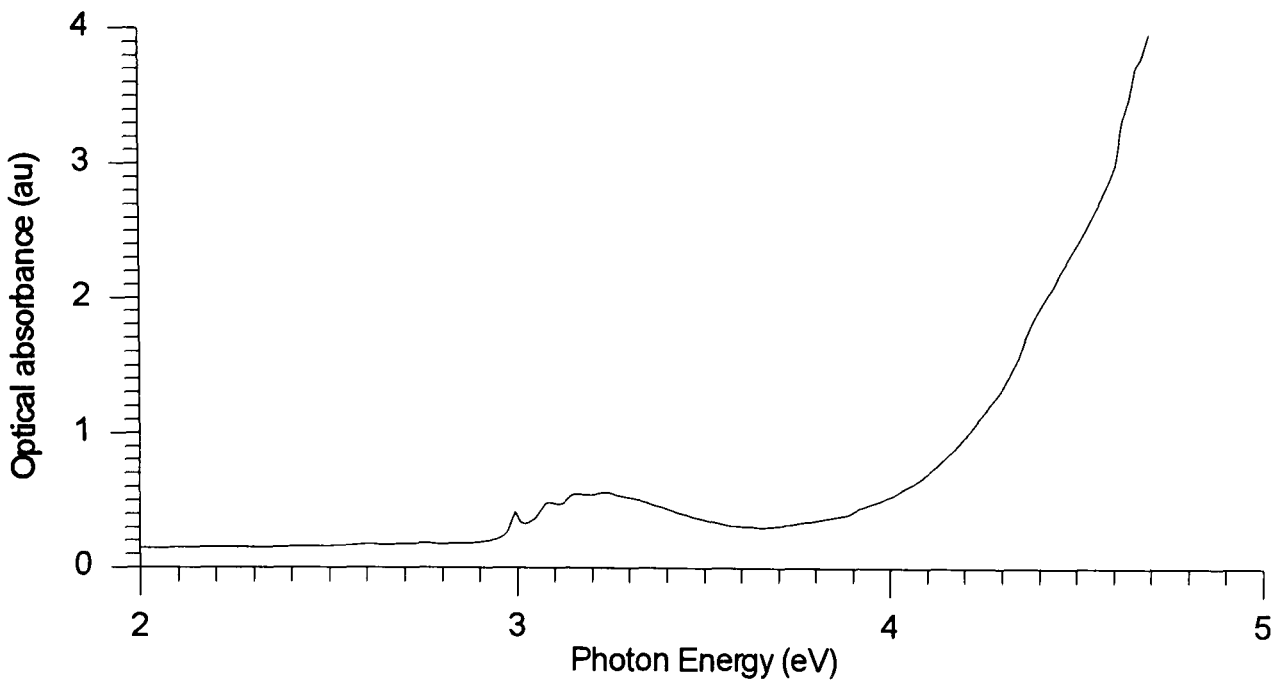



Figure 5.5: uv/visible absorption spectrum, measured at 298K with a slit width of 2 nm.

## 5.5 Measurements

### 5.5.1 Nitrogen ENDOR

In this experiment ENDOR was performed to:

1. Positively identify the nuclei involved thereby verifying the model.

2. Measure the hyperfine and quadrupole interaction parameters accurately to facilitate calculation of bond lengths and the unpaired electron distribution.

#### Measurements

ENDOR measurements were initially made on the $[N{-}C]^0$ system and these revealed a considerable amount of cross-relaxation. Simple ENDOR theory predicts that when the $^{14}N$, $m_N = \pm 1$, EPR transitions are saturated, two different pairs of ENDOR transitions should be observed, whereas four ENDOR transitions should be observed when the $^{14}N$, $m_N = 0$, EPR transition is saturated (Figure 5.6). However, it was found that four $^{14}N$ ENDOR lines could be detected from the $m_N = \pm 1$ EPR transitions as seen in Figure 5.7. The asymmetry in the $[N{-}C]^0$ line shapes was produced by passage effects and diminished when the rf modulation frequency was lowered. Similar cross

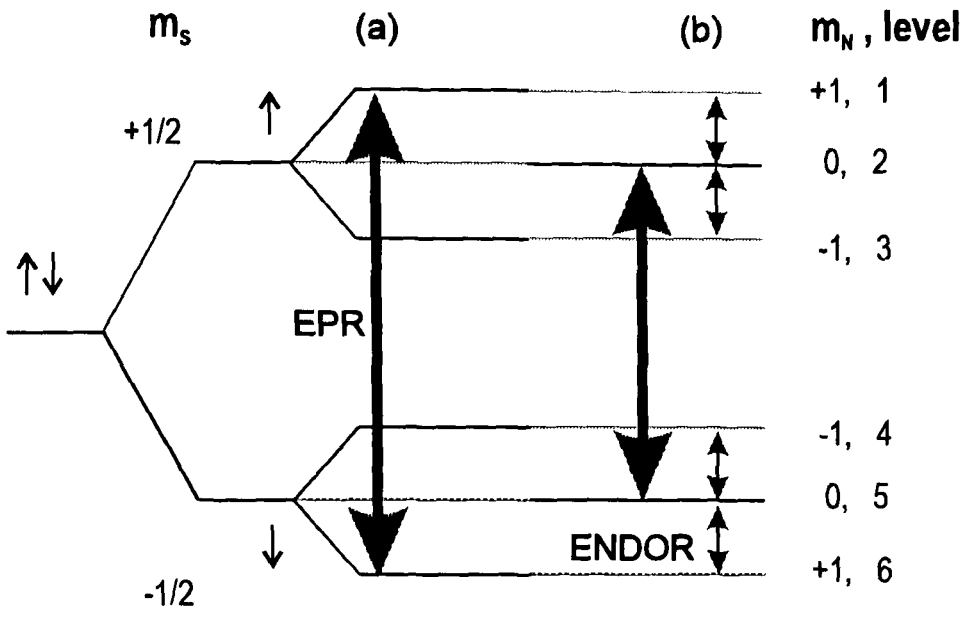



Figure 5.6: EPR and ENDOR transitions in the $[N–C]^0$ system. (a) corresponds to an EPR transition between $m_N = \pm 1$ and two ENDOR transitions, while (b) corresponds to an EPR transition between $m_N = 0$ and four ENDOR transitions.

relaxation behaviour has recently been reported by Cox *et al.* [57, 21] and has been discussed in §2.5. Cross relaxation was also observed in the $[N–N]^+$ ENDOR, and this obfuscated the assignment of transitions. A typical ENDOR spectrum is shown in Figure 5.8. EPR cross relaxation was also noted, with the intensity of the $[N–C]^0$ transitions being strongly affected by the pumping of the $[N_3V]^0$ system.

It was found that light was not needed while making the ENDOR measurements, though it was necessary to subject the sample to an initial illumination, thus indicating that the relaxation time for $[N–N]^+$ was very long. This effect is covered in §5.5.4 and §5.5.3. As a result of the long relaxation time some measurements were made with the light on, some with it attenuated and some with it off. In all cases the rapid-sweep rf was on as this had the largest desaturation effect (see §5.5.3 and Figure 5.14).

### Fitting

The $^{14}N$ ENDOR transitions from the $[N–N]^+$ centre were fitted to the spin Hamiltonian:

$$\mathcal{H} = g\mu_B \hat{\mathbf{S}} \cdot \mathbf{B} + \sum_{i=1}^{2} \left( \hat{\mathbf{S}} \cdot \underline{\mathbf{A}}_i \cdot \hat{\mathbf{I}}_i + \hat{\mathbf{I}}_i \cdot \underline{\mathbf{P}}_i \cdot \hat{\mathbf{I}}_i - g_N \mu_N \hat{\mathbf{I}}_i \cdot \mathbf{B} \right) \tag{5.3}$$

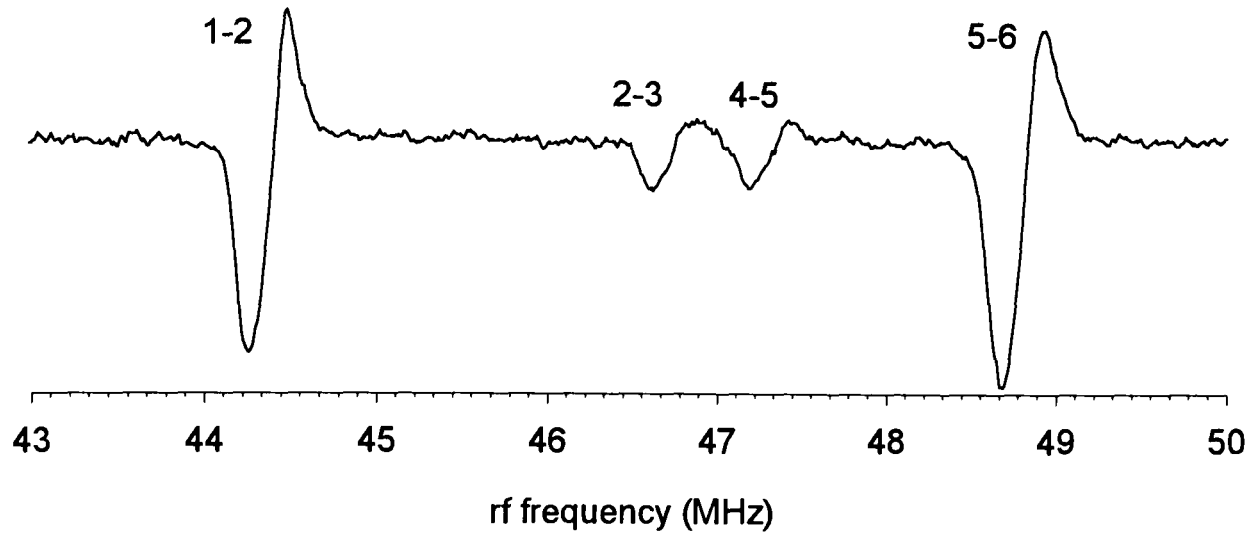



Figure 5.7: $[N–C]^0$ ENDOR while pumping EPR transitions from levels 1 to 6. Transitions between levels 1 & 2 and 5 & 6 are expected, however, cross relaxation also allows transitions between levels 2 & 3 and 4 & 5 to be observed. Collected at X-band, 10 $\mu$W microwave power, 5K, rf enhancement on, 100 W rf amplifier. $\mathbf{B}\|[100]$.

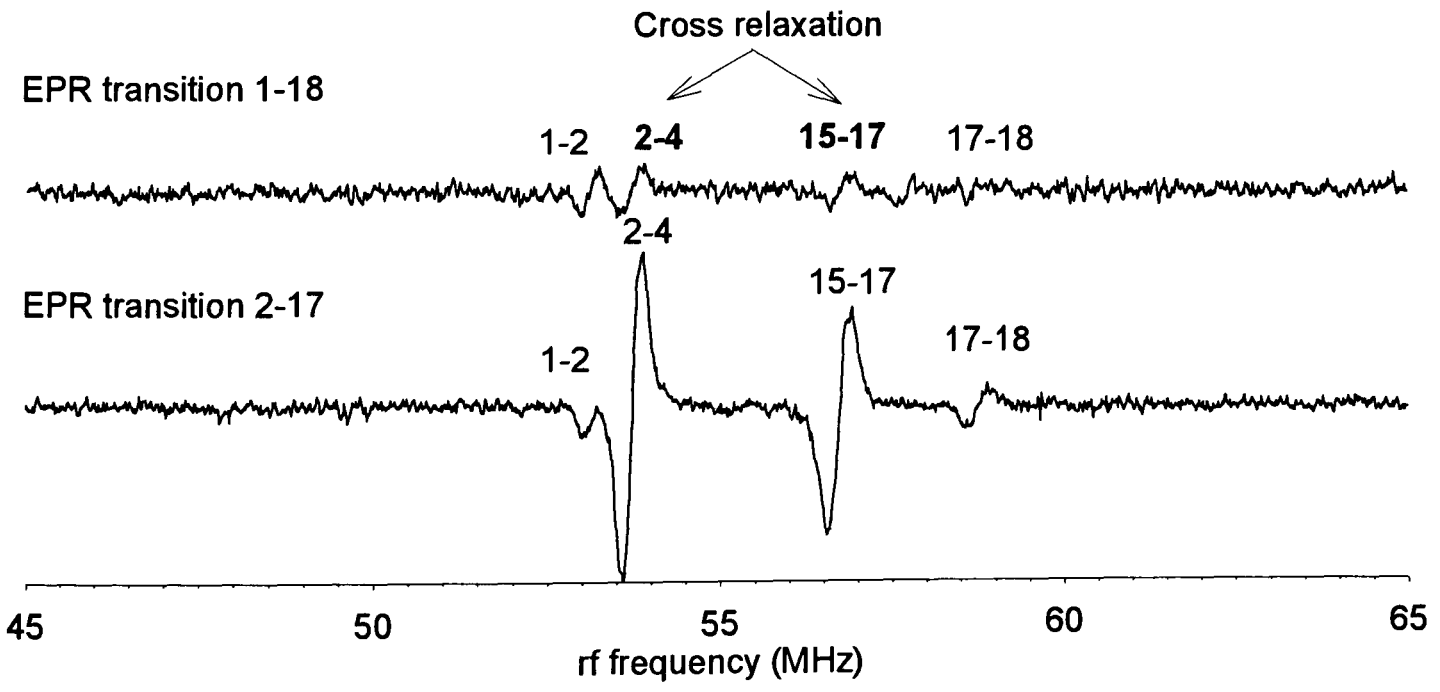



Figure 5.8: $[N–N]^+$ ENDOR from adjacent EPR lines showing cross relaxation (see text). The Zeeman field is parallel to [100]. Collected at X-band, 10 $\mu$W microwave power, 5K, rf enhancement on, 100 W rf amplifier.

The initial fitting assumed two equivalent nitrogen nuclei, with axially symmetric hyperfine and quadrupole matrices having principal axes along $\langle 111 \rangle$ and $\langle \overline{111} \rangle$ respectively. The electronic $g$-value was taken to be 2.0025 (consistent with EPR measurements both by van Wyk and Loubser [134], and in this study) and the nuclear $g$-value for both nuclei was set at 0.4037607: the value for a free $^{14}$N atom. Once all the ENDOR transitions had been allocated in accordance with this assumption, the hyperfine and quadrupole matrices were varied to optimize the fit to the experimental data. Various constraints were then systematically removed to investigate the validity of the assumptions. First the parameters constraining the nuclear $g$-values were relaxed, but the values converged to that of nitrogen. Then the equivalence of the nuclei was relaxed, however, the decrease in $\chi^2$ was countered by the increased number of parameters rendering it statistically equivalent to the constrained case. To check for the possibility of interaction between the nitrogen nuclei a term of the form:

$$\mathcal{H} = \hat{\mathbf{I}}_1 \cdot \underline{\mathbf{J}} \cdot \hat{\mathbf{I}}_2$$

was included. As the most probable direction for the interaction was along the line joining the two dipoles the interaction was assumed to have the same $\langle 111 \rangle$ symmetry as the A-tensor. The term did not improve the fit, it actually decreased the quality raising the RMSD.[2] An isotropic term was substituted for the axial term, however, this too did not produce an improvement. This was unfortunate because a measurement of a purely dipolar nuclear-nuclear interaction could have been used to determine the nitrogen-nitrogen separation accurately. An estimate of the expected coupling can be calculated using the N–N bond length of 1.86 Å (§5.6.2) and the formula for the interaction of two point dipoles (see equation 8.2 on p.202). This gives an expected interaction of 148 Hz which is within the error of the measurements in Table 5.2. Finally, the symmetry condition was relaxed, but the fitting algorithm still converged to axial symmetry. The RMSD for the final fit was 27 kHz. The observed peak-to-peak line width was 85 kHz so this error was well within the expected margin. The

[2]Root mean squared deviation, or root mean sum of squares of weighted differences between observed and calculated frequencies.

Table 5.2: $^{14}$N hyperfine and quadrupole parameters for [N–N]$^+$, measured at 5K.

| van Wyk and Loubser | Present Study |
|---|---|
| $g =$ 2.0025(5) | $g =$ 2.0025(5) |
| $A_{\|\|} =$ 154.7(3) MHz $\|\|$ ⟨111⟩ | $A_{\|\|} =$ 155.26(2) MHz $\|\|$⟨111⟩ |
| $A_\perp =$ 81.0(3) MHz | $A_\perp =$ 81.51(1) MHz |
| | $P_{\|\|} =$ -2.245(5) MHz $\|\|$ ⟨111⟩ |

results of the fit are given in Table 5.2.

## 5.5.2 EPR measurement of $^{15}$N and $^{13}$C hyperfine structure

### $^{15}$N hyperfine interaction

$^{15}$N has a natural abundance of 3.66% so in the [N–N]$^+$ centre the probability of having one $^{14}$N and one $^{15}$N is 0.73%, both $^{14}$N 99.27%, or both $^{15}$N 0.001%. The intensity ratio in the ⟨100⟩ direction is therefore [$^{14}$N–$^{15}$N]:[$^{14}$N–$^{14}$N] :: 1:136 (see §3.5.1). The signal to noise ratio[3] for an average of two scans over a $^{14}$N line was 2600:1, therefore the $^{15}$N system should be visible. The positions of the EPR transitions from the [$^{15}$N–$^{15}$N] pairs can be accurately estimated as the $^{15}$N hyperfine parameters, electronic $g$-value and ratio of nuclear $g$-factors are known. Both the isotropic and anisotropic portions of the hyperfine interaction (§3.2.4) are directly proportional to the nuclear $g$-factor. If there is no hyperfine anomaly (see Abragam and Bleaney, p.706 [91]) the hyperfine interaction will scale in the ratio of the respective nuclear $g$-factors. Figure 5.9 shows an experimental EPR spectrum and a simulation thereof; the lines from the [$^{14}$N–$^{15}$N] pairs are clearly visible. This result provides independent confirmation that the [N–N]$^+$ centre incorporates two nitrogen atoms. The sensitivity is high enough for the $^{13}$C hyperfine interaction to be visible on the [$^{14}$N–$^{15}$N] pairs shown in Figure 5.10.

[3]The signal to noise ratio was calculated as the peak-to-peak signal / RMSD noise, where the RMSD noise was computed by fitting a straight line to a signal-free portion of base line. The deviation between this line for each data point and the signal was squared and averaged, finally taking the square root to yield the root mean squared-deviation. The peak-to-peak height was determined by taking the maximum and minimum values of the first derivative line.

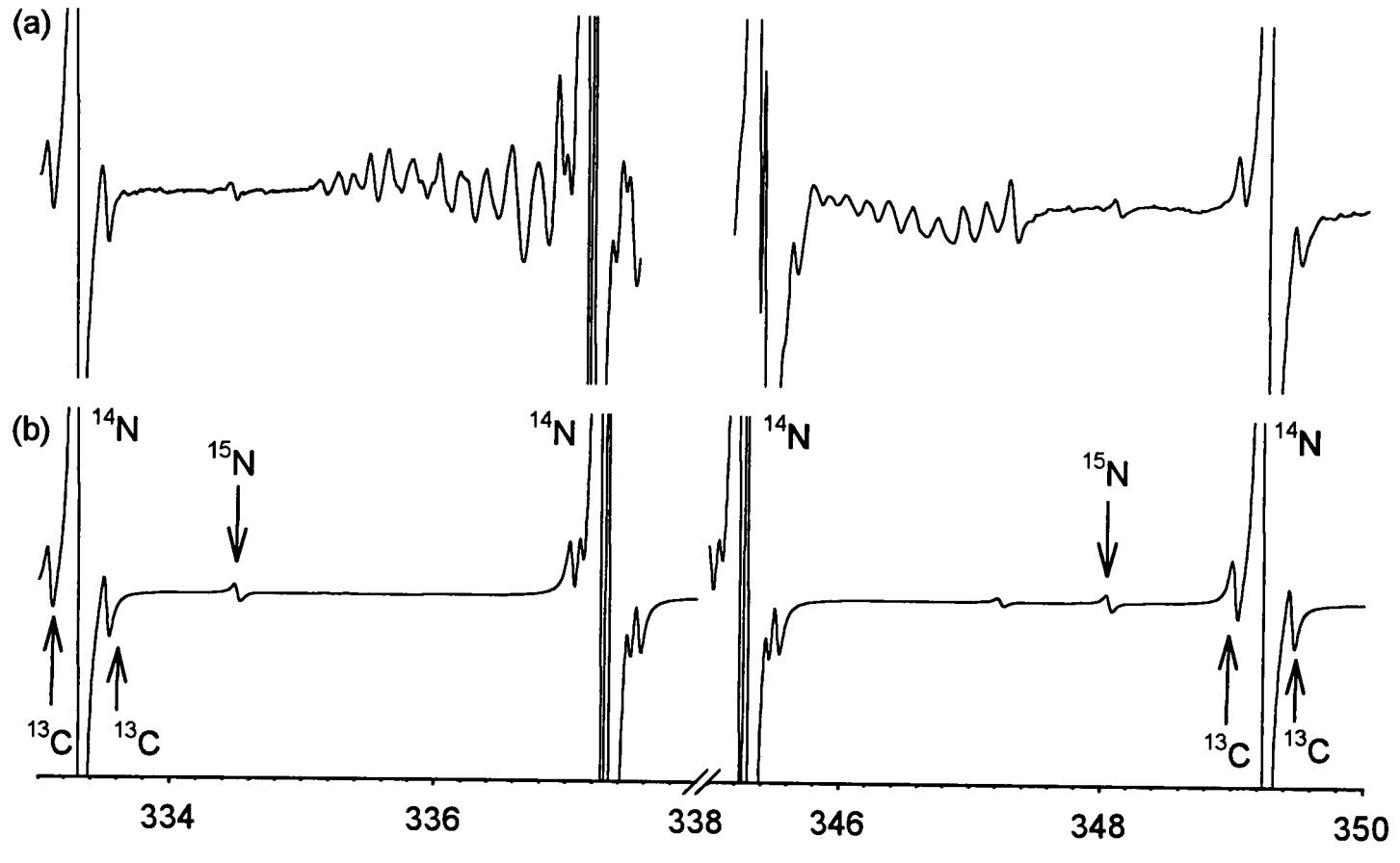



Figure 5.9: 9.65 GHz EPR spectra: (a) Experimental spectrum, $\mathbf{B}\|\langle 100\rangle$ and T=5K and (b) simulated $[N–N]^+$ spectrum, $\mathbf{B}\|\langle 100\rangle$, including $^{14}N$, $^{15}N$ and $^{13}C$ lines.

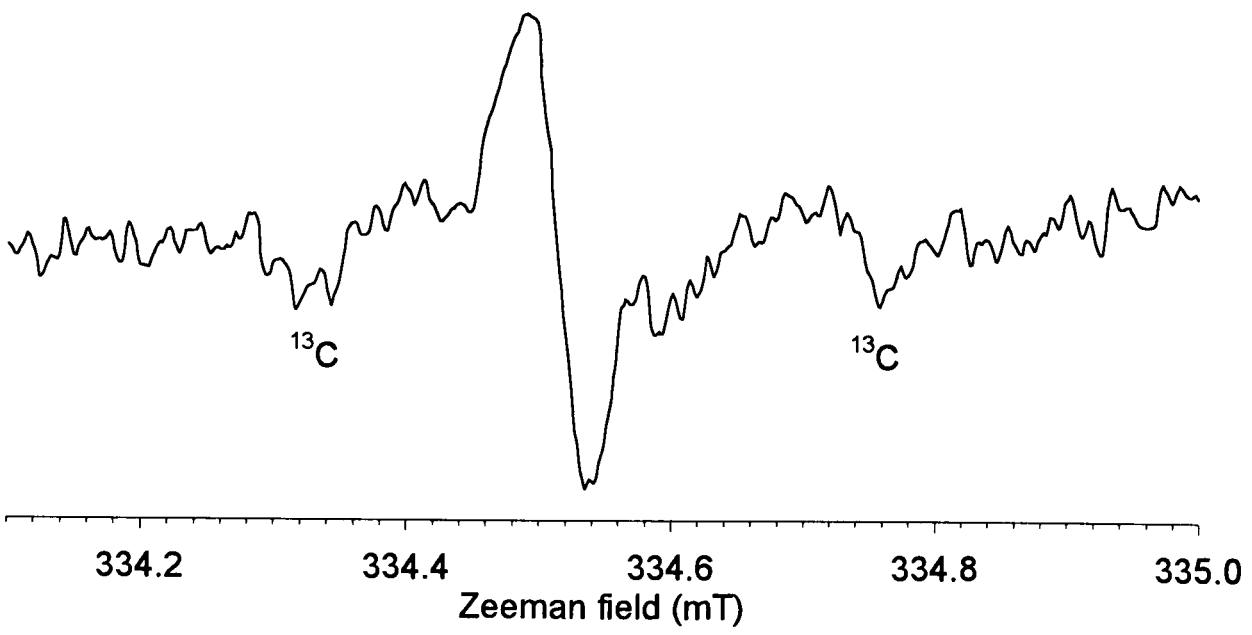



Figure 5.10: $^{13}C$ hyperfine structure on the EPR signal from a $[^{14}N–^{15}N]$ pair.

## $^{13}$C hyperfine interaction

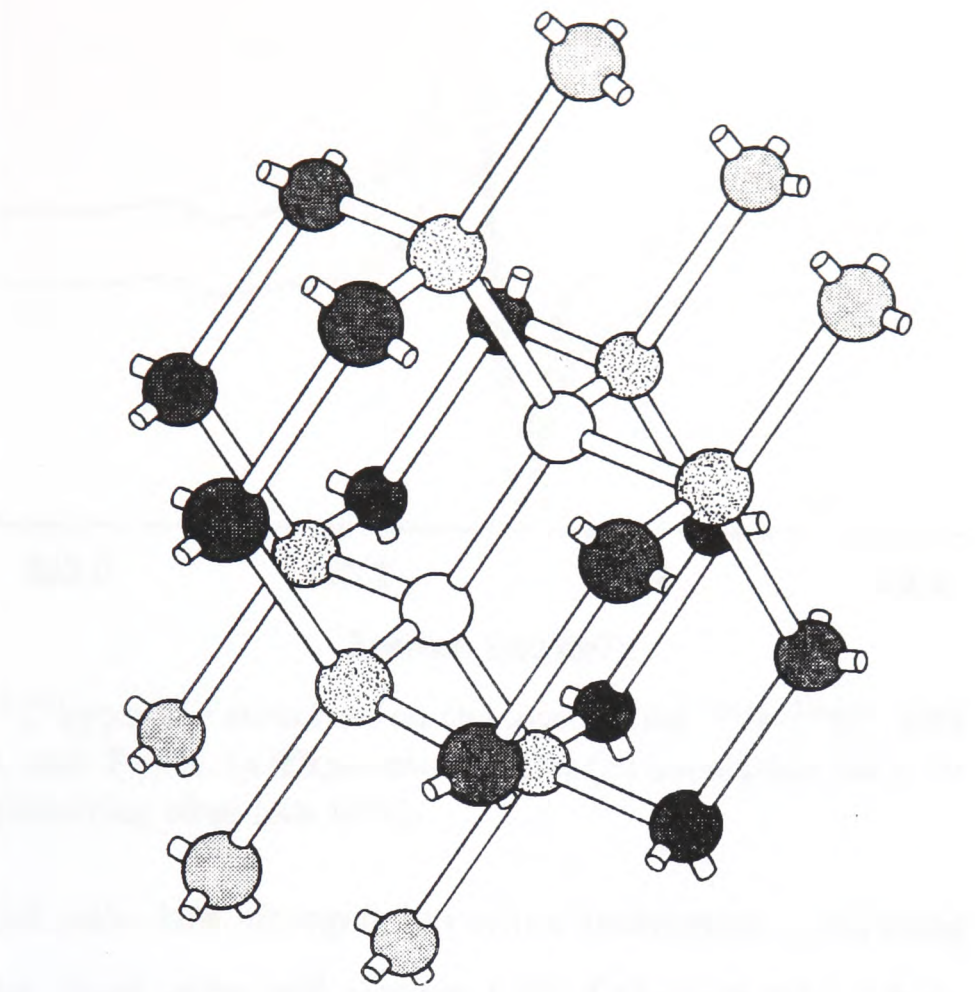


Figure 5.11: Diamond lattice showing the equivalent sets of C–neighbour positions for $[N–N]^+$. The white atoms are N, the light speckling denotes the six nearest neighbours, and the dark and light shading denotes two sets of next-nearest neighbours.

As mentioned in the previous paragraph, additional weak transitions are observed as a result of the coupling between the unpaired electron on the $^{13}$C ligand nuclei around the nitrogen atoms of the $[N–N]^+$ centre. The sets of equivalent neighbouring carbon atom sites are shown in Figure 5.11. There are six nearest neighbour carbon sites, and two groups of more distant equivalent neighbours containing six and twelve members. The natural abundance of $^{13}$C is 1.1% and the probability, $P$, that $r$ of a group of $n$ equivalent neighbours are $^{13}$C atoms is given by the Binomial distribution (equation 3.50). The probabilities for one $^{13}$C in various sites are listed, along with the ratio of the intensity of the $^{13}$C hyperfine lines to the central line without the $^{13}$C hyperfine interaction, in Table 5.3. The $^{13}$C interaction differs from the $^{15}$N case as it produces an additional interaction rather than modifying the magnitude of the existent hyperfine splitting. As the coupling is weak it acts as a perturbation and

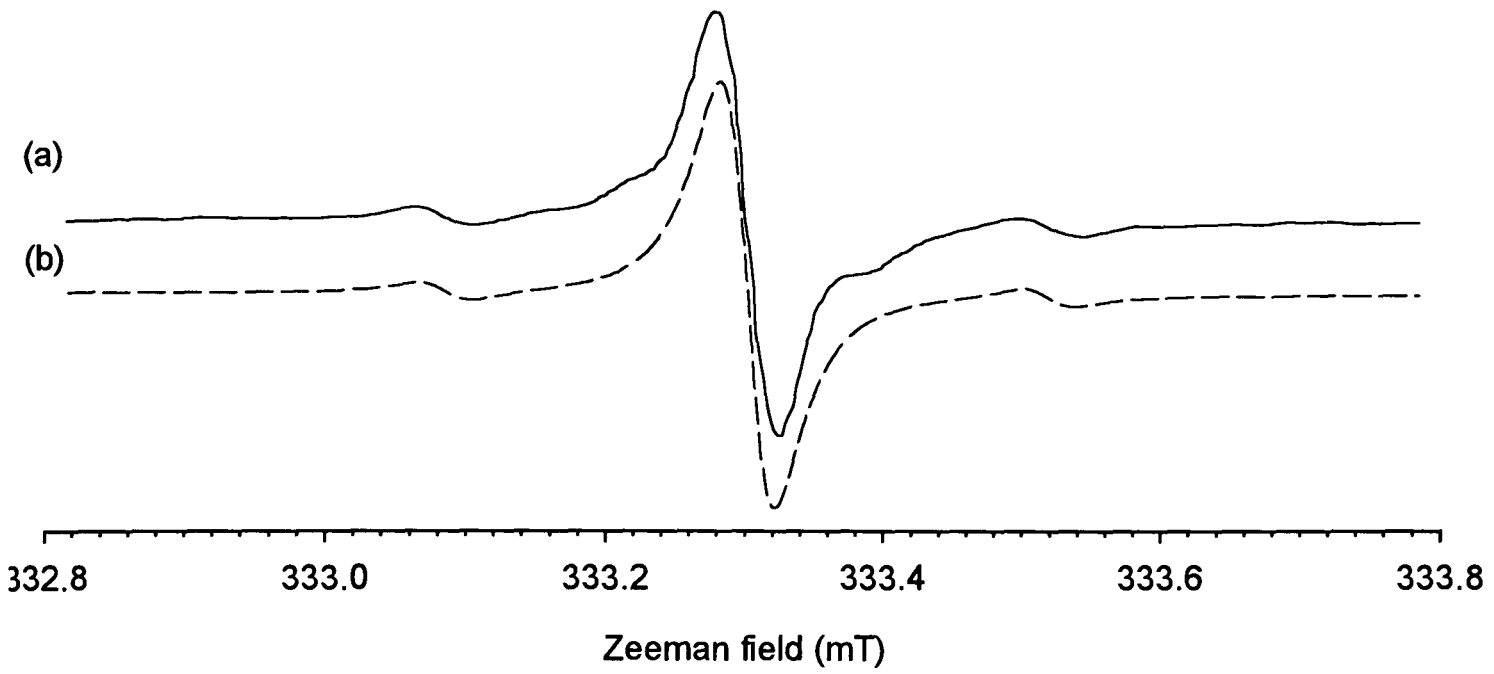



Figure 5.12: $^{13}$C hyperfine structure on the lowest field $[^{14}N–^{14}N]^+$ EPR line for $\mathbf{B}\|\langle 100\rangle$, $\nu_{\mu w}$=9.65 GHz, and T=5K. (a)Experimental and (b) simulation for a $^{13}$C atom in one of 6 equivalent neighbouring sites (see text).

is superimposed onto the nitrogen hyperfine interaction producing a pair of wings about each line. Each wing will contain half of the intensity tabulated in Table 5.3. In Figure 5.12 the lowest $^{14}$N hyperfine $[N–N]^+$ EPR line is shown, with the magnetic field in a $\langle 100\rangle$ direction. The line is clearly flanked by $^{13}$C satellites. The simulation is produced with the assumption of six equivalent neighbours, Lorentzian shape and a line width[4] of 0.042(2) mT; it is clearly an accurate reproduction of the experimental data.

The ratio of the amplitudes of the wings to the central lines was determined by fitting a superposition of first derivative Lorentzian lines[5] to each spectrum using the Levenberg-Marquadt minimization technique [140]. The ratio was found to be highly sensitive to the slightest misalignment as this produced broadening of the lines resulting in a deviation from the derivative Lorentzian shape. Incident microwave power also affected the ratio. In order to eliminate the orientation dependence, the sample was misaligned until each line from the $\langle 100\rangle$ direction split into four nitrogen

[4]Measured as the half width at half height (HWHH).

[5]The software was adapted from a program written by Dr M.McNamee.

Table 5.3: Probabilities and ratios for one $^{13}C$ and various numbers of neighbours at natural abundance.

| Number of neighbours (sites) | 3 | 6 | 12 |
|---|---|---|---|
| Probability that one site is occupied by $^{13}C$ | 0.032 | 0.063 | 0.117 |
| Ratio of one $^{13}C$ compared to none | 30.0 | 15.1 | 7.5 |

lines with accompanying $^{13}C$ wings. Multiple spectra were collected, with increasing and decreasing field sweeps to accommodate any passage effects, and signal averaged to increase the signal-to-noise ratio. These spectra were then fitted to systems of four nitrogen lines, each with their accompanying wings. The heights, offsets and widths of the wings, and the heights and widths of the central lines were all coupled. The ratio in this configuration tended towards $30 \pm 4$.

In general it was difficult to force the ratio to converge to fifteen or thirty as the presence of unresolved structure on the central lines, see Figure 5.12, confused the fitting algorithm. It was not possible to fit another set of Lorentzians to this structure, yet the program still tried to broaden the central line to compensate. Owing to this complication the problem was inverted, with the ratio fixed at fifteen or thirty and the $\chi^2$ ratio used as a guide to the quality of the fit. Using this technique the computer favoured thirty and chose a line width of 0.042 mT. The ratio obtained in the above two procedures indicated that the wings were produced by a set of six equivalent neighbours.

The dependence of the $^{13}C$ hyperfine coupling on Zeeman field direction was investigated. It was found that for all orientations only one set of satellites was observed around the main $[N–N]^+$ lines. To within the accuracy of the measurements the separation, 0.44(2) mT, of the satellites was found to be independent of orientation and they were always centred around the main hyperfine lines. The inner wings were not symmetrically positioned about the main $^{14}N$ hyperfine lines, and hence could not be satisfactorily ascribed to a weak hyperfine coupling to a $^{13}C$ neighbour. The separation of the outer satellites corresponds to an isotropic $^{13}C$ hyperfine coupling of 12.3(5) MHz.

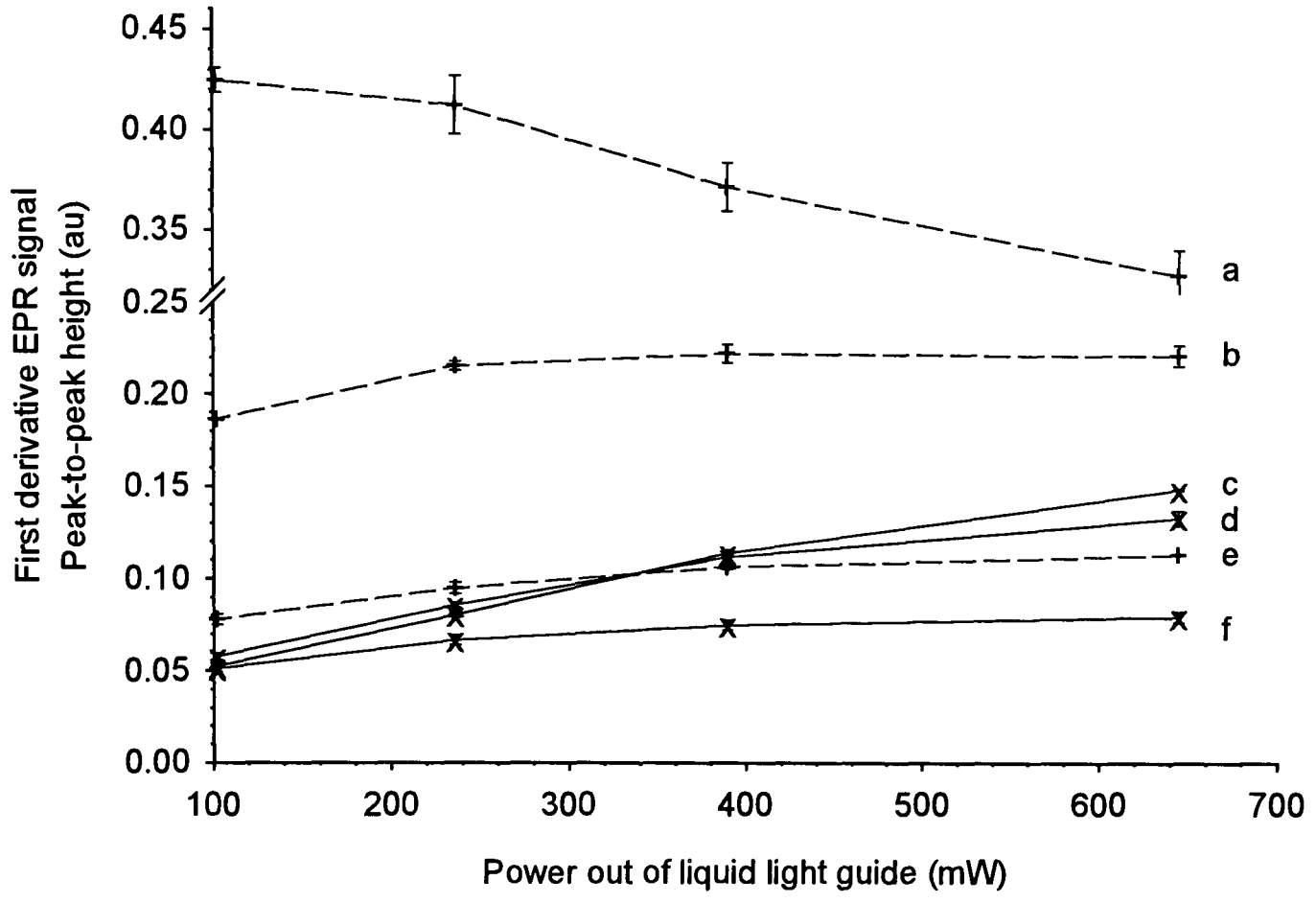



Figure 5.13: Peak-to-peak height of $[N–N]^+$ and $[N–C]^0$ EPR signals as a function of light power, at various microwave powers $P_{\mu w}$ ($\nu_{\mu w}$=9.65 GHz, and T=5K). $[N–C]^0$ EPR at attenuations $P_{\mu w}$ of (a) 50 dB, (b) 40 dB and (e) 30 dB. $[N–N]^+$ EPR at $P_{\mu w}$ of (f) 50 dB, (d) 40 dB and (c) 30 dB.

### 5.5.3 EPR saturation effects

Absolute and comparative EPR absorption measurements of the $[N–N]^+$, $[N–C]^0$ and $[N_3V]^0$ centres are difficult because of saturation and cross-relaxation effects. At helium temperatures the average lifetime of the $[N–N]^+$ centres created by illumination is very long (§5.5.4), and illumination has the secondary effect of desaturating the $[N–N]^+$, $[N–C]^0$ and $[N_3V]^0$ EPR signals. Two mechanisms contribute to the desaturation: the former being a heating effect produced by dumping 200 mW of light power onto the sample, and the latter being rapid saturation transfer via electrons temporarily excited to the conduction band (as has been previously observed in silicon [141]). Figure 5.13 illustrates the effect of varying light intensity on the peak-to-peak line heights for the $[N–N]^+$and $[N–C]^0$ EPR transitions at various microwave powers.

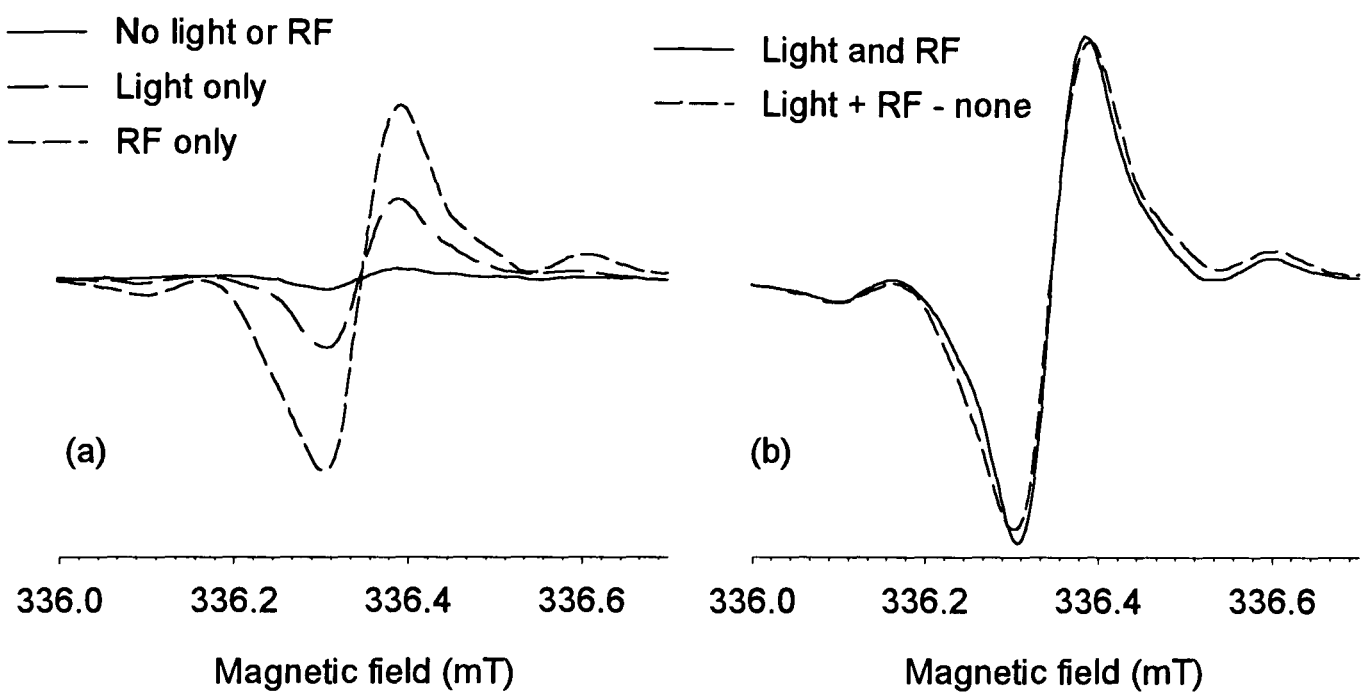



Figure 5.14: Enhancement of the $[N–N]^+$ EPR signal. Lowest field EPR line at 5K, $\nu_{\mu w}$=9.65 GHz, $\mathbf{B}\|\langle 100\rangle$. (a) Shows the relative contributions of the two enhancement effects, while (b) illustrates that the sum of the enhancements, applied separately, equals that obtained when applying both together, indicating that separate, non-interacting mechanisms are involved.

Clearly the effect of light on these centres is dependent on microwave saturation. Examination of the $[N–C]^0$ curves shows the transition from dominance of the light induced desaturation effect to that of ionization.

As mentioned earlier an rf enhancement technique was used to improve the EPR and ENDOR signal-to-noise ratios. The effect is illustrated in Figure 5.14 along with the desaturation produced by light. As is evidenced, the largest desaturating effect is produced by the rf, followed by the light. The effects occur by different paths, and the ENDOR's insensitivity to light (§5.5.1) showed that the light did not short-circuit the rf. If the rf does not short-circuit the light then the effects should be additive. This is seen in Figure 5.14(b) where the light only and rf only spectra are added (the non-enhanced spectrum is subtracted from the sum to remove its double contribution) before comparison with the combined rf-on and light-on spectrum.

As the light facilitated relaxation path is probably via conduction electrons, when the light is turned off the signal decrease will be rapid. This is likely to be the main contributor to the to the fast component of the decay discussed in §5.5.4. It is clear

that great care has to be taken when measuring intensities to avoid being misled by saturation effects.

### 5.5.4 Lifetime of the $[N–N]^+$ centre

The fact that it was necessary to illuminate the sample before $[N–N]^+$ resonance was observed implied that $[N–N]^+$ is an excited or metastable state. As the decay is slow, and no optical polarization occurred, the possibility of a polarized ground state (as in the case of the $[N–V]^-$ centre, §2.3) is eliminated. Cycling to room temperature reset the system, that is to say that any long lived $[N–N]^+$ centres were destroyed, therefore the decay showed some temperature dependence. van Wyk ([134] and §5.3) reported decay times at room temperature ranging from instantaneous (as in this case) to many hours.

When the resonance was observed on the oscilloscope it was noted that on removal of the light $[N–N]^+$ decayed rapidly then slowly. It was therefore necessary to investigate the sample on the millisecond and tens of seconds scale. The data collection software was re-written for this purpose as detailed in §4.4.2. To make the decay time measurements the magnetic field was set to the positive lobe of the first harmonic signal of an $[N–N]^+$ line and the light was removed. Measurements were made over various time periods, collecting up to 120 spectra and signal averaging for the very fast decays, and collecting for up to half an hour with a long time constant for the slow component. The effect of microwave power and the rf desaturation was investigated. The number of averages and spectrum collection time were limited to half an hour by the stability of the magnet and cryogenic system, despite efforts to improve this.

The rf desaturation technique was used to enhance the EPR for the slow measurements, minimizing the proportional effect of i) the initial decrease caused by the loss of electrons in the conduction band, and ii) the decrease produced by heating. The long term decay was measured at temperatures between 4.9K and 50K.

Figure 5.15 shows the dependence of the intensity of the low field EPR line after removal of the light, at temperatures between 6K and 54K. At 6K the $[N–N]^+$ EPR

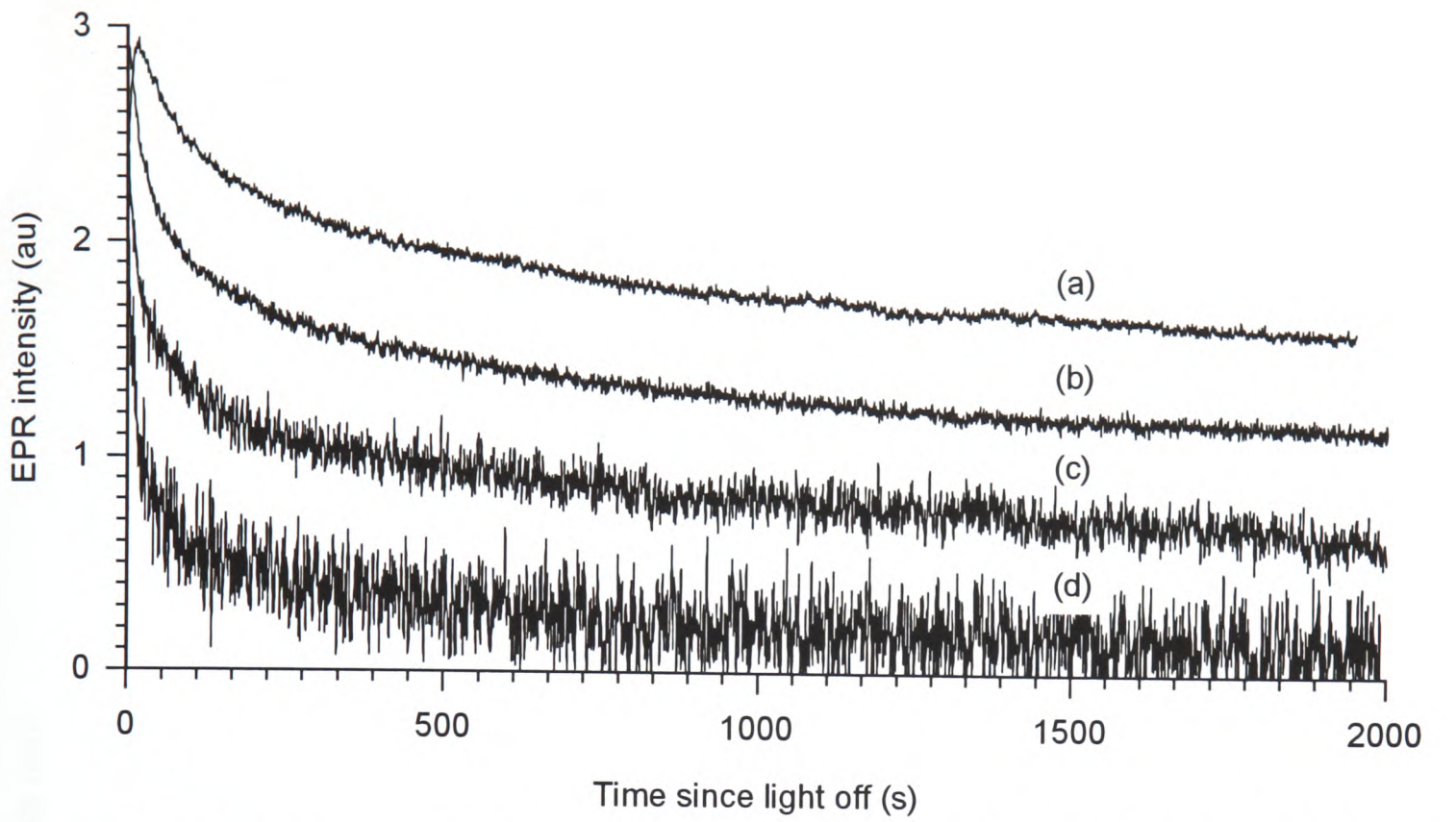



Figure 5.15: Change in the EPR intensity of the low field ($\mathbf{B}\|\langle 100\rangle$) $^{14}$N hyperfine line of $[N–N]^+$, at temperatures between 6K and 54K, with time after the light has been switched off. (a) 6K,(b) 10K,(c) 27K and (d) 54K.

was easily observed for more than 30 minutes after the light had been switched off, while at 54K the signal decayed almost entirely within 30 minutes. In the first few seconds of the 6K spectrum a rapid rise produced by cooling after the removal of the light can be seen.

In Figure 5.16 the spectra have been corrected for the Curie-Weiss temperature dependence and plotted against the logarithm of time. The temperature correction is applicable here as, although the centre is termed an excited state, it is created through ionization of an $[N–N]^0$ centre (or electron capture by an $[N–N]^{2+}$ centre) to form the $[N–N]^+$ centre which behaves as an electronic ground state and therefore obeys the Curie-Weiss law. It can be seen that at low temperatures the curves are straight and parallel showing that the decay was not exponential. The curves deviated from linearity as the temperature was raised.

Logarithmic time dependencies were first mentioned by Anderson [142] in conjunction with the specific heat in glasses. Phillips [143] was concurrently working

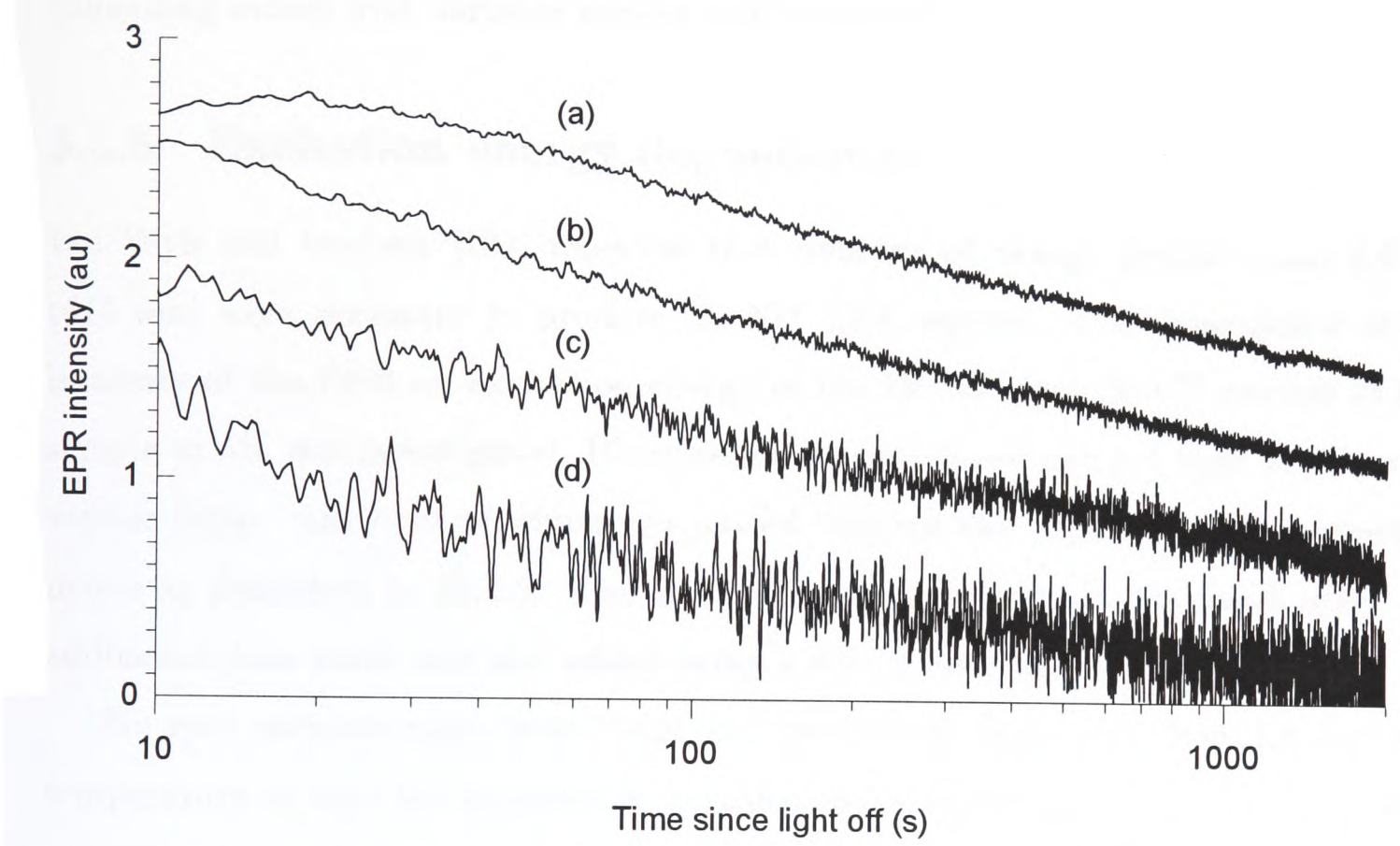



Figure 5.16: Change in the EPR intensity of the low field ($\mathbf{B}\|\langle 100\rangle$) $^{14}$N hyperfine line of $[N{-}N]^+$, at temperatures between 6K and 54K, with the logarithm of time after the light has been switched off. The EPR signal intensity has been corrected for the Curie-law variation with temperature. (a) 6K, (b) 10K, (c) 27K and (d) 54K.

on the same problem and both parties postulated a phenomenological model based on ionic tunnelling in a two level system (TLS) with variable barrier heights/widths. Jackle [144] extended this model to ultrasonic attenuation in glasses and applied slightly more rigour, introducing a probability distribution $P(E, \tau^{-1})$ for finding a TLS with excitation energy $E$ and relaxation rate $\tau^{-1}$. This result was subsequently applied to explain logarithmic time dependencies in spectral hole burning experiments [145, 146]. Logarithmic dependencies have recently been reported in optical measurements on the H2/H3 centre in diamond [147] and explained by invoking a tunnelling model with variable barrier widths (see §5.6.5).

### 5.5.5 Excitation energy dependence

van Wyk and Loubser [134] reported that photons of energy greater than 3.0 eV (415 nm) were necessary to produce $[N–N]^+$ EPR signals. The dependence of the intensity of the EPR on excitation energy of the $[N–N]^+$ and $[N–C]^0$ centres in this sample at 5K was investigated. Illumination was produced using a high pressure Hg vapour lamp – the light of which was passed through the $\frac{1}{4}$m Jarrel Ash monochromator as described in §4.3.5. The slit width was set for an 8 nm band pass. An additional data point was also added using a red diode laser (§4.3.5).

Six spot measurements were made and the system was cycled from 5K to room temperature to reset the populations between each measurement. The measurements are presented in Figure 5.17. Heating effects were negligible as the monochromator reduced the incident power to between 0.7 and 1.4 mW. The laser input had an intensity of 3.5 mW, however the sample was transparent at these wavelengths so absorption and hence heating was minimal. The maximum heating effect, extrapolated from the change when illuminated by the 200 mW full spectrum, was a decrease in signal amplitude of 0.9%. It is clear from the figure that photons of $E > \sim 2.9$ eV created more than an order of magnitude more centres when compared to photons with $E > \sim 2.9$ eV, however increasing the photon energy above 3.0 eV did not dramatically increase the number of $[N–N]^+$ centres created. The dependence on intensity of the $[N–C]^0$ centre on photon energy was much weaker.

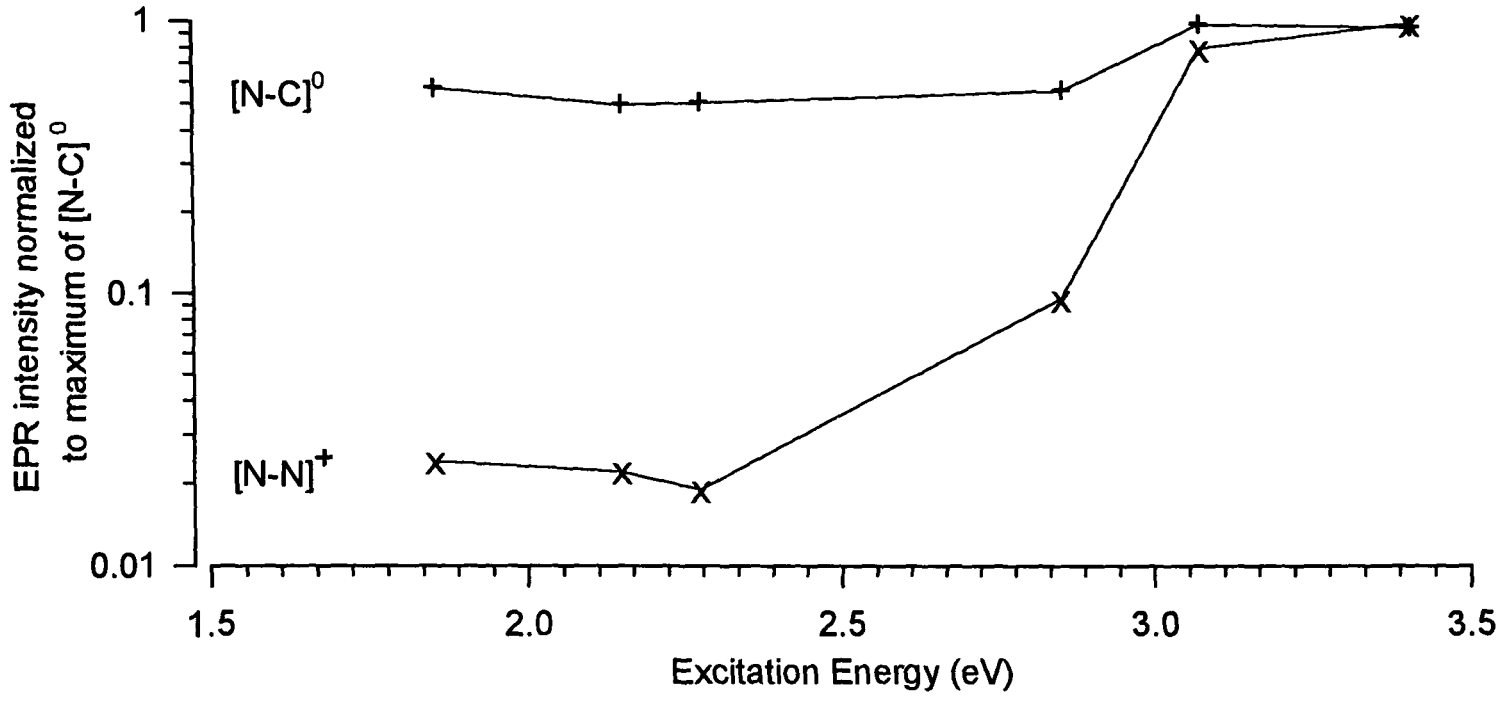



Figure 5.17: The $[N–N]^+$ and $[N–C]^0$ EPR intensity plotted against the photon energy of the incident radiation.

### 5.5.6 Distribution of $[N–N]^+$ centres created by illumination

As mentioned in §5.3, van Wyk and Loubser showed that the $[N–N]^+$ centre was not created uniformly throughout a diamond illuminated from one side. In order to investigate this the sample was cut into two pieces of different thickness, but with one face equal to give equal areas for illumination. The ratio of the masses of the two pieces was 5.051(4), whereas the ratio of the intensity of the $[N–N]^+$ EPR signals excited by illumination with the full spectrum of the Hg lamp was 3.1(3). The production was therefore not uniform, with the number of centres probably falling off with increasing distance from the illuminated face.

### 5.5.7 The $[N–N]^+$ centre in powdered diamond

Loubser [148] reported EPR measurements on natural diamond powders with average particle sizes in the range 0.5 to 30 $\mu$m. He suggested that the spectrum observed in natural diamond powder, which increased in intensity as the average particle size was decreased, was from the O1 centre observed in radiation damaged diamond. The O1 centre has been tentatively associated [149] with a vacancy and a carbon

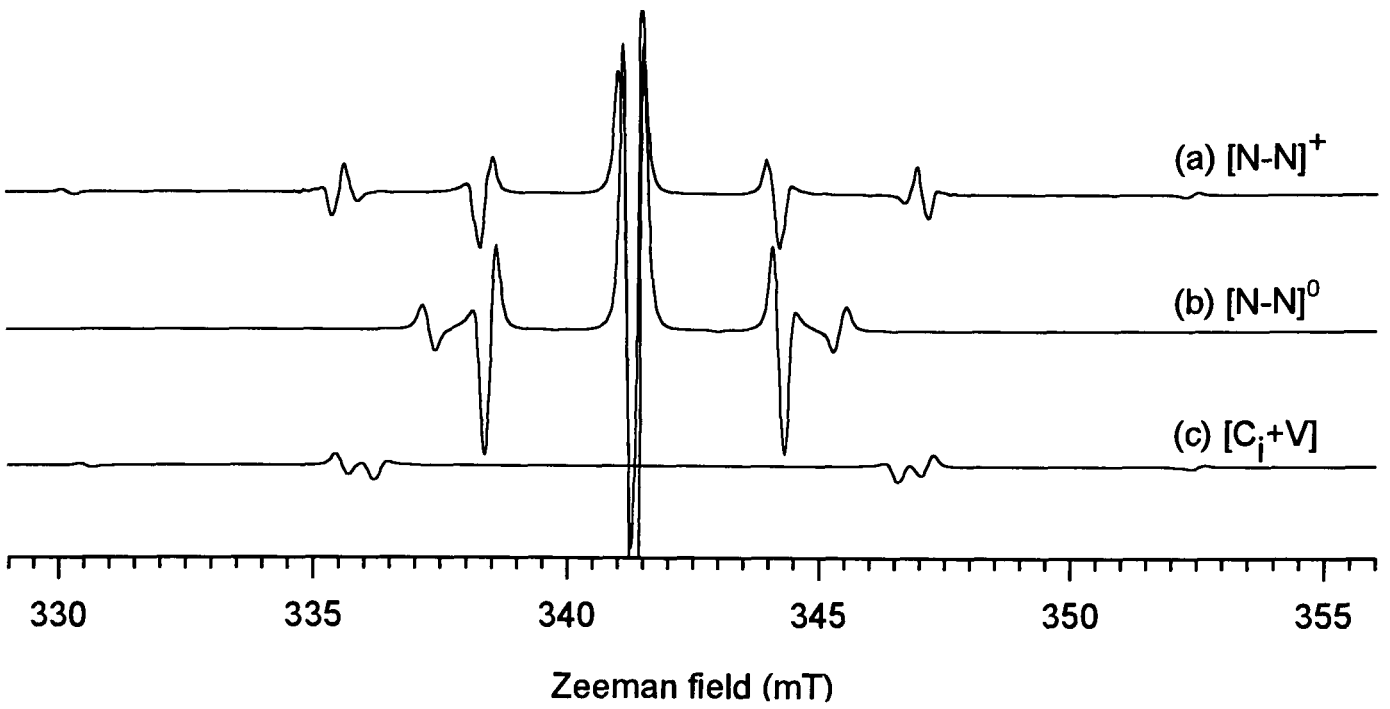



Figure 5.18: Simulation of second harmonic powder EPR spectra at 9.65 GHz for (a) [N–N]$^+$, (b) [N–C]$^0$, and (c) O1. Spectra were normalized such that the integrated intensity of the zeroth harmonic is unity in all cases.

interstitial [$C_i$+V]. As is shown in Figure 5.18 some of the features of the [N–N]$^+$ and O1 powder EPR spectra occur in approximately the same positions. This could lead to confusion if the outer [N–N]$^+$ lines are missed or are too weak to be observed. Loubser noted that the centre he had observed in natural powder samples did not follow the annealing behaviour of the O1 in single-crystal diamond. In single crystals the O1 annealed out at 1100°C while the centre observed in the powders was still undiminished after annealing to 1300°C.

The Loubser data have been re-examined and the centre observed in unirradiated natural diamond powders has been identified as the [N–N]$^+$ centre. It is important to note that the centre was observed without ultra violet illumination. To look for the occurrence of [N–N]$^+$ in powdered diamond, a large fraction of the single crystal used for all the other measurements was ground into powder having an estimated average particle size of about 50 $\mu$m. EPR of the [N–N]$^+$ centre was then observed *without* illumination, Figure 5.19. The signal intensity was observed to increase on illumination with photons of energy greater than 2.9 eV. Observations of the [N–N]$^+$ centre in synthetic crystals containing single substitutional nitrogen have not

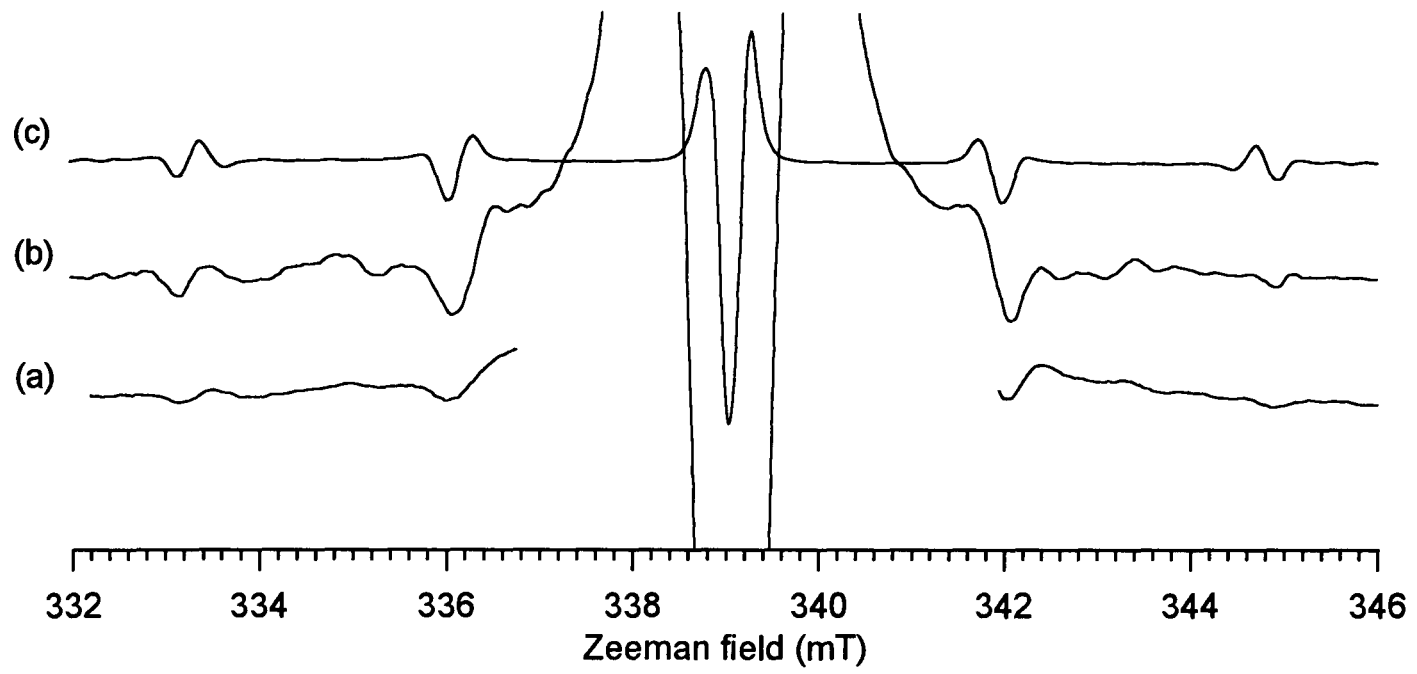



Figure 5.19: Second-harmonic 9.65 GHz EPR spectra from the powdered Cape Yellow sample: (a) No illumination, T=5K, (b) With Hg lamp illumination, T=20K, and (c) simulation for the $[N–N]^+$ centre.

been reported, however, it is possible that this is fairly common in powdered natural diamond containing $[N–N]^0$ centres. The identification of the centre observed by Loubser [148] as $[N–N]^+$ indicates that the intensity of the centre in powders correlates with the reciprocal of the particle radius, implying that a defect created at or near the surface may be acting as a trap/donor of an electron. It is evident that the charge state of the $[N–N]^0$ centre can depend on the presence of other defects close to or on the surface of diamond.

## 5.6 Discussion

### 5.6.1 Hyperfine interaction

The molecular orbital theory method outlined in §3.4.1 was used to calculate the fraction of the unpaired electron, and the hybridization ratio, from the hyperfine interaction parameters, at each atom in the $[N–N]^+$ and $[N–C]^0$ centres. These results, the hyperfine, and quadrupole parameters, are listed in Table 5.4.

If the simple calculations are correct then the sum of calculated electron densities

Table 5.4: Hyperfine and quadrupole parameters (measured at 5K) for $[N–N]^+$ and $[N–C]^0$, together with calculated wavefunction parameters.

| Defect | Atom | $A_s$(MHz) | $A_p$(MHz) | $\eta^2$ | $\lambda^2$ | $f_{2p}$ | $P_{\|\|}$(MHz) |
|---|---|---|---|---|---|---|---|
| $[N–C]^0$ | $^{14}N$ [57] | 92.223(2) | 10.905(2) | 0.247 | 3.85 | 0.196 | -3.973(1) |
| | $^{13}C$ [57] | 205.7440(5) | 66.213(5) | 0.671 | 11.32 | 0.616 | |
| $[N–N]^+$ | $^{14}N$ | 106.09(2) | 24.58(2) | 0.502 | 7.51 | 0.443 | -2.245(5) |

for electrons on the two atoms (N and C, or N and N) should be just less than unity, assuming a small contribution to the electron density from neighbouring carbon atoms. This is the case for the $[N–N]^+$ and $[N–C]^0$ centres. As mentioned in §3.4.1 the fraction of the unpaired electron on any atom is reduced if there is a non zero overlap integral $\mathcal{S}$. The overlap integral is calculated in §5.6.3 as a function of bond extension for $[N–N]^+$ and $[N–C]^0$. The simple one electron approach indicated for the $[N–C]^0$ that approximately 92% of the unpaired electron is in the antibonding orbital, composed of $2s$-$2p$ hybrids, formed between the N and C atoms. For the $[N–N]^+$ centre approximately 100% of the unpaired electron population is in the orbital between the two N atoms. Owing to the uncertainties in the theoretical parameters and the simplicity of the model these values must be used only as a guide, however valid comparisons between values, such as the above, which have been calculated in a consistent fashion using the same source of theoretical parameters can be made. The larger percentage for the $[N–N]^+$ centre may be a consequence of the extra positive charge, compared to the $[N–C]^0$ centre. For the $[N–C]^0$ centre most of the unpaired electron population is on the unique carbon neighbour (67% on C and 25% on N) while for $[N–N]^+$ the unpaired-electron population is shared equally between the two nitrogen atoms.

The distribution of the unpaired electron on the ligand atoms surrounding the $[N–C]^0$ centre was studied by Cox using ENDOR [57], and it was found that a small proportion ($\sim$15%) resided on the neighbouring carbon atoms. $^{13}C$ ENDOR measurements have thus far not been successful on the $[N–N]^+$ centre, however, a small isotropic hyperfine interaction was measured. This was assigned to $^{13}C$ atoms in one of two groups of six equivalent nearest neighbours (see Figure 5.11). The anisotropic

Table 5.5: Calculated and measured displacements of the nitrogen and carbon atoms, together with the extension ($\Delta r/r_0$ %) of the unique N–C or N–N bond, over the normal C–C bond length (1.54 Å), for the centres $[N–C]^0$, $[N–N]^0$, and $[N–N]^+$. Absent $\Delta C$ or $N$'s for $[N–C]^0$ were not given by the authors quoted.

| Defect | Author | Year | $\Delta C$ Å | $\Delta N$ Å | $\Delta r/r_0$ % |
|---|---|---|---|---|---|
| $[N–C]^0$ | Smith *et al.* [53] | 1959 | 0.22 | 0.17 | 11 |
| | Messmer and Watkins [61] | 1970 | | | 26 |
| | Mainwood [63] | 1979 | | | 5-10 |
| | Ammerlan [82] | 1981 | 0.22 | 0.17 | 36 |
| | Kajihara *et al.* [67] | 1991 | 0.22 | 0.17 | 25 |
| | Briddon and Jones [66] | 1993 | $\sim 0.2$ | $\sim 0.2$ | 28 |
| | Cunha *et al.* [69] | 1993 | | | 42 |
| | Mainwood [52] | 1994 | | | 24-25 |
| | Present study | 1994 | 0.22 | 0.05 | 20 |
| $[N–N]^0$ | Mainwood [63] | 1979 | | | $\sim 0$ |
| | Briddon and Jones [66] | 1993 | — | 0.3 | 39 |
| $[N–N]^+$ | Present study [103] | 1994 | — | 0.16 | 21 |

component of the hyperfine interaction, for a nearest neighbour $^{13}C$ (light shading, Figure 5.11) arising from the dipolar interaction between the unpaired electron in the N–N antibonding orbital and the $^{13}C$ nucleus, would be expected to be much larger than the uncertainty in the measured hyperfine coupling of 0.5 MHz. However, a very small anisotropic coupling at this site may arise from cancellation of contributions arising from different mechanisms, as in the case of the $N^+$ atom in this site in the $[N_1–C–N_2^+]$ centre [118]. In analogy with the $[N–C]^0$ centre, it might be expected that a $^{13}C$ atom at one of the six equivalent next-nearest neighbour sites (medium shading, Figure 5.11) has the largest $^{13}C$ hyperfine interaction owing to hyper-conjugation, but this would be expected to have a greater anisotropy than measured. With the information currently available the choice between two different types of 6 equivalent neighbours is difficult, however, the small anisotropy and small magnitude of the measured $^{13}C$ interaction indicate negligible delocalization of the unpaired electron onto neighbouring carbon atoms. This is consistent with the finding that almost all the unpaired electron population resides in the antibonding orbital between the two nitrogen atoms.

### 5.6.2 Determination of bond angles and bond lengths

The displacements of the carbon and nitrogen atoms away from their equilibrium positions were calculated from the EPR data for the $[N–N]^+$ and $[N–C]^0$ centres as detailed in §3.4.2. They are given in Table 5.5 along with extensions calculated from other experimental work, and those predicted by *ab initio* density functional and CNDO calculations. For $[N–C]^0$ the bond extension is of the same order as that calculated by Briddon and Jones [66] and Kajihara *et al.* [67]. However, a marked anisotropy in the relative displacements of the nitrogen and unique carbon is predicted here with the smaller being for the nitrogen. This small displacement might result from the limitations of the approach, or it may indicate that the N–C bonds are stronger than the C–C bonds. Equation 3.46 suggests that the N–N extension for the $[N–N]^+$ centre is approximately the same as for the $[N–C]^0$ centre. It would have been impossible for equation 3.46 to predict a non symmetric extension, however, this is consistent with the equal strength of all the N–C bonds. The 21% extension of the N–N bond in $[N–N]^+$ is much smaller than that predicted for $[N–N]^0$ suggesting that the accommodation of a second electron in the antibonding orbital produces a marked lengthening of the bond. This is feasible if the bond extension is primarily influenced by the placing of an electron in the antibonding orbital.

### 5.6.3 Overlap

As mentioned in §5.6.1 and §3.4.1, disregard of the overlap integral, $\mathcal{S}$, modifies the calculated unpaired electron density on each atom (equation 3.41). In order to gain an estimate of the effect the overlap integrals were calculated within a molecular orbital theory framework. It is important to stress at the outset that this is a molecular model applied to a solid state system, and is by definition an approximation. The results are dependent upon the basis used to approximate the real system, and three bases are compared in this calculation. Despite its being an approximation the analysis gives physical insight into the electron distributions in the defects and at the end a plot of the suggested distribution in the antibonding orbital in the $[N–N]^+$ centre will

be made.

The calculation of overlap integrals was investigated by Mulliken *et al.* in 1949 when they generated extensive sets of tables for the determination of overlaps at different atom separations [150]. These tables were used by Every and Schonland in 1965 to estimate an overlap of 0.43 for the $[N\text{–}C]^0$ defect assuming a bond extension of 11% [100].

In the treatment here the overlap integrals for C–C, N–C and N–N have been calculated using the following basis of Slater-like atomic wavefunctions:

$$\begin{aligned}
\Psi_{2s} &= \frac{1}{4\sqrt{2\pi}}\alpha^{\frac{3}{2}}(2-\alpha r)e^{-\frac{\alpha}{2}r} \\
\Psi_{2p_z} &= \frac{1}{4\sqrt{2\pi}}\alpha^{\frac{5}{2}}(-r\,\cos\theta)\,e^{-\frac{\alpha}{2}r} \\
\Psi_{2p_x} &= \frac{1}{8\sqrt{2\pi}}\alpha^{\frac{5}{2}}r\,\sin\theta\,e^{-\frac{\alpha}{2}r}\,\left[e^{-i\phi}-e^{i\phi}\right] \\
\Psi_{2p_y} &= -\frac{1}{8\sqrt{2\pi}}\alpha^{\frac{5}{2}}r\,\sin\theta\,e^{-\frac{\alpha}{2}r}\,\left[e^{-i\phi}+e^{i\phi}\right]
\end{aligned} \tag{5.4}$$

where $\alpha = Z^*/a_0$, $a_0 = 4\pi\epsilon_0\hbar^2/m_e^2$, the Bohr radius, and $Z^*$ is the effective atomic number related to the true atomic number by $Z^* = Z - \sigma$ with $\sigma$ the shielding constant. In molecular calculations the shielding constant is determined from a series of rules as given by Atkins [151] and improved values of $Z^*$ have been suggested by Clementi and Raimondi derived from self-consistent field functions [152]. The choice of Slater coefficient, $\alpha$, in diamond is not simple. An intuitive correction for the effect of being in a crystal would be the replacement of the free atom dielectric constant $\epsilon_0$ with that for diamond, but Smith *et al.* [53] suggest that the free atomic value for the dielectric constant should be used as:

1. The electron is tightly bound and hence orbits at too fast a frequency for electronic polarizations to develop, in contrast to nitrogen in silicon where the orbit is large compared to the atomic spacing.

2. The donor ionization energy predicted for a potential $V = \frac{e}{\varepsilon r}$ with $\varepsilon = 5.7$ is 0.4 eV, whereas the measured energy is 1.7 eV. This was confirmed by Messmer and Watkins [62] who state that the Kohn-Luttiger effective mass treatment,

Table 5.6: Values for the effective atomic number $Z^*$

| Coefficient type | C ($2s$) | C ($2p$) | N ($2s$) | N ($2p$) |
|---|---|---|---|---|
| Slater [151] | 3.25 | 3.25 | 3.90 | 3.90 |
| Clementi and Raimondi [152] | 3.2166 | 3.1385 | 3.8474 | 3.8340 |
| Harker and Larkins [154] | 3.53 | 3.53 | — | — |

which had been successful for shallow donors in silicon, "fails completely" in the diamond case.

Coulson and Kearsley also used the free atom Slater orbitals in their calculation on the vacancy in diamond [99], while Coulson and Larkins compare the effect of the choice of Slater or Clementi functions on the calculation of the energy levels of the neutral vacancy in diamond [153]. Harker and Larkins calculated an effective value for the Slater coefficient by varying this and other parameters within a "large unit cell-complete neglect of differential overlap" model until a best fit for experimental parameters such as internuclear distance, cohesive energy and valence bandwidth was found [154]. The effective atomic numbers $Z^*$ using Slater, Clementi, and Harker Slater coefficients for N and C are given in Table 5.6 (the Bohr radius was taken as its free atomic value).

The effect of the choice of parameters on the C–C overlap for two $sp_z^3$ hybrid orbitals pointing towards each other along the line joining the two nuclei was calculated. The hybrid orbitals were set up as a function of hybridization ratio $\lambda_i$, the distance of separation $d$, and Slater coefficient $\alpha_i$. A simplification was made in assuming both Clementi coefficients to have the $2p$ value. The integrals were evaluated by transforming to ellipsoidal coordinates. The initial integrations were performed by hand to check their validity and establish the best method of integration. Once this had been done all calculations were performed using an algebraic mathematics package.[6] Using this, the C–C overlap integral at the equilibrium distance (1.54 Å) was calculated as 0.659 using Slater coefficients, 0.675 using Clementi coefficients and 0.606 using the Harker coefficient. The variation of the overlap as a function of percentage

[6]Mathematica Version 2.2 running on an i486 PC under MS Windows 3.11.

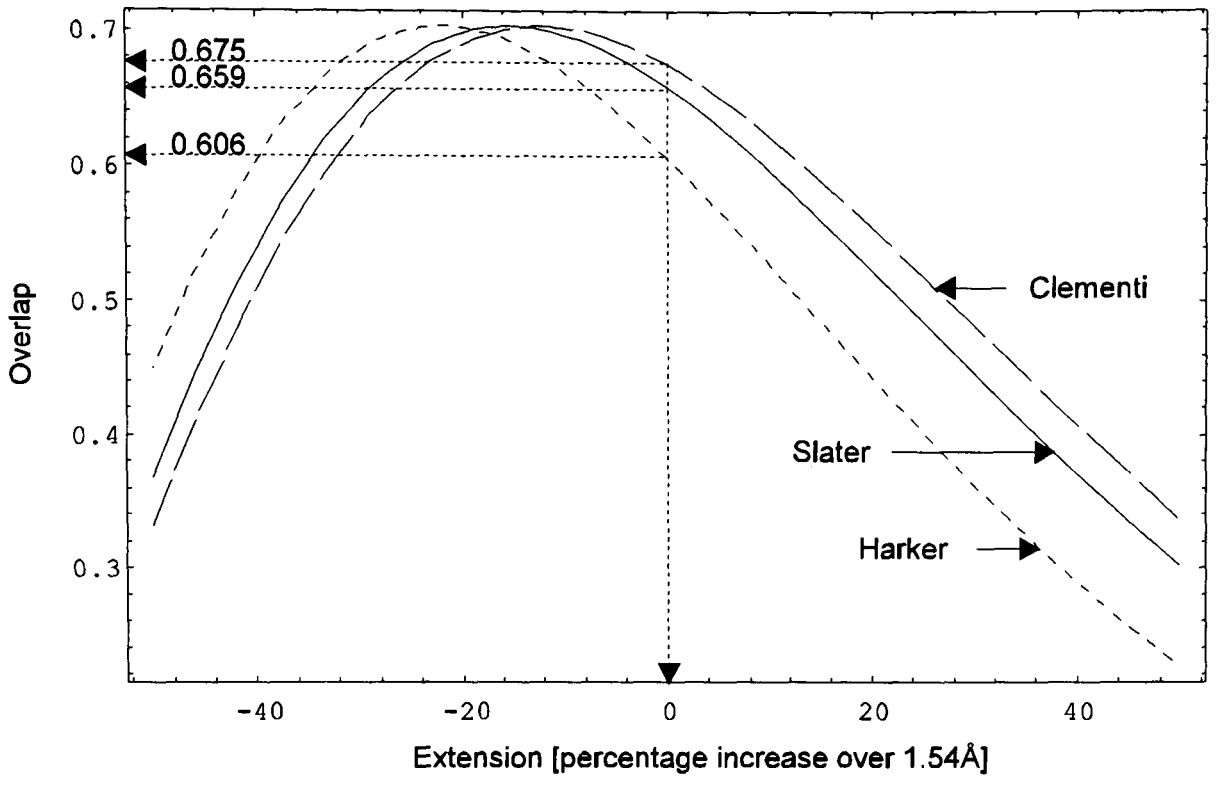



Figure 5.20: C–C overlap integral plotted as a function of the percentage extension from the equilibrium bond length of 1.54 Å, calculated using Slater, Clementi and Harker coefficients.

bond extension is shown in Figure 5.20. The Harker coefficient produced the smallest overlap. There is a spread of 0.069 in $\mathcal{S}$, giving values for the fraction of the electron on each atom $f_i = \eta_i^2$ for the bonding orbital of between 0.298 and 0.311, compared to 0.5 when the overlap is ignored.

The same calculation was performed for the N–C overlap in the $[N–C]^0$ defect. Harker did not estimate a Slater coefficient for nitrogen in diamond so a value of 4.2 was assumed. This is between the value of 4.18 produced by adding the difference between the Slater and Harker coefficients for carbon to that of nitrogen, and 4.23 produced by weighting the Slater nitrogen value with the ratio of the Slater and Harker coefficients for carbon. The calculated overlaps are plotted in Figure 5.21 as a function of bond extension. The figure should be read in conjunction with Table 5.5. The value at 11% bond extension, calculated using Slater coefficients of 0.461 should be compared with that of 0.43 obtained by Every and Schonland [100]. The difference is produced by changes to the hybridization ratio ($\lambda_N^2 = 4.36$, $\lambda_C^2 = 16.32$ in their calculation as opposed to 3.85 and 11.32 respectively here, see Table 5.5). The curve produced using the Harker and modified Slater value produced the smallest overlap. Using this it is now possible to calculate the expected fraction of unpaired

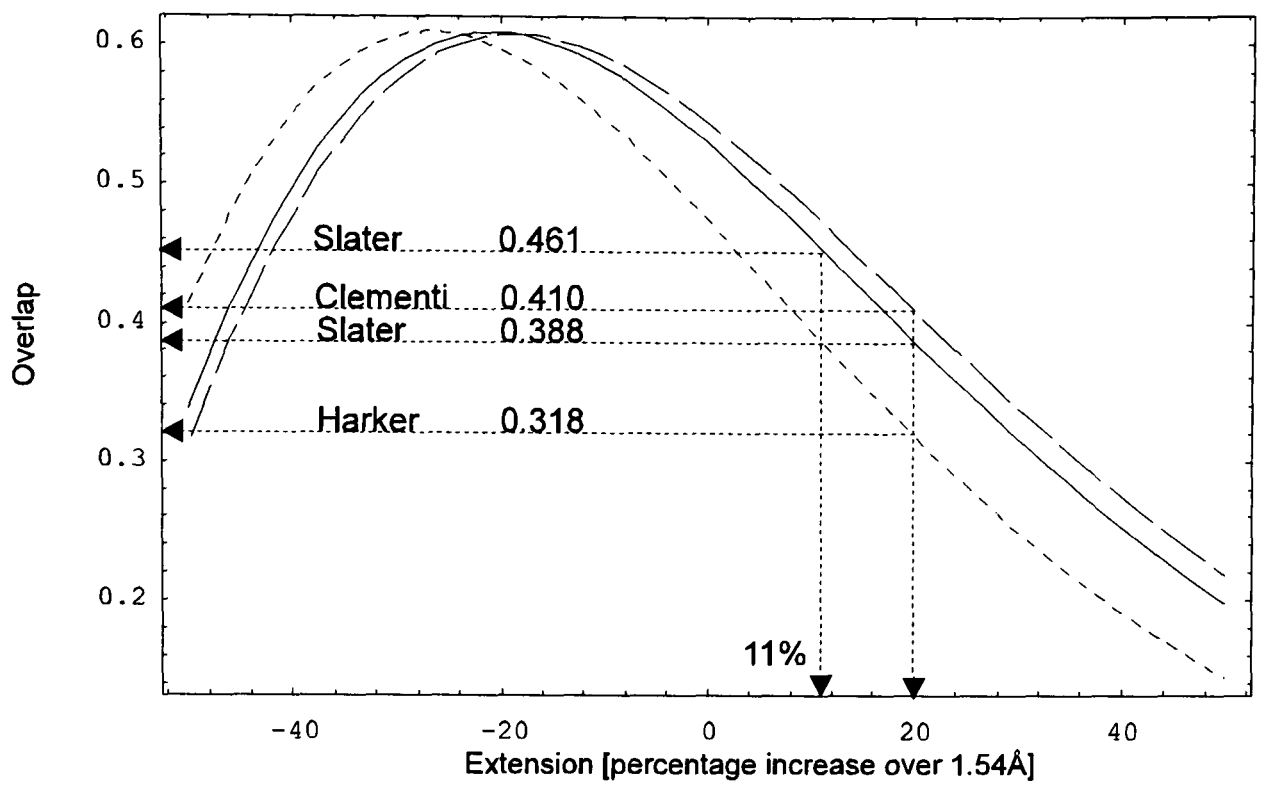



Figure 5.21: N–C overlap integral plotted as a function of the percentage extension from the equilibrium bond length of 1.54 Å, calculated using Slater, Clementi and modified Harker coefficients.

electron on each atom. To avoid confusion between the measured and calculated parameters $f_i = \eta_i^2$ is defined to be the measured value where $i = N, C$ and $\bar{f}_i = \bar{\eta}_i^2$ to be the calculated values. $k^2 = \eta_N^2/\eta_C^2$ is also defined. The normalized antibonding wavefunction can then be written as:

$$\Phi_{\mathrm{AB}} = \bar{\eta}_N \phi_N - \bar{\eta}_C \phi_C = \frac{\phi_N - k\phi_C}{N} \tag{5.5}$$

where:

$$N^2 = 1 + k^2 - 2k\,\mathcal{S} \tag{5.6}$$

Using the experimental value for $k$, which is independent of the overlap integral, and the calculated overlap, $\bar{\eta}_N = 1/N$ and $\bar{\eta}_C = k/N$ can be calculated. These are given in Table 5.7. Obviously these are too large, but this is a reflection of the model and the fact that not all the electron is contained in the antibonding orbital, some is in the other *sp* hybrids on the N and C atoms, and some is on the neighbouring carbon atoms. If $\Phi_{\mathrm{AB}}$ is weighted by a factor $\zeta$ such that $\zeta^2\bar{\eta}_i^2 = \eta_i^2$ an estimate of the amount of electron in the antibonding orbital for each choice of Slater coefficients can

Table 5.7: Calculated values for $\bar{\eta}_i^2$ and $\zeta^2$

| Defect | $[N–C]^0$ | | | $[N–N]^+$ | |
|---|---|---|---|---|---|
| Coefficient type | $\bar{\eta}_C^2$ | $\bar{\eta}_N^2$ | $\zeta^2$ | $\bar{\eta}_N^2$ | $\zeta^2$ |
| Slater [151] | 0.41 | 1.11 | 0.60 | 0.709 | 0.705 |
| Clementi and Raimondi [152] | 0.42 | 1.15 | 0.58 | 0.725 | 0.690 |
| Harker and Larkins [154] | 0.37 | 1.02 | 0.66 | 0.652 | 0.767 |

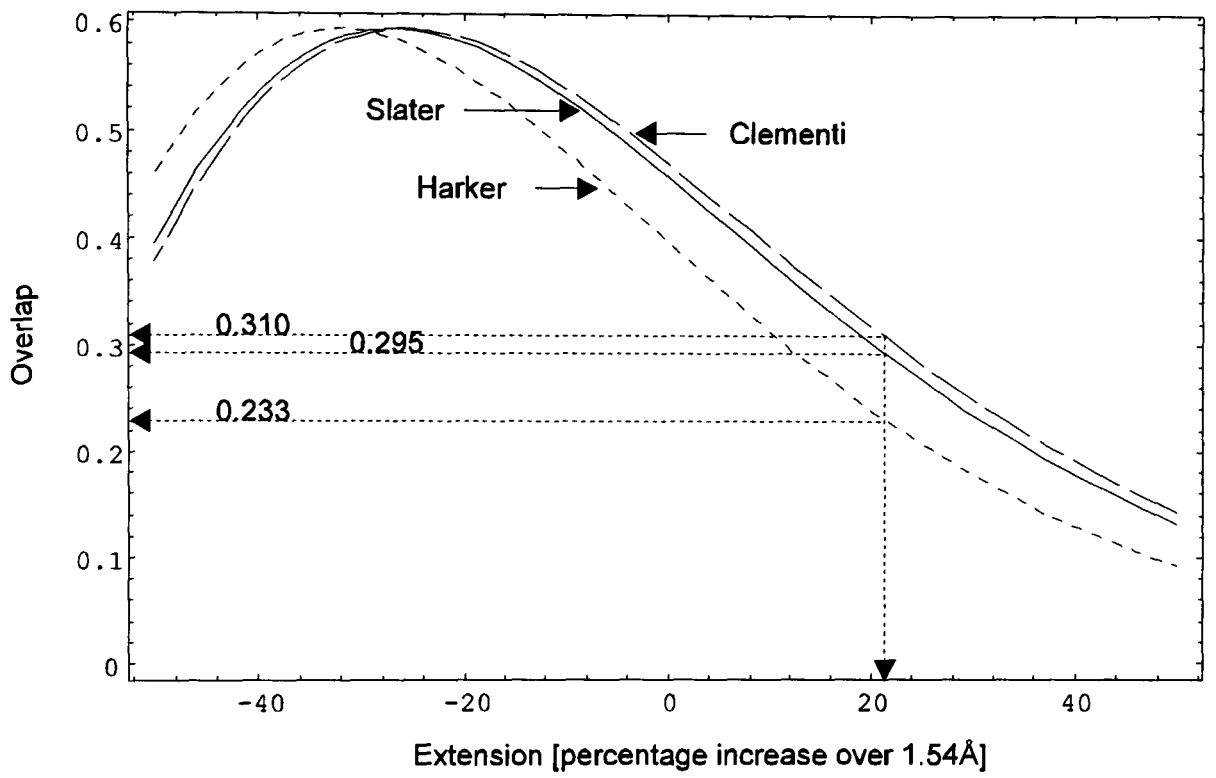



Figure 5.22: N–N overlap integral plotted as a function of the percentage extension from the equilibrium bond length of 1.54 Å, calculated using Slater, Clementi and modified Harker coefficients.

be made (see Every and Schonland [100]). The values of $\zeta^2$ are also given in Table 5.7. These values will also vary with the differing overlaps produced by different bond extensions such as those detailed in Table 5.5. As it is known that the majority of the electron resides in the antibonding orbital (about 15% is expected outside [104]) the Harker parameters, as could be expected, may be said to approximate the real wavefunction best for diamond, though $\zeta^2$ is still smaller than expected.

Repeating the calculation for the $[N–N]^+$ defect produces another set of similar curves (Figure 5.22), however the overlaps are noticeably smaller. This is to be expected as the effective atomic number is larger implying a smaller atomic radius, especially when the reduced shielding factor estimated from Harker's carbon value is

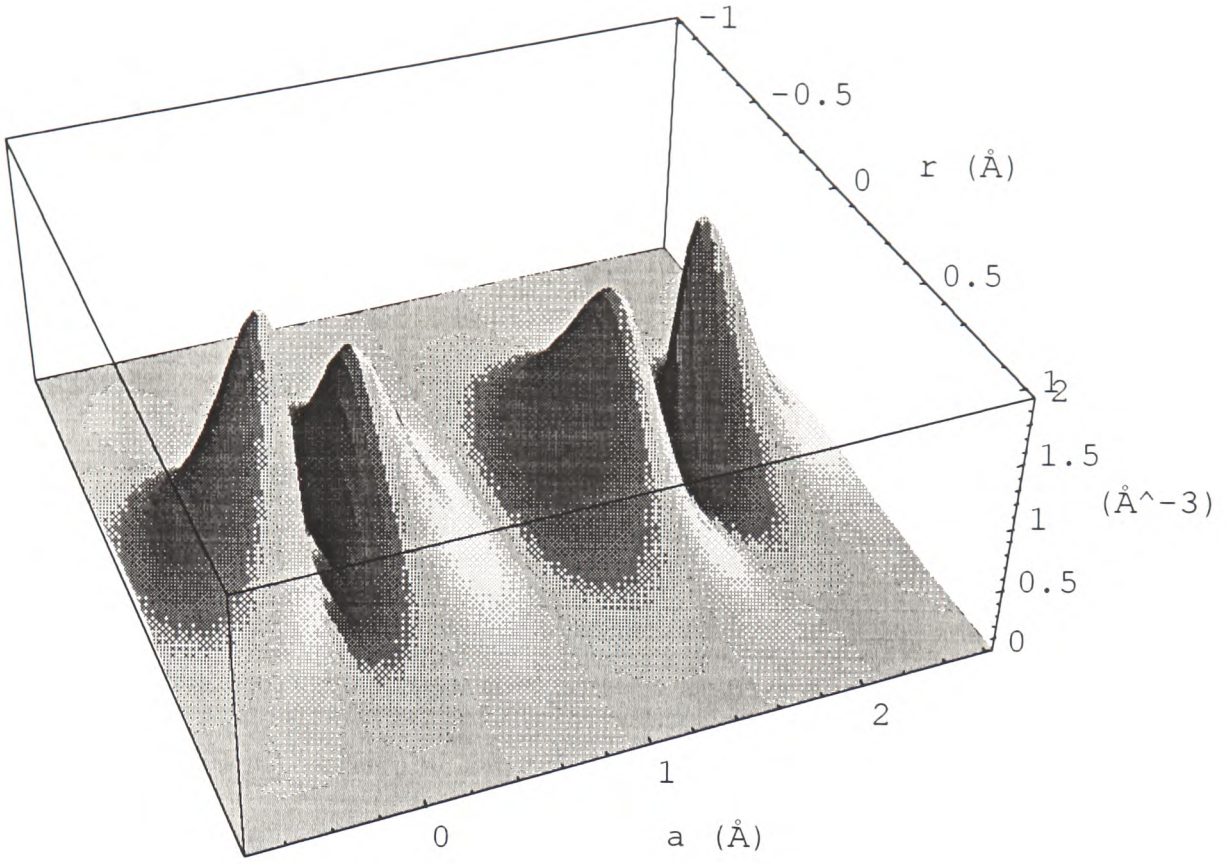



Figure 5.23: $|\Phi|^2$ for the $[N{-}N]^+$ antibonding orbital calculated using estimated Harker values for the Slater-coefficients. $a$ is the distance along the axis of the bond, measured from the left hand nitrogen atom position. $r$ is the distance normal to the bond. An extension of 21% from the equilibrium bond length of 1.54 Å was assumed.

used. The expected fraction of the $2p$ on each nitrogen and the weighting factors were calculated and are given in Table 5.7. Once again the Harker derived parameters give a better representation of the experimental results. The fraction of $s$ electron on each of six nearest neighbour carbon atoms was measured to be 0.3%, giving 1.9% over all six.

Using the model parameters it is possible to calculate the expected electron density for each centre. This was done for the electron in the antibonding orbital of the $[N{-}N]^+$ system and the result is plotted in Figure 5.23.

### 5.6.4 The $^{14}$N quadrupole interaction

The nuclear quadrupole interaction arises from the interaction between the nuclear quadrupole moment and the electric field gradient (which is produced by all electrons)

at the nucleus. It is therefore a probe of the environment at that nucleus. In this section the $[N–N]^+$ defect will be considered in conjunction with other substitutional nitrogen containing defects in an examination of the environment of the trigonally coordinated N atoms in diamond.

The quadrupole interaction in the $[N–N]^+$ effective spin Hamiltonian, equation 5.3, is a traceless tensor and in this case is axially symmetric. The $\underline{\mathbf{P}}$ matrix therefore takes on the form:

$$\underline{\mathbf{P}} = \begin{pmatrix} P_{xx} & 0 & 0 \\ 0 & P_{yy} & 0 \\ 0 & 0 & P_{zz} \end{pmatrix} \tag{5.7}$$

$$P_{xx} = P_{yy} = -P_{zz}/2 \tag{5.8}$$

$$P_{\|} = 3P_{zz}/2 \tag{5.9}$$

with $P_{\|}$ given by:

$$P_{\|} = \frac{3eqV_{zz}}{4I(2I-1)} \tag{5.10}$$

where $I$ is the nuclear spin, $eq$ the nuclear electric quadrupole moment, and $V_{zz}$ the gradient of the electric field at the nucleus. The electric field gradient, like the hyperfine interaction, receives its greatest contribution from electrons in orbitals on the central atom.

Plotting the measured $P_{\|}$ for the nitrogen atoms of the $[N–V]^-$ [44], $[N–C]^0$ and $[N–N]^+$ centres and for $N_1$ of the $[N_1–C–C–N_2^+]$ [119] and $[N_1–C–N_2]$ [118] centres, against the fraction of unpaired-electron population ($f_{2p}$) in a $2p$ orbital on the nitrogen atom (Figure 5.24) reveals a correlation between $f_{2p}$ and $P_{\|}$. The correlation between $f_{2p}$ and $P_{\|}$ operates over a wide range, from almost pure lone pair, ($f_{2p} \sim 0$) on the nitrogen in $[N–V]^-$, to $f_{2p} \approx 0.5$ in $[N–N]^+$, and suggests that $f_{2p}$ is linearly related to the electric field gradient at the nitrogen nucleus.

The correlation can be investigated by employing a simple molecular orbital calculation similar to that used in the analysis of the hyperfine interaction. An $sp$-hybrid orbital basis constructed from $2s$ ($\Psi_{2s}$) and $2p$ ($\Psi_{2p}$) atomic wavefunctions is defined while assuming that the atom has undergone a trigonal distortion producing an

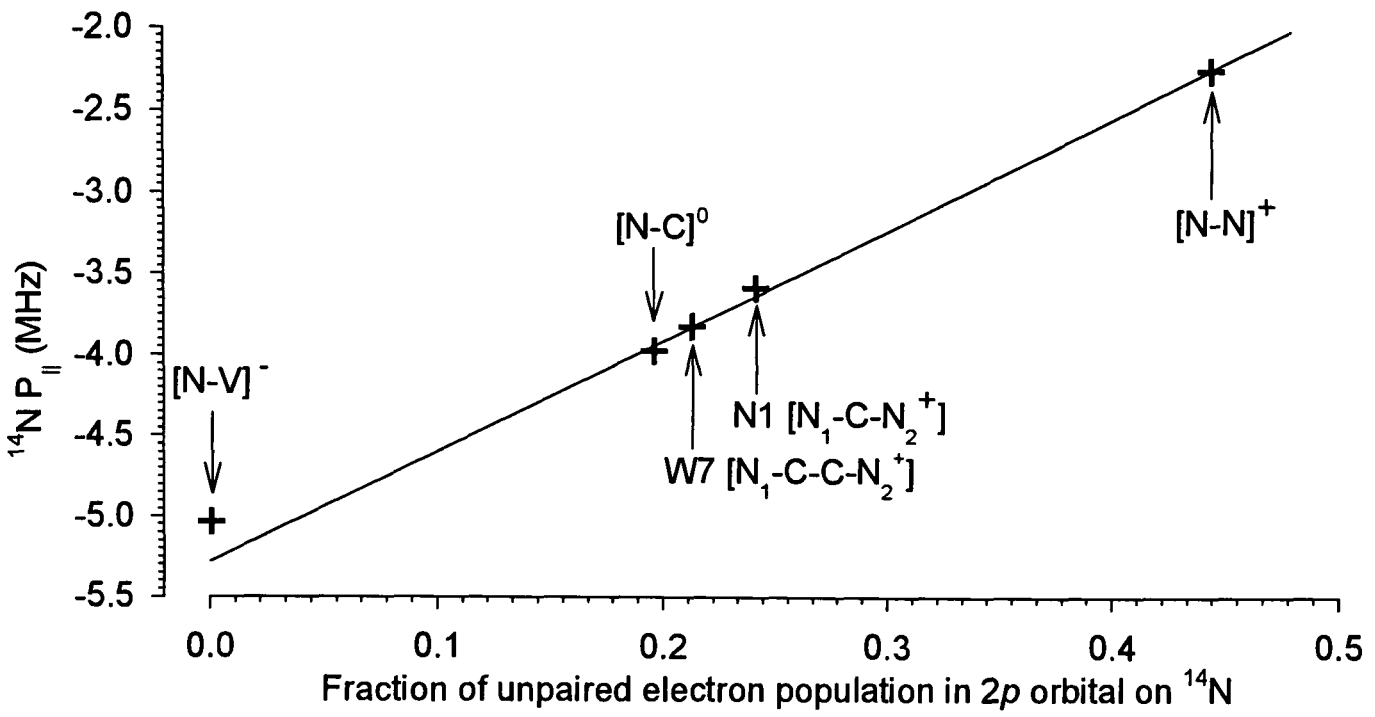



Figure 5.24: The fraction ($f_{2p}$) of the unpaired electron population in a $2p$ orbital directed along the trigonal symmetry axis for a substitutional nitrogen atom in the specified defects, plotted against the measured $^{14}N$ quadrupole parameters $P_{||}$(MHz). The straight line is a fit to the data shown excluding the lowest plotted point ($[N–V]^-$) because of the large uncertainty in $f_{2p}$ for this defect.

unique orbital ($\phi_1$) and three equivalent orbitals ($\phi_2, \phi_3, \phi_4$). Without loss of generality the axis system has been chosen such that $\phi_1$ is directed along $\hat{\mathbf{z}}$ and the other three orbitals make equal angles with $\hat{\mathbf{z}}$. The basis is given below:

$$
\begin{aligned}
\phi_1 &= \frac{1}{\sqrt{1+\lambda_1^2}}(\Psi_{2s} + \lambda_1 \Psi_{2p_z}) \\
\phi_2 &= \frac{1}{\sqrt{3}\sqrt{1+\lambda_1^2}}\left(\Psi_{2s} - \frac{1}{\lambda_1}\Psi_{2p_z} + \frac{\sqrt{2}\sqrt{1+\lambda_1^2}}{\lambda_1}\Psi_{2p_x}\right) \\
\phi_3 &= \frac{1}{\sqrt{3}\sqrt{1+\lambda_1^2}}\left(\Psi_{2s} - \frac{1}{\lambda_1}\Psi_{2p_z} - \frac{\sqrt{1+\lambda_1^2}}{\sqrt{2}\lambda_1}\Psi_{2p_x} + \frac{\sqrt{3}\sqrt{1+\lambda_1^2}}{\sqrt{2}\lambda_1}\Psi_{2p_y}\right) \\
\phi_4 &= \frac{1}{\sqrt{3}\sqrt{1+\lambda_1^2}}\left(\Psi_{2s} - \frac{1}{\lambda_1}\Psi_{2p_z} - \frac{\sqrt{1+\lambda_1^2}}{\sqrt{2}\lambda_1}\Psi_{2p_x} - \frac{\sqrt{3}\sqrt{1+\lambda_1^2}}{\sqrt{2}\lambda_1}\Psi_{2p_y}\right) \quad (5.11)
\end{aligned}
$$

The hybridization ratio $\lambda_1$ is determined from the hyperfine interaction (Table 5.4). It is assumed that the crystalline molecular orbitals are formed as linear combinations of these atomic orbitals on each atom. For the $j^{\text{th}}$ $N$–$X$ bond ($X$=$C$ or $N$) the orbitals

are:

$$\begin{aligned}\Phi_{j_A} &= |\eta^N_{j_A}|\phi^N_j - |\eta^X_{j_A}|\phi^X_j + \ldots \text{(antibonding)},\\ \Phi_{j_B} &= |\eta^N_{j_B}|\phi^N_j + |\eta^X_{j_B}|\phi^X_j + \ldots \text{(bonding)}.\end{aligned} \tag{5.12}$$

The ellipsis indicates admixture from other orbitals. To a first approximation these small admixtures may be ignored and it is possible to consider only orbitals of the two atoms between which the bond is formed. Orthogonality of the orbitals, and normalization, leads to:

$$\begin{aligned}|\eta^N_{j_A}||\eta^N_{j_B}| - |\eta^X_{j_A}||\eta^X_{j_B}| + \left(|\eta^N_{j_A}||\eta^X_{j_B}| - |\eta^N_{j_B}||\eta^X_{j_A}|\right)\left\langle\phi^N_j|\phi^X_j\right\rangle &= 0\\ |\eta^N_{j_B}|^2 + |\eta^X_{j_B}|^2 + 2|\eta^N_{j_B}||\eta^X_{j_B}|\left\langle\phi^N_j|\phi^X_j\right\rangle &= 1\\ |\eta^N_{j_A}|^2 + |\eta^X_{j_A}|^2 + 2|\eta^N_{j_A}||\eta^X_{j_A}|\left\langle\phi^N_j|\phi^X_j\right\rangle &= 1\end{aligned} \tag{5.13}$$

For the molecular orbital containing the unpaired electron, the measured hyperfine parameters determine $|\eta^N_{j_A}|$ and $|\eta^X_{j_A}|$. The values of $|\eta^N_{j_B}|$ and $|\eta^X_{j_B}|$ may be calculated if the overlap integral $\left\langle\phi^N_j|\phi^X_j\right\rangle$ is known. Although the overlaps calculated in §5.6.3 were not zero it was shown that they were influenced strongly by the choice of basis and that the simple model did not produce a complete description. This combined with the fact that the values of $|\eta^N_{j_A}|$ and $|\eta^C_{j_A}|$ for the $[\text{N–C}]^0$ and $[\text{N–N}]^+$ centres given in Table 5.4, give $|\eta^N_{j_A}|^2 + |\eta^X_{j_A}|^2$ and $|\eta^N_{j_A}|^2 + |\eta^X_{j_A}|^2$ approximately equal to one, make it valid to choose $\left\langle\phi^N_j|\phi^X_j\right\rangle \approx 0$ as a first approximation. The electric field gradient may then be expressed as:

$$V_{zz} = -|e|\left[2|\eta^N_{1_B}|^2 + |\eta^N_{1_A}|^2\right]\left\langle\phi_1\left|\frac{3\cos^2\theta - 1}{r^3}\right|\phi_1\right\rangle - 2|e|\sum_{j=2}^{4}|\eta^N_{j_B}|^2\left\langle\phi_j\left|\frac{3\cos^2\theta - 1}{r^3}\right|\phi_j\right\rangle \tag{5.14}$$

where $\theta$ is the angle between $\hat{\mathbf{z}}$ and the radial vector $\mathbf{r}$, $e$ the electron charge, and the factors of two account for the contribution from the two electrons in each bonding

orbital. Performing this summation over the orbitals in equation 5.14 gives:

$$V_{zz} = \frac{4|e|\lambda_1^2}{15(1+\lambda_1^2)} \left\langle r_{2p}^{-3} \right\rangle \left[ -2|\eta_{1_B}^N|^2 + |\eta_{1_A}^N|^2 + 2|\eta_{2_B}^N|^2 \right] \tag{5.15}$$

In this expression it has been assumed that $|\eta_{2_B}^N| = |\eta_{3_B}^N| = |\eta_{4_B}^N|$. The first two terms in the square brackets are determined from the hyperfine parameters, however the value of $|\eta_{2_B}^N|^2$ is unknown. The extra positive charge on the nitrogen atom may make $|\eta_{2_B}^N|^2 > |\eta_{2_B}^C|^2$, but the large value of $\langle \phi_2^N | \phi_2^C \rangle$ will reduce both. However, the large value of $\langle \phi_2^N | \phi_2^C \rangle$ also makes it invalid to consider only $\phi_2^N$ as contributing to $V_{zz}$ since the overlap region with high electron density will increase the contribution of these back bonds. Hence:

$$P_{\|} = P_0 \frac{\lambda_1^2}{1+\lambda_1^2} \left[ -2|\eta_{1_B}^N|^2 + |\eta_{1_A}^N|^2 + 2|\eta_{2_B}^N|^2 \right] \tag{5.16}$$

where $P_0 = -[e^2Q/5I(2I-1)]\langle r_{2p}^{-3} \rangle$, the quadrupole interaction parameter for a single electron in a pure $2p_z$ orbital. The values of $P_{\|}$, $\lambda_1^2/(1+\lambda_1^2)$, and $|\eta_{1_A}^N|^2$ are known from the experimental data. If it is assumed that $\langle \phi_1^N | \phi_1^C \rangle \approx 0$ and that the molecular orbital in bond 1 involves only N and C: $|\eta_{1_B}^N|^2 \approx 1 \approx |\eta_{1_A}^N|^2$ so that equation 5.16 can be written as:

$$P_{\|} = -P_0 \mathrm{f}_{2p} + \frac{2P_0\lambda_1^2}{1+\lambda_1^2} \left[ 1 - |\eta_{2_B}^N|^2 \right] \tag{5.17}$$

The experimental data in Figure 5.24 indicated that the measured quadrupole interaction was proportional to $\mathrm{f}_{2p}$, which is only consistent with equation 5.17 as long as the second term is constant over the the defects considered. The linear region implies that $P_0 = -6.7(3)$ MHz which is in excellent agreement with the value of $P_0 = -6.75$ MHz quoted as standard by reference [155]. Consideration of the second term in equation 5.17 shows that in order for it to remain constant a small increase in $\lambda_1^2/(1+\lambda_1)^2$ must be accompanied by an increase in $|\eta_{2_B}^N|^2$. For [N–N]$^+$ the quantity $\lambda_1^2/(1+\lambda_1)^2$ is 0.88 and for [N–V]$^-$ it is 0.5. For the other defects it is close to 0.8. For [N–V]$^-$ there is a large uncertainty in $\lambda_1^2/(1+\lambda_1)^2$ as a result of the ill determined anisotropic hyperfine interaction. Hence, equation 5.17 indicates a relative stability in the value of $|\eta_{2_B}^N|^2$. The value of $|\eta_{2_B}^N|^2$ can be deduced from the intercept

on the $P_{||}$ axis and yields about 0.5, which is not unreasonable considering the large contribution from the overlap region.

Once the quadrupole interaction is known $f_{2p}$ can be estimated from equation 5.17. For the $[N–V]^-$ centre the value calculated in this manner is $f_{2p} = 0.02$. This is an order of magnitude greater than that determined in the usual manner from the nitrogen hyperfine parameters [44]. As a result of numerous contributions to the hyperfine interaction not taken into account in the calculation of $f_{2p}$ from the hyperfine parameters, it is suggested that the value calculated here of 0.02 is more realistic.

### 5.6.5 The various ionization states of the [N–N] species

In the literature it has been assumed that the usual charge state of the A centre is neutral ie. $[N–N]^0$. This is logical as each nitrogen donates one electron to the antibonding orbital. As the lowest energy antibonding orbital is full it is unlikely that an $[N–N]^-$ centre with trigonal symmetry will form. $[N–N]^{2+}$ would probably exhibit no magnetic resonance signal being composed of two $S$=0 $[N–C]^+$ centres. This leaves $[N–N]^+$ as the only candidate for the magnetic resonance centre observed in this work.

van Wyk and Loubser [134] commented that $[N–N]^+$ could be created by ionization of $[N–N]^0$, or via electron capture by $[N–N]^{2+}$. In the sample studied, the concentration of $[N–N]^0$ centres is two orders of magnitude greater than the maximum concentration of $[N–N]^+$ centres produced by optical excitation. Thus either a very small fraction of the centres are ionized, limited perhaps by the number of suitable electron traps, or the $[N–N]^+$ centres observed are being produced by electron capture by $[N–N]^{2+}$, present in much lower abundance than $[N–N]^0$. As the infrared absorption can be successfully fitted without including any unusual features, and making the reasonable assumption that the $[N–N]^+$ and $[N–N]^{2+}$ centres would have characteristic one-phonon infrared absorption spectra, one deduces that the concentrations of the ionized centres must be much lower than that of the $[N–N]^0$ centre. If the $[N–N]^{2+}$ is present, the question arises as to what acceptor has soaked up the sur-

plus electrons? It must be a powerful electron trap, and it is not clear why this would not be compensated by the $[N–C]^0$ centre which has been seen to act as a donor. On the other hand, diamond is a wide band gap material, and it is not possible to be certain that the Fermi level is well defined, so species may well exist in unexpected charge states. Surface bending of the Fermi level may also play a role.

The $[N–N]^0$ centre produces an optical absorption line at 3.8 eV [124]. In IaA diamonds a secondary absorption edge at this energy is clearly visible. Production of the $[N–N]^+$ centre by photons of energy appreciably less than 3.8 eV indicates that the process is not simply ionization of the $[N–N]^0$ centre. The increase in the production of $[N–N]^+$ with excitation energy (Figure 5.17) correlates with the onset of optical absorption of the $[N_3V]^0$ centre (Figure 5.5), which suggests that this centre may be involved with its production. No clear change in the $[N_3V]^0$ EPR intensity was observed when creating $[N–N]^+$, however, any change in one of the $[N_3V]^0$ EPR lines would have been very small owing to the large number of lines and the much higher concentration of $[N_3V]^0$. Therefore, it is not possible to eliminate direct charge transfer from $[N_3V]^0$ to $[N–N]^{2+}$ creating $[N_3V]^+$ and $[N–N]^+$.

In §5.5.4, results showing the decay in the number of $[N–N]^+$ centres with time when the light is removed were presented. The observation of similar logarithmic dependencies was also mentioned. The most pertinent system of those discussed in §5.5.4 is the H2/H3 centre [156]. The H2 centre ($[N–V–N]^-$) is the negative charge state of the H3 centre ($[N–V–N]^0$). Mita *et al.* [156] showed that light of wavelength shorter than 600 nm excites an electron captured by a trap. When the light is switched off, the reverse process occurs and the optical absorption from the H2 centres increases. They reported that the recovery process for the H2 absorption depends linearly on the logarithm of time, and that the rate is independent of temperature below about 420K. The temperature independence indicates tunnelling of the electron from traps back to the H3 centres, converting them back to H2. There must be a large distribution in the separation of the H3 and trap centres, giving rise to a wide distribution of tunnelling rates and thus to the logarithmic time dependence of the recovery of the H2 absorption. At temperatures above 420K, thermally

excited hopping contributes to the recovery rate, and the recovery departs from the logarithmic dependence.

It is clear that the temporal dependence of the $[N–N]^+$ EPR signal after the exciting light is removed can be explained in the same way as for the H2 centre. The decay of the $[N–N]^+$ EPR intensity with the logarithm of time suggests that there is a wide distribution of lifetimes of the $[N–N]^+$ centres created, presumably resulting from a large variation in the separation between the $[N–N]^+$ centre and its electron donor/trap. Below about 20K, the decay rate is independent of temperature, indicating tunnelling between the donor/trap and the $[N–N]^+$ centre; at higher temperatures thermally activated hopping also contributes. Although the measurements showed that the $[N–C]^0$ and $[N_3V]^0$ EPR intensities also decreased slightly when the light was switched off, it was not possible to identify a one-to-one charge-transfer process between any of the defects studied. This does not, however, rule out the possibility that $[N–C]^0$ and $[N_3V]^0$ may be two of the donors/traps involved in the creation and subsequent decay of the $[N–N]^+$ centre.

The result in §5.5.7 that, in finely divided diamond, $[N–N]^+$ can be in equilibrium with $[N–N]^0$ whereas, in the single crystal, it is only observed after illumination, is of great interest. This implies that a defect created near the surface is acting as a trap/donor of an electron, transforming $[N–N]^0$ or $[N–N]^{2+}$ to the $[N–N]^+$ centre. It is presumed that the $[N–N]^+$ centres themselves are not to be found at the surface as the strained and irregular lattice near the surface would give rise to a spread in the measured hyperfine and quadrupole parameters of the nitrogens, which is not observed. There is no experimental information which facilitates the determination of the trap/donor nor is the average $[N–N]^0$ or $[N–N]^{2+}$ trap/donor separation known. What is known is that in crushed diamond an isotropic resonance at $g$=2.0027(2), with a line width of 0.55 mT, is created [157] which is attributed to defects near the surface. Strong absorption around $g$=2.0, produced by $[N_3V]^0$ and other centres, precludes study of this defect in the sample used here. The number of $[N–N]^+$ centres was increased by illumination indicating that not all the potential $[N–N]^+$ centres were activated by surface traps/donors.

In §5.5.6 it was confirmed that the $[N–N]^+$ centres are not created uniformly throughout a diamond when illuminated from one side. Assuming that the number of centres produced at a distance $x$ into the diamond falls off as $e^{-kx}$, it is possible to calculate from the data in §5.5.6 that $k \sim 0.7$ mm$^{-1}$, which is less than, but of the order of, the optical absorption coefficient measured for the $[N_3V]^0$ centre at 2.985 eV. It appears that excitation of this centre plays a role in the creation of $[N–N]^+$.

In summary, from the information available, it is not possible to determine whether $[N–N]^+$ is created by ionization of $[N–N]^0$ or electron capture by $[N–N]^{2+}$. If it is the latter, then the equilibrium concentration of $[N–N]^{2+}$ in the sample need only be 1% of the $[N–N]^0$ concentration. The study of the powdered sample is significant as it indicates that, given the correct traps/donors, $[N–N]^0$, $[N–N]^+$ and possibly $[N–N]^{2+}$ can all exist concurrently. The observation of different charge states of the same defect ($[N–C]^0$ and $[N–C]^+$, $[V]^0$ and $[V]^-$, $[N–V–N]^0$ and $[N–V–N]^-$) is becoming a common occurrence in diamond.

## 5.7 Conclusion

There can be no doubt that the W24 centre is $[N–N]^+$. For $[N–N]^+$, the hyperfine and quadrupole interactions show that both nitrogens are equivalent. In single-crystal diamond containing $[N–C]^0$ and $[N_3V]^0$ centres, $[N–N]^+$ is created by excitation with light of energy greater than 3.0 eV. It has not been possible to identify the electron trap(s) or donor(s) associated with the $[N–N]^+$ centre. It is clear that $[N–N]^+$ is not created homogenously throughout the diamond, but occurs close to the surface receiving the illumination. The rate of decay of $[N–N]^+$ after the exciting light is removed is sample dependent, however, for this sample it was shown that:

- at sufficiently low temperature the number of centres remaining after the excitation is switched off varies linearly with the logarithm of time, indicating a wide distribution in trap/$[N–N]^+$centre separations;

- the decay rate is temperature independent at low temperatures, indicating tunnelling between the trap and $[N–N]^+$ centre; and

- at higher temperatures, thermally activated hopping contributes to the decay of $[N–N]^+$ centres.

When a single-crystal diamond, in which the $[N–N]^+$ centre is only observed upon illumination, is crushed to a powder, the $[N–N]^+$ centre is observed without illumination. This suggests that defects at or close to the surface act as traps, converting $[N–N]^0$ to $[N–N]^+$.

A simple calculation of bond lengths from the hyperfine parameters suggests that the N–C bond length in the $[N–C]^0$ centre is similar to the N–N bond length in the $[N–N]^+$ centre. This result is interesting, but not unreasonable, and should be confirmed with more sophisticated calculations. The quadrupole interaction for the substitutional nitrogen atoms of the $[N–N]^+$ centre is consistent with those measured in other nitrogen defects in diamond and is explained remarkably well by a simple model. It is clear for the defects considered that the magnitude of the quadrupole interaction is directly related to the fraction of unpaired-electron population in a $2p$ orbital on a substitutional nitrogen atom.

# Chapter 6

# The Vacancy

## 6.1 Introduction

The vacancy is the most common radiation damage defect occurring in diamond and as such is of central importance to many of diamond's modern applications. Until now the neutral vacancy $[V]^0$ has been observable only through optical absorption and luminescence measurements, while the negative vacancy $[V]^-$ has been seen in optical absorption (but not luminescence) measurements and in paramagnetic resonance experiments. The positive charge state has yet to be identified.

This chapter describes the first ENDOR measurements on an optically excited state in diamond, and the first ENDOR study of the neutral vacancy. It builds on the work of van Wyk who discovered an EPR spectrum that appeared upon illumination and exhibited an unusual line shape [158]. The chapter begins by explaining the importance of the vacancy in diamond research, and then outlines previous optical, theoretical and magnetic resonance experiments performed on the various charge states of the vacancy. This is followed by an account of the measurements performed and a detailed discussion of the results. The chapter is rounded off with conclusions and a discussion of further work possible on the excited state of the vacancy $[V]^*$.

## 6.2 Background

The vacancy is of great importance in diamond. It is the primary product of radiation damage; and, depending upon the charge equilibrium within the diamond [159], can exist mainly in the neutral charge state (type IIa samples, impurity free), mainly in the negative charge state (type Ib samples containing nitrogen donors[1]), or in a combination of the two (type Ia diamonds containing combinations of the A and B aggregates) [159]. In the neutral charge state it gives rise to the GR1 optical absorption and luminescence band [161], and the GR2–GR8 optical absorption [161] and p-type photoconductivity bands [162]. In the negative charge state it produces the ND1 optical absorption band [127], associated photoconductivity [162], and a paramagnetic resonance spectrum [163, 164].

The vacancy becomes mobile at 550°C and can become trapped at other defects in the crystal [19]. When it is trapped at an isolated nitrogen atom it forms the $[N\text{–}V]^-$ centre (see §2.3 for a review), at the A-centre (or $[N\text{–}N]^0$) the H2 and H3 defects, and at the B-centre the H4 defect (see reference [159]).

In addition to its role in defining the intrinsic and extrinsic electronic and optical properties of diamond, the vacancy also dominates self diffusion. This is of vital importance in the growth of thin film diamond [165] which has rekindled interest in the vacancy and its role in diamond. The vacancy was experimentally shown to be important in the process of aggregation of nitrogen in diamond, participating in the following processes [166]:

$$\begin{aligned} N + V &\rightarrow N\text{–}V \\ N\text{–}V + N &\rightarrow N\text{–}V\text{–}N \rightarrow N\text{–}N + V \end{aligned}$$

The vacancy enhanced migration of nitrogen has been modelled by Mainwood [52] who calculated that the vacancy-assisted mechanism has an activation energy of 4.5 eV,

[1] In some natural type Ib samples the ratio of GR1 absorption to ND1 absorption may approach zero [27], but in synthetic samples the charge equilibrium is expected to be affected by the very different nitrogen concentrations in different growth sectors [160].

while a direct atomic exchange has an activation energy of 6.3 eV (see also §2.3). In addition to assisting in the aggregation of nitrogen it was found to be energetically favourable to produce nitrogen and vacancy defects rather than only nitrogen defects [52].

### 6.2.1 Formation of vacancies: radiation damage

Vacancies are formed from the interaction of an incoming particle with the crystal lattice. If the energy of the particle is high enough, a carbon atom can be permanently ejected to form an interstitial. The first experimental estimates of the threshold energy for formation were made by Clark *et al.* in 1961 [167] and were derived from high energy electron scattering measurements. Theoretical estimates based upon the sum of the bond-breaking and crystal strain energies [168] yielded a value of 20–30 eV. This estimate is well below the most recent experimental measurements [169], derived from ion bombardment studies, of 55 eV. Wu *at al.* [170] have recently modelled single-atom radiation damage events in diamond by a molecular-dynamics simulation and have found values dependent on the direction of initial displacement. These are 47 eV for the initial displacement parallel to $\langle 100 \rangle$, 50 eV $\|\langle 110 \rangle$, and 54 eV $\|\langle 111 \rangle$. The additional energy over the bond-breaking and crystal strain calculation was found to derive from a rapid transfer of kinetic energy from the displaced atom to incoherent vibrations of the surrounding crystal before the atom could reach the top of the energy barrier for defect formation. These values are consistent with those measured by Clark and Mitchell [171] and Prins *et al.* [169]. The vacancy's partner, the self interstitial, thought now to be stable as the $\langle 100 \rangle$ split interstitial [170, 172], migrates during electron irradiation at about 50K [159], possibly producing interstitial related paramagnetic centres [173, 174] or migrating to the surface or dislocations, but optical signals for this have not yet been observed.

### 6.2.2 The neutral vacancy: GR1 or $[V]^0$

The observation that, on bombardment with high energy particles, diamonds show optical absorption in a normally transparent region was first made by Crookes in

1909 [175] who discovered that colour changes were produced by radium radiation. Coulson [99] references the early experiments on the change of colour upon irradiation. In 1956 Clark *et al.* [161] identified the GR1 absorption peaking at 1.678 eV, and a set of higher energy absorptions, GR2–GR8, at photon energies of 2.88–3.04 eV merging into an absorption continuum. Uniaxial stress measurements [176] identified the GR1 centre as having full $T_d$ symmetry. The zero-phonon transition is between a doubly degenerate orbital ground state E, and a triply degenerate orbital excited state ($T_1$ or $T_2$ representation). Spectroscopy of additional transitions from the E ground state, combined with Photo-Hall measurements have led to the conclusion that the ground state of $[V]^0$ is located close to the centre of the energy gap, $E_g$~5.49 eV [159]. The radiative decay time of the GR1 photoluminescence band has been measured as 2.55±0.1 ns in the limit of low temperature, and this decreases with increasing temperature, indicating strongly competing nonradiative de-excitation channels [159].

The vacancy has been the subject of many theoretical models. The first attempt at simulation was the ground-breaking work of Coulson and Kearsley in 1957 [99]. They introduced the concept of a defect molecule and calculated the order of the energy levels using a molecular orbital treatment. In their model[2] the ground state is expected to be describable in terms of atomic orbitals derived primarily from the "dangling bonds" of the four neighbours to [V]. The vacancy has $T_d$ point group symmetry and the four orbitals must therefore transform as $a_1$ and $t_2$. The neutral vacancy must accommodate four electrons in these states which must satisfy Pauli's Exclusion Principle. The configurations $a_1^2t_2^2$, $a_1^1t_2^3$ and $t_2^4$ are then possible with $a_1^2t_2^2$ and $t_2^4$ producing the many electron states $^1A_1$, $^1E$, $^3T_1$ and $^1T_2$, and the $a_1^1t_2^3$ producing $^5A_2$, $^3A_2$, $^3E$, $^1E$, $^3T_1$, $^1T_1$, $^3T_2$ and $^1T_2$. Simple application of Hund's rules – maximization of the separation by placing one electron per atom and aligning their spins – suggests that the many-electron ground state will transform as $^5A_2$. However inclusion of the electron-electron interactions leads to the prediction of a $^1E$ ground state[3] and a $^1E \rightarrow {}^1T_2$ transition for the GR1. Their calculation illustrated the

[2]See [17] and references therein for additional information on the calculations and measurements made on vacancies.

[3]The calculated ground state is dependent on the parameters and basis functions chosen, for

importance of electron-electron correlation, not because it was particularly large, but because of the similarity of the energies of low-lying states. In a later paper Coulson [177] lists three major deficiencies of their model, videlicet:

- excessive localization of the defect electrons;
- an inability to take account of relaxation around the vacancy; and
- a neglect of the Jahn-Teller effect.

Further work was done on the defect molecule model by Coulson and Larkins [153], who performed an investigation into the effect of relaxation and the choice of basis functions. They showed that the order of the lowest $^1$E and $^3T_1$ levels depended upon the choice of basis functions with which to represent the $s$ and $p$ orbitals on the atoms nearest the defect.[4] They also calculated that for an inwards relaxation the $^3T_1$ level was predicted as the ground state for $[V]^0$ while for an outwards relaxation the $^1$E level was the most probable ground state with an allowed transition to a $^1T_2$ level.

Messmer and Watkins introduced a new approach in 1970/72 [61, 178] which addressed the problems of localization, relaxation, and lent insight into the Jahn-Teller interaction. The model achieved this by employing a cluster of seventy-five atoms, as opposed to four, and the use of extended Hückel theory, but had to pay the price of a simplification in the analysis. The extended Hückel theory considers all the electrons in the cluster but replaces their Coulomb and exchange interactions by an effective sum of one-electron Hamiltonians. The main results from this work were to predict only 40% localization on the nearest neighbour carbon atoms, a symmetric outward relaxation of 13%, and Jahn-Teller energies of $\sim\frac{1}{2}$ eV. Another interesting feature of their calculation was the prediction that the molecular-orbital coefficients for the $p$ functions on a given nearest neighbour atom were not equal. That is, if the localized state at the vacancy is viewed as composed of "dangling" orbitals from the

example, Coulson and Larkins [153] find $^1$E as the ground state using a basis of Slater atomic orbitals, and $^3T_1$ using Clementi functions. It is however now accepted that the ground state is $^1$E [159].

[4]Also see §5.6.3 for a comparison between different sets of basis functions in the calculation of overlap integrals for the $[N{-}N]^+$ centre.

neighbouring atoms, the orbitals are not pointing towards the centre of the vacancy (as in the usual $sp^3$ picture) but are tilted in the $\hat{\mathbf{z}}$ direction.[5] For the atom in the (1,1,1) position they calculated an angle of 5.4°. The angle varied with cluster size, however, agreement was found upon comparison with EPR results from the positive vacancy in silicon. Messmer and Watkins suggested that the angle of tilt was related to the proximity of the defect to the valence-band edge and mentioned that the $[V]^-$ centre in diamond was further removed from the edge and hence displayed negligible tilt. It should be noted that as a result of the 40% localization, they found that their cluster was too small to handle the whole wavefunction [62]. The localization also depended on cluster size. Later measurements on the negative vacancy (§6.2.3) showed that the localization on the nearest neighbours was in fact ~100%. The Messmer and Watkins calculation was the first cluster calculation applied to diamond. It failed mainly because of their neglect of the correlation interaction in their Hamiltonian. It must be stressed that their method produced a good description of the defects in silicon, for which it had initially been designed.

Subsequent to the calculations of Messmer and Watkins, the ground state of the vacancy was shown experimentally to be a $^1$E state [176], proving the importance of the configuration interaction. This has led to the development of a method which may be viewed as a combination of the Coulson-Kearsley and Messmer and Watkins model and are now employed in the calculation of the properties of the vacancy and of perturbed vacancies. These methods take account of the configuration interaction when calculating the properties of diamond and generally use so-called "zero differential overlap" techniques (see [60] and references therein for a detailed description of recent calculation techniques). In 1978 Mainwood [101] investigated the relaxation about the vacancy using a CNDO[6] technique. She found that the initial relaxation about the vacancy resulted from modifications in the local chemical bonding, with further relaxation occurring to lower the electronic degeneracy through the Jahn-Teller effect. An inwards relaxation of 25–30% (−0.77 to −0.93 Å) of the nearest

[5] Assuming that the $T_d$ defect is inscribed in a cube (see Figure 8.5).
[6] Complete Neglect of Differential Overlap.

neighbours was calculated. The Jahn-Teller energy was found to be 460 meV coupled to tetragonal modes. Recent calculations by Mainwood *et al.* have predicted a separation of between 40 and 200 meV between the $^3T_1$ ($a_1^2t_2^2$) excited state and the $^1E$ ($a_1^2t_2^2$) ground state [179]. It should be noted that there is also an excited vibronic state, $A_1$ lying 8 meV above the ground state [176]. A recent paper by Petrillio and Sachetti [180] reports the results of an x-ray scattering experiment measuring inelastic-scattering cross section integrated over energy. The measurements allowed calculation of the electron-electron correlation energy and also showed that the exchange and correlation energies contribute ~70% of the total cohesive energy in diamond. They also show that a description of the electrons in diamond based solely on Pauli principle correlations "would be inadequate". This experiment confirms the importance of the correlation interactions in pure diamond, a result which can surely be extended to intrinsic defects.

As mentioned earlier an additional spectrum with zero-phonon lines at higher energy than the GR1 has been observed. This consists of 13 lines and has been labelled GR2–GR8. It has been shown that the GR2–GR4 transitions are certainly from the vacancy, while the GR5–GR8 are probably from the same vacancy [181]. All transitions have $T_d$ symmetry and give rise to p-type photoconductivity [162]. They have been found to be very narrow being only a few meV wide.

Lowther [182, 183, 184] has presented an extension of the Coulson-Kearsley defect molecule, proposing that an electron moves into the dangling bonds in the region vacated by the carbon removed. This leaves a hole localized on the basal orbitals of the four carbon atoms adjacent to the vacancy. The GR2–GR8 states are considered to be electron-hole pair states and it is shown that transitions to these states can have approximately the correct intensity. The hole is considered to lie energetically in the valence band and to account for the p-type photoconductivity associated with the GR2–GR8 absorption.

Mainwood [185] noted that it is difficult to understand the sharpness of the levels in this model as they should be broadened by interaction with other valance band states. Stoneham [186] suggested an alternative explanation and proposed that absorptions

could rise through two-electron transitions, possibly because of the large electron-electron interaction in diamond. In this model there was no inconsistency between the photoconductivity and sharpness of the level, but it was not clear which two states were involved. There was difficulty in explaining the large number of $T_{1(2)}$ electronic transitions.

### 6.2.3 The negative vacancy: ND1 or $[V]^-$

The ND1 optical absorption was observed in type Ib diamonds by Dyer and DuPreez in 1965 [187] and assigned to the negative vacancy by Davies in 1977 [188]. The zero-phonon line occurs at 3.150 eV between an A ground state and a T excited state at a tetrahedral centre [127]. Like the GR2–GR8 bands the ND1 can be observed in photoconduction but not in luminescence and appears to de-excite by emission of an electron. Davies postulated the following relation between ND1 ($[V]^-$) and GR1 ($[V]^0$) [188]:

$$\begin{aligned} [V]^- + h\nu &\rightarrow [V]^0 + e^- \\ [V]^0 + h\nu &\rightarrow [V]^- + h^+ \end{aligned} \tag{6.1}$$

A magnetic circular dichroism signal has been measured [189] which is consistent with an A→T transition, and gives a positive $g$-value in the excited state.

The $[V]^-$ has been treated theoretically in the same fashion as $[V]^0$ and is expected to have electron configurations of $a_1^2t_2^3$, $a_1^1t_2^4$, $t_2^5$ (the symmetry of the resultant states is given in reference [99]). After inclusion of the configuration interaction the ground state was calculated to be $^4A_2$ [99]. In contrast to the $[V]^0$ the optical transition corresponds to an excitation from $a_1^2t_2^3$ to $a_1^1t_1^4$ rather than within the $a_1^2t_2^2$ states. There is therefore a re-arrangement of the electrons involved. The transition probability is larger than that for GR1 [183, 184]. Lowther [184] postulates that the vacated $a_1$ state is occupied by a bound-hole exciton thus preventing the transition $t_2 \rightarrow a_1$, and explaining the lack of luminescence.

As the ground state of the $[V]^-$ is $^4A_2$ and has a spin of $\frac{3}{2}$, it should be paramagnetic. Magnetic resonance from this defect was first observed by Baldwin in 1963

[163] while illuminating his sample with light of energy greater than[7] 2.83 eV. He observed a signal with $g$ near two, but mistakenly identified it as the positive vacancy. Isoya *et al.* correctly identified the defect by measuring its effective spin using ENDOR [164]. They also measured its $g$-value to be 2.0027(1), and verified that the defect retained its $T_d$ symmetry. The sum of the spin densities on the four nearest neighbours was estimated to be ~1 from the $^{13}C$ hyperfine interaction. The hyperfine interaction with the next-nearest neighbour $^{13}C$ atoms was found to be of dipolar nature. The sum of the spin densities on the twelve next-nearest neighbours was found to be ~0.04. The *sp*-hybrid ratio of 6.9 on the nearest neighbours indicated a "large symmetric relaxation" (no direction was given). Comparison of $[V]^-$ in silicon, $[V]^0$ in GaP, and $[V]^-$ in diamond, illustrated a tendency for the electron to be less delocalized beyond the nearest neighbours with increasing band gap [164]. Mainwood [101] calculated that the negative vacancy should have a "substantial totally symmetric inwards relaxation".

## 6.3 The sample

The sample selected for this study was a natural IaB diamond which had been cut and polished with one face parallel to a {110} plane, and the opposite face parallel to within two degrees of this plane. The sample was originally irradiated with 2 MeV electrons, to a dose of $9\times10^{17}cm^{-2}$. The excited state $[V]^*$ was present on illumination with uv light from a mercury lamp immediately after irradiation, but strengthened after moderate annealing. The sample was annealed at various temperatures, with a final anneal at 1500°C for 1 hour when the $[V]^*$ centre annealed out along with $[V]^-$. The diamond was then irradiated with the same electron dose as before and annealed at 600°C for 10 minutes. Only one of the treatments is necessary to produce the $[V]^*$ centre. The sample has two zones of different nitrogen concentration, as discussed

[7] It is useful to point out that there is a misprint in the paper [163] on page 221 where "greater than 1.10 eV" should read "greater than 3.10 eV" for quenching of the $[V]^-$. This misprint was faithfully reproduced by Loubser and van Wyk in their review paper [190] and caused no end of puzzlement, bother and the construction of an an infra-red diode laser system!

in §6.4.

## 6.4 Optical absorption measurements

Observation of the irradiated sample (§6.3) under an optical microscope, and even by eye, reveals that it is inhomogeneous in colour. One region is much darker with a light green colour, the other is clearer with a light blue tinge as shown in Plate II.

The infrared absorption spectra in the one phonon region are shown in Figure 6.1. The spectra were collected by masking off one of the different sectors of the diamond using dag: a colloidal suspension of amorphous graphite. Spectrum (a) from the dark region showed very strong absorption from B-centres; this sector can be categorized as IaB. The concentration of nitrogen in the form of B-centres was estimated as 800 atomic ppm. using the infrared absorption at 1130 $cm^{-1}$ and the parameter determined by Woods and co-workers [138]. The peak at 1405 $cm^{-1}$ originates from a C–H bending mode and is accompanied by a stronger line at the C–H stretch frequency of 3107 $cm^{-1}$. Spectrum (b) is from the lighter region and showed a much lower total absorption which was predominantly from B-centres with a small contribution from A-centres. No platelet peak was observable in either region (a) or (b). Using the infrared classification of diamonds the sample was categorized as *irregular*.

The uv/visible absorption spectra were measured in a similar fashion to the infrared and are shown in Figure 6.2.[8] The 1.673 eV and 3.150 eV zero-phonon lines of $[V]^0$ and $[V]^-$ respectively, are visible in both regions. The 2.463 eV zero-phonon line of the H3 ($[N–V–N]^0$ – a vacancy trapped at an A-centre) is visible in both regions but stronger in (b). The H4 centre (vacancy trapped at a B-centre) is clearly seen in region (a), but in region (b) it is much weaker and obscured by the phonon assisted structure on the H3 centre. All the zero-phonon lines in region (a) are broader than those in region (b). At 77K ZPL broadening is produced by random strain in the local environment of the defect and the B-centres are likely to be a major source of

[8]Spectra were taken by Dr P.Spear at the DTC research, Belmont Road, Maidenhead, SL6 6JW, UK.

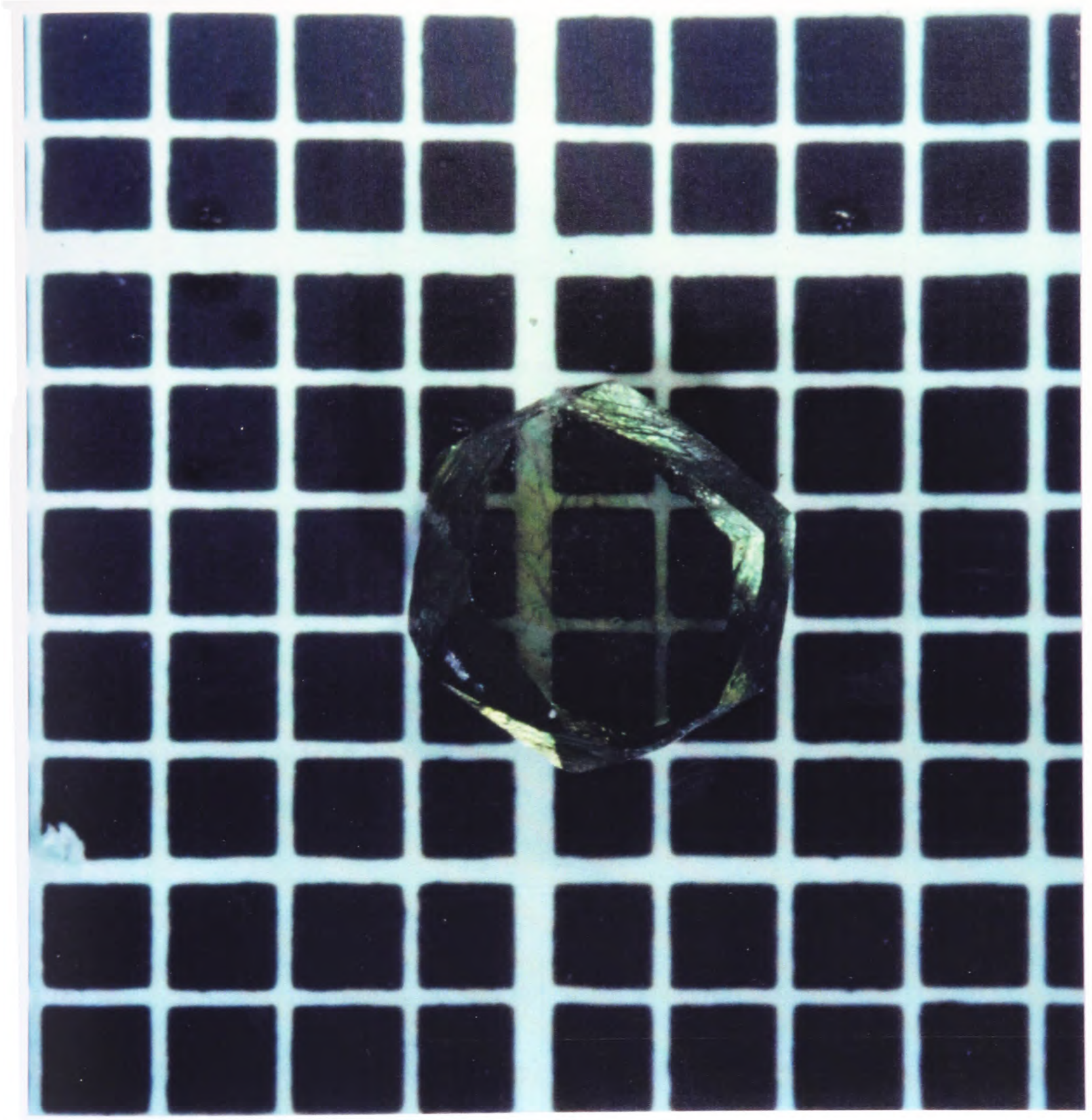


Plate II: Natural IaB sample. The difference in colour between the two regions is visible when looking at the white grid lines. The major grid size is 1 cm.

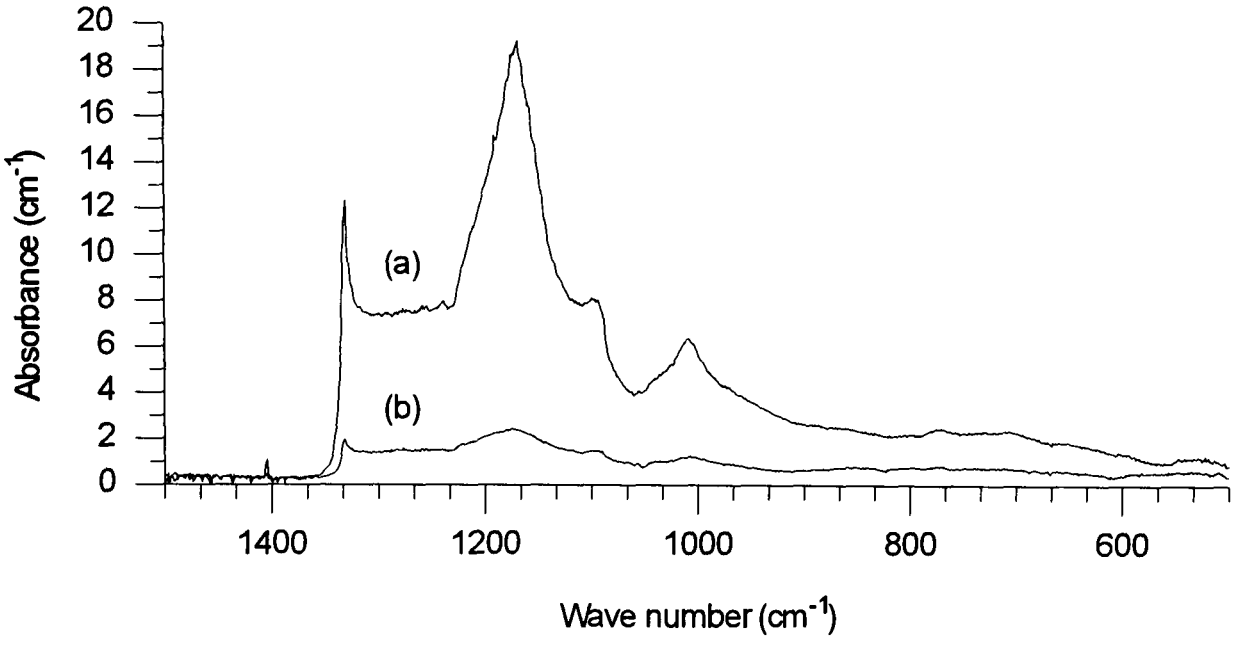



Figure 6.1: Infrared absorption spectra of the [V]* sample taken at room temperature. (a) The dark region, and (b) the light region. See text for details.

strain at high concentrations, probably causing the broadening in region (a). The concentration of $[V]^-$ and the ratio $[V]^-/[V]^0$ is higher in region (a) than in region (b), denotive of a higher concentration of electron donors in region (a). The concentrations of H3 and H4 centres reflect the concentrations of A- and B-centres in the respective regions. This difference in concentration and aggregation of nitrogen in the two regions leads to interesting questions regarding the growth and geological history of the sample.

## 6.5 EPR measurements

EPR measurements were made on the [V]* sample with the following aims in mind:

1. To obtain a detailed understanding of the microwave saturation behaviour of the [V]* EPR before attempting ENDOR.

2. Verify the [V]* EPR angular dependencies measured by van Wyk for the nearest neighbour $^{13}C$ hyperfine interaction [158].

3. Understand the anomalous [V]* EPR line shape and investigate the cause of the angular dependence of the EPR intensity.

4. Resolve the complex superposition of EPR spectra in the central region.

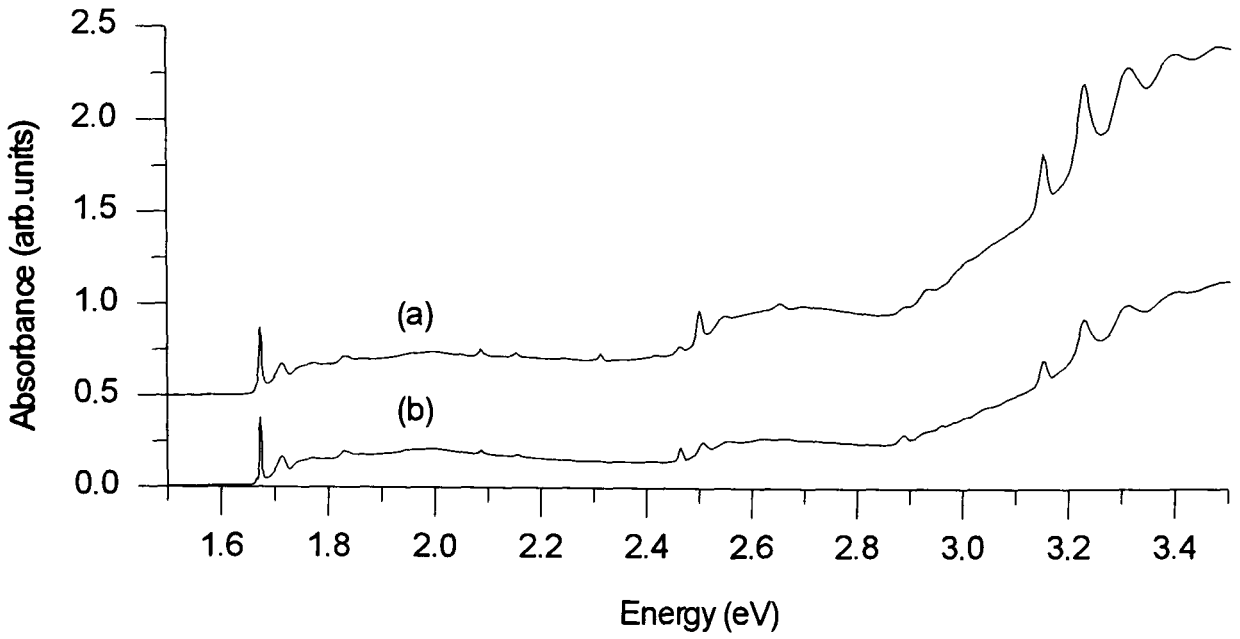



Figure 6.2: uv/visible absorption spectra for [V]* sample collected at 77K. (a) the dark region, and (b) the light region. See text for details.

5. Measure the concentrations of $[N\text{–}C]^0$ and $[V]^-$ EPR centres.

6. Investigate the temperature dependence of the [V]* EPR.

7. Determine the effect of photon wavelength on the [V]* and $[V]^-$ EPR signals.

8. Attempt to i) measure the time dependence of the EPR signals upon illumination and its removal and ii) investigate the dynamics of the paramagnetic centres within the sample.

Only item 1 was performed before commencing the ENDOR experiment as the success of the ENDOR measurements was a prerequisite to continuing with the EPR investigation. However, the EPR measurements will be described as a group before discussing the ENDOR experiments.

### Notation

The notation used in this thesis is described in §1.6, however, pertinent points will be repeated here for clarity. As will be explained later the excited state of the vacancy produced a single EPR line at $g$=2.0033. When one of the neighbouring $^{12}C$ atoms is replaced by a $^{13}C$ atom the hyperfine coupling produces the centre first observed

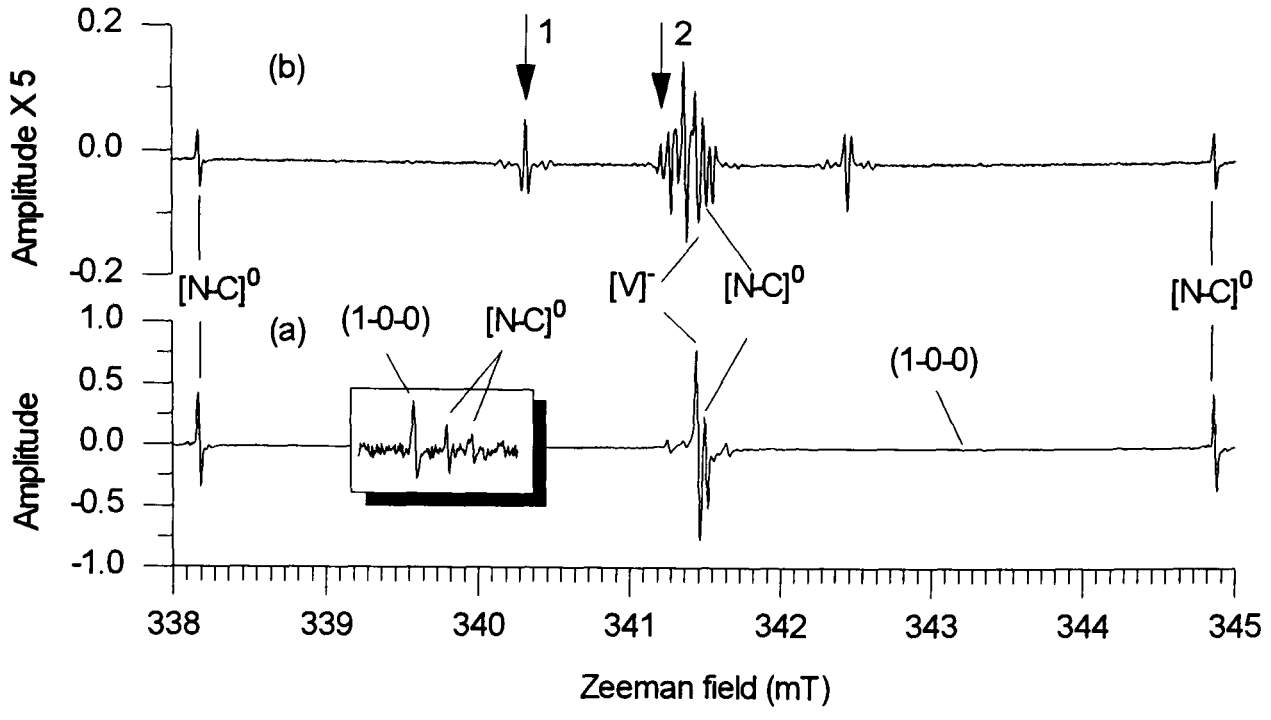



Figure 6.3: EPR spectra from the [V]* sample (a) before illumination; and (b) during illumination. The spectra were collected with B||[100] at X-band at 4K with the spectrometer tuned to give the first derivative of the absorption signal. The arrows label transitions referred to in §6.6.1 and §6.6.2. The transition labelled [N–C]$^0$ in the box is a forbidden hyperfine transition ($|\Delta m_s| = \pm 1, |\Delta m_N| = 1$), and those labelled (1-0-0) are from the nearest neighbour $^{13}$C interaction in [V]$^-$ (see Figure 6.4).

by van Wyk. When a next-nearest neighbour $^{12}$C atom is replaced by a $^{13}$C atom (occurring naturally with an abundance of 1.11%) a smaller hyperfine splitting results and another set of EPR lines is produced. To avoid ambiguity the following notation will be used: $[V]^*_{00}$ for no $^{13}$C atoms; $[V]^*_{10}$ for one nearest neighbour $^{13}$C atom; $[V]^*_{01}$ for one next-nearest neighbour $^{13}$C atom; and [V]* to refer to the system as a whole.

### 6.5.1 EPR spectra in principal directions

Figure 6.3a shows the EPR spectrum from the [V]* sample obtained without any illumination and with the Zeeman field aligned parallel to a [001] crystallographic axis. The characteristic three-line [N–C]$^0$ spectrum is visible along with a strong central line at $g$=2.0027(1) produced by [V]$^-$ centres. An enlargement of this region is shown in Figure 6.4 in which the hyperfine interactions with $^{13}$C atoms in the nearest and next-nearest neighbour positions can be resolved. Upon illumination with the full spectrum of the Hg lamp the [V]$^-$ and [N–C]$^0$ signals diminished and the [V]* spectrum became visible (Figure 6.3b). The [V]* system has a dispersion-

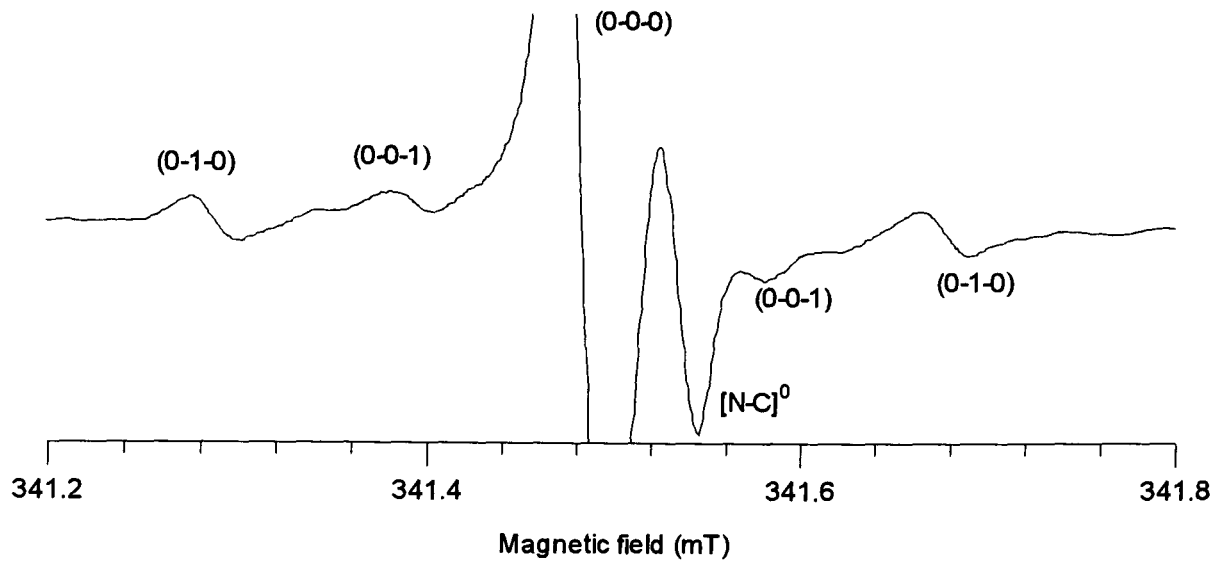



Figure 6.4: Enlargement of the central region from Figure 6.3b showing the $[V]^-$ spectrum. The numbers ($\alpha$-$\beta$-$\gamma$) denote $\alpha$ nearest neighbour, $\beta$ next-nearest neighbour, and $\gamma$ next-next-nearest neighbour $^{13}C$ atoms. The transitions corresponding to the nearest neighbour $^{13}C$ interaction are marked in Figure 6.3.

like line shape and the central region is complicated. An enlargement of the central region is presented in Figure 6.5 where the Zeeman field has been applied parallel to the [001], [111] and [110] crystallographic directions. The line shape originates from the superposition of slightly offset signals in emission and absorption as explained in §6.8.2 and §6.8.2.

### 6.5.2 Saturation behaviour

The microwave saturation behaviour of the $[V]^*_{10}$ system was measured at temperatures ranging from 5.5K to 295K. A typical saturation curve collected at 17K is shown in Figure 6.6. At temperatures below 100K the system was easily saturable with the curves peaking around 3 $\mu$W. The maximum moved to slightly higher powers of around 30 $\mu$W at 295K. A similar saturation behaviour was observed for the $[V]^*_{00}$ and $[V]^-$ centres, while the $[N–C]^0$ saturated more easily at low temperature with its 10K curve peaking around 0.3 $\mu$W.

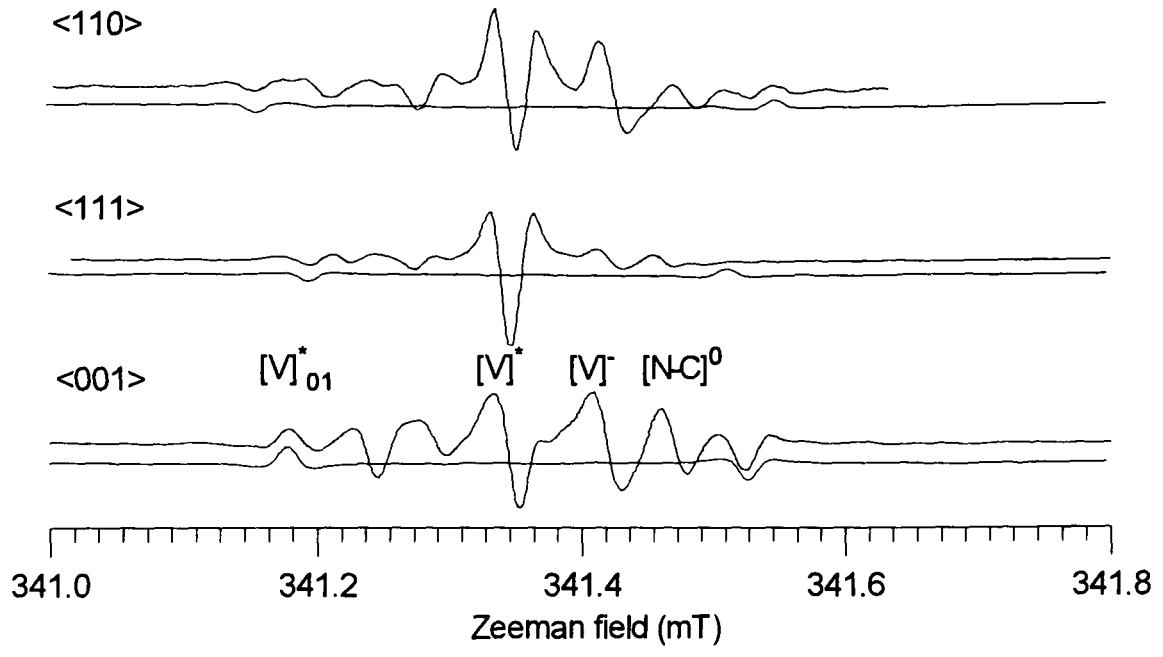



Figure 6.5: The central region of the spectrum showing the $[V]^*$, $[V]^-$ and $[N–C]^0$ systems. The simulations (lower curve in each direction) are for the interaction of one next-nearest neighbour $^{13}C$ with $[V]^*$. The additional structure is probably produced by the interaction of other neighbouring $^{13}C$ atoms with $[V]^*$. The spectra were collected under illumination with the full spectrum of the Hg lamp, at 4K at X-band. The directions of the Zeeman field is shown on each plot.

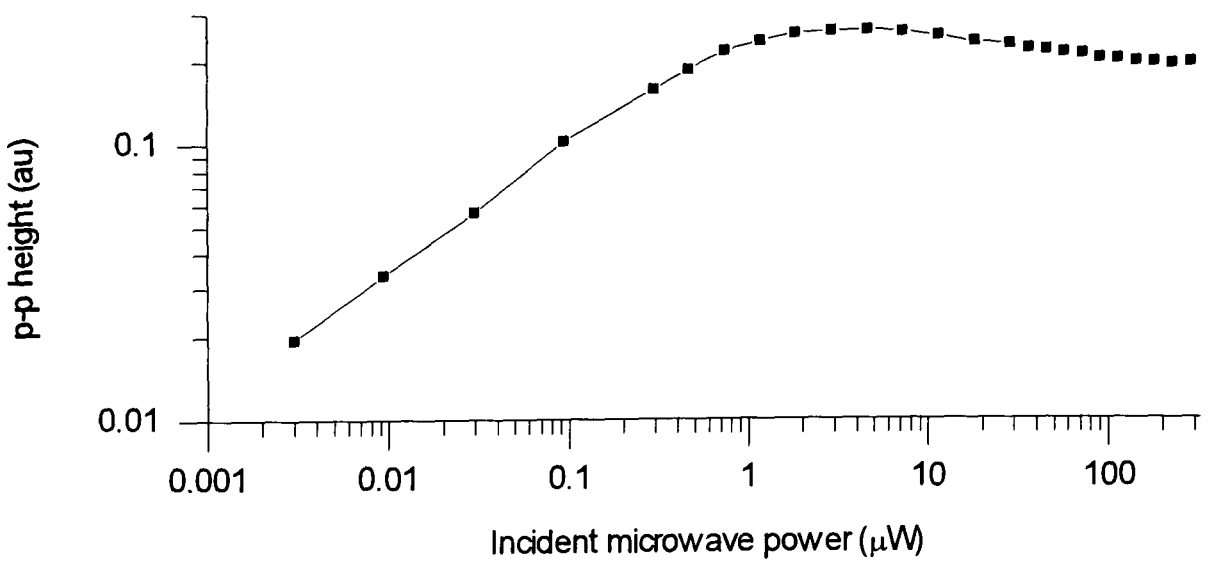



Figure 6.6: $[V]^*_{10}$ EPR saturation curve at 17K, X-band, in the Bruker cavity, with the spectrometer detecting the first harmonic of the 115 kHz field modulated absorption signal.

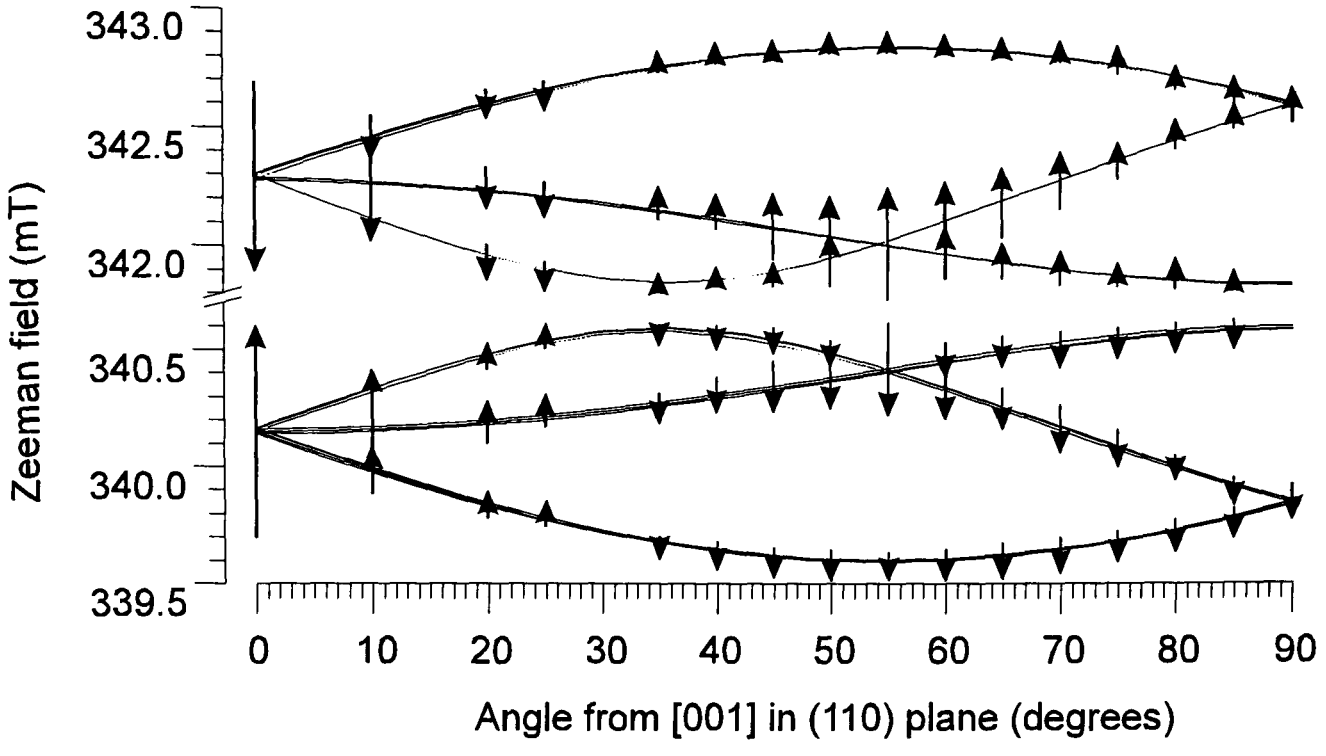



Figure 6.7: Angular variation of [V]* EPR in (110) plane showing intensity variation (see text). The solid line is a fit to the data using the parameters in Table 6.1. The arrow length corresponds to the intensity of the EPR signal (up for absorption, down for emission), while the horizontal position indicates the field at which the EPR transition was measured.

### 6.5.3 Angular variation

The angular variation of the position and intensity of the EPR transitions, assigned to the $[V]^*_{10}$ centre, as a function of angle from [001] in the (110) plane was collected and plotted in Figure 6.7.[9] The measurements were collected in a single session and the position of the lines was determined from spectra collected at three different combinations of microwave power and magnetic field modulation. A problem occurred during data collection as the ENDOR insert slipped in the goniometer. This has since been solved by the addition of locking screws. The angular measurements were corrected for errors introduced by this using the $[N–C]^0$ spectrum present in the sample. The angular dependence of the $[N–C]^0$ system has been accurately measured, and the magnetic field at the proton probe and the microwave frequency were known to a high degree of absolute accuracy, thus the measured positions of all the [N–

[9]Although the intensities were measured, van Wyk achieved a higher signal-to-noise as he was able to focus his light directly onto the sample, hence his intensities have been plotted here for clarity. The line positions plotted were measured in this work.

C]$^0$ lines could be used to determine the angle of the Zeeman field. Maintaining the coincidence of the pairs of [N–C]$^0$ lines ensured that the sample remained in a plane. The (110) plane was identified by the angular behaviour of the [N–C]$^0$ lines. In addition to the angular correction all spectra had to be adjusted for the field offset produced by the gradient between the proton probe position and the sample position within the cavity. The positions of the [N–C]$^0$ lines were simulated at 0.1° intervals and the measured positions of the [N–C]$^0$ lines were grouped as a function of angle. Software was developed to allow the offset in field of all spectra, and the offset in angle of each spectrum, to be varied to minimize the residual in field when compared to the simulated spectra. The method was both robust, as it highlighted a typing error, and successful in correcting the angles to around 0.2°. The field offset was found to be around 0.06(1) mT. The [N–C]$^0$ angular variation was then fitted to verify that the measured data produced the correct hyperfine parameters and to place an estimate on the validity of the $[V]^*_{10}$ fit. The RMSD error in the [N–C]$^0$ fit was 9 $\mu$T. The position of the $[V]^*_{00}$ centre was compared to that of the [N–C]$^0$ and $[V]^-$ centres, in the [001] direction, to verify further the assignment of $g$-value. $g$-values of 2.0024(1) [53] and 2.0027(1) [164] were assumed for the [N–C]$^0$ and $[V]^-$ centres respectively.

The angular variation in the (111) plane was also collected and the intensity behaviour investigated. This is shown in Figure 6.9. This measurement was used in the investigation of the intensity behaviour, although the axial symmetry had already been verified by the measurements in the (110) plane.

### 6.5.4 Concentrations

The concentrations of the [N–C]$^0$ and $[V]^-$ centres were determined by comparison with a calibrated[10] synthetic type Ib reference sample and were found to be 0.40(8) ppm., and 0.014(8) ppm. respectively.

[10]Using the infrared absorption at 1130 cm$^{-1}$, see [56] and equation 8.3 on page 206.

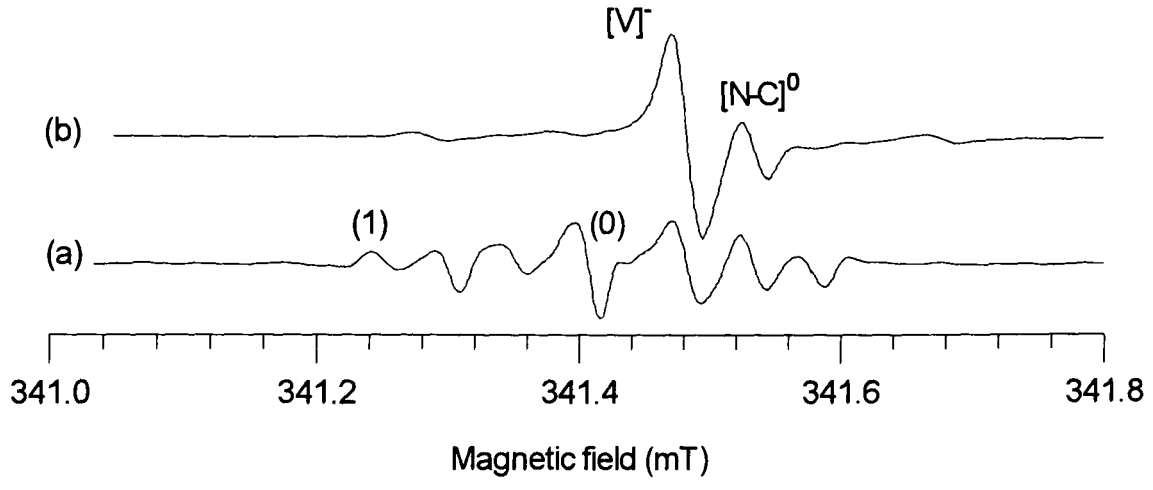



Figure 6.8: Effect of light on the central region of the [V]* spectrum. (a) light on, (b) light off. (1) denotes 1 next-nearest neighbour $^{13}C$ atom, and (0) no $^{13}C$ atoms in nearest or next-nearest positions. Collected at X-band, at 5K. The full spectrum of the Hg lamp was used for illumination.

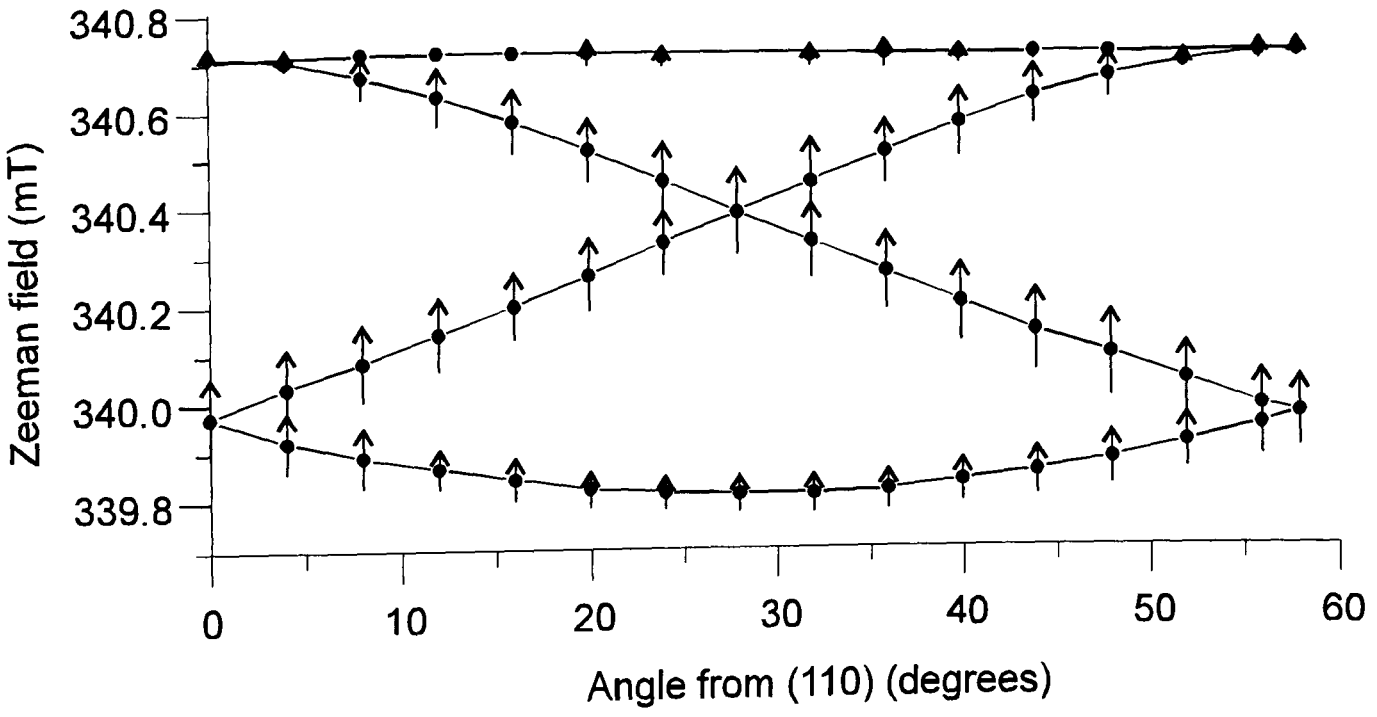



Figure 6.9: Angular variation for $[V]^*_{10}$ in (111) plane showing that all transitions retain the same phase when the magnetic field is rotated. Collected at 6K, at X-band.

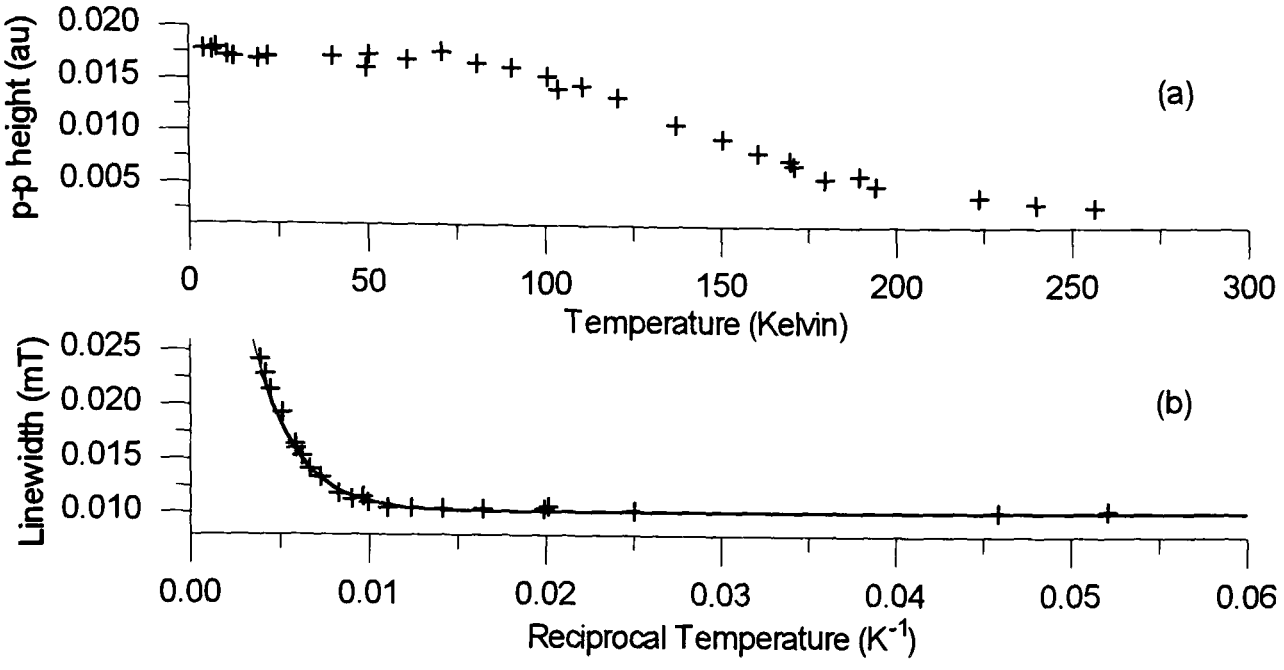



Figure 6.10: (a) Temperature dependence of the peak line height for the lowest field $[V]^*_{10}$ transition (B||[001]). The incident power was 30 nW and the system was illuminated with the full spectrum of the Hg lamp. (b) Variation of component line width with reciprocal temperature. The solid curve shows the fit to a single exponential decay (see text).

### 6.5.5 Temperature dependence

The [V]* centre was found to have an unusual temperature dependence. The intensity of all [V]* signals increased rapidly down to 100K and then remained constant down to 5K. This behaviour is depicted in Figure 6.10a. It was possible to employ this independence of temperature to associate signals in the central region with various defect centres. Two spectra, one at 87K and one at 6K, were collected under identical conditions of incident microwave power and illumination. Subtracting one from the other cancelled all contributions with anomalous temperature dependence, leaving just $[N\text{–}C]^0$ and $[V]^-$ which varied according to the Curie law (Figure 6.11). The subtraction indicated that all the EPR signals in the central region, with the exception of $[N\text{–}C]^0$ and $[V]^-$, were related to [V]*.

### 6.5.6 Dependence of $[N\text{–}C]^0$, $[V]^-$ & [V]* EPR on incident photon energy

Field swept and time resolved measurement techniques were employed to determine the wavelength dependence of the $[V]^-$, $[N\text{–}C]^0$, and [V]* paramagnetic centres. The

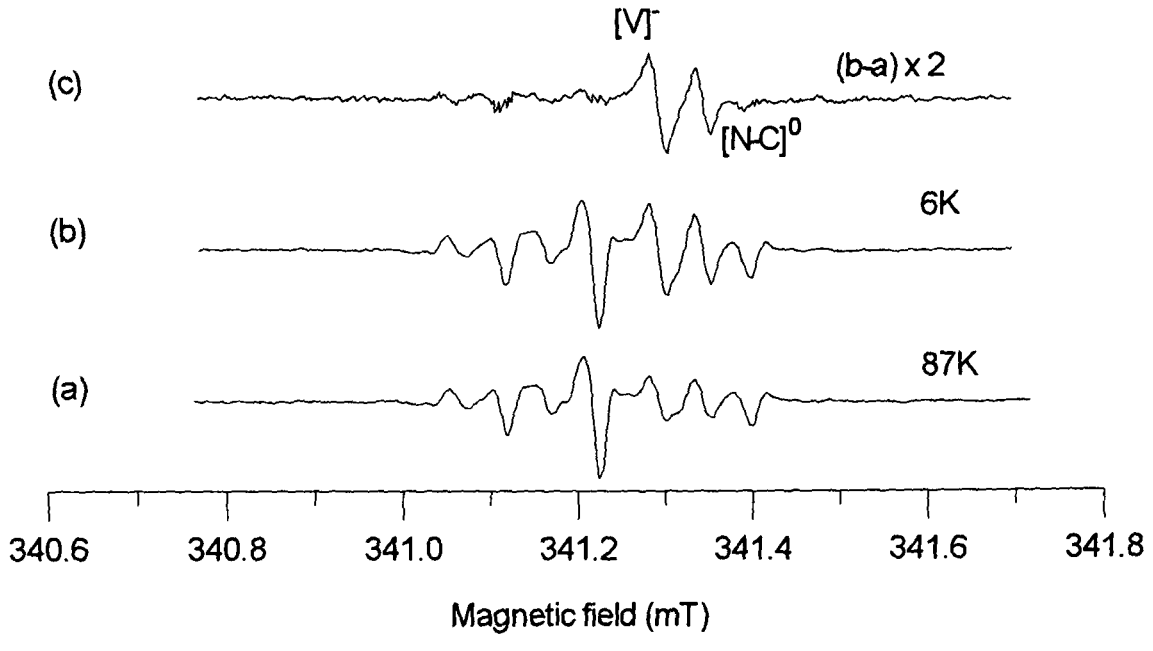



Figure 6.11: Subtraction of two spectra showing centre of $[V]^*$ spectrum at 87K (a) and 6K (b), B||[100]. The difference spectrum (c) clearly shows the $[N–C]^0$ and $[V]^-$ resonances as these obey the usual Curie law dependence.

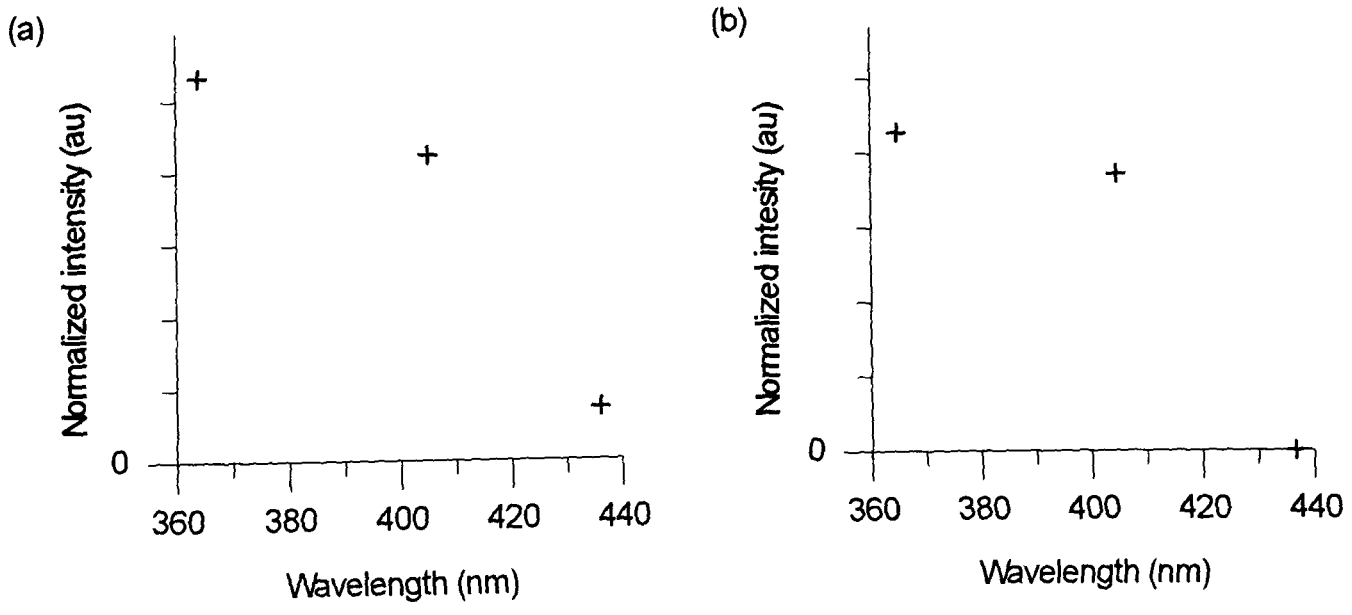



Figure 6.12: Intensity of the $[V]^*$ centre as a function of incident photon energy. (a) At room temperature, and (b) at 5K. Each point is normalized for photon intensity.

former were performed by exposing the sample to a set wavelength of light and collecting a spectrum; while the latter involved setting the field to an EPR resonance, then monitoring the amplitude of the resonance as the sample was exposed to light of various frequencies. The time resolved measurements were needed to understand the complicated behaviour of the $[V]^-$system.

The fixed wavelengths were chosen to coincide with peaks in the mercury emission spectrum and were produced using diffraction filters with a 10 nm band pass. For measurements on $[V]^-$ the sample was left in the dark at room temperature for several hours to allow charge equilibrium to be restored.

The behaviour of the $[V]^*$ system was found to be relatively simple and reversible. The normalized intensities taken from spot measurements at 5K and 295K are shown in Figure 6.12. The $[V]^-$ system was found to have a complicated behaviour which depended upon sample preparation. This behaviour was finally deconvoluted by performing two time resolved experiments, one at 5K and one at room temperature. In these experiments the Zeeman field was stabilized on the the central $[V]^-$ line (see Figure 6.4) and the wavelength specific illumination was turned on. The intensity as a function of time was collected for up to 200 s. The illumination was then switched off and another time-resolved spectrum collected. This was repeated increasing the energy of the incident photons at each iteration. The results are plotted in Figures 6.13 and 6.14. In each figure the zero of the y-axis corresponds to zero EPR intensity. Examination of the figures revealed that each wavelength reset the system to a specific level, unique to that wavelength, and independent of what had occurred previously. Thus, the same wavelength of light could appear to enhance the signal if applied when the system had previously been quenched, or quench the signal if applied after it had previously been enhanced. The majority of the responses were slow (of the order of 10 s to 60 s) while the 364.9 nm photons produced a rapid response (in under 1 s).

### 6.5.7 Lifetimes, quenching, and recovery

The following measurements were made with the full illumination of the Hg lamp. Figure 6.15 shows that the amplitude of the EPR signal from the $[V]^*_{10}$ centre at 5K

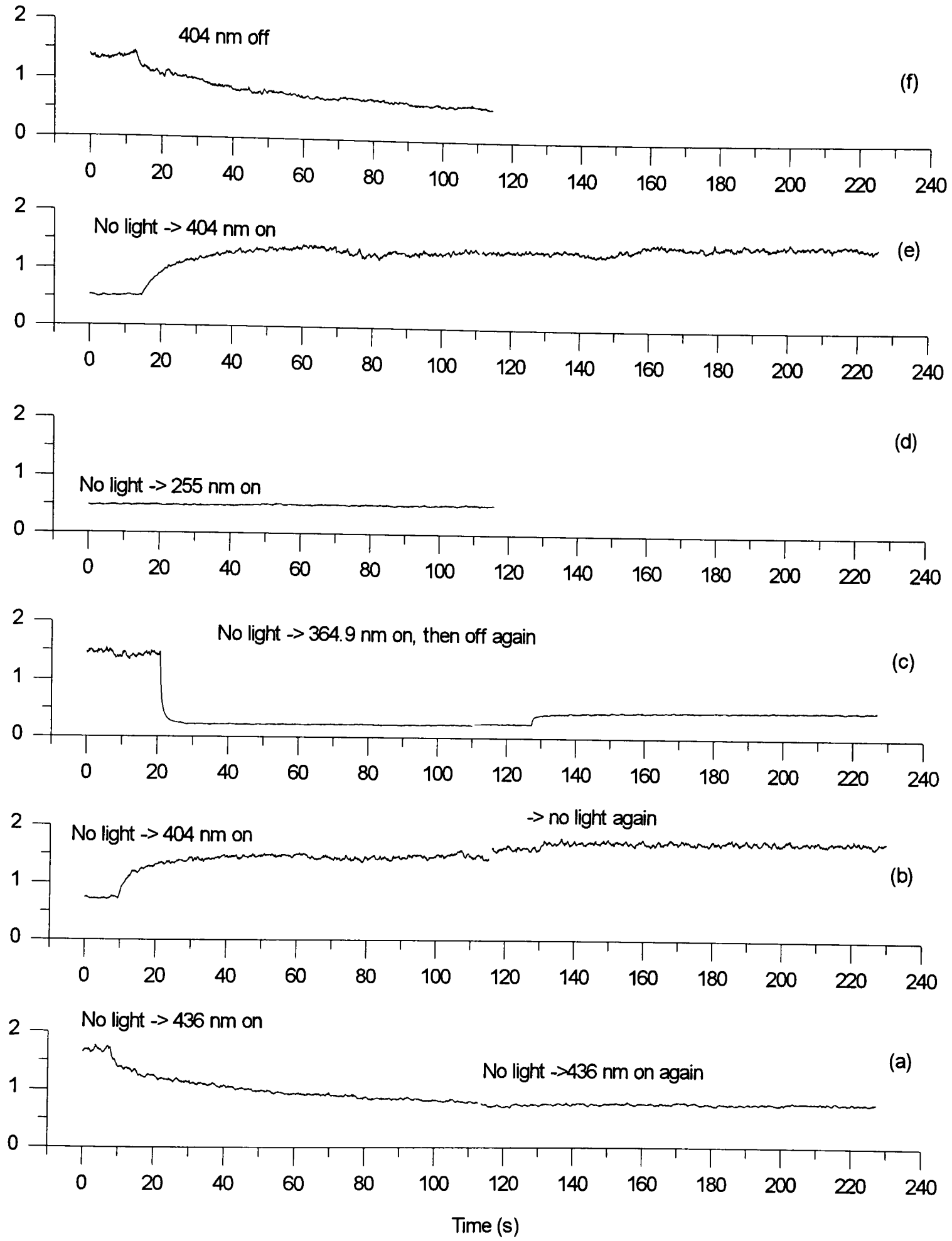



Figure 6.13: Decay, recovery and enhancement of $[V]^-$ at 5K as a function of time. The plots were taken consecutively from (a) to (f). The zero of the y-axis represents zero EPR intensity and the scale is constant throughout all plots. No attempt has been made to correct for photon intensity.

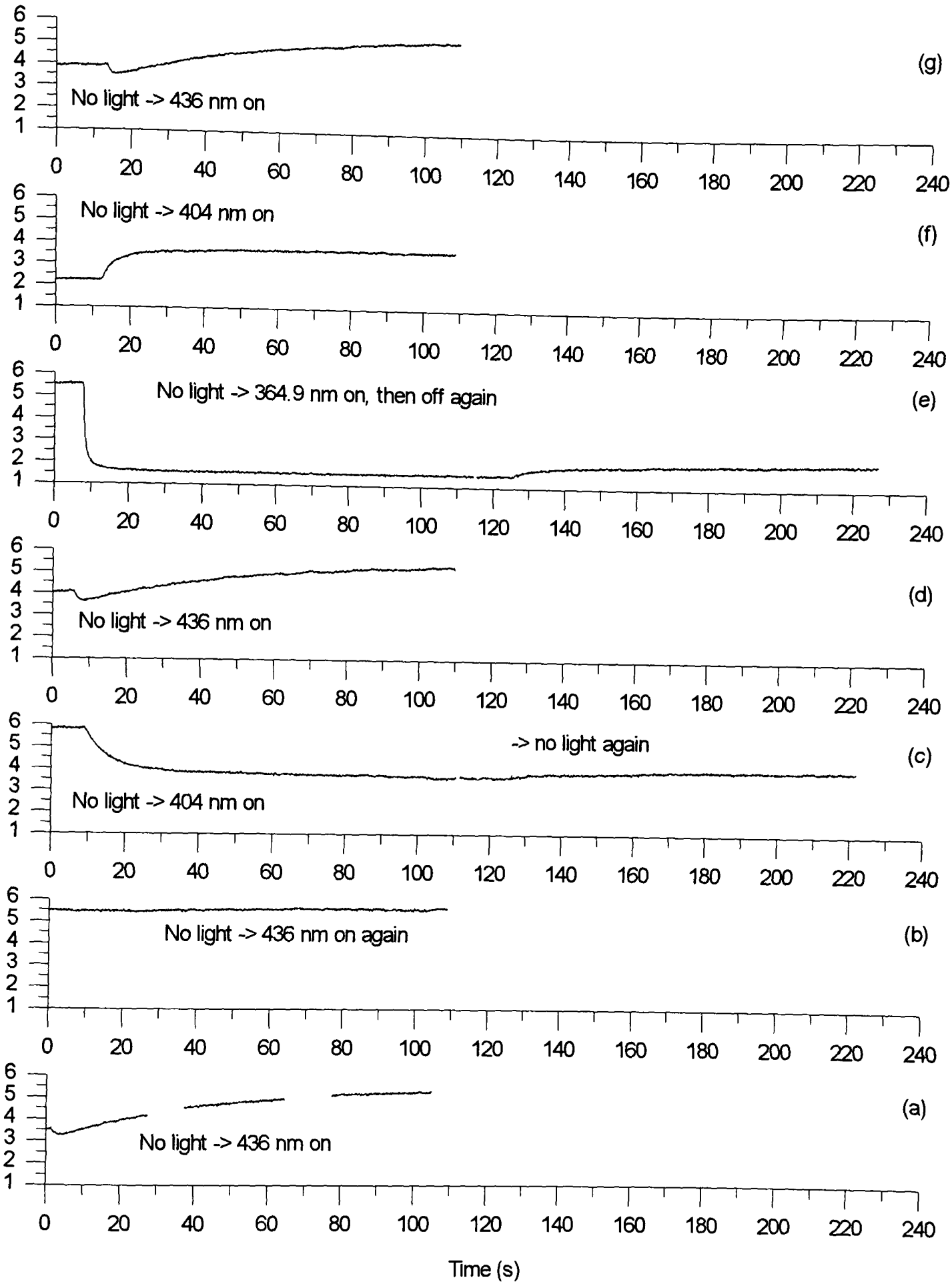



Figure 6.14: Decay, recovery and enhancement of $[V]^-$ at room temperature as a function of time. The plots were taken consecutively from (a) to (g). The zero of the y-axis represents zero EPR intensity and the scale is constant throughout all plots. No attempt has been made to correct for photon intensity.

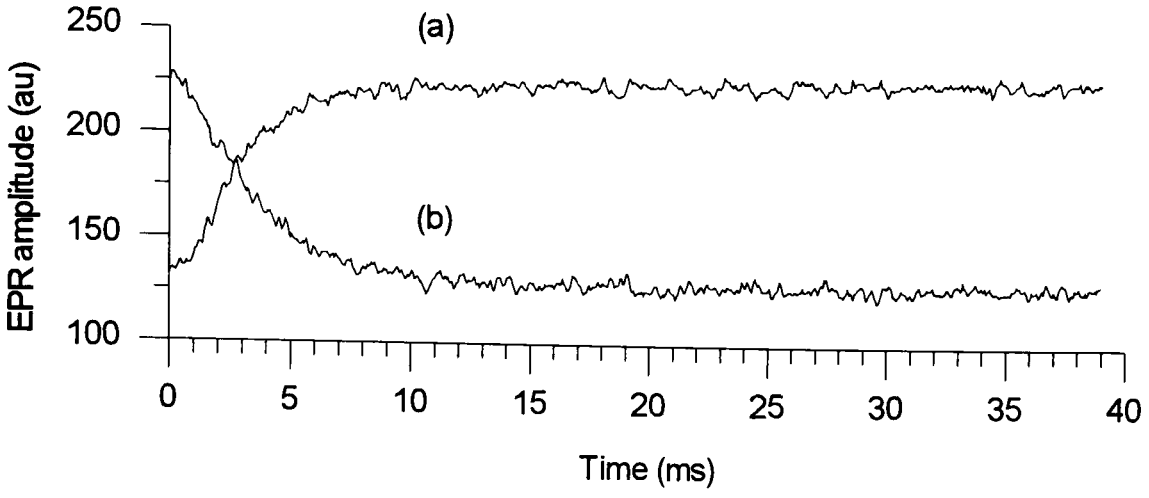



Figure 6.15: Temporal dependence of $[V]^*_{10}$ EPR signal on (a) illumination with full spectrum of the Hg lamp, and (b) removal of illumination. Zeeman field along [001], 5.0K and 7.5 $\mu$W incident microwave power.

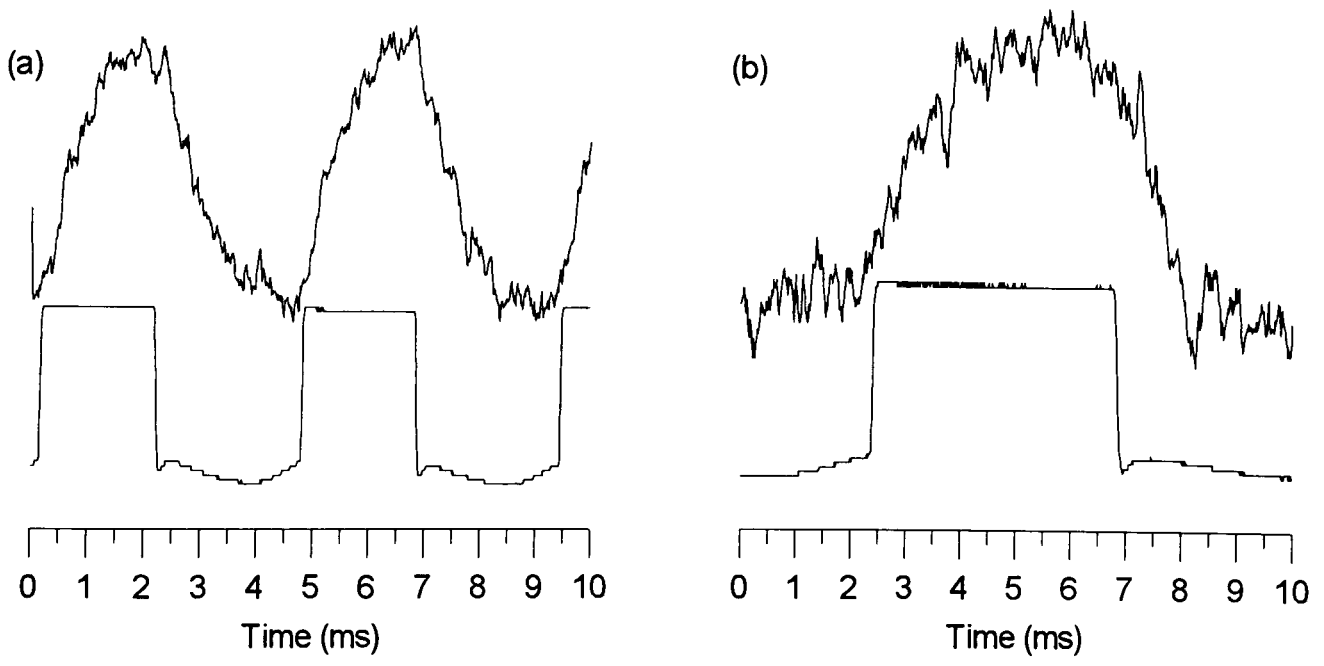



Figure 6.16: Temporal dependence of $[V]^*_{10}$ EPR signal at room temperature. (a) chopping at 211 Hz, taking about 0.25 ms to break the light beam and (b) chopping at 98 Hz taking about 0.5 ms to break the beam.

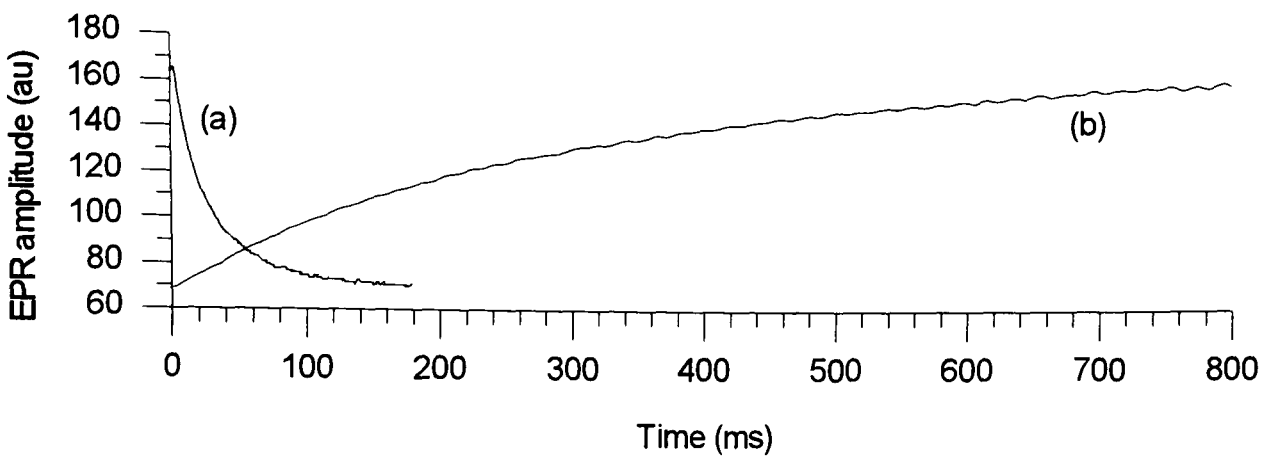



Figure 6.17: Temporal dependence of $[V]^-$ EPR signal on (a) illumination will full spectrum Hg lamp, and (b) removal of illumination. Zeeman field along [001], microwave power 9.4 $\mu$W at 5K.

decayed rapidly when the excitation was removed and the intensity of the EPR signal maximized rapidly upon illumination. The measured decay and recovery times depended upon incident microwave power, with the decay time being reduced at higher microwave powers where the EPR signal was saturated. Attempts were made to measure the decay and recovery at room temperature using the chopper wheel. These are shown in Figure 6.16. As can be seen a poor signal-to-noise ratio was achieved owing to the small amplitude of the signal at room temperature, and the limited averaging ability of the digital storage adaptor used (see §4.3.6). The poor signal-to-noise precluded characterization of the saturation dependence of the decay, thus the information provided is limited, however, the measurements tentatively show that the decay time is reduced by a factor of at least five when compared to unsaturated measurements at 5K. Measurements made between 5K and 74K indicated that the decay remained constant in that region. The decay and recovery at 5K were fitted to exponentials and the results extrapolated to zero microwave power. The decay on removal of light, when fitted to a single exponential decay ($e^{-t/\tau_d}$), indicated that $\tau_d = 9.0(8)$ ms at 5.0K. The growth upon illumination was fitted to an increasing exponential function ($1 - e^{-t/\tau_r}$) and indicated that $\tau_r = 9.0(8)$ ms at 5.0K.

The rate of recovery of the $[V]^-$ ground state EPR signal was found to be much slower than the rate of decay of the $[V]^*$ excited state (Figure 6.17). The recovery was fitted to a rising exponential and yielded a time constant of $\tau_r = 300(10)$ ms at 5.0K. The quenching of the EPR signal upon illumination was more rapid ($\tau_q = 28(1)$ ms

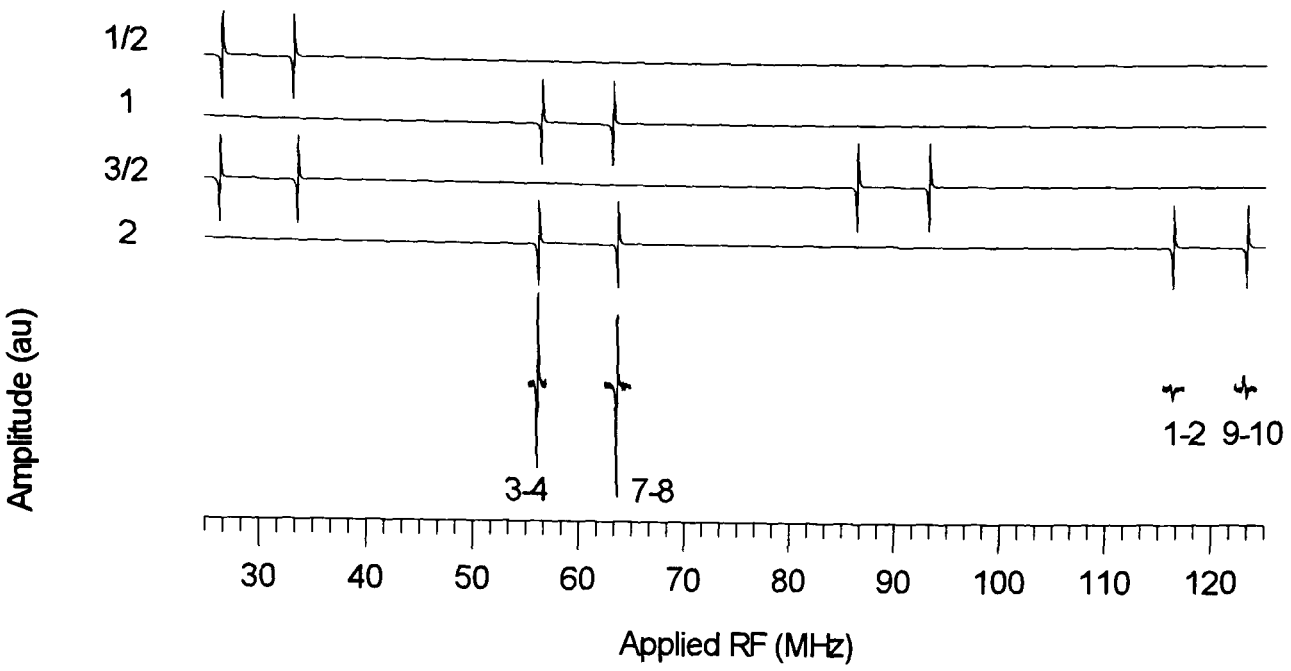



Figure 6.18: $^{13}$C ENDOR from the $[V]^*_{10}$ centre. Zeeman field along [001] and set to the lowest field EPR line (arrow 1, Figure 6.3), 0.3 mW incident microwave power. The upper traces show simulated ENDOR transitions for effective spins of 2, $\frac{3}{2}$, 1, and $\frac{1}{2}$. The levels between which the transitions occur on the experimental spectrum are labelled.

at 5.0K) but still slow when compared to the [V]* centre.

The decay of the EPR from $[N\text{–}C]^0$ upon application of light and subsequent recovery upon removal of illumination were slower even than $[V]^-$. Upon illumination $\tau_q = 120(5)$ ms and $\tau_r = 470(10)$ ms at 5.0K.

## 6.6 ENDOR measurements

The ENDOR measurements were vital to the investigation of the [V]* system as they proved incontrovertibly that the effective electron spin was two. They also accurately defined the hyperfine interaction on the $[V]^*_{10}$ centre and helped to identify the $[V]^*_{01}$ centre.

### 6.6.1 $^{13}$C nearest neighbour ENDOR

ENDOR spectra were recorded from the nearest neighbour $^{13}$C atoms of the $[V]^0$ excited state (referred to here as the $[V]^*_{10}$ centre). The sample was continuously illuminated with the full spectrum of the Hg lamp and data were collected at temperatures between 5.0K and 100K as the ENDOR, like the EPR, was found to be

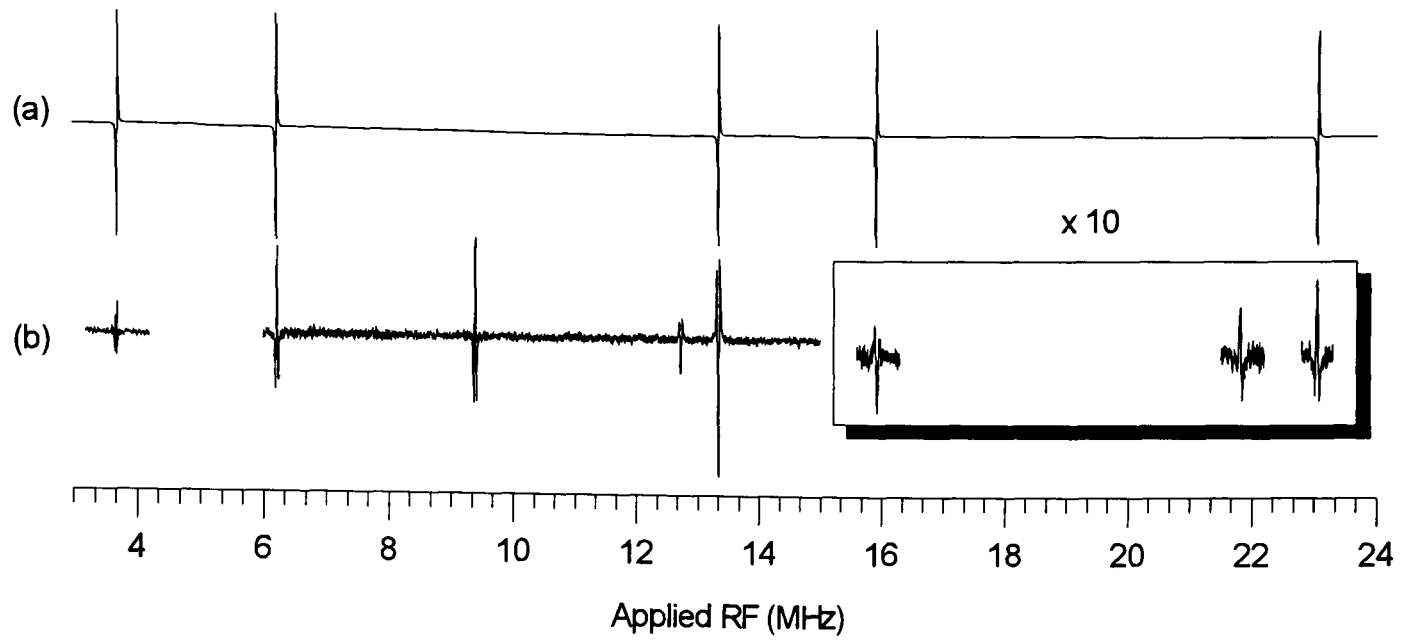



Figure 6.19: $^{13}$C ENDOR from the $[V]^*_{01}$ centre. Zeeman field along [001] and set to EPR line 2 in Figure 6.3, 0.2 mW incident microwave power, 50 W rf power. The spectrum simulated from the measured hyperfine parameters is shown in (a) while the experimental spectrum is shown in (b).

insensitive to temperature below 100K. The ENDOR signal-to-noise was low as the $^{13}$C was present in natural abundance with the result that it was only possible to make measurements on the large EPR transitions observed when the Zeeman field was parallel to [001] and [111]. Alignment to better than 0.1° was achieved using the $[V]^*_{10}$ and $[N\text{–}C]^0$ EPR, and the $[N\text{–}C]^0$ ENDOR signals. Figure 6.18 shows the ENDOR transitions obtained (after signal averaging) whilest saturating the low field EPR transition labelled with arrow 1 in Figure 6.3. The $S$=2 spin state was identified by the measurement of pairs of lines centred approximately on $A_{Eff}$ and $2A_{Eff}$ and separated by $2g_N\mu_N B$. $A_{Eff}$ is the hyperfine splitting in a given orientation and $g_N$=1.404 identifying the nucleus as $^{13}$C. Simulations for the other possible effective spin states are shown in Figure 6.18. ENDOR spectra were collected over the whole range shown in Figure 6.18 but these are not plotted as they were not signal averaged to the same extent and obscure the detail.[11]

[11]Even with reduced signal averaging the full scan took over one day to collect for each Zeeman field direction.

### 6.6.2 $^{13}$C next-nearest neighbour ENDOR

Figure 6.19 shows $^{13}$C ENDOR from next-nearest neighbours (denoted by $[V]^*_{01}$) while saturating the low field EPR transition labelled by arrow 2 in Figure 6.3. The spin of two was verified once more and that $g_N$=1.404, thereby identifying $^{13}$C. The ENDOR line shape reproduced the EPR line shape, not the absorption shape observed from the nearest neighbours. This line shape was obtained after a number of optimizations of the ENDOR signal amplitude owing to the very low intensity obtained when using the same rf and microwave powers as for the $[V]^*_{10}$ centre. When these new settings were used to observe $[V]^*_{10}$ the same shape and phases as for the $[V]^*_{01}$ were obtained. It is suggested that two ENDOR mechanisms occur and that varying the probe conditions allows preferential selection of one or the other. The additional lines in Figure 6.19 probably originate from a coupling to more distant $^{13}$C neighbours or possibly a different centre as it is clear from Figure 6.3 that there are other EPR lines around $g$=2.0033. These EPR lines were shown to have the same temperature and excitation dependence as the other [V]* lines and were therefore probably produced by more distant $^{13}$C neighbours.

## 6.7 Fitting

### 6.7.1 $^{13}$C nearest neighbours: $[V]^*_{10}$

The angular variation (§6.5.3) in the (110) plane was least-squares fitted in conjunction with the ENDOR. As ENDOR only depends on the electron $g$-value to second order, the EPR angular variation was used to determine this, while the ENDOR was fitted for the hyperfine coupling constants. These fits were performed iteratively (it was not possible to couple them using *EPR.FOR*[12]) until no further variation in the parameters was obtained. The spin Hamiltonian is given below:

$$\mathcal{H} = g\mu_B \hat{\mathbf{S}} \cdot \mathbf{B} + \hat{\mathbf{S}} \cdot \underline{\mathbf{A}} \cdot \hat{\mathbf{I}} - g_N \mu_N \hat{\mathbf{I}} \cdot \mathbf{B} \tag{6.2}$$

[12]See §4.4.5 for details on *EPR.FOR*.

Table 6.1: Nearest neighbour $^{13}C$ hyperfine parameters measured and the wavefunction parameters calculated for $[V]^-$ and $[V]^*$. The $[V]^-$ parameters are taken from reference [164].

| Defect | $A_{\|\|}$(MHz) | $A_\perp$(MHz) | $A_s$(MHz) | $A_p$(MHz) | $\eta^2$ | $\lambda^2$ |
|---|---|---|---|---|---|---|
| $^4A_2$:$[V]^-$ (n.n) | 121.6 | 61.9 | 81.8 | 19.9 | 0.630 | 6.9 |
| $^4A_2$:$[V]^-$ (n.n.n) | 13.42 | 9.40,9.23 | 10.68 | 1.37 | 0.016 | 4.5 |
| $^5A_2$:$[V]^*_{10}$ (n.n) | 91.13(9) | 35.03(5) | 53.73(5) | 18.70(3) | 0.753 | 12.2 |
| $^5A_2$:$[V]^*_{01}$ (n.n.n) | 12.0(1) | 8.36(6) | 9.6(1) | 1.2(1) | 0.014 | 4.4 |

n.n $\Leftrightarrow$ nearest neighbour

n.n.n $\Leftrightarrow$ next-nearest neighbour

where all terms have their conventional meanings and $S$=2, $I$=$\frac{1}{2}$. The results of the fit are given in Table 6.1.

### 6.7.2 $^{13}C$ next-nearest neighbours: $[V]^*_{01}$

The absence of fine structure indicated that the symmetry was $T_d$, it was therefore assumed that the $^{13}C$ hyperfine interactions of the next-nearest neighbours were axially symmetric with the principal axis along a [111] direction. If the symmetry had been broken, or had the axis veered from [111] by more than a degree – as in the case of the next-nearest neighbours of $[V]^-$ at 4K – all the ENDOR lines in Figure 6.19, except the one close to the nuclear Zeeman frequency, would be split into doublets with a 2:1 intensity ratio. The ENDOR transitions were not split. ENDOR measurements with the Zeeman field parallel to the [001] and [111] crystallographic directions were least-squares fitted to equation 6.2 and the results are tabulated in Table 6.1. An additional check upon the axial symmetry was made by transforming the experimental data into the principal value coordinate system of the hyperfine interaction making it possible to vary the axis of symmetry within *EPR.FOR*. This revealed that changes of up to a degree were not significant.

### 6.7.3 Additional crystal field terms for $S$=2

When a centre has $T_d$ symmetry second-degree terms such as the fine structure splitting are forbidden [191]. There is therefore no term of the form $\hat{\mathbf{S}}\cdot\underline{\mathbf{D}}\cdot\hat{\mathbf{S}}$ in equation 6.2. When the defect spin is equal to two fourth-degree interactions are permitted and these are not forbidden by the $T_d$ site symmetry. Under tetrahedral symmetry there is only one varied parameter and the interaction can be represented in the following operator form:[13]

$$\frac{a}{6}\left\{\hat{S}_x^4+\hat{S}_y^4+\hat{S}_z^4-\frac{1}{5}\hat{S}\left(\hat{S}+1\right)\left(3\hat{S}^2+3\hat{S}-1\right)\right\} \tag{6.3}$$

where $a$ is the magnitude of the interaction. The term is generally vanishingly small, and its inclusion into equation 6.2 did not improve the quality of fit. The magnitude of $a$ was estimated to be less than 1 MHz, which is equivalent to a splitting of 0.07 mT. This value was comparable to the resolution of the magnetic field measurements and hence no splitting could be resolved. However, as will be seen in §6.8.3, the small octupolar interaction term can be used to explain the difference in line shapes between the low and high field transitions of the $[V]^*_{10}$ centre, and also to explain the shape of the EPR transitions from the $[V]^*_{00}$ centre. The $T_d$ symmetry was confirmed by the lack of need for a second order, or fine structure, term in the fitting.

## 6.8 Discussion

### 6.8.1 Identification of the $^5A_2$ excited state of the neutral vacancy, $[V]^*$

The EPR and ENDOR measurements show that the new centre has:

- tetrahedral symmetry;
- an effective spin of two;

[13] For more detail see [91] p.142ff.

- four equivalent carbon neighbours; and
- is possibly created when $[V]^-$ is ionized.

There is no doubt that the centre is intrinsic and is the $^5A_2$ state of the neutral vacancy. No $S$=2 state is possible for the $[V]^{2+}$, $[V]^+$, $[V]^-$and $[V]^{2-}$ charge states [99]. The self-interstitial in the $T_d$ site is ruled out as (i) it becomes mobile at 50K, and (ii) calculations show that it is energetically unfavourable for it to adopt this site, with the ⟨100⟩ split-interstitial being favoured (see §6.2, p.132). This identification confirms the prediction of the Coulson-Kearsley model [99] and subsequent calculations (§6.2.2) that the $^5A_2$ state is a low lying state located in the band gap.

The creation of $[V]^*$ correlates with the loss of $[V]^-$ on illumination. As the GR1 uv-band overlaps with the ND1 band, it is possible that $[V]^*$ is created by internal excitation of $[V]^0$, or by charge transfer from, or related to, the GR2–GR8 bands. These bands do not exhibit luminescence decay, but GR1 luminescence is produced instead [60]. Two possible models for these transitions are discussed on page 136 of §6.2.2. The $[V]^*$ state has, however, not been observed in diamonds containing $[V]^0$ centres but no $[V]^-$ centres, and it is well known that ionization of $[V]^-$ produces $[V]^0$ [192, 187]. The distribution of $[V]^-$ is not isotropic, however, it is not known if $[V]^*$ is created uniformly throughout the sample. The evidence lends credence to a model of formation involving ionization of $[V]^-$ leaving the $[V]^0$ in an excited state: namely $[V]^*$.

### 6.8.2 Line shapes I - second order hyperfine interaction

Figure 6.20 shows an enlargement of the low-field $[V]^*$ EPR transitions and the simulated contributions from nearest and next-nearest neighbouring $^{13}C$ atoms. They are described below:

- The central transition is produced by the hyperfine interaction with a nearest neighbour $^{13}C$ nucleus (Figure 6.20c). This interaction also produces forbidden transitions symmetrically placed on either side of the main transitions, the

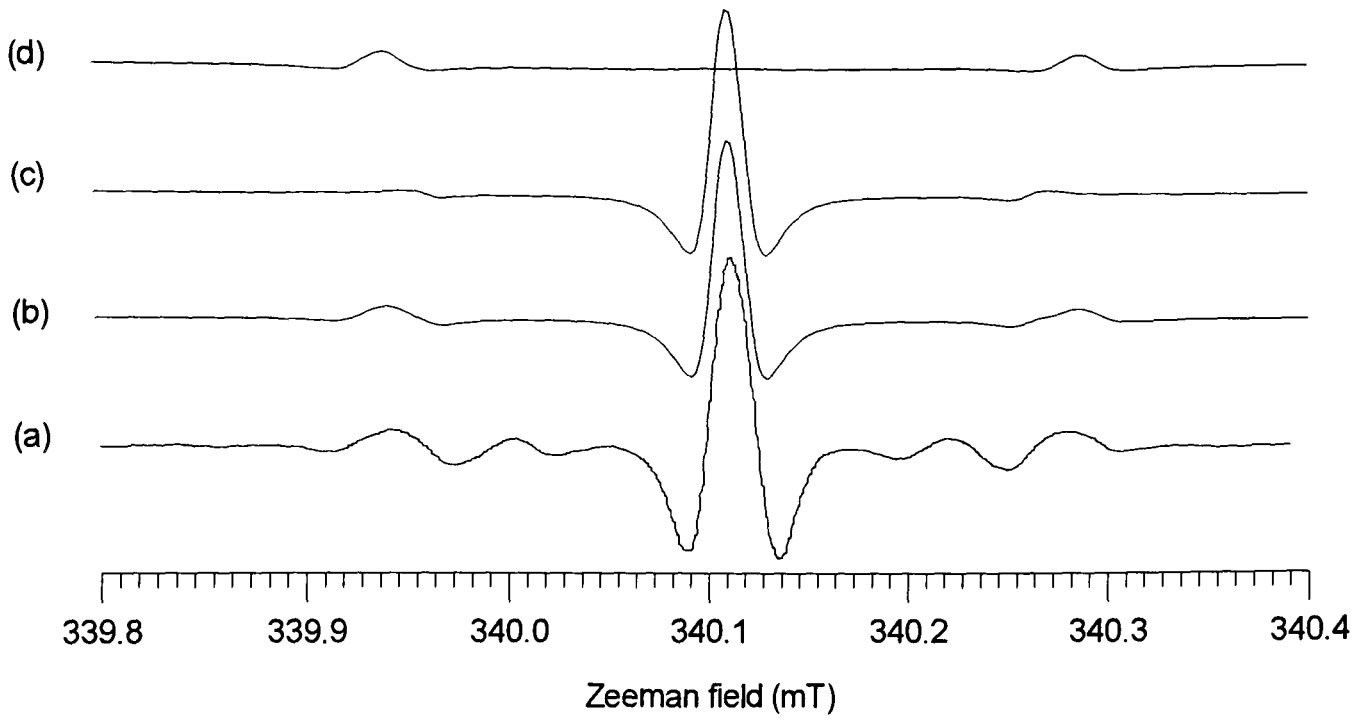



Figure 6.20: Low-field [V]* EPR transitions. $\mathbf{B}\|[100]$ (a) Experimental spectrum (signal averaged). (b) Simulation for $[V]^*_{11} + [V]^*_{10}$. (c) Simulation for $[V]^*_{10}$ showing the spin dependent forbidden transitions (4 nearest neighbours). (d) Simulation for $[V]^*_{11}$(12 next-nearest neighbours). All simulations are shown in the correct proportions corresponding to isotopic abundancies and the probability of site occupancy. Note how the forbidden transitions modify the shape of the coupled next-nearest neighbour lines. The lines unaccounted for in (a) are thought to be produced by couplings with more distant $^{13}C$ nuclei.

separation of which is dependent on the defect effective spin. In the absence of other obscuring transitions these can be used to determine the effective spin.

- The large wings of either side of the central transition are produced by the interaction with a next-nearest neighbour $^{13}C$ nucleus and a nearest neighbour $^{13}C$ nucleus (termed $[V]^*_{11}$, and shown in Figure 6.20d).

- Combination of $[V]^*_{11}$ and $[V]^*_{10}$ is shown in Figure 6.20b. The forbidden transitions from $[V]^*_{10}$ serve to broaden to $[V]^*_{11}$ transitions.

- The wings inside the $[V]^*_{11}$ wings on the experimental trace Figure 6.20a are probably from interactions with more distant $^{13}C$ neighbours.

The line shapes in Figure 6.20 are not the characteristic first derivative shape expected for first harmonic detection of a field-modulated absorption signal, collected under conditions of slow passage. Reference to Figure 6.3 reveals that, in addition to the anomalous line shape, the high and low field lines have opposite phases. The

anomalous line shape, and changing phase behaviour arise from the anisotropic population of the different $m_s$ sublevels of the pentuplet in combination with small second order shifts in the positions of the otherwise coincident $m_s \leftrightarrow m_{s+1}$ transitions. The origin of the anisotropic population is discussed in §6.8.3. Without the second order hyperfine shifts the transitions in emission and absorption, corresponding to the various level populations, would cancel. In Figure 6.21 the EPR spectra for $\mathbf{B}\|[001]$ and $\mathbf{B}\|[110]$ have been simulated and compared with experimental spectra. The following assumptions were made:

- the level populations are as shown in the figure;
- the EPR transition intensities are proportional to the transition probability and the population difference between the levels; and
- the line shape is Lorentzian, and pseudomodulation [193, 194] has been applied to simulate the operation of the spectrometer.

The asymmetry between high and low field line widths and heights is caused by the inclusion of the octupolar crystal field splitting term, equation 6.3. This asymmetry is further evidence for the inclusion of this term with $a$=1 MHz. The effect of the term on the $[V]^*_{10}$ transitions is to change the line positions slightly, however, its magnitude is less than that of the second order hyperfine interaction.

The line shapes from the $[V]^*_{01}$ centres arise in the same way as for the $[V]^*_{10}$ centres, Figure 6.5. However, the line at $g$=2.0033(1) from the $[V]^*_{00}$ centre does not behave in the same manner. Because there is no hyperfine coupling to $^{13}C$ nuclei, there are no second order hyperfine shifts and the octupolar term becomes dominant. When the magnetic field is rotated in a (110) plane the EPR lines are strongest with $\mathbf{B}\|[001]$ and decrease in intensity as the field is rotated away, disappearing when $\theta \sim 30°$ because (i) the different $m_s$ states are equally populated, and (ii) the octupolar splitting tends to zero, hence the absorptive and emissive components cancel. On rotating further the populations of the $m_s$ states change such that the EPR transition would change phase, however, the octupolar effect has also produced a phase change. The signal

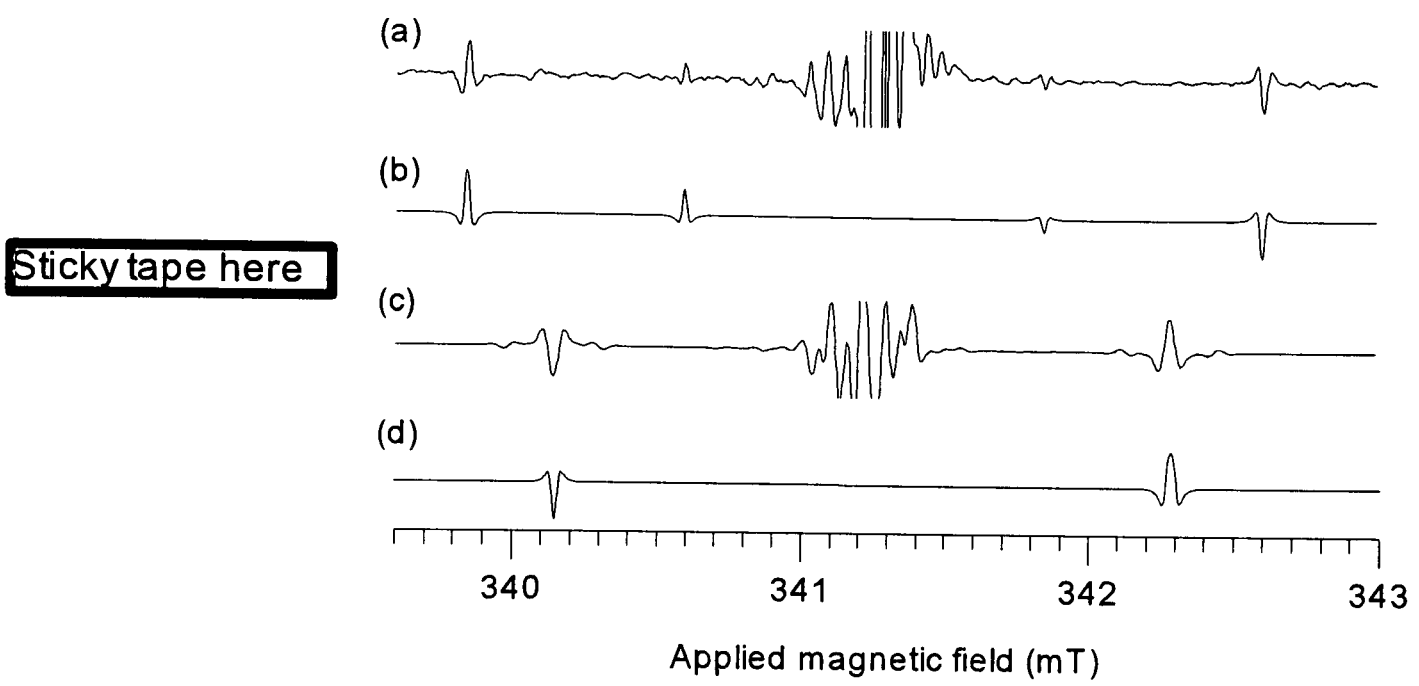



Figure 6.21: Simulated and experimental data for the $[V]^*_{10}$ centre. An octupolar interaction with $a$=1 MHz has been included which produces the asymmetry between the high and low field shapes and intensities. The populations of the pentuplet sublevels used in calculation of the line shapes are given on the left. The wings in the experimental traces are from the $[V]^*_{11}$ defect (see Figure 6.20). (a) and (b) are experimental and simulated spectra respectively with $\mathbf{B}\|[110]$. (c) and (d) are experimental and simulated spectra respectively with $\mathbf{B}\|[100]$.

therefore starts to increase but with the same phase as before, ie. it simply goes through a minimum.

### 6.8.3 Line shapes II - selective population of levels

Non Boltzmann spin populations have been reported in the $^3B_1$ state of the $F_2^{2+}$ centre in CaO [195] and the G9 and S1 centres in Si [196, 197] where the orientation dependent intensities of the EPR signals were ascribed to spin orbit mixing between states. The spin orbit coupling operator $\mathcal{H}_{so} = \sum_i \xi_i \hat{\mathbf{l}}_i \cdot \hat{\mathbf{s}}_i$ has rotational symmetry and in a $T_d$ system transforms as $T_1$. Taking the direct product with the $^5A_2$ state gives $A_2 \times T_1 = T_2$. The operator, $\mathcal{H}_{so}$, is linear in spin, hence the spin selection rule is $\Delta S = 0, \pm 1$. Mixing is therefore only possible with the $^3T_2$ state (§6.8.6), however despite its triplet nature EPR has not been observed, possibly because the lifetime is too short.

The orientation dependence of the interaction derives from the angular momentum operator. As the electrons orbit in a crystal field the possibility for quenching of various components of the angular momentum exists. If this, for example, occurs direction dependent mixing between states of differing spin projection is produced, and the $|m_s = \pm 1\rangle$ levels in $^5A_2$ can be coupled to other energy levels producing an orientation dependent preferential population and depopulation of the $|m_s = \pm 1\rangle$ levels within the $^5A_2$ manifold.

### 6.8.4 The electronic $g$-shift

Taken in isolation it would be expected that the angular momentum of the $^5A_2$ state would arise solely from spin angular momentum and the $g$-matrix would be isotropic with $g = g_e = 2.00232$. The measured deviation, $\Delta g = 0.0010(1)$ arises from a contribution of the orbital angular momentum from other excited states. As discussed above only $^3T_2$ is mixed with $^5A_2$ via the spin-orbit coupling. Similarly the $^4A_2$ ground state of $[V]^-$ contains an admixture of $^2T_2$ and has a small $g$-shift of $\Delta g = 0.0004(1)$. Lowther [198] uses this to estimate that the separation between the states is 2 eV. By analogy with Lowther's calculation a separation of about 1 eV between the $^5A_2$

and $^3T_2$ states is estimated here.

### 6.8.5 The unpaired electron and relaxation

A similar approach to that followed for the $[N–N]^+$ centre was adopted for the calculation of the electron distribution (see §3.4.1). This simple one-electron approach indicated that for the $^5A_2$ state of $[V]^0$ and the $^4A_2$ ground state of $[V]^-$ 75% and 85% of the unpaired spin density was located in the dangling orbitals of the four nearest neighbours respectively. For both centres the magnitude of the anisotropic part of the hyperfine interaction with the next-nearest neighbour $^{13}C$ atoms was consistent with predominantly dipolar coupling between the nucleus and the unpaired electron density in the dangling orbitals of the nearest neighbours. The value of 85% above for $[V]^-$ was calculated from the hyperfine parameters for the nearest neighbour $^{13}C$, measured by Isoya [164], using the calculated hyperfine interactions of Morton and Preston [95] (see §3.4.1). These give the hyperfine interaction for an electron localized in a carbon $2s$ orbital to be $a_0$=3777 MHz, and in a $2p$ to be $b_0$=107.4 MHz. Isoya used parameters given by Goodman and Raynor [199] which had values of $a_0$=3136 MHz and $b_0$=89.4 MHz and calculated a value of 103% for the unpaired spin density on the four nearest neighbours. This is therefore another area where the choice of theoretical parameters strongly influences the results (see also §5.6.3).

Following the method for estimating displacements of atoms from the hybridization ratio (§3.4.2), it was estimated that in the $^4A_2$ state of $[V]^-$ the nearest neighbours relax by about 0.05 Å and in the $^5A_2$ state of $[V]^0$ they relax by about 0.23 Å. In both cases the relaxation is outwards, with the dangling bond becoming more $p$-like. This is energetically favourable, there being no reason to have more $s$-nature to increase the bonding energy in a dangling bond (see Atkins p.271 [20]). In other words the material is becoming locally more graphite-like with the removal of a carbon atom. This result is at odds with the prediction of Mainwood [101] and casts doubt upon her calculation, though it might be possible that the next-nearest neighbours relax towards the vacancy more than the nearest neighbours, however it is not clear why this would happen. The hyperfine parameters of the next-nearest neighbours do sug-

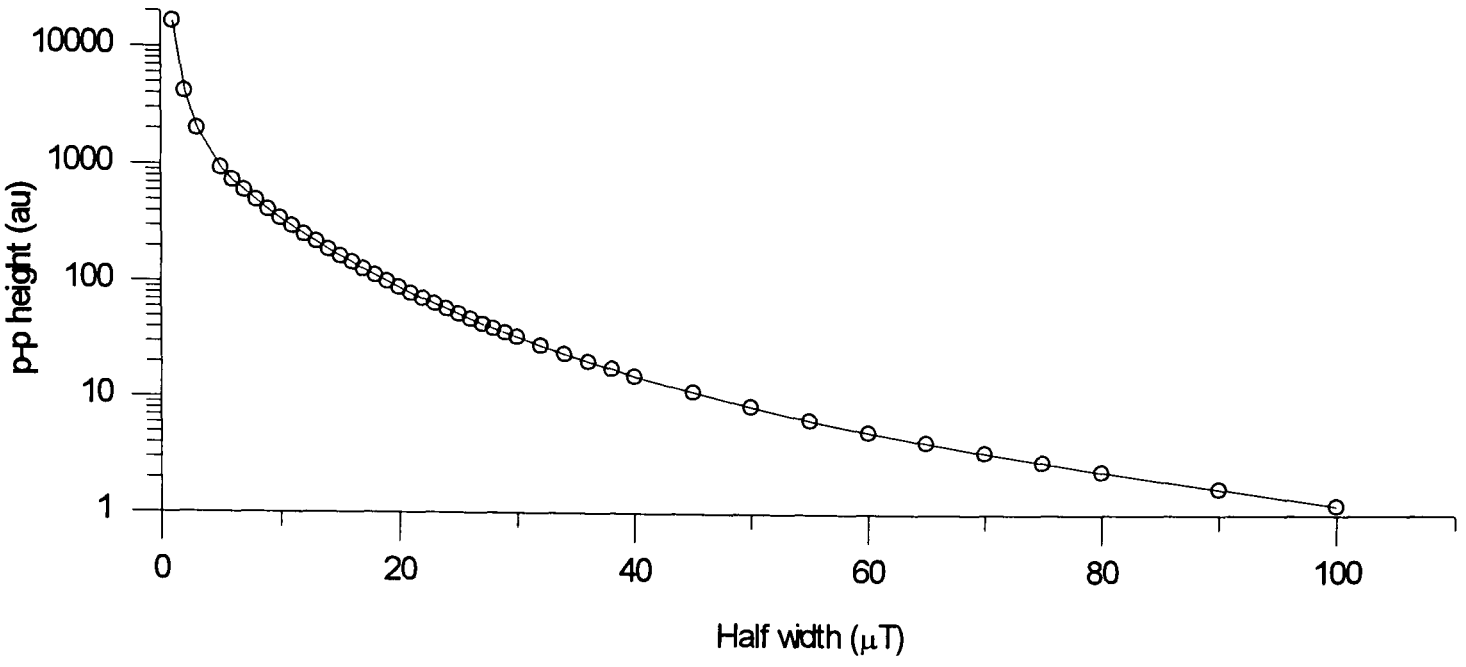



Figure 6.22: Calculated $[V]^*_{10}$ p-p height of the first derivative line as a function of line width. The individual lines in emission and absorption are beginning to be resolved below 5 $\mu$T and do not cancel, hence the rapid increase.

gest that there is little distortion, as well as very little localization of the unpaired electron density away from the vacancy.

### 6.8.6 Temperature dependence

The [V]* EPR signal strength exhibits a marked temperature dependence, with it increasing with decreasing temperature between 300K and about 100K, then remaining constant down to 4K. This is not a Curie Law dependence, neither is it that of a thermally excited state. If the $m_s$ level populations are determined by the spin-orbit coupling introducing selective de-excitation, then it would be expected that the relative populations, and hence EPR intensities, would be approximately temperature independent. An explanation of the dependence upon temperature is forthcoming if it is recognized that the EPR signal shape is a synthesis of closely spaced lines in emission and absorption. This suggests that the signal strength could depend strongly on the EPR line width. At helium temperatures the lifetime ($\tau_d$) and spin-lattice relaxation time ($T_1$) are both long ($T_1 \geq \tau_d$ in order to see lines in emission). It is therefore not possible for $T_1$ to determine the line width, but *lifetime* broadening is possible.

The EPR signal from the $[V]^*_{10}$ centre with $\mathbf{B}\|[001]$ was simulated as a function of line width and a strong dependence was observed (Figure 6.22). After estimation of a residual low temperature line width (caused by dipolar broadening, stress etc.) the line width of the component lines was calculated, interpolating between the points in Figure 6.22, as a function of temperature. The component line width as a function of reciprocal temperature is plotted in Figure 6.10b. At high temperatures an exponential behaviour was observed which can be modelled by an Arrhenius-type expression with an activation energy of about 40(5) meV. It is possible that, as the temperature rises, thermal excitation from the $^5A_2$ state to a higher short lived state occurs. If this explanation is correct then the $^5A_2$ state is placed close to another mid-gap state with a short lifetime, possibly $^1T_2$, which has an allowed dipole transition to the ground state. This effect is similar to that observed in diamond luminescence from the $S_3$ centre (ZPL at 2.496 eV) and centres with ZPL's at 2.082 eV and 2.052 eV [200, 201].

### 6.8.7 Lifetime and excitation energy dependence

The time taken for the $[V]^*$ EPR signal to decay on removal of uv light, and the time for the signal to grow to its equilibrium value on application of uv light were shown to be equal at 5K. The characteristic lifetime decreased with increasing microwave power and at vanishingly low microwave power was about 9 ms. A long radiative lifetime is expected because optical transitions to lower lying states are spin-forbidden and only gain intensity via spin-orbit coupling mixing of states. The measurements made here indicated that the lifetime was temperature independent up to 80K, however, a detailed study was not performed.

The lifetime behaviour can be explained by the following model. Assume that the $^5A_2$ state is created directly upon ionization of $[V]^-$, and decays to the ground state of the $[V]^0$, rather than by reconverting to $[V]^-$ by electron capture. Creation by ionization suggests that no Zeeman level should be preferentially populated, thus the unequal distribution within the pentuplet levels must be produced by a spin selective de-excitation. Selective mixing of the $^1T_2$ state into the different Zeeman levels of the pentuplet via the spin-orbit coupling could provide the required mechanism. In

Figure 6.21a for **B**||[110] it was presumed that the removal of electrons from the $m_s$=0 level occurred at a higher rate than from any other Zeeman level. The lifetime of the EPR signal upon removal of the uv excitation should depend on the decay rate out of this level, and on the microwave power. Similarly, the time taken to establish equilibrium on application of the light should be equal to the lifetime measured on removal of the light. This is based upon the assumption that the isotropic population of the $^5A_2$ state is created immediately upon illumination: the EPR can only be observed once a population difference between those states is established. The decay rate from the $[V]^*$ centre is therefore the limiting step. Since the recovery time of $[V]^-$ is much greater than the decay time of $[V]^*$ it is clear that the lifetime of $[V]^*$ is not determined by the vacancy electron capture rate.

The maximum reduction in $[V]^-$ achieved by illumination with uv light was 85–90%. The creation of $[V]^0$ centres in different excited states (which decay rapidly to the ground state avoiding the $^5A_2$ state) by $[V]^-$ loosing one of three $t_2$ electrons is possibly more likely than $[V]^-$ loosing one of two $a_1$ electrons to create $[V]^0$ in the $^5A_2$ state. Since the concentration of $^5A_2$ states cannot be measured, it is not possible to determine the fraction of $[V]^-$ centres ionized directly to the $^5A_2$ state. The disparity in decay and recovery times of $[V]^-$ is simply explained by the different mechanisms in action. Without illumination, an equilibrium number of $[V]^-$ and $[V]^0$ centres is eventually reached which depends upon the number of electron donors and traps in the sample. On illumination with uv light $[V]^-$ centres are ionized, with some of the electrons immediately recombining with $[V]^0$ centres, and some being captured by other traps. In addition to the destruction of $[V]^-$ centres others are also created in the process. A new dynamic equilibrium is finally reached with fewer $[V]^-$ centres and more $[V]^0$ centers plus other traps which have captured an electron. When the light is removed the electrons tunnel or hop back to $[V]^0$ centres from the electron traps and the original equilibrium is restored. The recovery of $[V]^-$ is much slower than the original decay because the limiting factor is the lifetime of the traps.

The single substitutional nitrogen centre $[N\text{–}C]^0$ shows a similar behaviour to the $[V]^-$ centre upon illumination. The maximum reduction of $[N\text{–}C]^0$ achieved with the

100 W Hg lamp was about 80%. The decay and recovery times were longer than those for $[V]^-$. The $[N–C]^0$ centre is known to be an electron donor capable of converting $[V]^0$ to $[V]^-$. It is presumed that on illumination with uv light, $[N–C]^0$ is ionized to $[N–C]^+$ with the extra electron being captured by a trap. The final trap is not a $[V]^-$ centre as the number of $[V]^-$ centres does not increase. The decay and recovery in the number of $[V]^-$ and $[N–C]^0$ centres both fit to single exponential functions. This is in marked contrast to the results on the $[N–N]^+$ centre where the EPR signal decayed linearly with the logarithm of time on removal of the excitation (§5.5.4).

The discussion above has centred on the time resolved results collected with the full spectrum of the mercury lamp. This spectrum is peaked strongly at the uv end of the spectrum. In §6.5.6 time resolved measurements at different wavelengths for the $[V]^-$ centre were reported. These showed that the equilibrium concentration of $[V]^-$ is dependent upon the illumination wavelength (Figures 6.14 and 6.13). Four points of interest resulted from the investigation:

i The effect of 436 nm photons, in an initial application after the sample had been kept in the dark at room temperature, differed at 5K and room temperature.

ii The magnitude and rate of the decay and recovery induced by 364 nm photons was much larger and faster than that from less energetic photons.

iii An additional slow recovery, after quenching, was observed at room temperature.

iv Each wavelength re-set the system to a specific concentration of $[V]^-$ centres.

All decays were still much slower than the $[V]^*$ decay. The difference in the effect of 436 nm (2.85 eV) photons at room temperature and 5K can be explained in terms of thermally activated hopping and tunneling to centres (traps) ionized by the light. The hopping would have *frozen out* by 5K. The slower decays or recoveries indicate the establishment of a new equilibrium with the ionization of traps or donors other than $[V]^-$and subsequent tunnelling (5K and room temperature) or hopping (room temperature) and tunnelling. The rapid response to the 364 nm (3.4 eV) light must indicate a reaction involving the $[V]^-$ centre directly.

## 6.9 Conclusions

In this chapter it has been demonstrated that the new centre observed on illumination with uv light is the $^5A_2$ state of the neutral vacancy. The unpaired electron, with an effective spin of two, is predominantly located in the carbon dangling orbitals of the vacancy. The EPR line shape is produced by a combination of second order shifts in the positions of transitions between different $m_s$ states and the anisotropic population of the different states. The electronic $g$-shift is satisfactorily explained by spin-orbit coupling mixing the $^3T_2$ state into $^5A_2$. The separation of the two levels is estimated to be about 1 eV. Lifetime broadening of the EPR line width can be modelled with an Arrhenius-type expression having an activation energy of 40(5) meV. The reason for the centre's creation in this sample, but not many others, is not yet understood.

This is the first time ENDOR of an optically excited state has been performed in diamond, and methods for measuring optical effects by means of magnetic resonance have been demonstrated. The first ENDOR measurements on a state of the neutral vacancy, which had only been observed using optical techniques, have been performed and the Coulson-Kearsley model has been shown to describe the system.

## 6.10 Further work

The investigation into the $[V]^*$ centre presented here has highlighted a number of further experiments that may be performed in order to gain a greater insight into the creation and properties of the excited state of the neutral vacancy. Some of these are listed below.

- A detailed study of the temperature dependence of the lifetime can give insight into the nature of the couplings between the states of the vacancy.
- Determination of sector dependence of $[V]^*$ state will yield information on the position of the Fermi surface needed to form this centre. Remember that the sample studied here consisted of two zones with different $[V]^-$ concentrations.

- Spectroscopy of the other $^{13}C$ lines will yield more information regarding the environment of the vacancy and its effect on the lattice. This should be possible with the use of a more powerful illumination source to improve the signal-to-noise ratio for ENDOR.

- Using optically detected EPR (ODMR), it might be possible to detect the decay luminescence from or associated with the $^5A_2$ state. This technique can also be used to investigate the possibility of spin-dependent interdefect electron transfer between $[V]^-$ and $[V]^*$ similar to that associated with the vacancy in GaP (see Omling *at al.* [202]).

- Use of a narrow-band illumination source, and detailed mapping of the wavelength dependence, could lend insight into the creation mechanism.

- A new theoretical study of the system should be performed to model the experimental data (relaxation, electron distribution, population inversion), and to correct for the inadequacies in the previous theoretical analyses.

# Chapter 7

# W11–W14

## 7.1 Introduction

In this chapter work on the radiation damage defects in type Ib diamond labelled W11–W14 is reported. Knowledge of the effective spin of any paramagnetic defect is vital for the determination of its structure. In this case determination of the effective spin of the defects had been hampered by the complexity of the spectra in the $g$=2 region. The work herein aimed at resolving this problem by employing two mechanisms that rely on transitions well clear of the complicated $g$=2 zone. The first method examined the effect of Boltzmann depopulation upon the populations within a spin multiplet; the second used spectroscopy of partially *forbidden* transitions between levels with $\Delta m_s > 1$.

An additional benefit of the Boltzmann depopulation technique was its facilitation of the measurement of the absolute sign of the fine structure interactions in W11–W14, and R1 radiation damage defects. This knowledge yields information on the nature of the interactions between the electrons in the system. This was the first time that the Boltzmann depopulation technique had been applied to defects in diamond.

The chapter begins by summarizing previous work on the W11–W14 system, and then examines the different methods of effective spin determination. In the discussion it is shown that the results for W11–W13 were as expected from theory, however, W14 differed strikingly from its expected Boltzmann depopulation values. Reasons for this

discrepancy are explored.

The definitive answer to the question of the effective spins of the defects was not obtained and further work is required to confirm some of the initial measurements and subsequent analyses. Experiments to this effect are discussed in §7.8. The discussion of the R1 system is deferred until Chapter 8.

## 7.2 Previous work on W11–W14

The W11–W14 centres are so named as they were the $11^{th}$, $12^{th}$, $13^{th}$ and $14^{th}$ EPR centres to be classified at the University of the Witwatersrand, South Africa.[1] The centres were reported by Loubser and van Wyk in 1978 [190] and subsequently at Diamond Conferences in 1987, 1989 and 1991 [203, 204, 205]. The work in this chapter was initiated in response to these presentations. It was performed in 1992 and presented at the Diamond conference and at the meeting of the International EPR society in 1993 [206, 207]. van Wyk published on the centres in 1994 [208]. In the paper he reported the following:

1. The centres were found in electron or neutron irradiated type Ib diamonds (nitrogen concentration typically ~200 ppm.).

2. The centres become detectable for either electron or neutron doses[2] around $1.0 \times 10^{17}$ cm$^{-2}$. The samples worked on usually received doses between $5.0 \times 10^{17}$ cm$^{-2}$ and $5.0 \times 10^{18}$ cm$^{-2}$ independent of the type of irradiation.

3. The centres anneal out at different temperatures: W11 between 250°C and 300°C, W12 and W13 just under 400°C, and W14 just above 400°C.

4. The data were fitted using the following Hamiltonian:

$$\mathcal{H} = \mu_B \mathbf{B} \cdot \underline{\mathbf{g}} \cdot \hat{\mathbf{S}} + \hat{\mathbf{S}} \cdot \underline{\mathbf{D}} \cdot \hat{\mathbf{S}} \tag{7.1}$$

[1] As the structure of the defects is still not known it is not possible to adopt the usual structurally motivated notation employed thus far in this thesis.

[2] Energy not given.

with $S$=1, in accord with radiation damage defects in type IIa diamonds [209], however, the quality of fit was low. As the centres of the spectra (around $g$=2) were complicated, it was not possible to verify the presence or absence of the transitions between $|\pm\frac{1}{2}\rangle$ which would identify the effective spins as $S$=$\frac{3}{2}$. However, when $S$=$\frac{3}{2}$ was assumed the quality of fit of the outer transitions to equation 7.1 increased. The fitted results are given in Table 7.1.

5. The R1 system was fitted, with $S$=1, as a check on the results and a small deviation from the isotropic $g$-value was found.

6. After annealing until only W14 remained, a set of lines was found near $g$=2.0 which was assigned to $m_s = \frac{1}{2} \rightarrow -\frac{1}{2}$ transitions in W14. This was taken as additional evidence that $S$=$\frac{3}{2}$.

7. W12, W13 and W14 did not fit as well as W11 and R1.

8. The transitions from W13 defects observed when rotating in the {110} plane normal to the {110} plane containing the principal axis of the fine-structure coupling tensor, varied in intensity as a function of angle from the ⟨110⟩ direction.

van Wyk presented possible models for the centres and pointed out that, when considering models, the following facts should be considered:

1. The centres were only observed in diamonds containing large concentrations of isolated substitutional nitrogen ($[N–C]^0$).

2. The electron spin was $\frac{3}{2}$, implying that three electrons are unpaired.

3. W11–W14 anneal out well below 450°C. Any model proposed must therefore involve an entity that becomes mobile between 250°C and 450°C.

4. Annealing studies showed that, as the less stable of the defects annealed out, increases in the concentrations of the remaining centres occurred. This suggested the possibility that, in the annealing process, the constituents of the defects are rearranged, leading to a conversion of one defect into another.

Table 7.1: Spin Hamiltonian parameters and direction cosines (with respect to the cube axes {[100],[110],[111]}) of principal axes of W11–W14 centres using $S=\frac{3}{2}$. Values of $D$ are given in MHz.

| | $g$-tensor | | $D$-tensor | |
|---|---|---|---|---|
| | value | dir. cosine | value | dir. cosine |
| W11 | $g_x = 2.0022$ | ‖( 0.3508,-0.2830, 0.8927) | $D_x =$ -241.33 | ‖( 0.0226, 0.6651, 0.7464) |
| | $g_y = 2.0022$ | ‖(-0.5484,-0.8348,-0.0491) | $D_y =$ -199.61 | ‖( 0.7135, 0.5123,-0.4780) |
| | $g_z = 2.0022$ | ‖(-0.7591, 0.4723, 0.4480) | $D_z =$ 440.94 | ‖( 0.7003,-0.5434, 0.4630) |
| W12 | $g_x = 2.0043$ | ‖(-0.8072, 0.5459,-0.2245) | $D_x =$ -143.61 | ‖(-0.4001, 0.3765, 0.8356) |
| | $g_y = 1.9970$ | ‖( 0.5840, 0.6832,-0.4384) | $D_y =$ -338.25 | ‖( 0.6721, 0.7403,-0.0118) |
| | $g_z = 1.9989$ | ‖( 0.0859, 0.4850, 0.8703) | $D_z =$ 481.86 | ‖( 0.6231,-0.5569, 0.5492) |
| W13 | $g_x = 1.9984$ | ‖( 0.0000, 0.7071, 0.7071) | $D_x =$ -193.00 | ‖( 0.0000, 0.7071, 0.7071) |
| | $g_y = 1.9972$ | ‖( 0.7804,-0.4421, 0.4421) | $D_y =$ -309.07 | ‖( 0.6686, 0.5258,-0.5258) |
| | $g_z = 2.0037$ | ‖( 0.6252,-0.5518, 0.5518) | $D_z =$ 501.07 | ‖( 0.7436,-0.4728, 0.4728) |
| W14 | $g_x = 1.9976$ | ‖( 0.0000, 0.7071, 0.7071) | $D_x =$ -346.98 | ‖( 0.0000, 0.7071,-0.7071) |
| | $g_y = 1.9954$ | ‖( 0.8208,-0.4040,-0.4040) | $D_y =$ -194.11 | ‖( 0.7960,-0.4280,-0.4280) |
| | $g_z = 2.0037$ | ‖( 0.5713,-0.5804,-0.5804) | $D_z =$ 540.09 | ‖( 0.6053,-0.5629,-0.5629) |

Parameters from reference [210]. No uncertainties given.

5. The W-centres were present in larger amounts than the R1 centre, but smaller than P1.

He presented three possible models. The simplest involved the capture of an electron by a neutral vacancy to make a negative vacancy. The negative vacancy would have to be perturbed, possibly by a nearby nitrogen atom, which would lower the symmetry from $T_d$ allowing a zero-field splitting to occur. The next model postulated one or more interstitial atoms to be trapped near the vacancy, however, it was not clear how the arrangement would be stable, or why it did not occur in type Ia diamonds. The final possibility proposed was the formation of a $C_i^-$–$[N–C]^+$ pair, that is a charge transfer between an interstitial carbon and an $[N–C]^0$ defect. Unbonded $C_i^-$ would have the correct $2p^3$ valence state which would give rise to a $^4S$ state with $S=\frac{3}{2}$.

Lowther and van Wyk [198] investigated the effect of distorting the negative vacancy theoretically and found that it is possible to produce a zero-field splitting

Table 7.2: Comparison of methods of effective spin determination in continuous wave EPR for $S$=1 and $S$=$\frac{3}{2}$ in a system having a fine structure splitting, but no resolved hyperfine interaction.

| Method | Tran | Advantages | Disadvantages |
|---|---|---|---|
| Allowed transitions | O,C | direct method | central transitions often obscured |
| Second order shifts | O | does not rely on observation of central transition | requires very accurate measurement in many field directions |
| Boltzmann depop. | O | does not rely on observation of central transition<br>yields sign of $D$-tensor<br>yields information on excited states | requires high EPR frequencies (35 GHz) and low temperatures (pumped helium)<br>can be complicated by nearby energy levels<br>can not measure excited states which depopulate |
| Forbidden transitions | $\frac{1}{2}$,$\frac{1}{3}$ | clear of complicated allowed transitions<br>not influenced by doublets<br>observation of third field transitions unambiguously identifies triplet<br>more sensitive to $g$-anisotropy | must work at low microwave frequencies to increase state mixing<br>transitions are weak |

O – outer transitions
C – central transitions
$\frac{1}{2}$,$\frac{1}{3}$ – half and third field transitions

through the mixing of the negative vacancy molecular states by a spin-orbit interaction.

## 7.3 Methods of effective spin determination

Various methods of effective spin determination in a continuous wave experiment are compared in Table 7.2 and are described in sections 7.3.1 to 7.3.2.

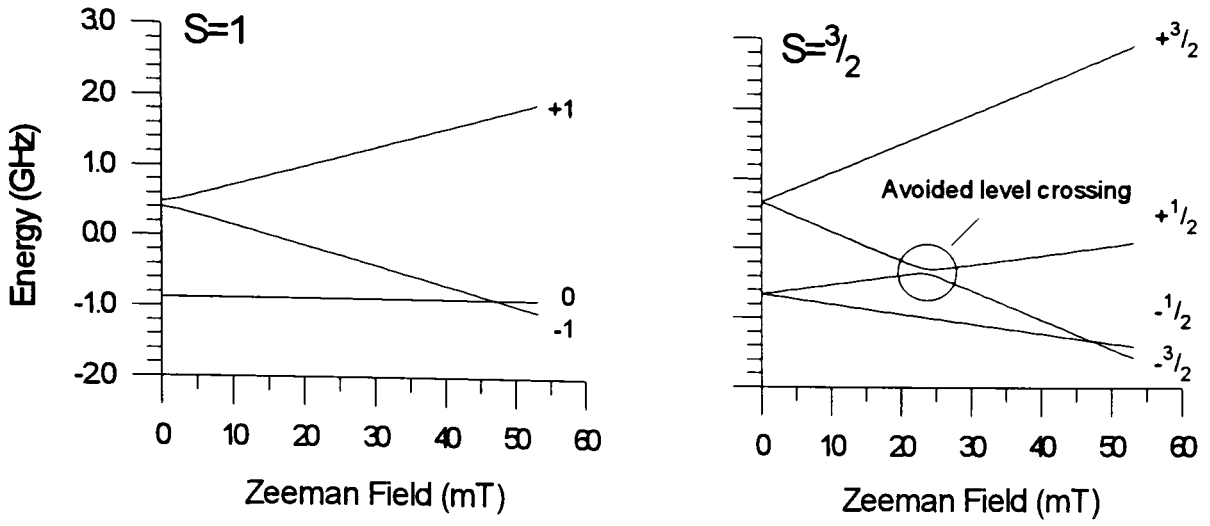



Figure 7.1: Calculated energy levels for the W11 centre, assuming $S$=1 and $S$=$\frac{3}{2}$. The Zeeman field is aligned along $\langle 111 \rangle$.

### 7.3.1 $S$=1 and $S$=$\frac{3}{2}$ energy levels

In the absence of a nuclear hyperfine interaction, with a symmetry lower than cubic, and an effective spin of $S$=1 or $S$=$\frac{3}{2}$, the spin Hamiltonian is written:

$$\mathcal{H} = \mu_B \mathbf{B} \cdot \underline{\mathbf{g}} \cdot \mathbf{S} + \mathbf{S} \cdot \underline{\mathbf{D}} \cdot \mathbf{S} \tag{7.2}$$

When the external magnetic field is applied along $\hat{\mathbf{z}}$, the energy levels can be expressed in closed form. The Hamiltonian then reduces to:

$$\mathcal{H} = g_z \mu_B B \hat{S}_z + D\left\{\hat{S}_z^2 - \tfrac{1}{3}\hat{S}(\hat{S}+1)\right\} + E(\hat{S}_x^2 - \hat{S}_y^2) \tag{7.3}$$

where $D$ and $E$ are defined as in equation 3.12, acknowledging that there are only two independent parameters in the fine structure tensor. For $S$=1 the energy levels are:

$$\begin{aligned} \epsilon_{+1} &= \langle +1|\mathcal{H}|+1\rangle &&= +\tfrac{1}{3}D + \sqrt{G^2+E^2} \\ \epsilon_{0} &= \langle 0|\mathcal{H}|0\rangle &&= -\tfrac{2}{3}D \\ \epsilon_{-1} &= \langle -1|\mathcal{H}|-1\rangle &&= +\tfrac{1}{3}D - \sqrt{G^2+E^2} \end{aligned} \tag{7.4}$$

where $G = g_z \mu_B B$, and for $S$=$\frac{3}{2}$ the energy levels are:

$$\begin{aligned} \epsilon_{\pm\frac{3}{2}} &= \langle \pm\tfrac{3}{2}|\mathcal{H}|\pm\tfrac{3}{2}\rangle &&= \pm\tfrac{1}{2}G + \sqrt{(D \pm G)^2 + 3E^2} \\ \epsilon_{\mp\frac{1}{2}} &= \langle \mp\tfrac{1}{2}|\mathcal{H}|\mp\tfrac{1}{2}\rangle &&= \pm\tfrac{1}{2}G - \sqrt{(D \pm G)^2 + 3E^2} \end{aligned} \tag{7.5}$$

Note that the nomenclature $|m_s\rangle$ is only a correct description of the states in the limit of a strong magnetic field. It is however helpful to think of states in terms of the high field eigenstates. The energy level manifolds, calculated using the parameters of the W11 centre, are plotted in Figure 7.1 for both the $S$=1 and $S$=$\frac{3}{2}$ cases. The manifolds have been plotted for applied magnetic fields below 60 mT to show the structure produced by the inclusion of the $D$ and $E$ terms. The larger the $E$-term the larger the separation at the avoided level crossing, and between the $|+1\rangle$ and $|-1\rangle$ levels at zero-field. The $D$-term produces the zero-field splitting between the doublet and singlet ($S$=1), or the two doublets ($S$=$\frac{3}{2}$). Note that if the signs of the components of the tensor are inverted, the order of the doublet and singlet, and that of the two doublets, in Figure 7.1 is reversed. In the figure the values of the components of the $D$-tensor have been modified in the $S$=1 case to produce the same transition fields, to first order, as for the outer lines of the magnetic resonance spectrum obtained in the $S$=$\frac{3}{2}$ case. However, despite having the same separation between energy levels with $\Delta m_s = 1$, comparison of the two cases reveals that the separation between the lowest and highest levels is greater for $S$=$\frac{3}{2}$.

### Allowed transitions: Full spectrum

When the full spectrum of allowed ($\Delta m_s = 1$) transitions is observable the triplet system produces two EPR lines separated by approximately $2D$ (assuming $E$ to be small) centred on the $g$-value of the system, while the quadruplet produces a third EPR line at the $g$-value. Thus if the third line can be observed, and distinguished from transitions arising from spin doublets, the system can be identified as a quadruplet.

### Allowed transitions: Second order effects

To first order, assuming that the system has axial symmetry[3] the transition $m_s \leftrightarrow m_s - 1$ occurs at:

$$h\nu = g\mu_B B + D''(m_s - \tfrac{1}{2}) \tag{7.6}$$

[3]Following the analysis of Abragam and Bleaney, p.157ff [91].

where $D''$ has the angular dependence:

$$D'' = D\left\{\frac{3g_{\|}^2}{g^2}\cos^2\theta - 1\right\} \tag{7.7}$$

and $\theta$ is the angle subtended by the Zeeman field and the $z$-axis in the $xz$-plane. Examination of equations 7.6 and 7.7 reveals that, as long as $D$ is scaled accordingly, there will be no difference in the angular behaviour of a $S$=1 and a $S$=$\frac{3}{2}$ system. The off diagonal terms in the energy matrix, however, introduce small shifts in the energy levels which produce corresponding shifts in the lines. To account for this the following has to be added to equation 7.6:

$$\begin{aligned}&\left(\frac{g_{\|}^2 g_{\perp}^2}{g^4}\right)\left(\frac{D^2\cos^2\theta sin^2\theta}{2G}\right)\underbrace{\{24m_s(m_s-1)+9-4S(S+1)\}}_{\mathsf{A}}\\ &+\left(\frac{g_{\perp}^4}{g^4}\right)\left(\frac{D^2\sin^4\theta}{8G}\right)\underbrace{\{2S(S+1)-6m_s(m_s-1)-3\}}_{\mathsf{B}}\end{aligned} \tag{7.8}$$

For an $S$=1 system the terms labelled A and B are both 1, while for $S$=$\frac{3}{2}$ A=12 and B=0. These introduce additional angular dependencies, of the order of $D^2/G$, into the angular variation. If the quality of the measurement is good enough it is possible to discriminate between the different dependencies upon fitting the angular variation of the outer lines.

### Allowed transitions: Boltzmann depopulation

Allowed magnetic resonance transitions occur when $\Delta m_s = 1$. The number of transitions per second between levels of energy $\epsilon_i$ and $\epsilon_j$ induced by an oscillatory field of amplitude $B_1$, angular frequency $\omega$, normal to the Zeeman field is:[4]

$$\omega_{ij} = \frac{\pi B_1^2}{2\hbar^2}|\mu_{ij}|^2 f(\omega), \tag{7.9}$$

where $|\mu_{ij}|^2$ is the square of the magnetic dipole matrix element between states $i$ and $j$. The *shape function* $f(\omega)$ is a function of the applied frequency $\omega$, the resonance

[4]After [91], p.119.

frequency $\omega_0$, and a parameter describing line width [91]. The net absorption of energy per second is:

$$\frac{dW}{dt} = \omega_{ij}(\hbar\omega)(N_i - N_j), \tag{7.10}$$

where $N_i$ is the population of the lower state, $N_j$ that of the upper state. Assuming that the spin lattice relaxation time is short enough for the Boltzmann distribution to be preserved, the line intensities will be proportional to the thermal equilibrium populations of the states. The population of a state is then given by:

$$\frac{N_i}{N} = \frac{e^{-\varepsilon_i(B,T)}}{\mathcal{Z}(B,T)} \tag{7.11}$$

where $\mathcal{Z}$ is the canonical partition function, $N$ the total number of spins, and $\varepsilon_i$ is related to the energy of the state, all defined below:

$$\mathcal{Z}(B,T) = \sum_{l=1}^{n} e^{-\varepsilon_l(B,T)} \tag{7.12}$$

$$N = \sum_{l=1}^{n} N_l \tag{7.13}$$

$$\varepsilon_i(B,T) = \epsilon_i(B)/kT \tag{7.14}$$

with $k$ Boltzmann's constant and $n$ the number of energy levels. Combination of equations 7.10 and 7.11, noting that the energy of each level is a function of the Zeeman field, gives the intensity of a particular transition when $\omega_{ij}$ is assumed constant:

$$I_{i\leftrightarrow j}(B,T) \propto \frac{e^{-\varepsilon_i(B,T)} - e^{-\varepsilon_j(B,T)}}{\mathcal{Z}(B,T)} \tag{7.15}$$

Thus the observed ratio of the intensities of transitions between different levels within the same manifold should equal the ratio of intensities calculated from equation 7.15.

It is possible to achieve a physical feel for the results if it is assumed that:[5]

$$\mathcal{Z}(B_1) \approx \mathcal{Z}(B_2)$$

[5]Labelling the transitions 1 and 2.

and:

$$\epsilon_i - \epsilon_{i+1} \approx \delta \ \forall \ i \text{ st } 0 < i < n-1$$

Also note that the energy separation at resonance equals the microwave quantum: $\delta(B_{\text{res}}) = h\nu$. The ratios of the transition intensities then reduce to:

$$\frac{I_{(0\leftrightarrow 1)}}{I_{(-1\leftrightarrow 0)}} \propto e^{h\nu/kT} \tag{7.16}$$

$$\frac{I_{\left(\frac{1}{2}\leftrightarrow\frac{3}{2}\right)}}{I_{\left(-\frac{3}{2}\leftrightarrow-\frac{1}{2}\right)}} \propto e^{2h\nu/kT} \tag{7.17}$$

Thus, when the logarithm of the intensity ratio between the high and low field transitions is plotted against inverse temperature, the gradient arising from a quadruplet system should be near to twice that arising from a triplet system. It is often possible to use equations 7.16 and 7.17. Their validity depends on ratio of the partition function at the two fields. Thus for the ratio of the high field to low field line the correction factor by which equation 7.17 should be multiplied is:

$$\mathcal{C} = \frac{\mathcal{Z}(B_2)}{\mathcal{Z}(B_1)} \tag{7.18}$$

This depends in the size of the energy level separation compared to the temperature and on the separation in field between the high and low field transition as shown in Figure 7.2.

### 7.3.2 Half and third field transitions

Half and third field transitions occur when there is a non-zero matrix element between states differing in spin projection by more than one. If the simplification of axial

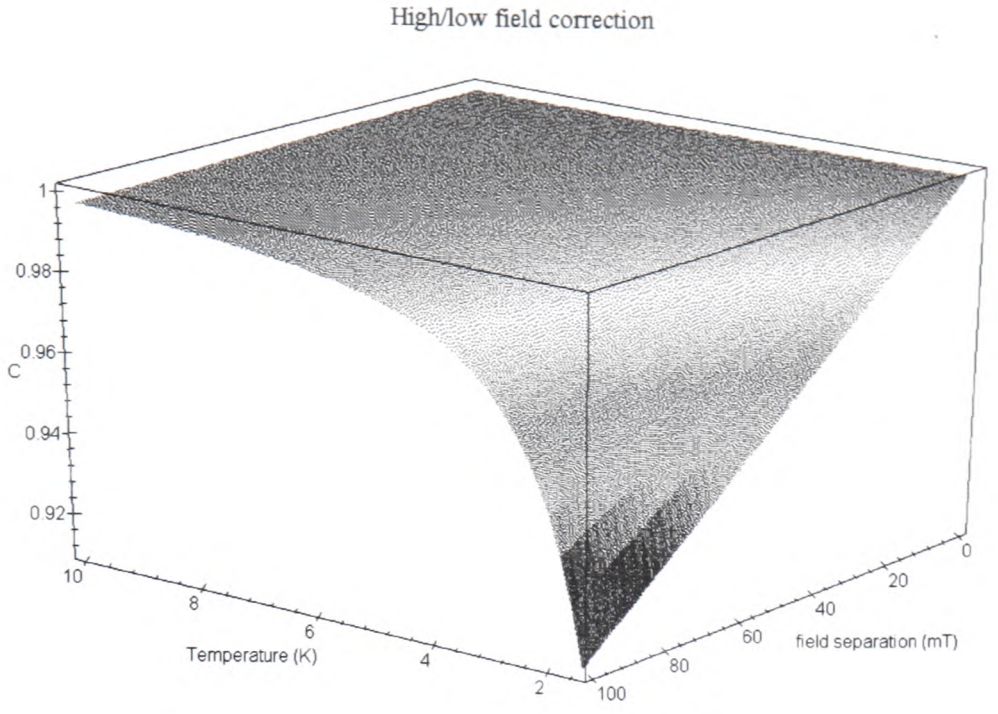



Figure 7.2: The effect of inclusion of the partition function in the calculation of the intensity ratio of high to low field transitions. The correction factor (equation 7.18) is plotted as a function of temperature and the separation of the high and low field EPR transitions, for a microwave frequency of 33 GHz, $S=\frac{3}{2}$.

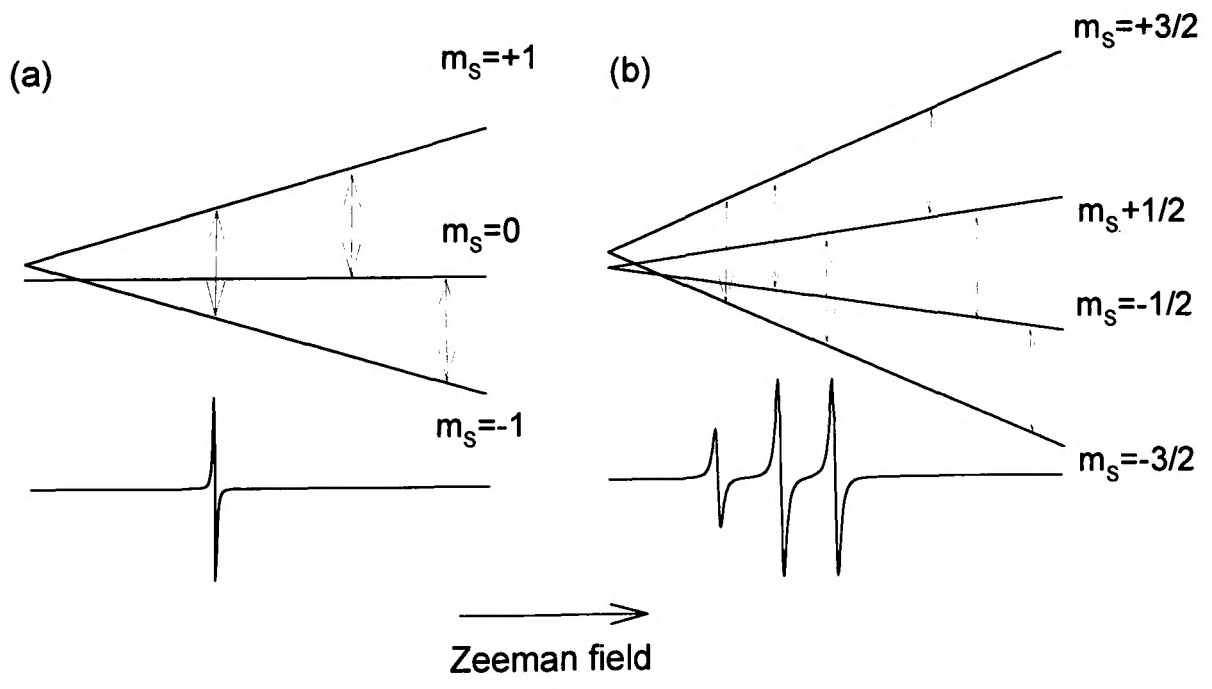



Figure 7.3: Schematic energy levels and transitions for (a) a triplet and (b) quadruplet state showing the occurence of half and third field $\Delta m_s$=2 and $\Delta m_s$=3 transitions. The allowed transitions are shown with broken arrows.

symmetry is invoked the energy differences from equations 7.4 and 7.5 become:

$$\left.\begin{aligned} \epsilon_1 - \epsilon_0 &= G + 2D \\ \epsilon_0 - \epsilon_{-1} &= G - 2D \end{aligned}\right\} \Delta m_s = 1$$
$$\left.\begin{aligned} \epsilon_1 - \epsilon_{-1} &= 2G \end{aligned}\right\} \Delta m_s = 2$$

$$\left.\begin{aligned} \epsilon_{\frac{3}{2}} - \epsilon_{\frac{1}{2}} &= G + 2D \\ \epsilon_{\frac{1}{2}} - \epsilon_{-\frac{1}{2}} &= G \\ \epsilon_{-\frac{1}{2}} - \epsilon_{-\frac{3}{2}} &= G - 2D \end{aligned}\right\} \Delta m_s = 1 \qquad (7.19)$$
$$\left.\begin{aligned} \epsilon_{\frac{3}{2}} - \epsilon_{-\frac{1}{2}} &= 2G + 2D \\ \epsilon_{\frac{1}{2}} - \epsilon_{-\frac{3}{2}} &= 2G - 2D \end{aligned}\right\} \Delta m_s = 2$$
$$\left.\begin{aligned} \epsilon_{\frac{3}{2}} - \epsilon_{-\frac{3}{2}} &= 3G \end{aligned}\right\} \Delta m_s = 3$$

Observe that the $\Delta m_s = 2$ transitions have a dependence of $2G$ on the Zeeman interaction, while for $\Delta m_s = 3$ it is $3G$. A $\Delta m_s = 1$ transition has a dependence of $1G$. To satisfy the requirement for resonance the $\Delta m_s = 2, 3$ transitions therefore have to occur at roughly one half and one third the normal resonance field, as illustrated in Figure 7.3. The multiplier of 2 or 3 magnifies the effect of $g$-anisotropy facilitating more accurate measurement than in the allowed transition case. In addition, for the triplet state the half field transitions are independent of the zero-field splitting, while for the quadruplet state only the third field transitions are independent. This gives another method of discrimination between the triplet and quadruplet states. The transitions have the additional advantage of being offset from the complicated central region of the spectrum and are often simpler owing to the absence of contributions from defects with $S{=}\frac{1}{2}$, and no third field transitions for $S{=}1$.

### 7.3.3 Thermally populated excited states

A thermally populated excited state can be identified from depopulation measurements in a similar manner to that used to discriminate between quadruplet and triplet states. In this experiment an excited state was identified by comparison of its intensity with that of a ground state defect, as a function of temperature. Equation

7.11 can once again be employed to define the population of a specific state. For an excited state, the ground state at energy $\epsilon_0$ is simply added to the ensemble and the intensities of transitions from the centres are given by equation 7.15. The energy of the excited state can then be calculated by performing a non-linear regression on the ratio of the intensities, solving for $\epsilon_0$. A rough idea of the temperature dependence can be obtained by approximating the full distribution with that of a two level Boltzmann distribution, yielding:

$$\frac{\text{Intensity of excited state defect}}{\text{Intensity of ground state defect}} \propto e^{-\Delta/kT} \tag{7.20}$$

where $\Delta$ is the separation between the ground and excited states of the defect.

## 7.4 The sample

The crystal was a synthetic type Ib (that is containing a high concentration of isolated nitrogen ~200 ppm.) and had been neutron irradiated receiving a dose of $\sim 10^{18}$ cm$^{-2}$. The sample had been examined by van Wyk (§7.2) and the history is not fully known, however judging by the strength of the W11, W13 and R1 centres it would appear that it has not been annealed.

## 7.5 Experimental techniques

The experiments were performed at Q-band and X-band. Q-band has the advantage of a larger microwave quantum than X-band ($\nu \sim 33$ GHz as opposed to $\nu \sim 9$ GHz). The Q-band microwave quantum has an equivalent temperature of $\frac{h\nu}{k} = 1.58$K, with $k$ the Boltzmann constant, as opposed to 0.43K for X-band. Q-band was therefore chosen to make Boltzmann depopulation measurements, as a significant and observable fractional depopulation can be achieved when working with pumped helium at 1.5K. The Q-band assembly for these measurements is described in §4.2. The sample was X-ray aligned, using Laue back scattering, and mounted in araldite adhesive with $[1\bar{1}0]$ vertical, facilitating rotation in the $(1\bar{1}0)$ plane.

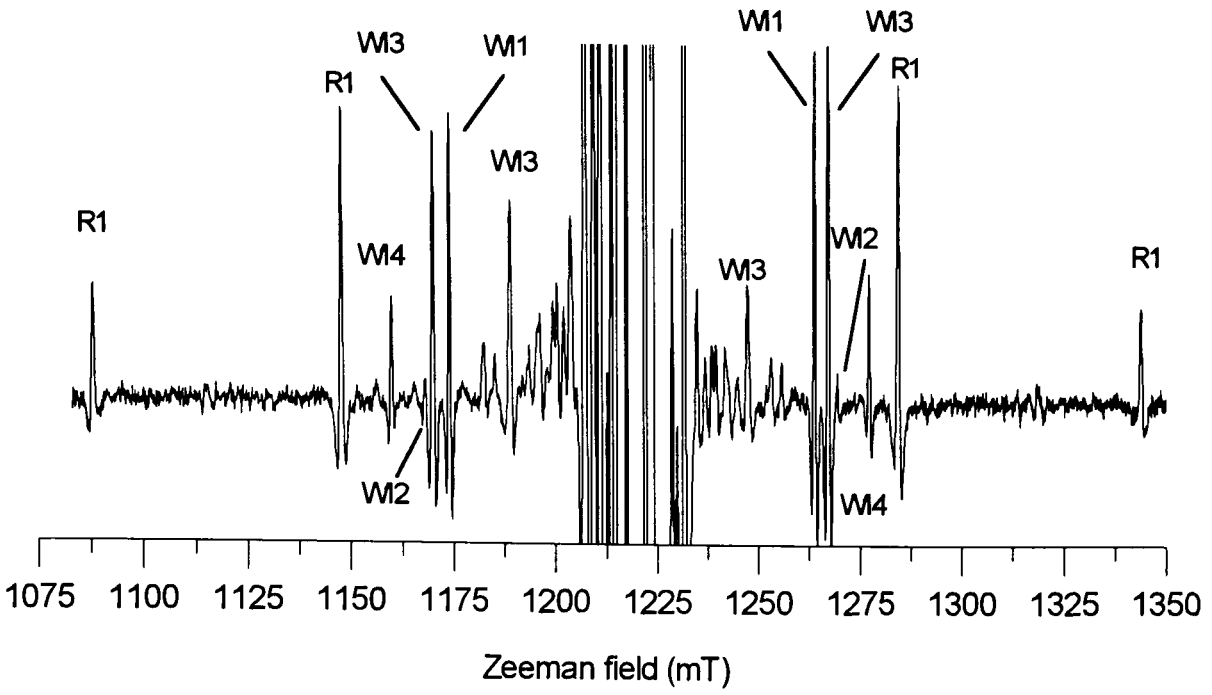



Figure 7.4: Q-band experimental spectrum with $\mathbf{B}\|\langle 111\rangle$, T=10K. The intensity differences between corresponding low and high field lines from the same defect are a product of the depopulation of the energy levels.

At X-band the spacing between the Zeeman energy levels, $\sim h\nu$, is less than at Q-band. As a result there is a greater mixing between the spin projection eigen states and the previously forbidden $\Delta m_s = 2$ transitions occur with an observable intensity. X-band was therefore chosen for examination of these transitions and the X-band spectrometer is described in §4.3.

All spectra were recorded by detecting the second harmonic of the modulation frequency, that is phase sensitive detecting at 230 kHz (with a field modulation frequency of 115 kHz). This had the advantage of narrowing the lines thereby providing better resolution of the superimposed spectra.

## 7.6 Results and Discussion

### 7.6.1 Spin Hamiltonian parameters and the spectrum

The experiments in this chapter were aimed primarily at the determination of the effective spins of the defects, not at accurate measurement of the components of the Hamiltonian parameters. Despite this Q-band's increased sensitivity to anisotropy in the $g$-tensor exposed inconsistencies in the parameters determined at X-band by van

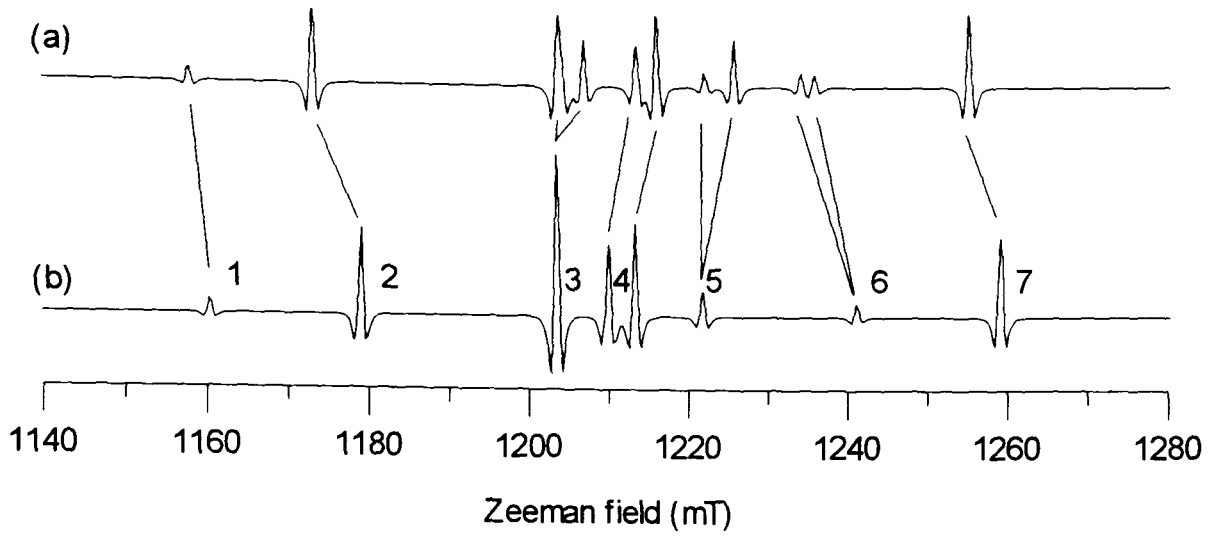



Figure 7.5: Simulated spectra for W13 at $\sim$ 33.7 GHz with $\mathbf{B}\|\langle 111\rangle$ at 1.6K: (a) using published parameters, and (b) using parameters calculated from fitted X-band and Q-band data (see text). See Figure 7.7 for an experimental spectrum.

Wyk [203, 198].

Figure 7.4 shows a typical spectrum collected at Q-band with $\mathbf{B}\|\langle 111\rangle$. The spectrum is roughly symmetric about the central region, with lines from defects in more than one symmetry related orientation being visible for some centres. The intensity differences between corresponding low and high field lines are evidence of the onset of observable population differences between the levels in the spin manifolds. The excited state W11 has not fully depopulated, however it has reduced to less than half its room temperature intensity. The central region is confused by the presence of inner transitions from the W-defects, transitions from other defects such as $[N\text{–}C]^0$, $[V]^-$and $^{13}C$ hyperfine interactions.

When the parameters for W13 from reference [198] were used to simulate the Q-band spectrum in the $\langle 111\rangle$ direction, the $g$-anisotropy split transitions arising from defects making a large angle with the Zeeman field.[6] However, the experimental spectrum (Figure 7.4) showed no evidence of such a splitting. To resolve this problem the experimental data collected at X-band, including the half and third field transitions, and the Q-band data were fitted, and a spectrum simulated in the $\langle 111\rangle$ direction.

[6]The symmetry of the $D$-tensor is nearly $\langle 111\rangle$, and the principal component is in a $\{110\}$ plane. With $\mathbf{B}\|\langle 111\rangle$ one site will subtend a vanishingly small angle while the others will subtend larger angles.

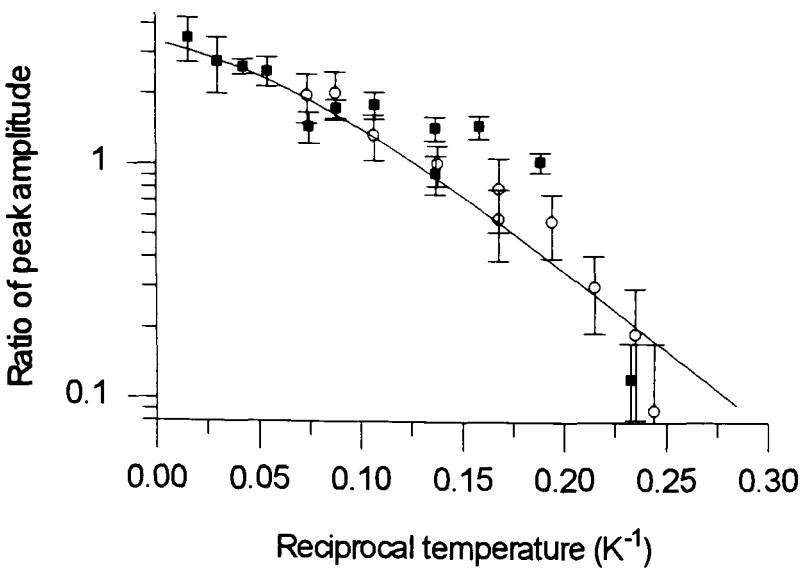



Figure 7.6: Intensity of the W11 excited state as a function of temperature. The excitation energy was found to correspond to 17.5(7)K or 1.50(6) meV by fitting the circles. The circles were collected using 0.3 mW microwave power. The black squares were collected using 1.0 mW and, although they have smaller error bars, suffer from saturation effects.

This was compared with that simulated from the published parameters [198] and both are plotted in Figure 7.5. The difference in intensities between transitions between different energy levels arises from the Boltzmann depopulation at 1.6K. Two differences are apparent when contrasting the simulations. i) Spectrum (a) (calculated from reference [198]) is offset to the low field side, and ii) a number of transitions are superimposed in spectrum (b) which are not in (a). The field offset is produced by a lower average $g$-value in the fitted parameters, while the splitting, or lack of it, is produced by changes in the principal axes and anisotropy of the $g$-matrix. Only one Q-band field direction was used to constrain the fit, hence the fitted parameters may not be unique and are therefore not tabulated, however, the analysis serves as a caution to placing too much value in $g$-matrix parameters determined from X-band data alone.

### 7.6.2 Depopulation measurements

Initial depopulation measurements were performed at temperatures between room temperature and 3.5K. Spectra were collected with $\mathbf{B}\|\langle 111\rangle$ and the intensity ratio of the low to high field lines was measured. The following observations were made:

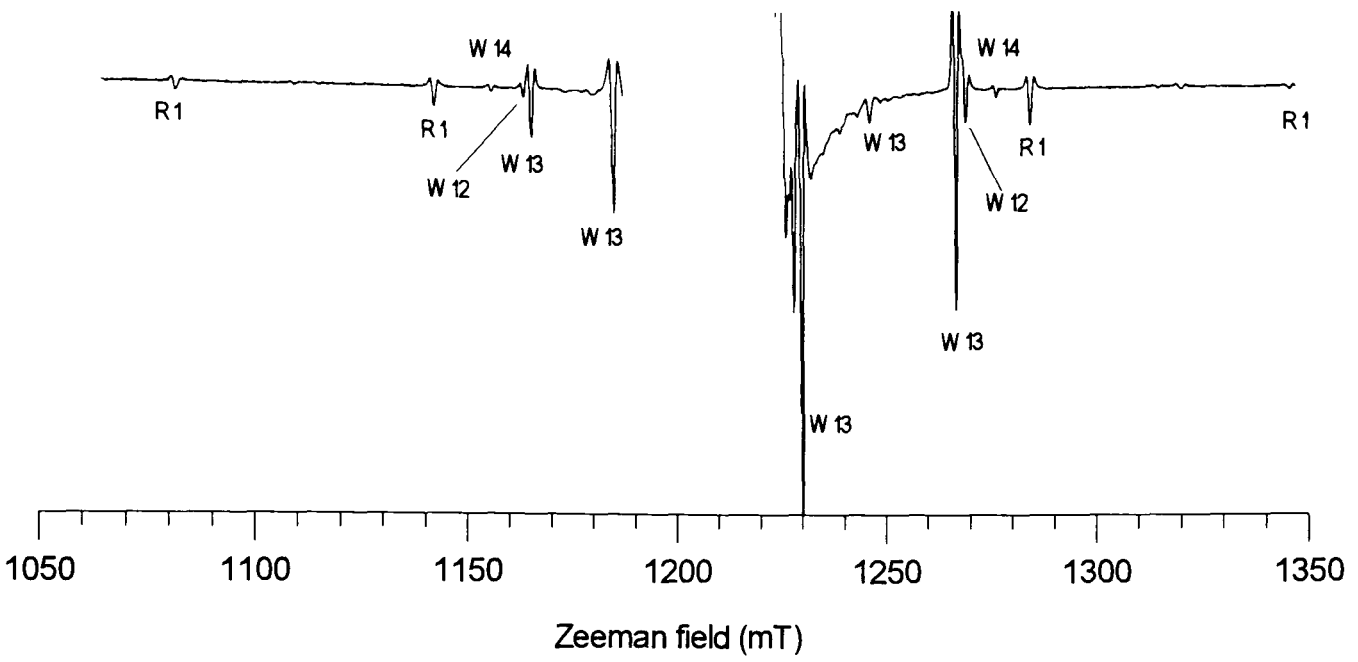



Figure 7.7: 1.6K spectrum collected with the Zeeman field $\|\langle 111\rangle$ showing the anisotropic depopulation of W12–W14 and R1. Compare the large intensity difference between the high and low field transitions of $S=\frac{3}{2}$ W13 to those of $S=1$ R1. Also note that the intensity ratio for the outer transitions of R1 is opposite to that for W12–W14.

- The measurements allowed the determination of the absolute sign of the $D$-tensor, but were inconclusive with regard to discrimination between the triplet and quadruplet nature as the errors were of the same order as the calculated intensity difference between the two states.

- The W11 centre depopulated at low temperatures. The depopulation curve is plotted in Figure 7.6 where the intensity of the W11 centre is divided by that of the R1 centre and plotted against inverse temperature. It was necessary to assume that the R1 system behaved in a Curie Law fashion, however, no evidence to the contrary was forthcoming. The W11 state was shown to be 1.50(6) meV above an unidentified ground state (see §7.3.3).

To increase the magnitude of the depopulation effect, and increase the signal to noise ratio, the system was cooled to 1.5K. Care had to be exercised to eliminate saturation effects at these temperatures. A typical spectrum collected at 1.6K is shown in Figure 7.7. The ratio of high to low field lines was again measured and the results are plotted in Figure 7.8 which also includes the data measured between 300K and 3.5K. The importance of the low temperature measurement is self-evident. Error bars have been omitted from the figure for clarity, but the figure including errors is

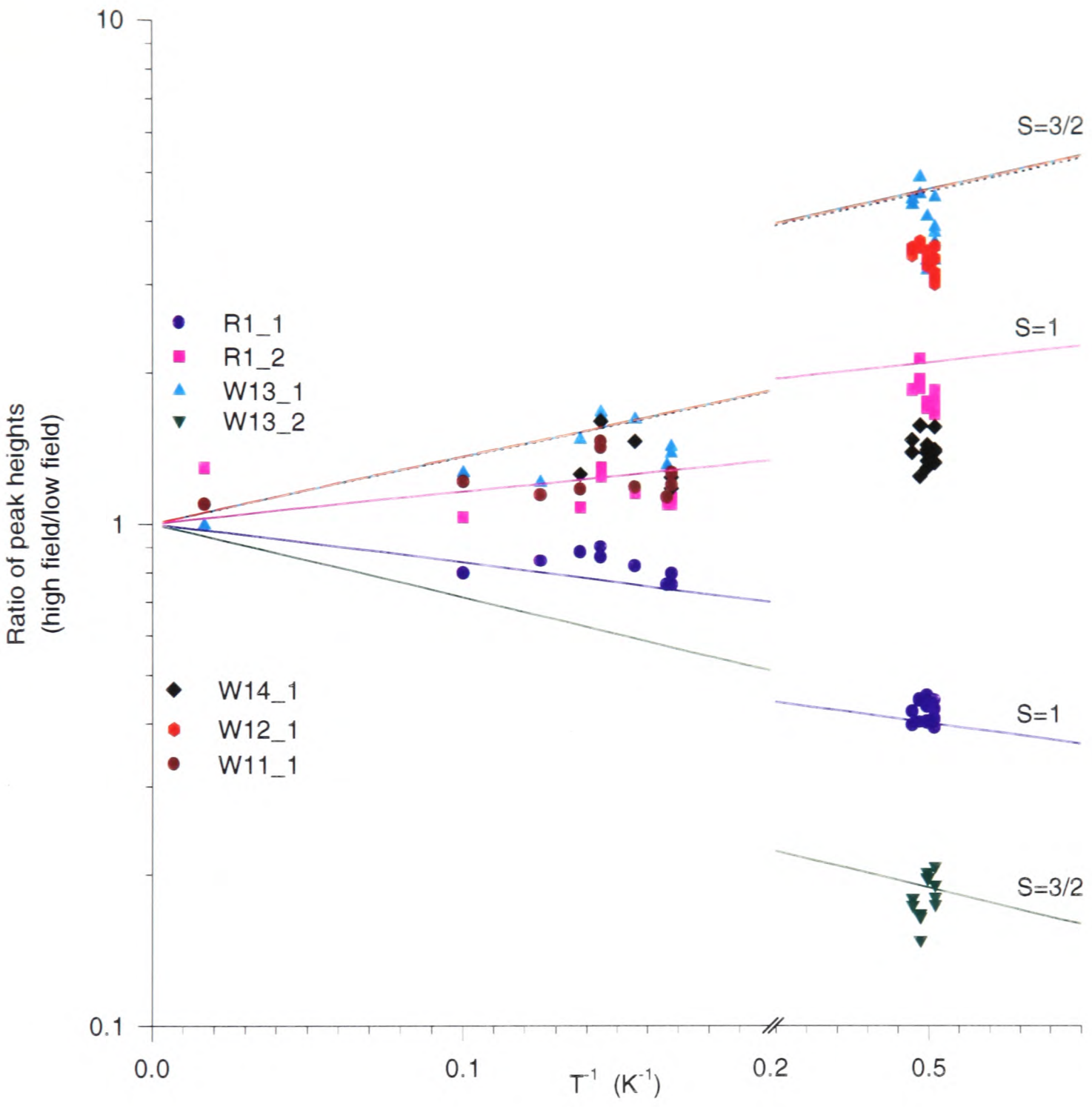



Figure 7.8: Ratio of transitions between upper and lower levels of the spin manifolds for W11, W12, W13, W14 and R1 plotted as a function of temperature. The W11 centre depopulates and no result can be reached. Theoretical curves are plotted with the colours matching the data points to which they refer. Data collected at Q-band, $\mathbf{B}\|\langle 111\rangle$.

included in Appendix A. The energy levels at each transition field were calculated using *EPR.FOR* (§4.4.5) and the spin Hamiltonian parameters from Table 7.1 and used in equation 7.15 to determine the theoretical intensity ratios. The results were as follows:

- R1 shows a good agreement with theory confirming its $S$=1 nature, and showing that there are no effects from nearby states like those discussed in §7.6.4. Note that the ratio of the outer lines for R1 (denoted R1_1) is less than one, whereas the same ratio is greater than one for the other defects. This is immediately obvious from Figure 7.7 and reflects the negative sign of the principal component of the R1 $D$-tensor, compared to a positive sign for W11–W14 (see §7.3.1).

- W13 also shows a good agreement with theoretical ratio for an $S=\frac{3}{2}$ centre (§7.3.1).

- W12 fits within the error bars, especially when it is noted that the signal was small and partially overlapped with W13 (see Figure 7.7).

- W14 presents a problem. It is obviously not $S=\frac{3}{2}$, but the ratio is smaller than expected even for $S$=1. Saturation effects were eliminated during the experiment by collecting values over a range of microwave powers. The ratios of line widths and heights were nearly independent of microwave power at 1.5K and the ratio of the widths was very near unity at all powers used. Thus, although the ratio was determined by using peak heights, inclusion of the line width[7] would not affect the intensity ratio. The reasons for the behaviour of the W14 defect will be explored further in §7.6.4.

### 7.6.3 Half and third field transitions

The sample was transferred to the X-band spectrometer and measurements of the half and third field transitions were performed. The R1 and W13 transitions were successfully identified, but as can be seen, the spectrum was still complicated and

[7]Intensity $\propto$ height $\times$ (half width)$^2$.

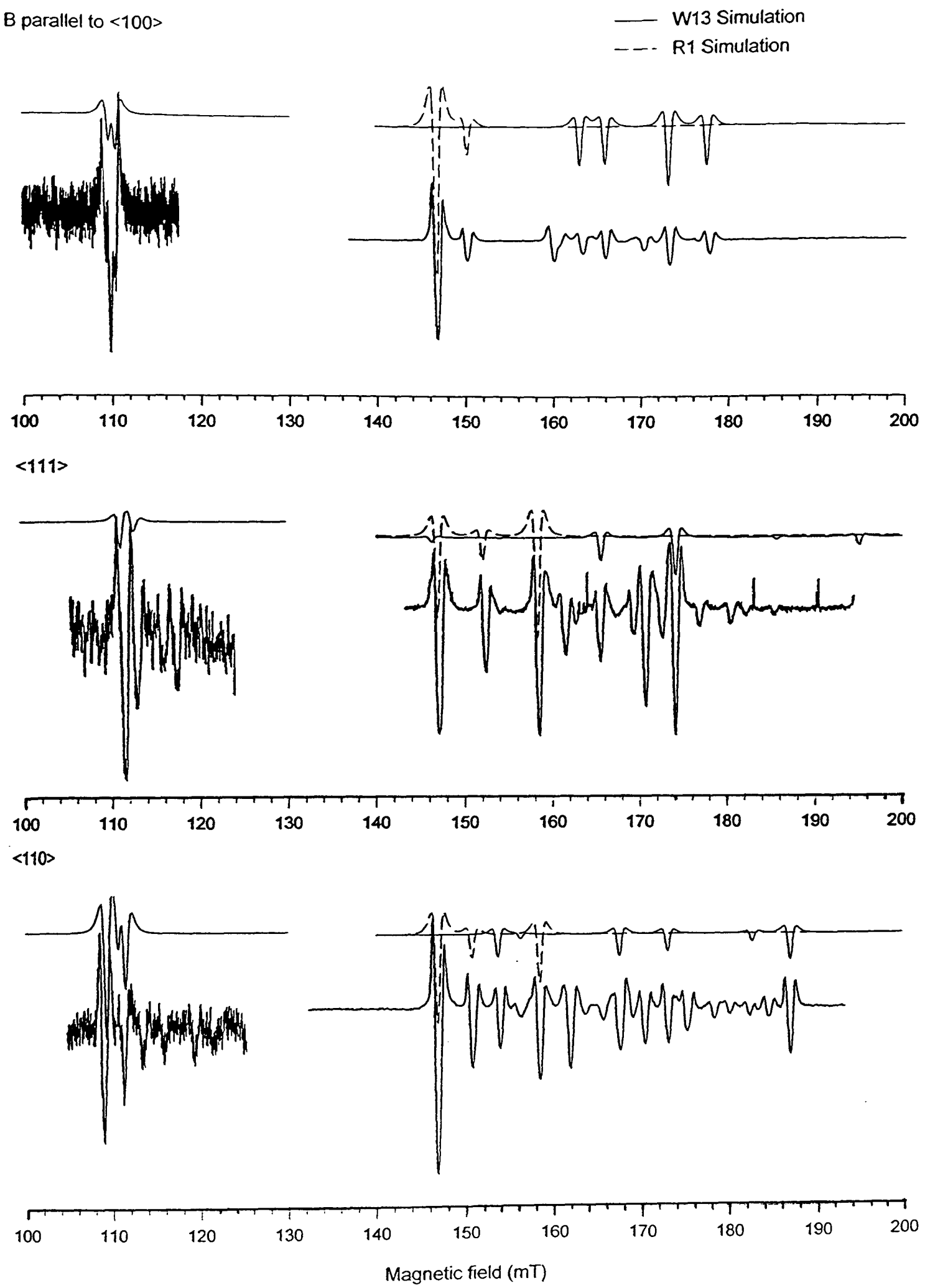



Figure 7.9: Half and third field transitions at X-band for $\mathbf{B}\|\langle 100\rangle$, $\|\langle 111\rangle$, and $\|\langle 110\rangle$. The positions of the R1 and W13 transitions are simulated above each experimental spectrum.

it was not possible to assign transitions unambiguously to all the lines. Spectra in the ⟨001⟩, ⟨111⟩ and ⟨110⟩ directions, with corresponding simulations, are plotted in Figure 7.9. Owing to experimental constraints it was not possible to perform the angular variation needed to facilitate the fitting of the other half field transitions.

### 7.6.4 General discussion

#### Effective spin

The effective spins of W12 and W13 were found to be $S{=}\frac{3}{2}$ in agreement with van Wyk, however the measured ratio for W14 was less than that expected for even an $S{=}1$ system. A cursory glance at the 1.6K spectrum (Figure 7.7) appears to rule out the possibility of a quadruplet state for W14 as defined in §7.3.1, yet this is the centre for which van Wyk identified lines corresponding to $m_s = \frac{1}{2} \leftrightarrow -\frac{1}{2}$ transitions. The angular variation of the outer transitions fitted by van Wyk was re-fitted using *EPR.FOR* (§4.4.5) and was found to fit to $S{=}\frac{3}{2}$ better than $S{=}1$. W14 was however the defect which produced the worst fit having an RMSD[8] of 0.34 mT which should be compared to 0.22 mT for W13 and 0.036 mT for W11. van Wyk also found structure on the residuals for the fit hinting at some unexplained feature. There were additional inconsistencies between fitting the $g$-matrix when using the $m_s = \frac{1}{2} \leftrightarrow -\frac{1}{2}$ transitions or the $m_s = \pm\frac{1}{2} \leftrightarrow \pm\frac{3}{2}$ transitions, but it was shown in §7.6.1 that little weight can be placed upon anisotropy in $g$-values determined at X-band.

An explanation of the behaviour of the W14 system might be forthcoming if the presence of excited states is considered. A nearby excited state can affect the system in the following ways:

1. It will affect the ratio of the high to low field lines by modifying the correction factor of equation 7.18.

2. State mixing with the excited state can alter the transition probabilities between the levels of the manifold.

[8]Root mean squared deviation between the fit and experimental data for each data point.

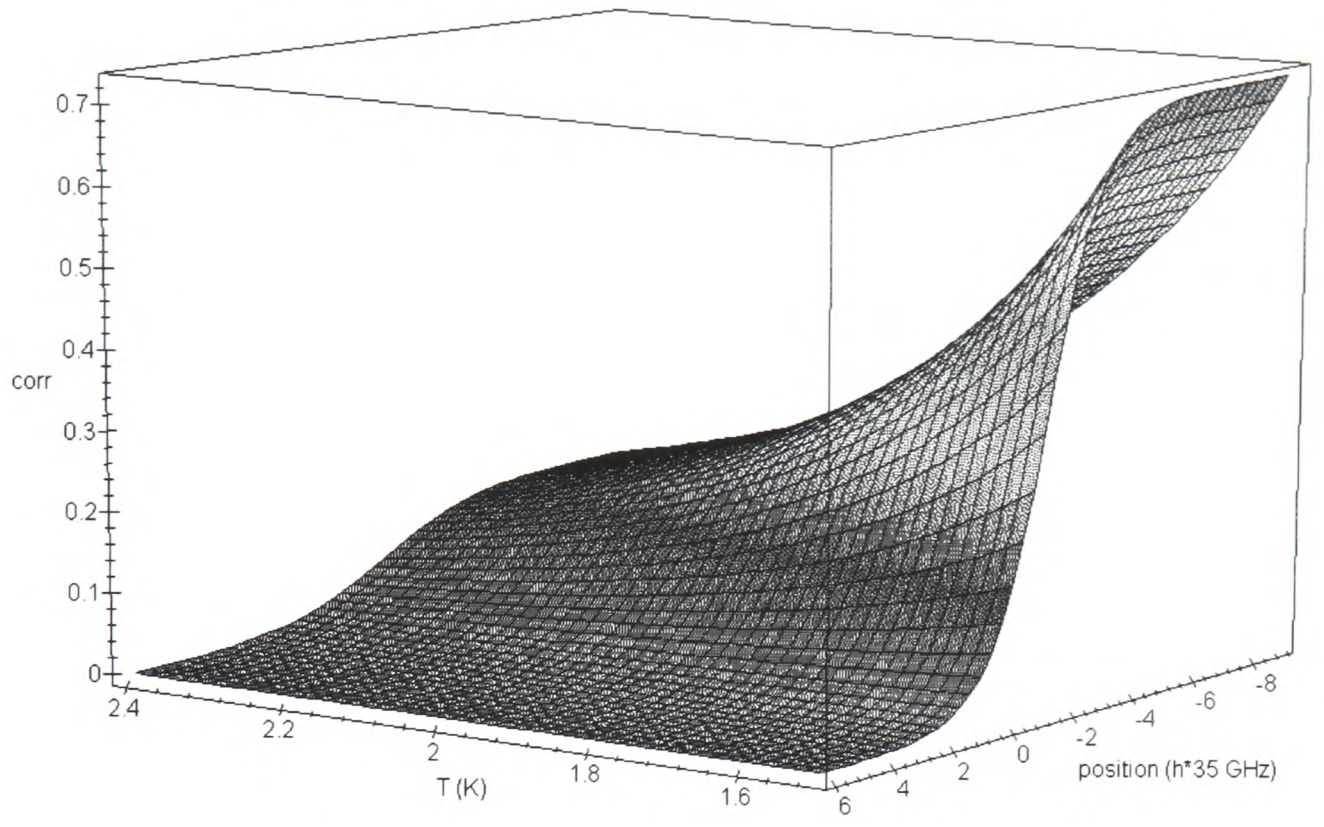



Figure 7.10: Effect on the ratio of the high to low field transition intensities for W14 of introducing a singlet into the quadruplet manifold. The position of the singlet with respect to the centre of the quadruplet is represented as position times the microwave quantum, a positive position corresponding to the singlet above the quadruplet. corr is the correction added to the no-singlet case to obtain the singlet case, ie. corr = singlet – no-singlet case.

The effect of introducing an additional level into a $S=\frac{3}{2}$ manifold was investigated by constructing the energy levels of the quadruplet using equation 7.5. The singlet was defined with respect to the zero of the quadruplet. The transition fields for the low and high field transitions were computed, and the canonical partition function was constructed, along with the explicit populations of the energy levels. The ratio of the high and low field energy transitions was determined as a function of both the offset of the additional singlet from the centre of the quadruplet, and of temperature. The result is given in Figure 7.10.[9] The effect of the singlet is only felt as it nears the

[9]The calculations were performed using an algebraic mathematics package, Maple V release 3, running on an i486DX-33 PC and on a Dec Alpha workstation.

quadruplet manifold, with the largest effect being produced when the singlet is below the quadruplet. The effect of the singlet reaches a maximum and does not continue to increase. This is intuitively correct as the singlet can only affect the size of the partition function, and reduction of the energy of the singlet increases its contribution to $\mathcal{Z}$ with respect to the other levels. When the contribution of the singlet dominates, the correction to the intensity ratio of equation 7.18 tends to 1 and can not increase further. As the correction reduces the intensity ratio between the low and high field lines, the effect of the singlet is to increase it. It can therefore not be responsible for the anomalous W14 intensity ratio.

The only remaining explanation is that the transition probabilities of the two lines are not the same. This is feasible as it is known that W13 has an intensity dependent on the direction of the Zeeman field which indicates mixing of excited state energy levels via the Zeeman interaction [211]. It is likely that excited state levels are mixed to a greater extent with the upper levels of the W14 manifolds than with the lower levels, producing a difference in the transition probabilities. If this interaction is large enough it could reduce the depopulation ratio from that for a quadruplet to that of a triplet, however, such a large discrepancy would be visible at higher temperatures where the populations are nearly equal – examination of Figure 7.4 shows that this is not true. The additional Zeeman term in the Hamiltonian could affect the behaviour of the angular variation and, as it is a Zeeman term, it would be more pronounced at higher Q-band fields than X-band fields. Such a term could be responsible for a slight reduction in W14 ratio, the better fit when using an $S{=}\frac{3}{2}$ Hamiltonian at X-band than an $S{=}1$ Hamiltonian, and would explain the failure of the X-band parameters to satisfactorally fit the Q-band spectra. It could also be responsible for the anisotropic behaviour of the W13 transition intensities.

### Signs of the *D*-tensors

The signs of the principal components of the $D$-tensors for all the W-defects were positive. This could correspond to a dominance of an exchange interaction term in the fine structure, however, it is not possible to differentiate between the spin-

orbit interaction (§3.2.3), dipole-dipole interaction (§3.2.3) or anisotropic exchange interaction (§3.2.3), though the spin-orbit interaction is expected to be small owing to the small $g$-shift. The sign of the principal component of the $D$-tensor in the R1 system was negative. This supports the model of a dipolar interaction (§3.2.3 and [212]) and shows that the $m_s = 0$ spin projection is higher in energy than the $m_s = \pm 1$ pair.

## 7.7 Conclusion

The effective spins of the defects have been measured. It was found that W12 and W13 corresponded to quadruplet states, in agreement with the findings of van Wyk. W14 corresponded neither to a quadruplet or a triplet state and reasons for this have been proposed. It was not possible to determine the spin of W11 as it was found to be an excited state with an excitation energy of 1.50(6) meV (364(15) GHz) above the singlet or doublet (depending on $S$=1 or $S$=$\frac{3}{2}$) ground state.

The results from this work have placed further constraints upon the theoretical model proposed by Lowther and van Wyk [198] for the W11–W14 centres. It is not evident how the distorted negative vacancy model can account for the excited state nature of the W11 defect, while still predicting the correct zero-field splitting.

The measured sign of the $D$-tensor for R1 has a significant bearing upon the theoretical analysis of Lowther and Mainwood [102] (see §8.3), yielding information on the magnitude of the Jahn-Teller interaction and thus the ordering of the E and $A_1$ levels within their distorted neutral vacancy model.

## 7.8 Further work

During this thesis development work was performed on a cavity to facilitate measurement of EPR spectra with the microwave field parallel to the Zeeman field. This increases the transition probability for the half and third field transitions, while suppressing allowed transitions, thus enabling spectroscopy to be performed on the half

and third field transitions. The cavity was designed to permit coupling to either a $B_{\|}$ or a $B_{\perp}$ mode, allowing easy alignment and optimization of the experimental parameters using the $\Delta m_s = 1$ transitions, before switching to the $\Delta m_s > 1$ transitions. The cavity is, however, still in the development stage. Detailed spectroscopy of the half and third field transitions, combined with annealing, would provide additional information for the resolution of the spin debate.

Any ENDOR coupling is necessarily small – less than the EPR line width of about 20 MHz – but it is conceivable that it could now be measured using the new ENDOR system developed for work on the $[V]^-$ system and described in Chapter 4. Performing ENDOR on the system would identify any nitrogen interaction, and would also provide another measure of the spin.

Further experiments involving annealing of the sample are now planned, following the delivery of a high temperature furnace (after the completion of the experimental work for this thesis). It will also be possible to repeat the cooling measurements using a new superheterodyne Q-band spectrometer which is under development. Initial measurements with the new system show it to have a much higher sensitivity than the spectrometer used in this thesis for Q-band spectroscopy. Careful measurements of the intensity dependence of the W12, W13 and W14 centres as a function of temperature, could expose any non-Curie Law behaviour and facilitate the determination of the energy separations to excited singlet or doublet states. A complete determination of the intensity dependence of the centres as a function of angle, and the fitting of Q-band and X-band angular variations using both forbidden and allowed transitions should be performed to identify any additional contributions to the spin Hamiltonian, and thus provide information on the electronic energy levels.

# Chapter 8

# Isotopically enriched diamond

## 8.1 Introduction

This chapter presents a preliminary investigation of irradiation damaged, synthetically produced, isotopically enriched type IIa diamond. The diamond studied was composed of 50% $^{13}C$ and had a level of impurities undetectable using electron paramagnetic resonance spectroscopy. The sample therefore presented an opportunity to investigate the properties of intrinsic radiation damage defects via the $^{13}C$ hyperfine interaction. The results are provisional and no definitive answers can be presented, rather, they serve to show just how many questions there are to ask, and suggest what some of those questions might be.

The chapter will start with a brief review of large single-crystal synthetic diamond, followed by a review of previous work performed on the R1 and R2 radiation damage centres studied in the sample. The simulation of the $[V]^-$ spectrum in isotopically enriched diamond is discussed. This is followed by a presentation of the results of the preliminary investigation, and a discussion of some of the questions these raise.

## 8.2 Isotopically pure and enriched diamond

The development of technology facilitating the controlled growth of diamond of known composition has been an important step forward in the study of diamond, removing

at least one of nature's variables. Large synthetic diamond crystals, with weight greater than a carat, have been grown since 1970. The development of the synthesis techniques is detailed by Burns [213], Kanda and Sekine [214], and Yoder [215]. The history of published work up until 1990 is presented in Table 8.1. Since 1990 the synthesis of large, high quality synthetic crystals has become commonplace within De Beers, General Electric, Sumitomo and NIRIM,[1] and a few experiments have been reported on General Electric and NIRIM isotopically enriched crystals [164, 216, 217]. Isotopically pure (99.9% $^{12}$C) diamond has been grown by General Electric. The material has a very high thermal conductivity, up to 50% greater than that of 1.11% $^{13}$C (natural abundance) diamond [218]. The increased thermal conductivity can be explained in terms of reduced phonon-isotope scattering events and the dominance of normal scattering processes at low isotopic compositions (see Berman for a detailed explanation [219] and also [220]). Other carbon isotope effects in diamond are reviewed in [221, 222, 223].

## 8.3 Previous work

The R1 and R2 centres were originally observed in electron irradiated natural type IIa diamond in 1962 [212]. EPR spectra were measured in four natural samples irradiated with 2 MeV electrons, at doses ranging from $3\times10^{17} \rightarrow 8\times10^{19}$ cm$^{-2}$. These were fitted to the following effective spin Hamiltonian with $S$=1:

$$\mathcal{H} = g\mu_B \hat{\mathbf{S}} \cdot \mathbf{B} + \hat{\mathbf{S}} \cdot \underline{\mathbf{D}} \cdot \hat{\mathbf{S}} \tag{8.1}$$

The defects were found to have the same magnitude of $D$-tensor, but the principal axes pointed along ⟨994⟩ for R1 and ⟨100⟩ for R2. The Hamiltonian parameters have since been measured to a higher accuracy and are given in Table 8.2. The measured EPR line width of R1 was about 0.5 mT while for R2 it was substantially larger being between 2.5 and 5.0 mT. The absolute sign of the $D$-tensor was unknown, however

[1] National Institute for Research in Inorganic Materials, Japan.

Table 8.1: Large synthetic diamonds

| Year | Colour | Weight(carats) | Comments |
|---|---|---|---|
| *General Electric:* | | | |
| 1970 | Near colourless | 0.735 | Conductive |
| 1970 | Yellow | 0.221 | Non-conductive |
| 1970 | Greyish blue | 0.157 | Conductive |
| 1990 | Colourless | 0.95 | 99.93% $^{12}C$ |
| *Sumitomo:* | | | |
| 1985 | Deep yellow | $\leq 2$ | Non-conductive |
| 1990 | Yellow | $>9$ | Non-conductive |
| *De Beers Diamond Research Laboratory:* | | | |
| 1979 | Brownish yellow | 6.85 | Non-conductive |
| 1987 | Yellow | 0.97 | Non-conductive |
| 1987 | Greenish yellow | 0.44 | Surface conduction |
| 1987 | Brownish yellow | 11.14 | Non-conductive |
| 1987 | Brownish yellow | 5.23 | Non-conductive |
| 1989 | Blue | 1.3 | Conductive |
| 1990 | Brownish yellow | 14.2 | Non-conductive |

Taken from reference [213] p.417.

Table 8.2: Tabulated parameters for R1 and R2.

| | | | |
|---|---|---|---|
| **R1** | $g = 2.0034(5)$ | $D_1 = +1411(5)$ | $[1\bar{1}1]$ |
| | | $D_2 = -2806(5)$ | [9 9 4] |
| | | $D_3 = +1395(4)$ | $[\bar{2}\ \bar{2}\ 9]$ |
| **R2** | $g = 2.00$ | $D_1 = \mp 2760$ | [100] |
| | | $D_2 = D_3 = \pm 1380$ | |
| *Excited state 37 meV above ground state* | | | |

Data from reference [224], $D$-values in MHz.

Table 8.3: R1 $^{13}C$ hyperfine parameters. $A_2$ and $A_3$ were not observed for Set 3.

| | Set 1 | | Set 2 | | Set 3 | |
|---|---|---|---|---|---|---|
| | MHz | axis | MHz | axis | MHz | axis |
| $A_1$ | 44.4 | $[1\bar{1}0]$ | 30.6 | $[1\bar{1}0]$ | 122.9 | $[1\bar{1}0]$ |
| $A_2$ | 43.8 | $[22\bar{9}]$ | 27.3 | $[22\bar{9}]$ | — | — |
| $A_3$ | 39.9 | [994] | 24.3 | [994] | — | — |

Data from reference [225].

Table 8.4: Additional lines possibly associated with R1.

| System | Reduction in $D$-value | | Intensity as % |
|---|---|---|---|
| | MHz | % | of the main line |
| R1a | 34.5 | 0.82 | 0.38 |
| R1b | 46.5 | 1.10 | 0.51 |
| R1c | 51.3 | 1.21 | 0.16 |
| R1d | 87.2 | 2.07 | 0.54 |
| R1e | 107.3 | 2.54 | 0.07 |
| R1f | 116.3 | 2.76 | 1.45 |

Data from reference [225].

it was assumed to be negative and hence mainly dipolar in origin. The relation:

$$D = -\left(\frac{\mu_0}{4\pi}\right)\frac{3}{2}\frac{g^2\mu_B^2}{r^3} \tag{8.2}$$

was used to determine an average inter-electron spacing of 2.66 Å. This was very close to $\frac{3a}{4}$, where $a$ is the lattice parameter for diamond.[2] Faulkner and Lomer proposed models for R1 and R2, involving the interaction of a vacancy (or impurity) with a split interstitial or divacancy [212].

$^{13}$C hyperfine interactions in the R1 centre have been measured [225] and are listed in Table 8.3. Additional sets of lines labelled R1a → R1f were were also measured in four samples. The parameters were found to have identical symmetry to R1, but smaller $D$-values and lower intensities. The $D$-values and intensities are given in Table 8.4.

The annealing behaviour of R1 and R2 has been investigated [226], with R1 annealing out at ~300°C and R2 at ~400°C. Walker [227] showed i) a linear dose dependence for the intensity of R2 when irradiating with electrons for low doses; and ii) that saturation occurred at high electron doses. A similar dependence was measured for R1 [225]. R1 and R2 can also be created using fast neutrons, but no correlation has been found between the EPR intensities and the neutron dose [228].

Walker [229] has found a correlation between the R2 and the 1.685 eV optical absorption centre, with both being proportional to the electron radiation dose at low doses, with saturation observed at around $10^{18}$ $e^-$ cm$^{-2}$. Mainwood *et al.* [179] have proposed a theoretical model for the R2 and 1.685 eV centres, where the defect responsible is a highly strained vacancy. They worked within the Coulson-Kearsley model [99] of the neutral vacancy, and applied a ⟨100⟩ uniaxial stress. They calculated that the stress would lower the symmetry of the lowest $^1$E, $^3$T$_1$ and $^1$T$_2$ levels. This predicts that the 1.685 eV transition occurs between the $^1$A state derived from the $^1$E ground state, and the $^1$B$_2$ state derived from the first excited state. The EPR transition is predicted to arise from components of the $^3$T$_1$ state, which has been

[2]The nearest neighbour distance is given by $\sqrt{3}\frac{a}{4} = 1.54$ Å.

lowered in energy to place it 37 meV above the ground state. From the measured stress parameters they calculated that the unperturbed $^3T_1$ state lay between 40 and 200 meV above the $^1E$ ground state.

In the same paper Mainwood *et al.* argue that the R2 EPR signal can not arise from a split-interstitial. Although the split interstitial is predicted to have a mid-gap doubly degenerate one-electron state split by Jahn-Teller distortion, the calculated energy levels showed too large a splitting to be associated with the R2 properties.

Lowther and Mainwood [102] have proposed a similar model for the R1 system. In this model R1 is produced by application of a $\langle 111 \rangle$ axial distortion to the neutral vacancy. An important point in the model is the inclusion of the spin-orbit coupling which affects the interpretation of fine structure measurements – such as those made using EPR. Lowther and Mainwood proposed that the R1 EPR is caused by a near degeneracy between the low lying $A_1$ and E states, which then collectively appear as a spin triplet with a zero-field splitting. The magnitude of the Jahn-Teller interaction dictates the order of the energy levels and the sign of the fine structure splitting.[3]

## 8.4 Results and Discussion

### 8.4.1 The sample

The sample was produced by General Electric Corporation and was synthesized using the large-gem temperature gradient catalyst process invented at the General Electric Research and Development centre [230, 231]. The seed crystal, and metallic inclusions from the FeAl catalyst, were removed using laser cutting and drilling, resulting in the production of three crystals, having masses[4] (a) 0.1814, (b) 0.1173 and (c) 0.0132 g.

The work in this thesis was performed mainly on sample (b). Sample (a) which was not irradiated is shown in Plate III.

The infrared absorption spectrum for sample (b) is depicted in Figure 8.1. This shows:

[3]This is measured in §7.6.2.

[4]Sample (b) was later cut into two portions weighing 0.0993 and 0.0181 g.

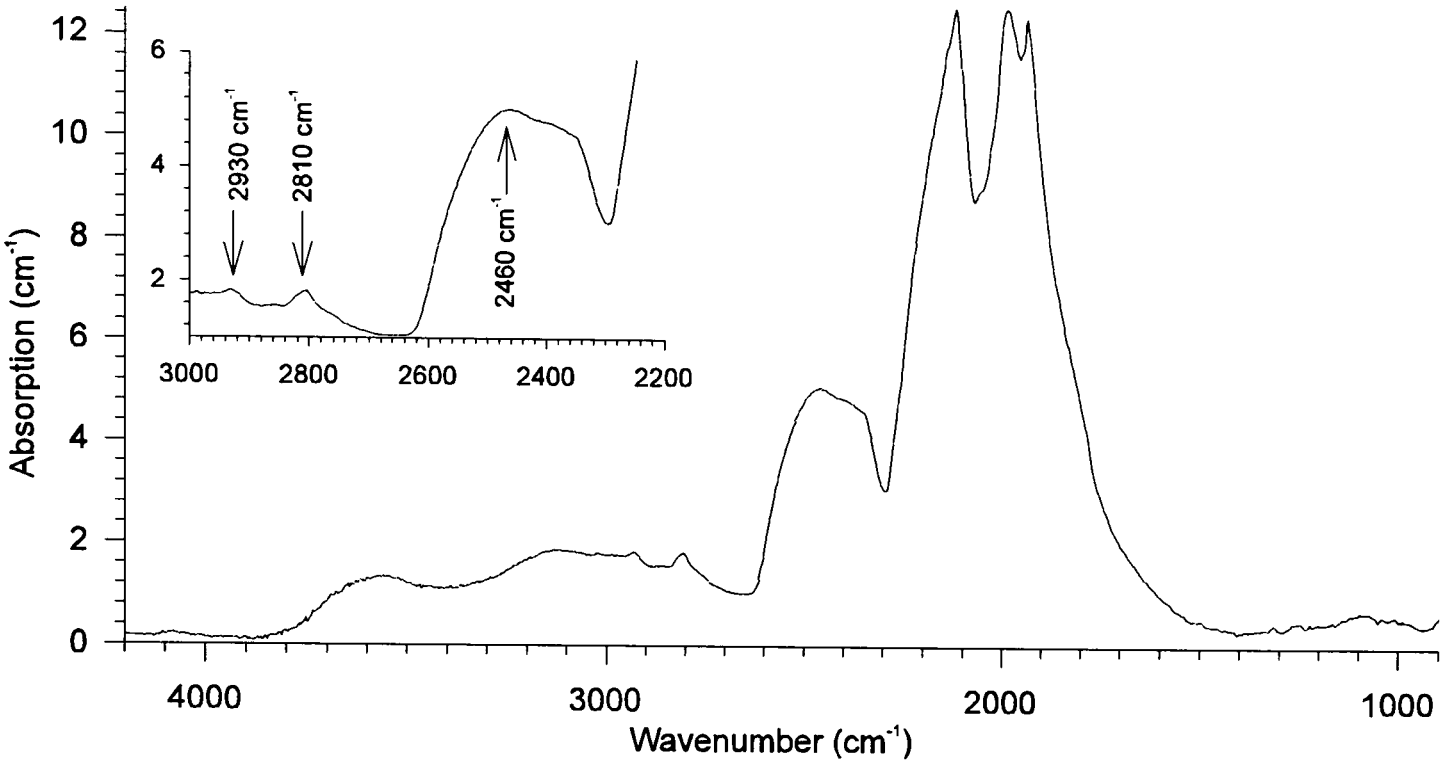



Figure 8.1: Infrared absorption of sample (b) prior to irradiation. See text for details.

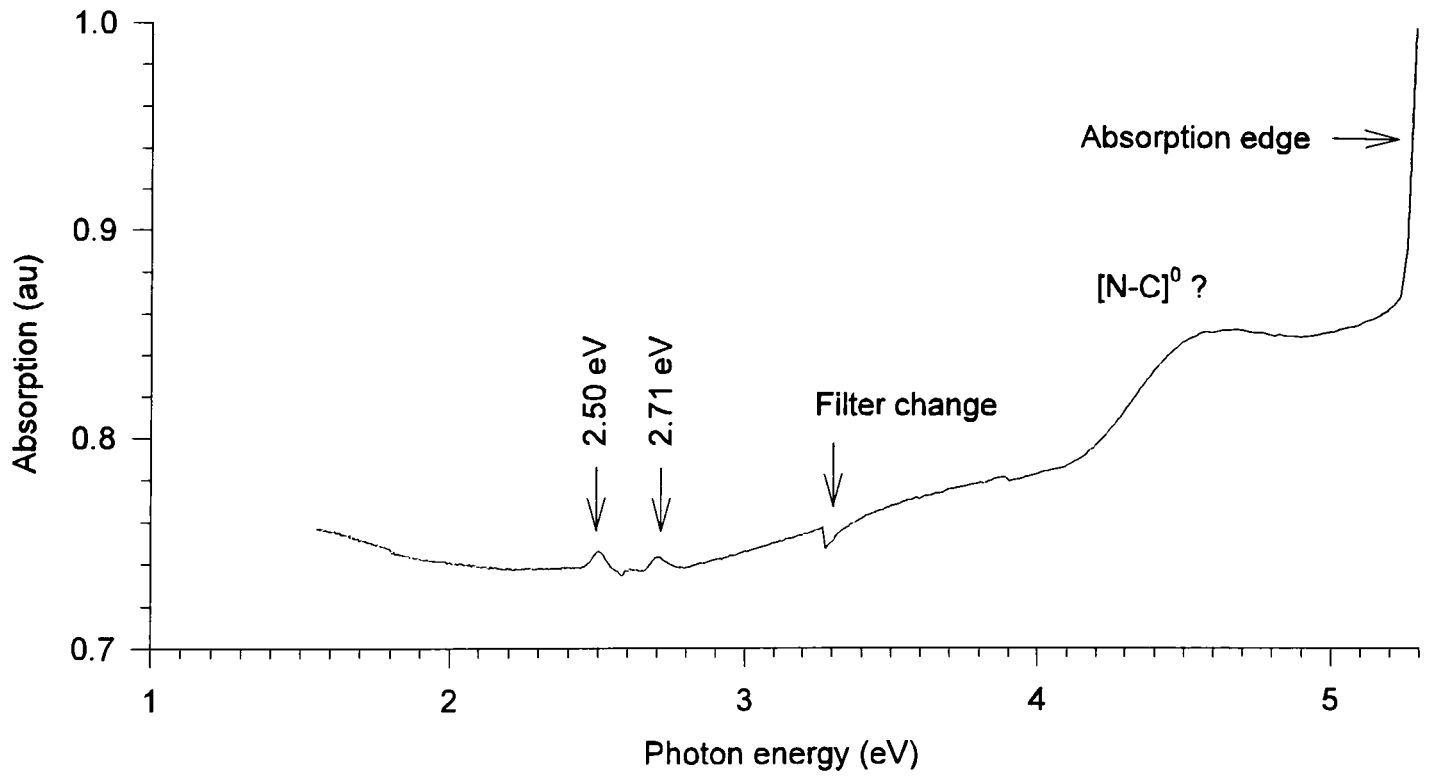



Figure 8.2: uv/visible absorption of sample (b) prior to irradiation. See text for details.

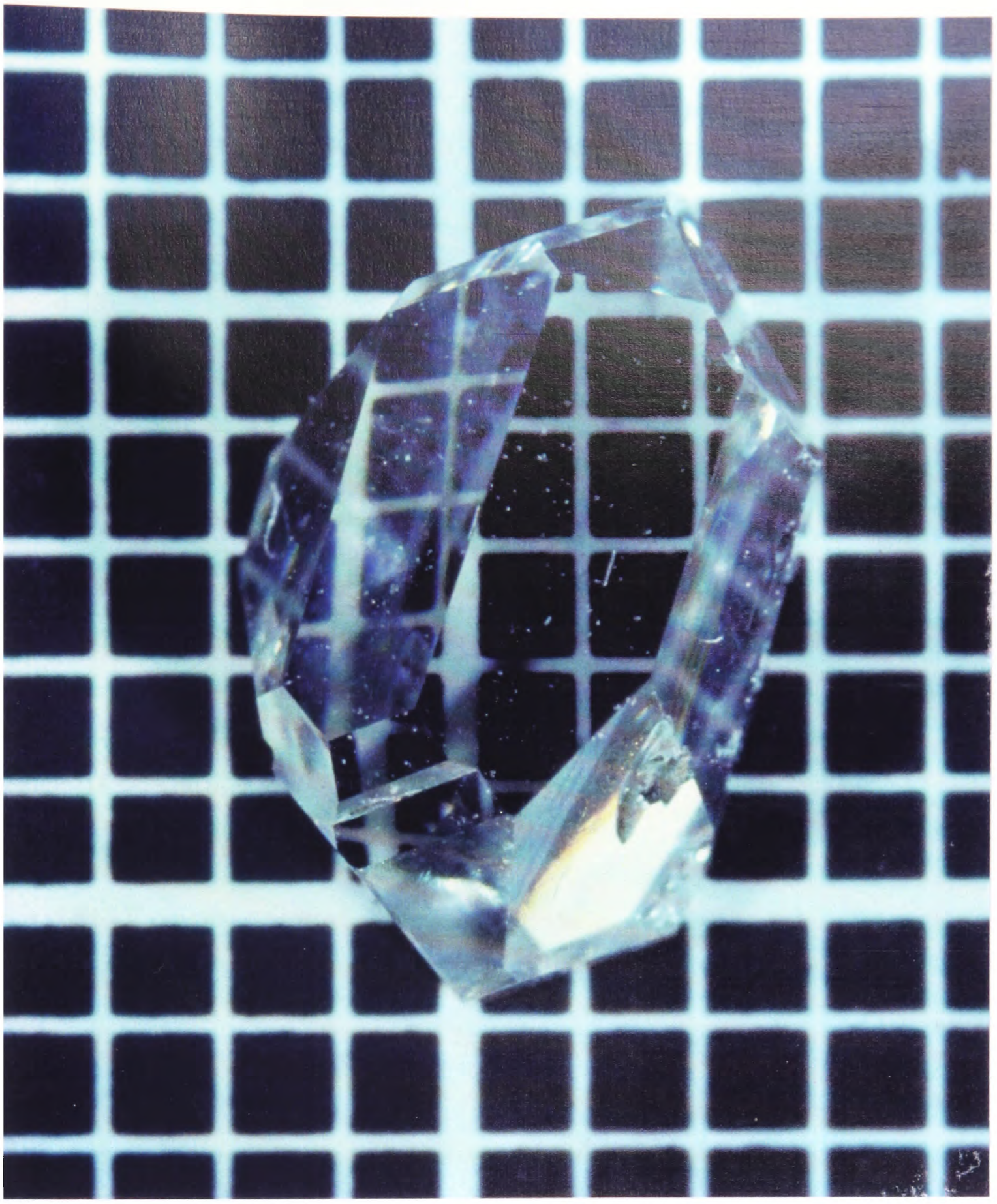


Plate III: Sample (a): 50% $^{13}C$ isotopically enriched synthetic diamond which has not been irradiated. The major grid size is 1 cm.

1. The absence of absorption in the zero-phonon region (900–1500 $cm^{-1}$), specifically any absorption at 1130 $cm^{-1}$ must be less that the sensitivity of about 0.2 $cm^{-1}$.

2. The characteristic two and three phonon diamond absorption (reference [23], p.32).

3. Peaks at 2460 $cm^{-1}$, 2810 $cm^{-1}$ and 2930 $cm^{-1}$, corresponding to the first, second and third excited states of boron acceptors (reference [23], p.32). The concentration is low, and the spectrum is poorly defined as is generally the case in synthetic diamond [19].

The room temperature uv/visible absorption spectrum is given in Figure 8.2. There appears to be an underlying absorption produced by a low number of nitrogen donor to valence band transitions. The features at 2.50 eV and 2.71 eV are not accounted for as the only optical absorption defects at these wavelengths are (see Bridges *et al.* [16]):

- H4 at 2.499 eV, associated with a vacancy;
- 2.51 eV centre associated with nickel, but the diamond was grown using an FeAl solvent;
- 2.699 eV and 2.721 eV defects, but these are observed in luminescence not absorption.

It is however possible that these absorptions are an artifact of the spectrophotometer. The absorption coefficient at 4.64 eV, $\mu_s^{(4.6)}$, is related to the infrared absorption at 1130 $cm^{-1}$, $\mu_s$, and to the EPR $[N–C]^0$ concentration, $N_s$ (in ppm.), by [56]:

$$N_s = \frac{5}{9}\mu_s^{(4.6)} \tag{8.3}$$

$$\mu_s^{(4.6)} = 45\mu_s \tag{8.4}$$

Using this in conjunction with the minimum observable absorption at 1130 $cm^{-1}$ of $\sim$0.2 $cm^{-1}$ gives a maximum of 5 ppm. single substitutional nitrogen which is

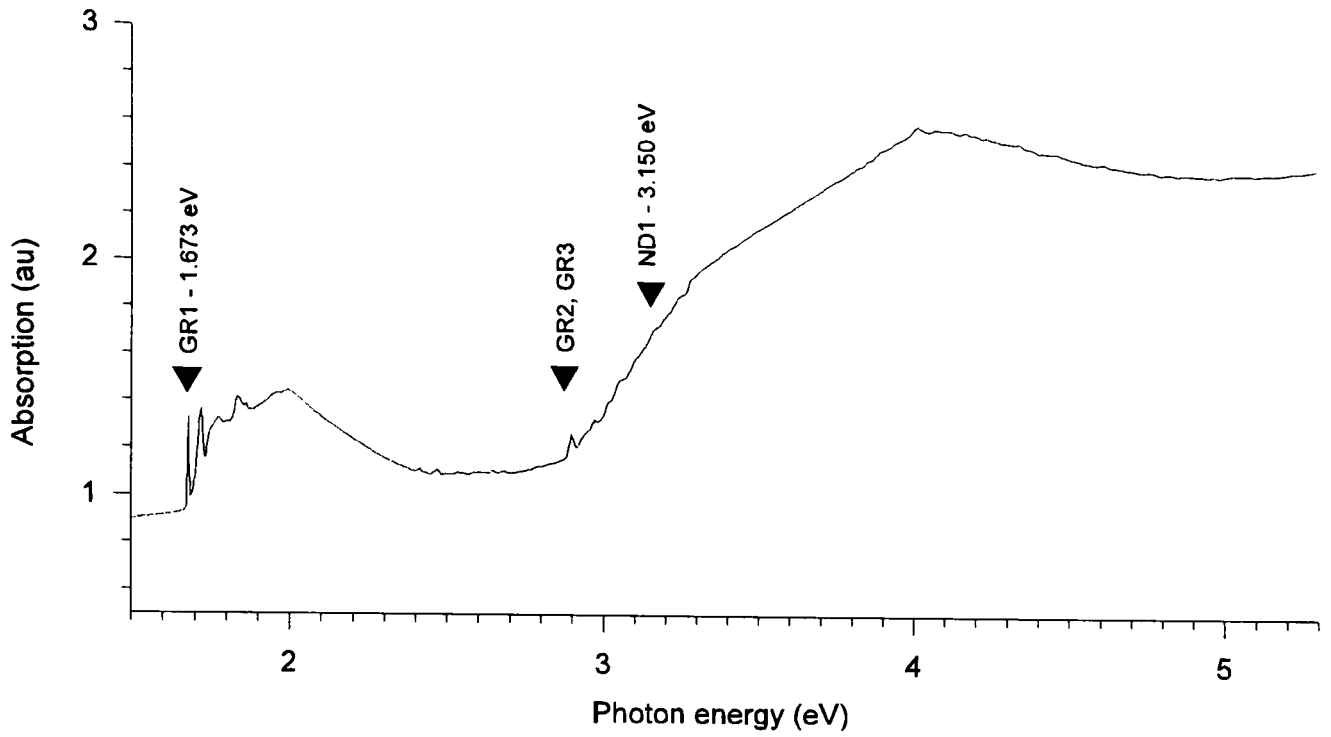



Figure 8.3: uv/visible absorption of sample (b) after to irradiation. See text for details.

consistent with the observation of the absorption centred at 4.64 eV in Figure 8.2 (see Collins [19]).

Diamond classification is performed on the basis of the infrared spectrum which here only shows evidence for a small boron concentration. The sample can therefore be identified as type IIa. The uv/visible absorption indicates a small concentration of nitrogen donors. EPR was performed on sample (b) at X-band at 4.5K and room temperature, and on sample (c) at Q-band at 1.5K and 4.2K. Both these investigations failed to observe any paramagnetic resonance, therefore the neutral single substitutional nitrogen concentration must be less than about 300 ppb..[5] Because of the presence of boron acceptors the nitrogen could be positively ionized and from the optical measurements could have a concentration of up to 5 ppm..

Sample (b) was irradiated with a dose of $5 \times 10^{18}\text{cm}^{-2}$ 2 MeV electrons. The crystal turned the characteristic green colour as depicted in Plate IV. A slice was cut from the sample for optical work and this showed that the green colouration did not

[5]This was estimated from the sensitivity achieved for $[\text{N–C}]^0$ detection in CVD diamond with narrow line widths. A simple criterion for the detection of a line is that its peak-to-peak (p-p) height is greater than the p-p noise. A line width of 1.2 mT was assumed for $[\text{N–C}]^0$ (assuming the $^{13}\text{C}$ hyperfine structure to be unresolved) and the detection limit was scaled according to the square of the ratio of this and the 0.01 mT line in CVD samples.

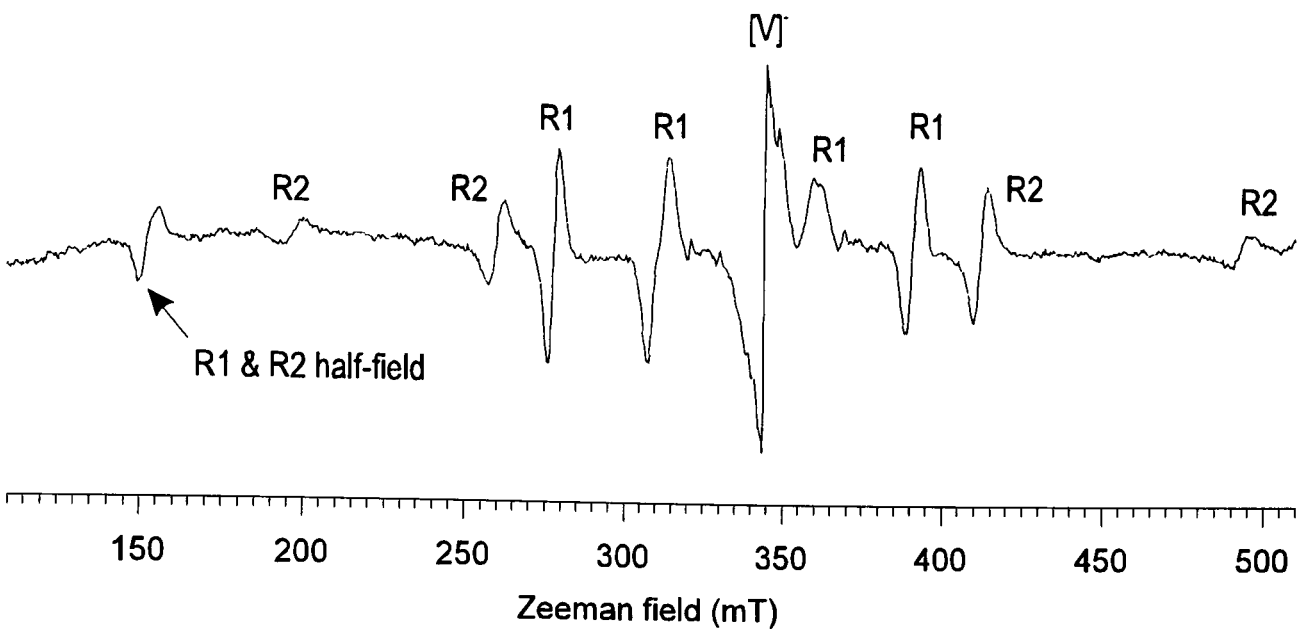



Figure 8.4: Room temperature X-band EPR spectrum of sample (b) after to irradiation, with Zeeman field parallel to ⟨100⟩. See text for details.

penetrate evenly through the sample as show in in Plate V. The uv/visible absorption spectrum, subsequent to irradiation, is shown in Figure 8.3. The underlying structure corresponds to that for irradiated type IIa samples (reference [23] p.34). A very weak ND1 ($[V]^-$) absorption could be present at 3.150 eV, and GR1 ($[V]^0$) absorption is evident at 1.673 eV, with phonon assisted structure above this energy. GR2 and GR3 absorptions can be seen just below 3.0 eV. These are thought to be related to $[V]^0$ (see §6.2.2 and reference [23] p.40). The transition probability for ND1 zero-phonon absorption is 2.5 times larger than for GR1 [183] showing that the ND1 concentration is substantially lower than that of GR1. This is consistent with the existence of boron acceptors which would compensate any nitrogen donors, tending to leave the vacancy in its neutral or possibly even positive charge state.

The room temperature X-band EPR spectrum after irradiation is shown in Figure 8.4. The Zeeman field is parallel to ⟨100⟩. R1 and R2 are immediately identifiable, while ND1 or $[V]^-$ was identified from measurements made at 4K. The concentrations of R1 and R2 are estimated to be of the order of $10^{16}$ and $10^{17}$ $cm^{-3}$ respectively by analogy with reference [212]. The peak-to-peak widths of R1 and R2 were about 4.1 and 4.5 mT respectively. This contrasts with the result of Faulkner and Lomer

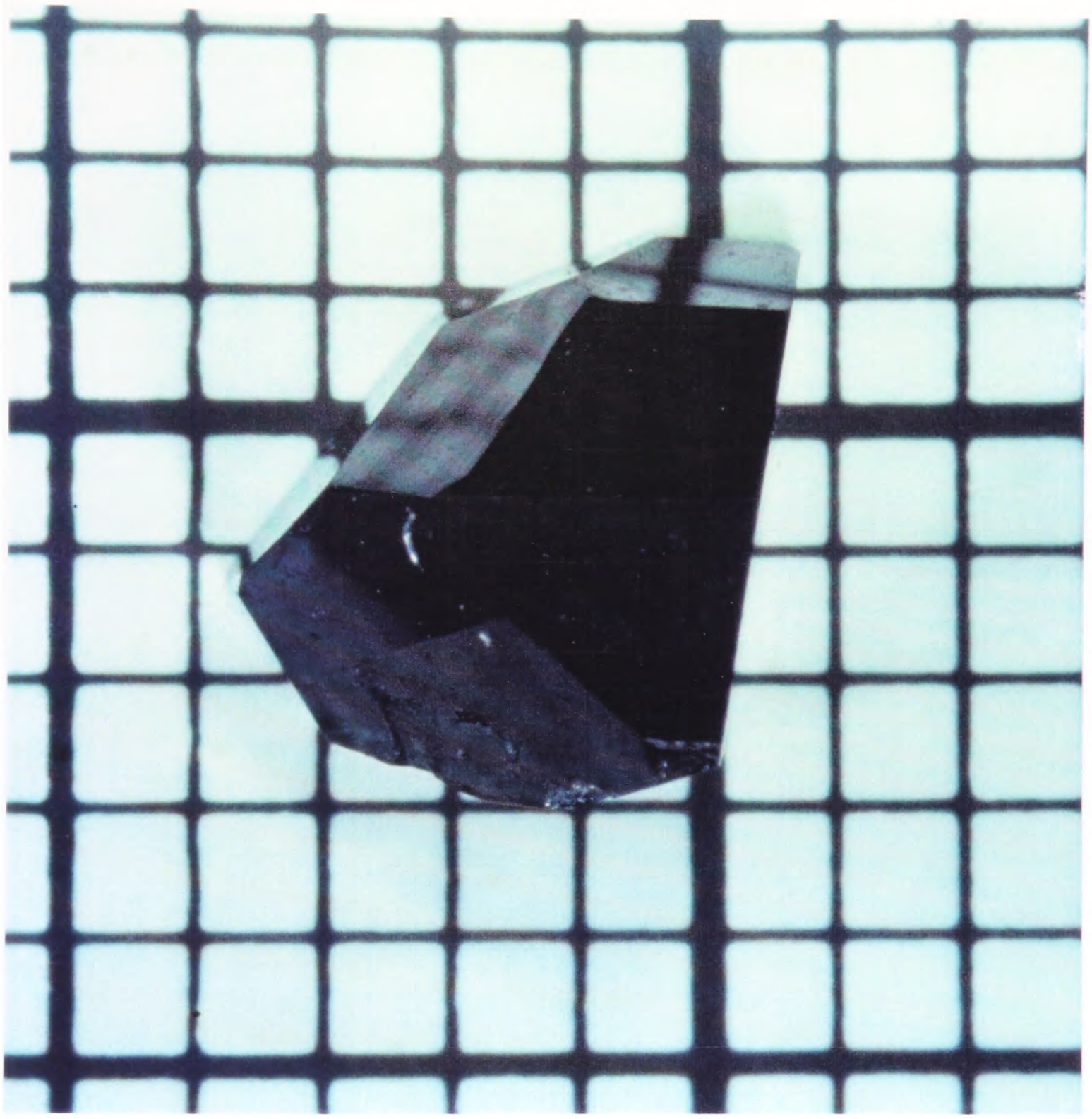


Plate IV: Sample (b): 50% $^{13}C$ isotopically enriched synthetic diamond after irradiation with 2 MeV electrons at a dose of $5 \times 10^{18} cm^{-2}$. The major grid size is 1 cm.

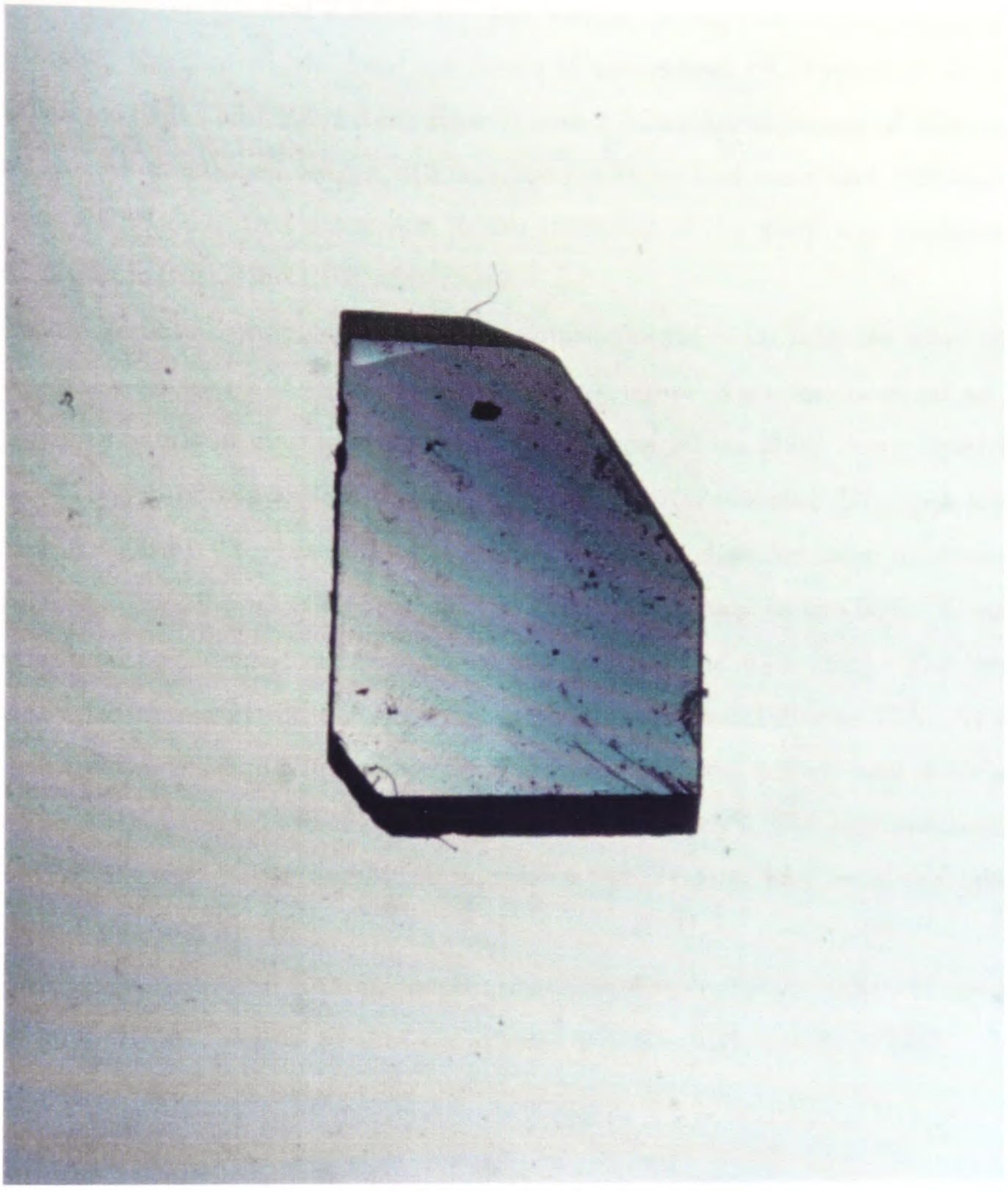


Plate V: Slice through sample (b) showing the uneven penetration of the green colouration

[212], who observed 0.5 and 2.5–5.0 mT line widths for R1 and R2 respectively, and suggests that the line widths here are result of unresolved $^{13}C$ hyperfine structure. The existence of R1 and R2 in very pure diamond is further evidence of their intrinsic nature. As mentioned earlier, R2 is a thermally excited state and will therefore be absent for most of this discussion as the majority of the work was performed at around 5K to increase the EPR sensitivity.

The unirradiated sample was found to luminesce for $\sim 20$ minutes after illumination with a standard 245 nm diamond viewing lamp. This was unusual as most luminescence bands in diamond have a lifetime below 50 ms [232]. Long lived luminescence is not unknown and has been observed in natural samples. One such sample, reported in 1909 by Crookes [175], phosphoresced in the dark for some minutes after exposure to a "small pocket electric light". The luminescence in the 50% $^{13}C$ sample was examined by Bowmar between room temperature and 77K [232]. The lifetime was found to increase from 680 s at room temperature to 2100 s at 77K. At room temperature the diamond luminescence was blue (between 2.2 eV and 3 eV), but below 200 K this turned green (between 1.8 eV and 2.4 eV). The luminescence was ascribed to electron-hole recombination, where the electron had been captured by $[N–C]^0$ and the hole by $[B]^-$.

Bowmar also collected Raman spectra from the sample which confirmed the presence of 50% $^{13}C$ and indicated that the crystal was of a high quality [232].

### 8.4.2 $[V]^-$

The structure of the $[V]^-$ defect is depicted in Figure 8.5. The vacancy is surrounded by four nearest neighbour carbon atoms in a tetrahedral arrangement. As the diamond studied was composed of 50% $^{13}C$, the hyperfine interaction with the ligand atoms was significant, and has to be taken into account in any discussion of the defect. The probabilities of having between zero and four nearest neighbour $^{13}C$ atoms, calculated by application of the binomial distribution (equation 3.50), are given in Table 8.5 for natural and 50% abundance of $^{13}C$. As the interaction of the electron with the $^{13}C$ is small it acts as a perturbation on the energy levels of the

Table 8.5: Probability of having $n$ $^{13}C$ nuclei in any of the four sites surrounding the negative vacancy for natural and 50% abundance of $^{13}C$.

| $\%^{13}C \rightarrow$ | 1.11% | 50.0% |
|---|---|---|
| $n^{13}C$'s | Probability | |
| 0 | 0.957 | 0.0625 |
| 1 | 0.0426 | 0.250 |
| 2 | $7.10\times10^{-4}$ | 0.375 |
| 3 | $5.27\times10^{-6}$ | 0.250 |
| 4 | $1.46\times10^{-8}$ | 0.0625 |
| Total | 1.00 | 1.00 |

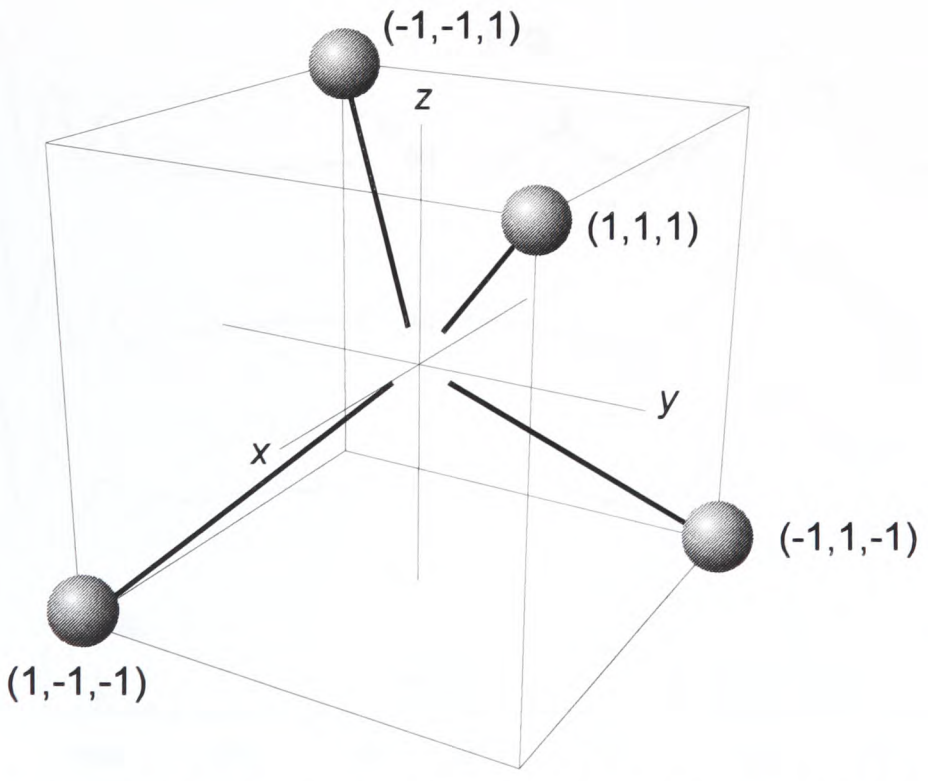



Figure 8.5: $[V]^-$ defect inscribed in a cube showing the four nearest neighbours and the cube coordinates assigned to them. The vacancy is at (0,0,0).

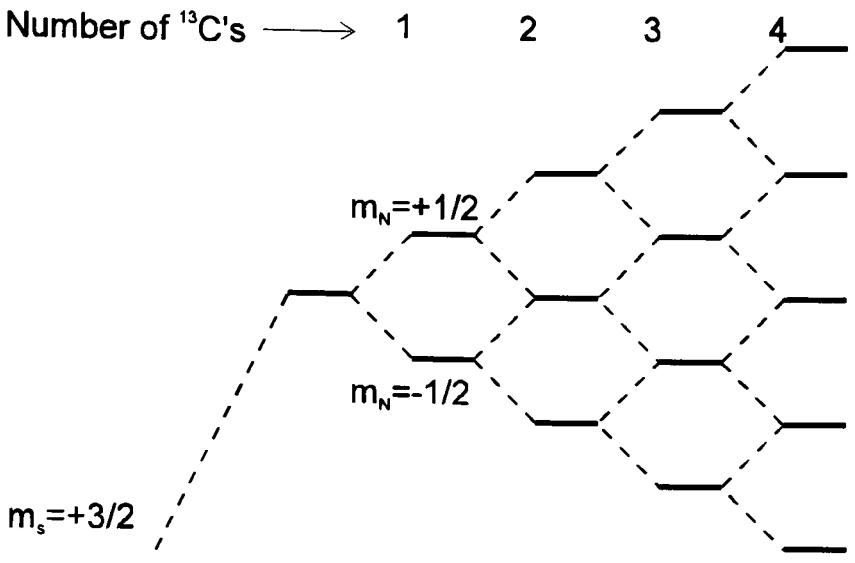



Figure 8.6: $^{13}$C hyperfine splittings in the $[V]^-$ centre, for one, two, three and four nearest neighbour $^{13}$C atoms, shown for the $m_s = \frac{3}{2}$ portion of the manifold.

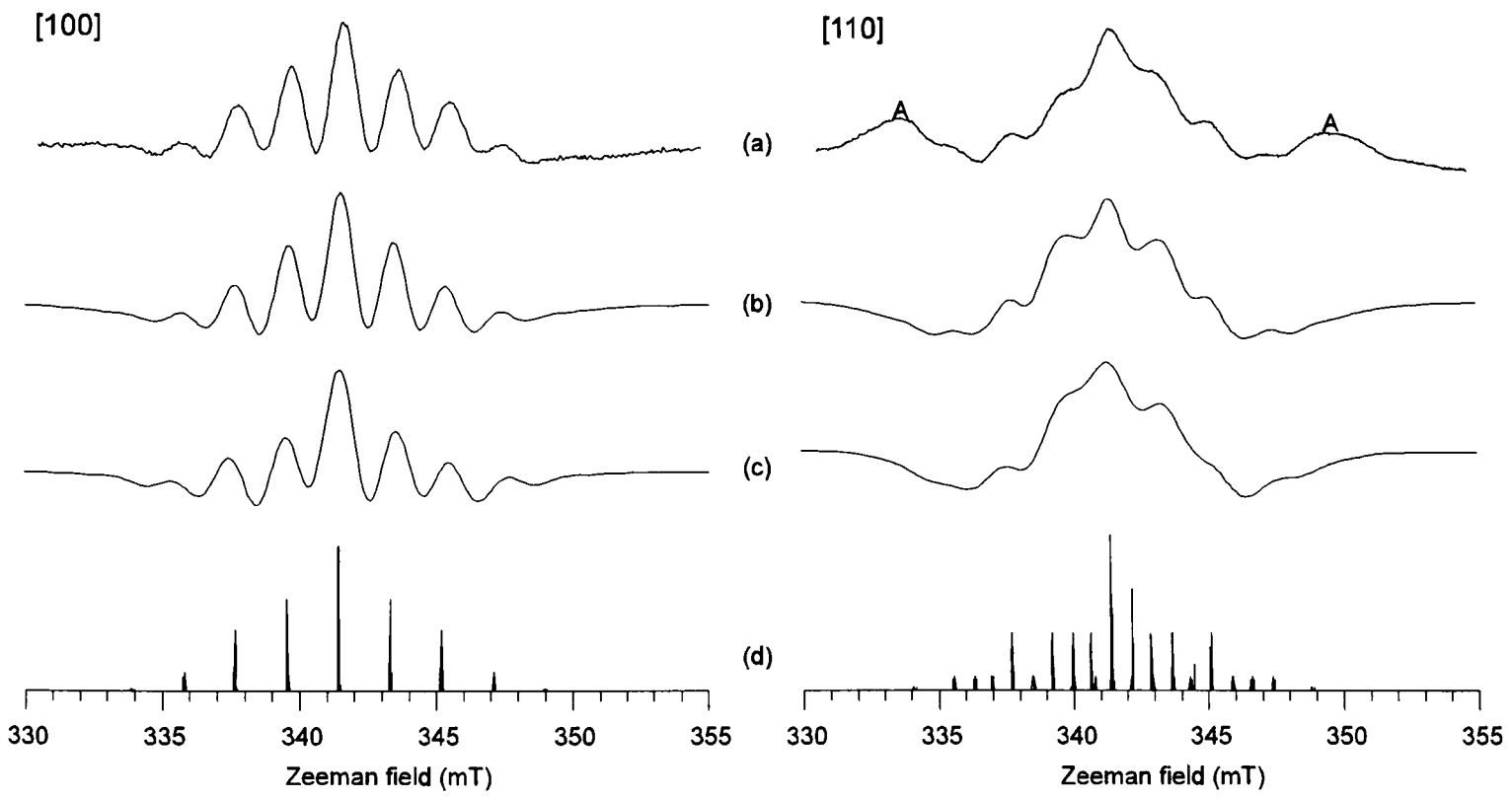



Figure 8.7: (a) Experimental and (b,c) simulated spectra for $[V]^-$ with 50% $^{13}$C. Zeeman field parallel to [100] and [110]. The stick plots (d) show the positions and intensities of the lines. The lines were simulated as second derivative (b) Lorentzians and (c) Gaussians. The broad lines labelled A have not been identified.

system, as seen in Figure 8.6, with each successive $^{13}$C interaction splitting each level in two. The system is then described by the following Hamiltonian:

$$\mathcal{H}_n = \mu_B \hat{\mathbf{S}} \cdot \underline{\mathbf{g}} \cdot \mathbf{B} + (1 - \delta_{0n}) \sum_{i=1}^{n} \left[ \hat{\mathbf{S}} \cdot R_i^T \underline{\mathbf{A}}_i R_i \cdot \hat{\mathbf{I}}_i - g_N \mu_N \hat{\mathbf{I}} \cdot \mathbf{B} \right] \tag{8.5}$$

where $n = 0 \ldots 4$ is the number of $^{13}$C atoms, $\delta_{0n}$ is the Kronecker delta function, and $R_i,\ i > 0$ runs over successive elements of $\mathcal{R}_1 = \{E, C_{2x}, C_{2y}, C_{2z}\}$, the 3D rotation matrix representation of the T group.

The experimental spectra were simulated by diagonalizing the $\mathcal{H}_n$ using *EPR.FOR* (§4.4.5). Each Hamiltonian was rotated by all twenty-four $T_d$ symmetry operations[6] and the resulting spectra were combined as detailed in §3.5. The simulations are compared to the experimental data in Figure 8.7. The following points about the simulations and their comparison to the experimental data should be noted:

1. Both Gaussian and Lorentzian line shapes were used. The best agreement with experiment was found when using line widths[7] of 1.14 mT ($\mathbf{B}\|[100]$) and 1.18 mT ($\mathbf{B}\|[110]$) for the Gaussian lines, and 1.80 mT for the Lorentzian lines.

2. The Lorentzian line shape *looks* better, however it must be remembered that the next-nearest neighbour hyperfine interactions have been omitted.

3. The next-nearest neighbour $^{13}$C hyperfine interactions will produce anisotropic splittings of between 4.8 and 3.3 mT, with the largest splitting with $\mathbf{B}\|[111]$ and the smallest with $\mathbf{B}\|[100]$.

4. The simulations in the [110] direction would fit the data better if they were reflected about the vertical axis. The asymmetry in the bulges next to the central bump is produced by second order terms in the hyperfine interaction. It is possible that the disagreement between the simulated and experimental data is caused (a) by omitting the next-nearest neighbours; or (b) by other defects

[6]There were only four distinct sites, however, it was simpler to use all 24.
[7]Half width at half height.

in the same region of the spectrum. Owing to the complexity of the hyperfine interaction it was not possible to distinguish between (a),(b).

5. The peaks marked with A are unidentified. These approach the centre more closely in the [111] direction and obscure the $[V]^-$ spectrum. They are not visible in the [100] direction.

### 8.4.3 R1

The R1 system exhibited surprisingly large line widths; when accurately aligned it was possible to simulate the R1 system using a Gaussian line with a half width of 3.0(1) mT, which was substantially wider than the $[V]^-$ hyperfine components.

A Gaussian line shape is expected, and is produced by dipolar broadening from the $^{13}C$ nuclei [233], however the total line width is unlikely to be caused by these distant interactions alone. In addition to distant dipolar contributions there will be stronger hyperfine interactions with the nearest and possibly next-nearest neighbour $^{13}C$ atoms. The $^{13}C$ hyperfine interactions measured by Lea-Wilson and Lomer [225] (Table 8.3) produce pairs of lines centred on the $^{12}C$ lines, with separations of between 1.0 and 4.0 mT, for a single interacting nucleus. As the structure of the R1 defect is unknown, it is not possible to write down the Hamiltonian for the nearest neighbours, as was done for $[V]^-$, and then simulate the system. Despite this it is reasonable to assume that the dipolar broadening produces a line width of around 1 mT [234] which, when combined with the hyperfine interaction from the many neighbouring $^{13}C$ atoms, produces broad Gaussian shaped lines with a half width of about 3 mT. The dipolar broadened line width could be less if the paramagnetic electron wavefunction is sufficiently dispersed to interact directly with the next-nearest neighbouring ligand atoms. It is also not obvious as to how the interaction labelled *set 3* in Table 8.3 would be produced. These questions should be answered by experiments currently in progress[8] on a 5% $^{13}C$ sample, where hyperfine lines are resolved owing to the smaller dipolar broadening.

[8]Performed by Daniel Twitchen at the University of Oxford.

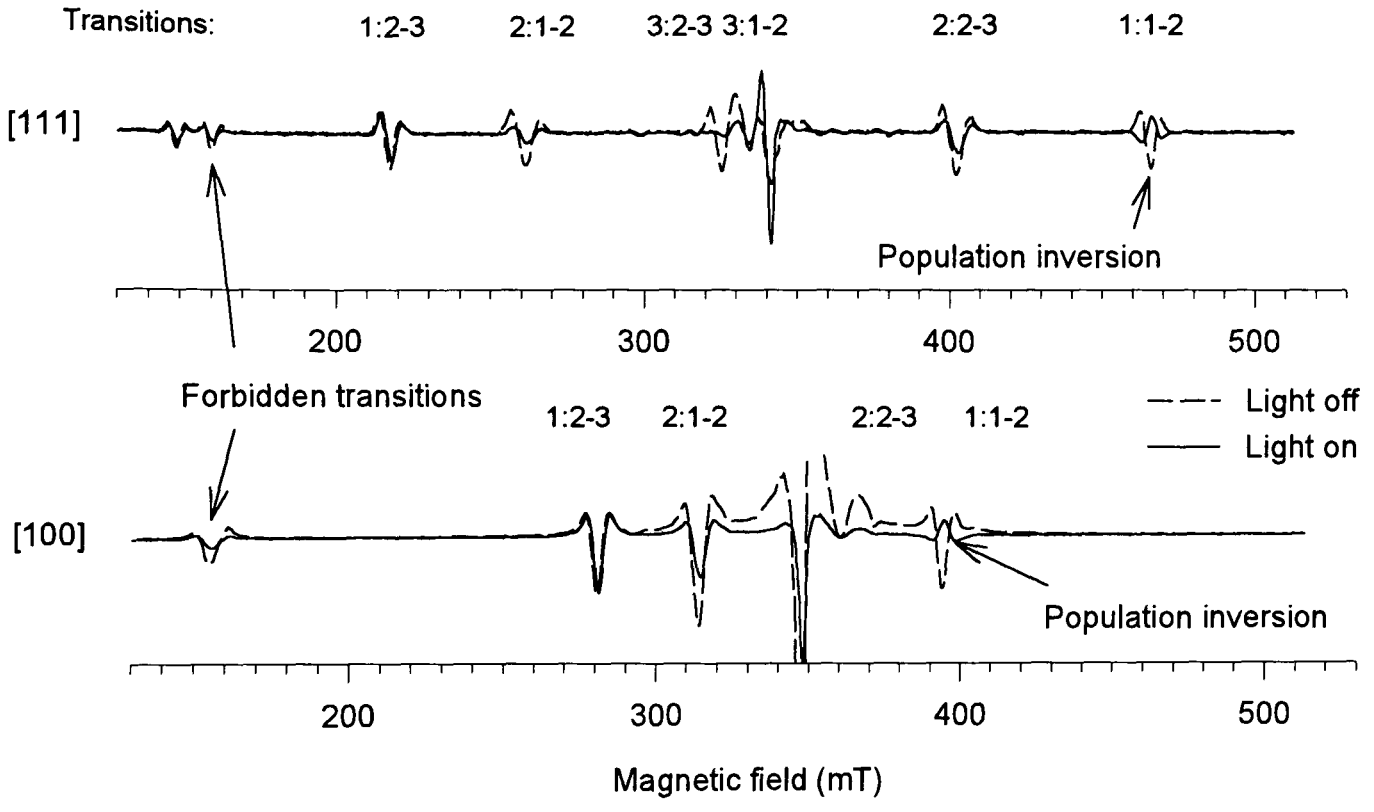



Figure 8.8: Effect of illumination with the full spectrum of Hg lamp on the R1 system for Zeeman field parallel to [100] and [111], at 4K, X-band, collecting the second harmonic of the field modulated absorption signal.

When the R1 was illuminated with the full spectrum of the Hg lamp, a population inversion was observed. The spectra for $\mathbf{B}\|\langle 111\rangle$ and $\langle 100\rangle$ are shown in Figure 8.8. The labelling in the figure is based upon the symmetry of the fine structure tensor. The symmetry dictates that in the [100] direction degeneracies exist such that only two sets of lines (out of a possible twelve) occur, and in the [111] direction three sets of lines occur. The lines appear in pairs corresponding to the transition between the upper two (1–2) or lower two (2–3) levels in the $S$=1 manifold. Each transition is therefore labelled by a number denoting the set of lines, counting from the outside in, and the levels between which it occurs, for example 1:2–3. From the figure it is evident that transitions from different sites and between different energy levels behave differently under the influence of light. Transitions from the [100] direction serve as a good example. Transition 1:2–3 is hardly affected by the light, whereas the phase of 1:1–2 is inverted with respect to the other transitions. Transition 1:1–2 is therefore emitting microwaves and the system is acting as a maser. The half-field

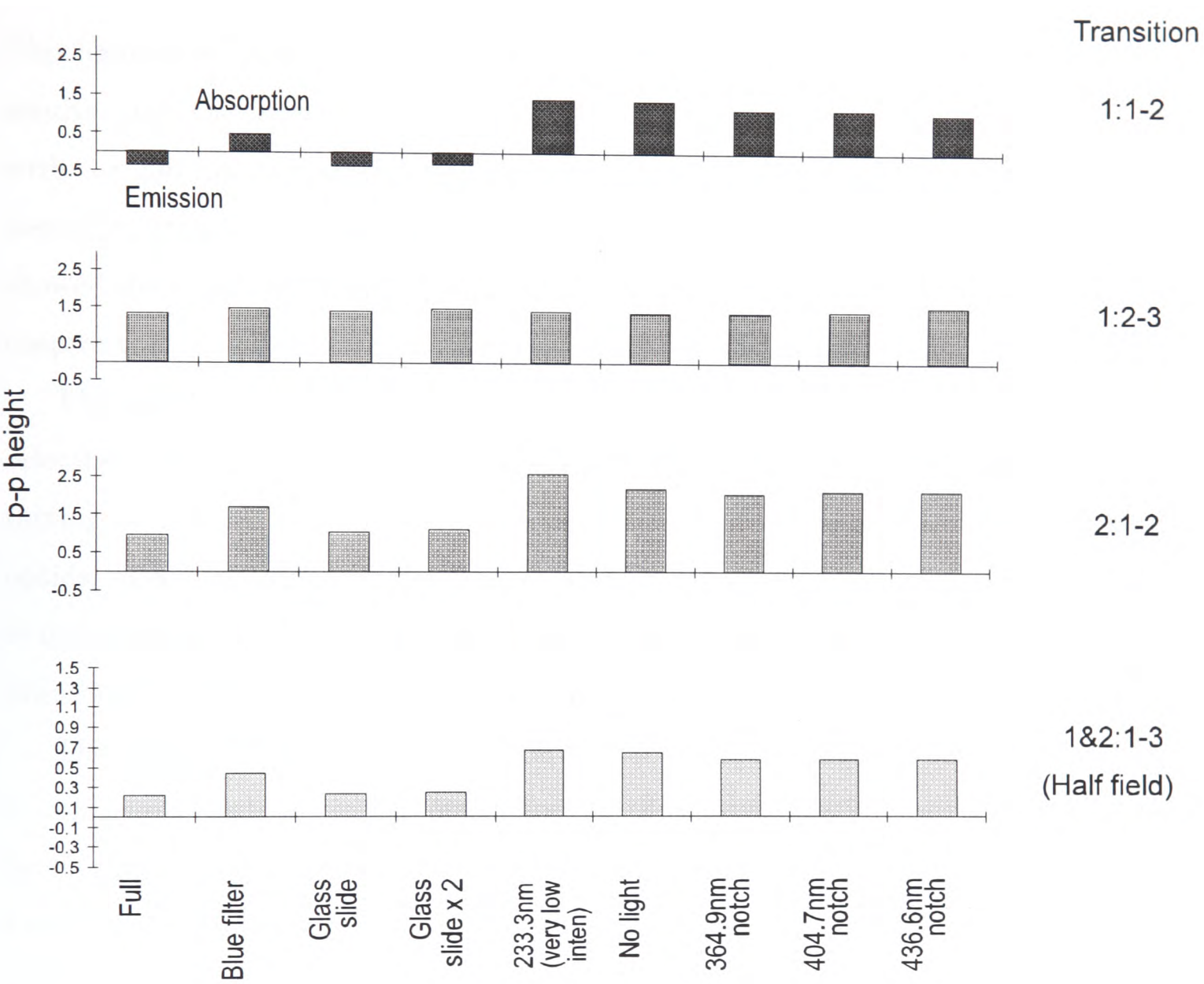



Figure 8.9: Quantitative effect of light of different wavelengths on the R1 system. The transition 1–2 for site 2 was not resolved from the $[V]^-$ system. The *Blue filter* transmitted light with $\lambda < 400$ nm, while the glass slides transmitted light with $\lambda > 300$ nm. $\mathbf{B}\|[100]$.

transitions[9] are also affected, but it must be noted that here transitions from both sites are superimposed. Thus, for site 1, population is probably being added to level 1 or removed from levels 2 and 3 in equal amounts. A similar result holds for site 1 in the [111] direction. Figure 8.9 shows the effects of light of various wavelengths on the transitions in the [100] direction. The transition 2:2–3 is omitted as quantitative results could not be obtained owing to the overlap with the spectrum from $[V]^-$. This figure also shows that 1:2–3 remains almost unaffected in contrast to 1:1–2. The results from the insertion of a glass slide into the beam, which blocked all photons with $\lambda < 230$ nm and attenuated 300 nm photons by 80%, show that uv light in not needed to create the defect. Careful comparison of the 10 nm band pass (notch) filters showed that the largest effect was produced by the 436 nm filter, not the 364 nm filter, despite the fact that there was more intensity in the 364 nm Hg line.

The results from the preliminary optical measurements are consistent with a spin-selective, orientation-dependent, optical transition (like that facilitated by spin-orbit mixing of states) which changes the populations of the spin manifold. Unlike the optical effects obtained in the $[N–N]^+$ and $[V]^-$ centres, high energy (uv) radiation is not needed to produce the population changes. This sample was the first to be illuminated using the system described in §4.3.5.

The measurement of the sign of the fine structure interaction as negative in §7.6.2 is consistent with a dipolar origin for the fine structure interaction, as proposed by Faulkner and Lomer [212]. When viewed within the strained vacancy model of Lowther and Mainwood [102], the sign defines the order of the low-lying energy levels and yields information regarding the magnitude of the Jahn-Teller interaction.

### 8.4.4 ENDOR

Attempts at ENDOR failed because it was not possible to produce enough field modulation in the ENDOR cavity. The maximum modulation was $\sim 0.1$ mT while the narrowest line in the sample had a half width of about 1.2 mT. It therefore impossible to observe steady state EPR from the sample, let alone ENDOR, and the experiment

[9] See §7.3.2 for a description of the origin half-field lines.

was postponed until an ENDOR cavity with greater field modulation could be constructed.

## 8.5 Conclusions

In the preliminary investigation of radiation damaged 50% $^{13}C$ enriched type IIa diamond the presence the $[V]^-$, R1 and R2 radiation damage defects were identified. All the EPR transitions were dipolar broadened to an extent that in most cases the transitions produced by the $^{13}C$ interaction were not resolvable. The exception was the $[V]^-$ centre with $\mathbf{B}\|[100]$, which was successfully simulated by taking account of the $^{13}C$ interactions. Creation of large concentrations of R1 and R2 in very pure diamond lends credence to an intrinsic model for the centres.

Optical activity was observed upon exposure of the R1 system to light, with some transitions undergoing a full phase reversal and appearing in emission. The effect was dependent on orientation and was produced by light with wavelengths longer than 300 nm. It was similar to that observed in the $[V]^*$ centre studied in Chapter 6, and by analogy might be produced by orientation dependent mixing with an excited state, such as that induced by the spin-orbit interaction. Optical activity in the EPR system yields information about the electronic energy levels, and can provide a bridge between optical and magnetic resonance spectroscopy. This is the first time that optical coupling has been observed in the R1 EPR system.

Additional information has been gained about the electronic energy levels within the R1 system, with the measurement of the negative sign of the fine structure interaction in §7.6.2. This was the first time that this measurement had been made in diamond, and it has served to constrain further any theoretical model of the system.

The investigation was preliminary, and has not been pursued further because the $^{13}C$ concentration was too large, broadening the lines and resulting in a complex hyperfine structure. A new sample has recently been donated by General Electric which has 5% $^{13}C$ enrichment, as mentioned in §8.4.3. This sample has been irradiated, and clearly resolved hyperfine interactions can be observed. It is hoped that

the new sample will have the same properties as the one studied here, without the problem of very broad lines, and will facilitate ENDOR measurement of the hyperfine interaction, finally resolving the structure of the R1 and possibly R2 systems.

# Appendix A

# W11–W14 depopulation curves

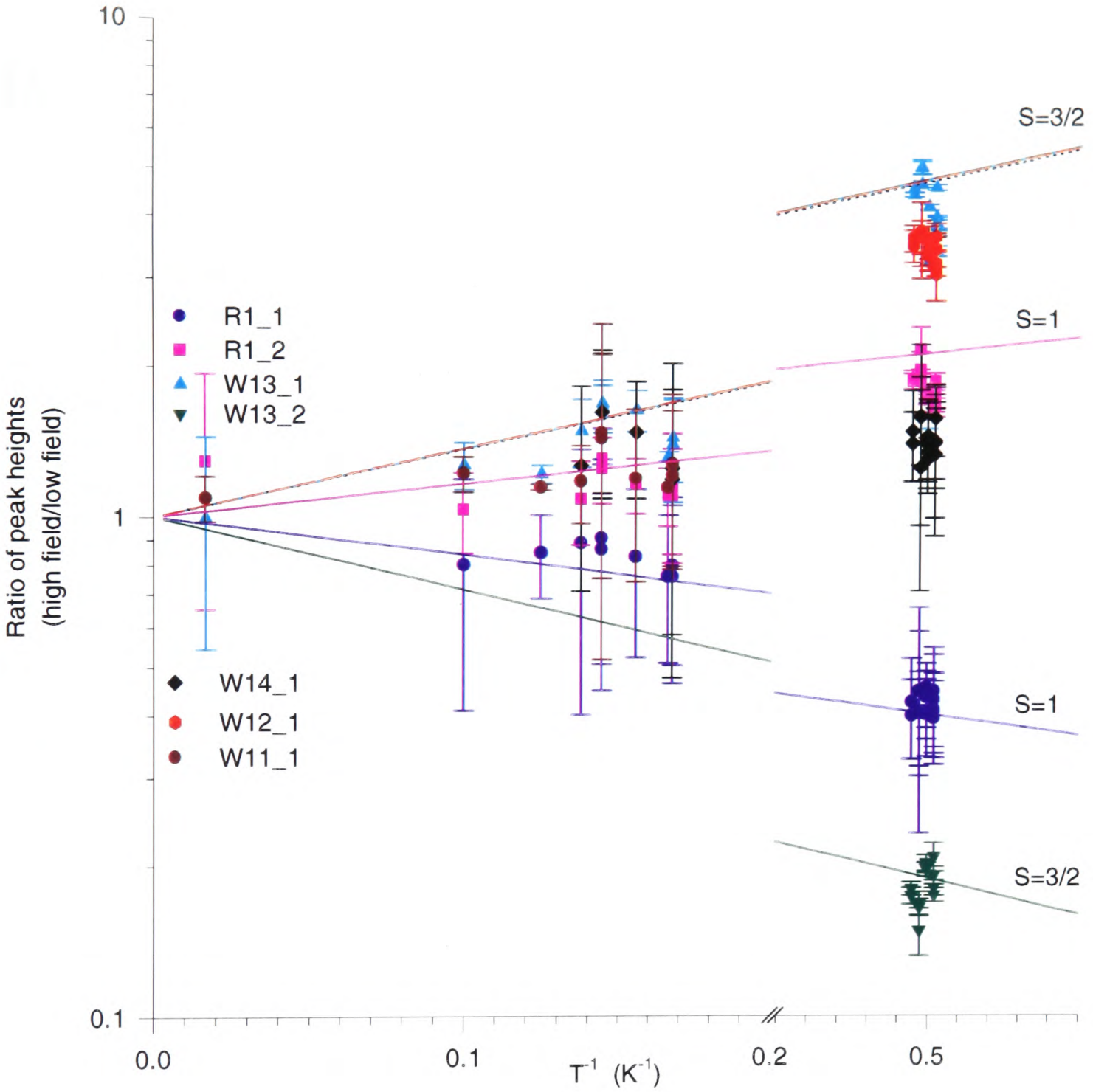



Figure A.1: Ratio of transitions between upper and lower levels of the spin manifolds for W11, W12, W13, W14 and R1 plotted as a function of temperature. The W11 centre depopulates and no result can be reached. Theoretical curves are plotted.

# Bibliography


[1] E.Bruton. *Diamonds.* N.A.G.Press,London, 1970.

[2] D.E.Eicholz (translator). *Pliny's Natural History*, volume X, Libri XXXVI-XXXVII. Heineman, London, 1962.

[3] Marcus Manilius. *Astronomica.* Harvard University Press, Cambridge, Mass., 1977. Translated by G.P.Gould.

[4] C.Plini Secundi. *Naturalis historia*, volume V, Libri XXXI–XXXVII. Lipsia, London, 1875. edidit C.Mayhoff.

[5] C.M.Welbourn. In S.Saito, N.Fujimori, O.Fukunaga, M.Kamo, K.Kobashi, and M.Yoshikawa, editors, *Advances in New Diamond Science and Technology*, pages 327–332. Scientific Publishing Division of MYU, Tokyo, Japan, 1994.

[6] E.Wilks and J.Wilks. *Properties and Applications of Diamond.* Butterworth-Heineman, Oxford, 1991.

[7] M.Seal. High technology applications of diamond. In J.E.Field, editor, *The Properties of Natural and Synthetic Diamond*, chapter 16, pages 607–636. Academic Press, London, 1992.

[8] R.C.Eden. *Diamond and Related Mat.*, 2:1051–1058, 1993.

[9] G.Lu, K.J.Gray, E.F.Borchelt, and L.K.Bigelow. *Diamond and Related Mat.*, 2:1064–1068, 1993.

[10] C.A.Klein. *Diamond and Related Mat.*, 2:1024–1032, 1993.

[11] D.R.Kania, M.I.Landstrass, M.A.Plano, L.S.Pan, and S.Han. *Diamond and Related Mat.*, 2:1012–1019, 1993.

[12] H.K.Gan, F.Borchelt, W.Dulinski, D.Fujino, R.Gilman, S.Han, J.Hassard, A.Howard, H.Kagan, D.Kania, R.Kass, S.Kim, G.Kumbartski, M.H.Lee, G.Lu, E.Nygard, R.Malchow, L.S.Pan, S.Chnetzer, R.Stone, J.Straver, R.J.Teserek, W.Trischuk, G.Thomson, P.Weilhammer, C.White, R.L.Woodin, S.Zhao, M.Zeoller, and Y.Sugimoto. Diamond detectors for experiments at high luminosity colliders. In S.Saito, N.Fujimori, O.Fukunaga, M.Kamo, K.Kobashi,

and M.Yoshikawa, editors, *Advances in New Diamond Science and Technology*, pages 687–696. Scientific Publishing Division of MYU, Tokyo, 1994.

[13] H.Kagan. Diamas, a diamond based detector for the SSC. In D.Axes, D.Bryman, and M.Comyn, editors, *The Vancouver Meeting, Particles and Fields '91*, volume 2, pages 1194–1196. World Scientific, Singapore, 1992.

[14] K.Okano, H.Kiyota, T.Iwasaki, T.Kurosu, M.Iida, and T.Nakamura. *Appl. Phys. Lett.*, 58:840–841, 1991.

[15] K.Miyata, K.Kobashi, and D.L.Dreifus. *Diamond and Related Mat.*, 2:1107–1111, 1993.

[16] F.Bridges, G.Davies, J.Robertson, and A.M.Stoneham. *J. Phys. C.*, 2:2875–2928, 1990.

[17] G.Davies, editor. *Properties and Growth of Diamond.* INSPEC, London, 1994.

[18] R.Robertson, J.J.Fox, and A.E.Martin. *Phil. Trans. Roy. Soc. A*, (232):463ff, 1934.

[19] A.T.Collins. *Physica B*, 185:284–296, 1993.

[20] P.W.Atkins. *Molecular Quantum Mechanics.* Oxford University Press, Oxford, 2nd edition, 1983.

[21] A.Cox. D.Phil thesis, University of Oxford, 1993.

[22] M.E.Newton. D.Phil thesis, University of Oxford, 1989.

[23] J.E.Field, editor. *The Properties of Diamond.* Academic Press, London, 1979.

[24] J.E.Field, editor. *The Properties of Natural and Synthetic Diamond.* Academic Press, London, 1992.

[25] I.Herbert. *The Diamond Diggers.* Tom Stacey, London, 1972.

[26] L.du Preez. PhD thesis, University of the Witwatersrand, South Africa, 1965.

[27] G.Davies and M.F.Hamer. *Proc. R. Soc. (London) Series A*, 348:285–298, 1976.

[28] C.D.Clark and C.A.Norris. *J. Phys. C.*, 4:2223–2229, 1971.

[29] G.Davies. *J. Phys. C.*, 7:3797–3809, 1974.

[30] J.H.N.Loubser and J.A.van Wyk. *Diamond Res., Suppl. to Ind. Diamond Rev. (UK)*, 11:11–14, 1977.

[31] A.T.Collins, M.F.Thomaz, and M.I.B.Jorge. *J. Phys. C.*, 16:2177–2181, 1983.

[32] R.T.Harley, M.J.Henderson, and R.M.Macfarlane. *J. Phys. C.*, 17:L233–L236, 1984.

[33] N.R.S.Reddy, N.B.Manson, and E.R.Krausz. *J. Lumin*, 38:46–47, 1987.

[34] E.van Oort, N.B.Manson, and M.Glasbeek. *J. Phys. C.*, 21:4385–4391, 1988.

[35] D.A.Redman, S.Brown, R.H.Sands, and S.C.Rand. *Phys. Rev. Lett.*, 67(24):3420–3423, 1991.

[36] E.van Oort and M.Glasbeek. *Phys. Rev. B*, 40(10):6509–6517, 1989.

[37] E.van Oort, P.Stroomer, and M.Glasbeek. *Phys. Rev. B*, 42(13):8605–8608, 1990.

[38] I.Hiromitsu, J.Westra, and M.Glasbeek. *Phys. Rev. B*, 46(9):5303–5310, 1992.

[39] I.Hiromitsu, J.Westra, and M.Glasbeek. *Phys. Rev. B*, 46(17):10600–10612, 1992.

[40] M.Glasbeek, I.Hiromitsu, and J.Westra. *J. Lumin.*, 58:74–77, 1994.

[41] D.A.Redman, Q.Shu, S.W.Brown, A.Lenef, Y.Liu, J.Whitaker, S.C.Rand, S.Satoh, K.Tsuji, and S.Yazu. *Mat. Res. Soc. Symp. Proc.*, 242:127–132, 1992.

[42] D.Redman, Q.Shu, A.Lenef, and S.C.Rand. *Optics Lett.*, 17(3):175–177, 1992.

[43] K.Holliday, X.-F.He, P.T.H.Fisk, and N.B.Manson. *Optics Lett.*, 15(17):983–985, 1990.

[44] X.-Fe.He, N.B.Manson, and P.T.Fisk. *Phys. Rev. B*, 47(14):8809–8815, 1993.

[45] X.-Fe.He, N.B.Manson, and P.T.Fisk. *Phys. Rev. B*, 47(14):8816–8822, 1993.

[46] N.B.Manson, X.-F.He, and P.T.H.Fisk. *Optics Lett.*, 15(19):1094–1096, 1990.

[47] C.J.M.Tavares, M.A.Costa Neto, R.Sitters, N.B.Manson, and M.Glasbeek. *Phys. Rev. B*, 50(18):13795–13798, 1994.

[48] E.van Oort, B.van der Kamp, R.Sitters, and M.Glasbeek. *J. Lumin.*, 48 & 49:803–806, 1991.

[49] D.Redman, S.Brown, and S.C.Rand. *J. Opt. Soc. Am. B*, 9(5):768–774, 1992.

[50] C.Wei and N.B.Manson. *Phys.Rev.A*, 49(6):4751–4764, 1994.

[51] H.Hanzawa, H.Nishikori, Y.Nisida, S.Sato, T.Nakashima, S.Sasaki, and N.Miura. *Physica B*, 184:137–140, 1993.

[52] A.Mainwood. *Phys. Rev. B*, 49(12):7934–7940, 1994.

[53] W.V.Smith, P.P.Sorokin, I.L.Gelles, and G.J.Lasher. *Phys. Rev.*, 115(6):1546–1552, 1959.

[54] W.K.Kaiser and W.L.Bond. *Bull. Am. Phys. Soc. Ser. II*, 4:27, 1959. paper J5.

[55] W.K.Kaiser and W.L.Bond. *Phys. Rev.*, 115:857–863, 1959.

[56] M.H.Nazaré. Isolated substitutional nitrogen in diamond. In G.Davies, editor, *Properties and Growth of Diamond*, chapter 3.2, pages 85–87. INSPEC, London, 1994.

[57] A.Cox, M.E.Newton, and J.M.Baker. *J. Phys. C.*, 6:551–563, 1994.

[58] S.Zhang, S.C.Ke, M.E.Zvanut, H.T.Tohver, and Y.K.Vohra. *Phys. Rev. B*, 49(21):15392–15395, 1994.

[59] M.E.Newton, 1994. Private communication.

[60] A.M.Stoneham. Diamond: Recent advances in theory. In J.E.Field, editor, *The Properties of Natural and Synthetic Diamond*, chapter 1, pages 3–34. Academic Press, London, 1992.

[61] R.P.Messmer and G.D.Watkins. *Phys. Rev. Lett.*, 25(10):656–659, 1970.

[62] R.P.Messmer and G.D.Watkins. In J.E.Whitehouse, editor, *Radiation Damage and Defects in Semiconductors (1972):IOP Conf. Proc. No.16*, pages 255–261. Institute of Physics, London, 1973. paper 29.

[63] A.Mainwood. *J. Phys. C.*, 12:2543–2549, 1979.

[64] P.R.Briddon, M.I.Heggie, and R.Jones. In R.Messier, T.J.Glass, J.E.Butler, and R.Roy, editors, *Proc. 2nd Int. Conf. on New Diamond Science and Technology*, page 63. Mater.Res.Soc.Symp.Int.Proc. NDST2-C3 Pittsburg, PA., 1991.

[65] R.Jones, P.R.Briddon, and S.Öberg. *Phil. Mag. Lett.*, 66(2):67–74, 1992.

[66] P.R.Briddon and R.Jones. *Physica B*, 185:179–189, 1993.

[67] S.A.Kajihara, A.Antonelli, J.Bernholc, and R.Car. *Phys. Rev. Lett.*, 66:2010–2013, 1991.

[68] S.A.Kajihara, A.Antonelli, and J.Bernholc. *Physica B*, 185:144–149, 1993.

[69] C.Cunha, S.Canuto, and A.Fazzio. *Phys. Rev. B*, 48(24):17806–17810, 1993.

[70] A.B.Anderson and S.P.Mehandru. *Phys. Rev. B*, 48(7):4423–4427, 1993.

[71] A.R.Lang, M.Moore, A.P.W.Makepeace, W.Wierzchowski, and C.M.Welbourn. *Phil. Trans. Roy. Soc. A*, (337):497–520, 1991.

[72] A.Mainwood and A.M.Stoneham. *J. Phys. C.*, 6:4917–4927, 1994.

[73] Y.Ma, P.Skytt, N.Wassdahl, P.Glans, D.C.Mancini, J.Guo, and J.Nordgren. *Phys. Rev. Lett.*, 71(22):3725–3728, 1993.

[74] I.Kiflawi, A.E.Mayer, P.M.Spear, J.A.van Wyk, and G.S.Woods. *Phil. Mag. B*, 69(6):1141–1147, 1994.

[75] S.C.Lawson, H.Kanda, and M.Sekita. *Phil. Mag. B*, 68(1):39–46, 1993.

[76] S.C.Lawson and H.Kanda. *J. Appl. Phys.*, 73(8):3967–3973, 1993.

[77] V.A.Nadolinny and A.P.Yelisseyev. *Diamond and Related Mat.*, 3:17–21, 1993.

[78] V.Nadolinny and A.Yelisseyev. *Diamond and Related Mat.*, 3:1196–1200, 1994.

[79] J.Isoya, H.Kanda, and Y.Morita. ESR studies of point defects in synthetic diamond crystals. In S.Saito, N.Fujimori, O.Fukunaga, M.Kamo, K.Kobashi, and M.Yoshikawa, editors, *Advances in New Diamond Science and Technology*, pages 351–354. Scientific Publishing Division of MYU, Tokyo, Japan, 1994.

[80] J.E.Lowther. *Phys. Rev. B*, 51(1):91–96, 1995.

[81] A.T.Collins and E.C.Lightowlers. Electrical properties. In J.E.Field, editor, *The Properties of Diamond*, chapter 3, pages 79–105. Academic Press, London, 1979.

[82] C.A.J.Ammerlan. Defects and radiation effects in semiconductors. In *Defects and Radiation Effects in Semiconductors*, page 81ff. Institute of Physics, London, 1981.

[83] C.A.J.Ammerlan and R.van Kemp. *J. Phys. C.*, 18:2623–2629, 1985.

[84] J.H.N.Loubser and J.A.van Wyk. *S. Afr. J. Phys.*, 10:165ff, 1987.

[85] B.Dischler, W.Rothemund, C.Wild, R.Locher, H.Biebl, and P.Koidl. *Phys. Rev. B*, 49(3):1685–1689, 1994.

[86] S.J.Breuer and P.R.Briddon. *Phys. Rev. B*, 49(15):10332–10336, 1994.

[87] N.D.Samsonenko, V.V.Tokil, and S.V.Gorban. *Sov. Phys. -Solid St.*, 33(8): 1409–1410, 1992.

[88] M.A.Lea-Wilson, J.N.Lomer, and J.A.van Wyk. *Phil. Mag. B*, 70(1):101–107, 1994.

[89] G.E.Uhlenbeck and S.Goudsmit. *Nature*, 117:264–265, 1926.

[90] E.Merzbacher. *Quantum Mechanics.* John Wiley & Sons, New York, 2nd edition, 1970.

[91] A.Abragam and B.Bleaney. *Electron paramagnetic resonance of transition ions.* Dover, New York, 1986.

[92] S.Geschwind, editor. *Electron Paramagnetic Resonance.* Plenum Press, New York, 1972.

[93] J.E.Wertz and J.R.Bolton. *Electron spin resonance: Elementary Theory and Practical Applications.* Chapman and Hall, New York, 1986.

[94] W.Weltner. *Magnetic Atoms and Molecules.* Dover Publications, Inc., New York, 1983.

[95] J.R.Morton and K.F.Preston. *J. Magn. Reson.*, 30:577–582, 1978.

[96] G.Feher. *Phys. Rev.*, 105:1122–1123, 1957.

[97] J.A.Weil, J.R.Bolton, and J.E.Wertz. *Electron Paramagnetic Resonance: Elementary theory and practical applications.* Wiley, New York, 1994.

[98] J.A.van Wyk and J.H.N.Loubser. *J. Phys. C.*, 5:3019–3026, 1993.

[99] C.A.Coulson and M.J.Kearsley. *Proc. R. Soc. (London) Series A*, 241:433–454, 1957.

[100] A.G.Every and D.S.Schonland. *Solid State Comm.*, 3:205–207, 1965.

[101] A.Mainwood. *J. Phys. C.*, 11:2703–2710, 1978.

[102] J.E.Lowther and A.Mainwood. *J. Phys. C.*, 6:6721–6724, 1994.

[103] O.D.Tucker, M.E.Newton, and J.M.Baker. *Phys. Rev. B*, 50(21):15586–15596, 1994.

[104] J.M.Baker and M.E.Newton. *Appl. Magn. Reson.*, 7:209–235, 1994.

[105] C.A.Coulson. *Valence.* Oxford University Press, Oxford, 1960.

[106] A.H.Edwards and W.B.Fowler. *Phys. Rev. B*, 41:10816–10823, 1990.

[107] S.J.Joshua. *Symmetry Principles and Magnetic Symmetry in Solid State Physics.* Adam Hilger, London, 1991.

[108] E.Kreyszig. *Advanced Engineering Mathematics.* John Wiley & Sons, New York, 1988.

[109] D.G.McGavin, M.J.Mombourquette, and J.A.Weil. Written at the Department of Chemistry, University of Saskatchewan, Saskatoon, Saskatchewan, Canada, S7N 0W0. Any correspondence should be addressed to Prof.J.A.Weil.

[110] C.P.Poole. *Electron spin resonance: A Comprehensive Treatise on Experimental Techniques.* John Wiley, New York, 1983.

[111] A.J.O'Connell. D.Phil thesis, University of Oxford, 1992.

[112] J.S.Hyde, M.E.Newton, R.A.Strangeway, T.G.Camenisch, and W.Froncisz. *Rev. Sci. Instrum.*, 62(12):2969–2975, 1991.

[113] C.Hoentzch, J.R.Niklas, and J.M.Spaeth. *Rev. Sci. Instrum.*, 49(8):1100–1102, 1978.

[114] G.Grampp. *Rev. Sci. Instrum.*, 56(11):2050–2051, 1985.

[115] S.L.Dexheimer and M.P.Klein. *Rev. Sci. Instrum.*, 59(5):764–766, 1988.

[116] F.N.H.Robinson. *J. Phys. E.*, 20:502–504, 1987.

[117] R.C.Weast, editor. *Handbook of Chemistry and Physics.* The Chemical Rubber Co., Cleveland, USA, 52nd edition, 1971.

[118] A.Cox, M.E.Newton, and J.M.Baker. *J. Phys. C.*, 4:8119–8130, 1992.

[119] M.E.Newton and J.M.Baker. *J. Phys. C.*, 3:3591–3603, 1991.

[120] P.T.Robinson. D.Phil thesis, University of Oxford, 1985.

[121] G.B.B.M.Sutherland, D.E.Blackwell, and W.G.Simeral. *Nature*, 174(4437):901–904, 1954.

[122] J.F.H.Custers and F.A.Raal. *Nature*, 179(4553):268–269, 1957.

[123] E.V.Sobolev, V.I.Lisoivan, and S.V.Lenskaya. *Sov. Phys. -Dokl.*, 12(7):665–668, 1968.

[124] G.Davies. *J. Phys. C.*, 9:L537–L542, 1976.

[125] E.T.Evans. In *Diamond Conference, Bristol.* Unpublished, 1972. paper 7.

[126] M.D.Crossfield, G.Davies, A.T.Collins, and E.C.Lightowlers. *J. Phys. C.*, 7:1909–1917, 1974.

[127] G.Davies. *J. Phys. C.*, 3:2474–2486, 1970.

[128] L.A.Turk and P.G.Klemens. *Phys. Rev. B*, 9(10):4422–4428, 1974.

[129] R.Berman, P.R.W.Hudson, and M.Martinez. *J. Phys. C.*, 8:L430–L434, 1975.

[130] R.Mykolajewycz, J.Kalnais, and A.Smakula. *J. Appl. Phys.*, 35:1773–1778, 1964.

[131] M.Ya.Shcherbakova, E.V.Sobolev, N.D.Smsonenko, and V.K.Aksenov. *Sov. Phys. -Solid St.*, 11:1104–1106, 1969.

[132] G.S.Woods. Interconversion between the various forms of nitrogen in diamond. In G.Davies, editor, *Properties and Growth of Diamond*, chapter 3.8, pages 98–100. INSPEC, London, 1994.

[133] S.R.Boyd, I.Kiflawi, and G.S.Woods. *Phil. Mag. B*, 69(6):1149–1153, 1994.

[134] J.A.van Wyk and J.H.N.Loubser. *J. Phys. C.*, 16:1501–1506, 1983.

[135] J.H.N.Loubser, J.A.van Wyk, and C.M.Welbourn. *J. Phys. C.*, 15:6031–6036, 1982.

[136] C.D.Clark and S.T.Davey. *J. Phys. C.*, 17:1127–1140, 1984.

[137] G.S.Woods. *Proc. R. Soc. (London) Series A*, 407:219–238, 1986.

[138] G.S.Woods, G.C.Purser, A.S.Mtimkulu, and A.T.Collins. *J. Phys. Chem. Solids*, 51:1191ff, 1990.

[139] G.S.Woods, J.A.van Wyk, and A.T.Collins. *Phil. Mag. B*, 62:589–595, 1990.

[140] W.H.Press, B.P.Flannery, S.A.Teukolsky, and W.T.Vetterling. *Numerical Recipes in Pascal: the art of scientific computing.* Cambridge University Press, 1989.

[141] G.Feher and E.A.Gere. *Phys. Rev.*, 114(5):1245–1256, 1959.

[142] P.W.Anderson, B.I.Halperin, and C.M.Varma. *Phil. Mag*, 25:1–9, 1972.

[143] W.A.Phillips. *J. Low Temp. Phys.*, 7(3/4):351–360, 1972.

[144] J.Jackle. *Z. Physik*, 257:212–223, 1972.

[145] W.Breinl, J.Freidrich, and D.Harrer. *Chem. Phys. Lett.*, 106:487–490, 1984.

[146] W.E.Moerner, P.Pokrowsky, F.M.Schellenberg, and G.C.Bjorklund. *Phys. Rev. B*, 33(8):5702–5716, 1986.

[147] Y.Mita, Y.Ohno, Y.Adachi, H.Kanehara, Y.Nisida, and T.Nakashima. *Diamond and Related Mat.*, 2(5-7):768–772, 1993.

[148] J.H.N.Loubser. *Solid State Comm.*, 22:767–770, 1977.

[149] D.P.Erchak, R.B. Gelfand, N.M.Penina, V.F.Stelmakh, V.P.Tolstykh, A.G.Ulyashin, V.S.Varichenko, and A.M.Zaitsev. *Phys. Status Solidi A*, 121:63–72, 1990.

[150] R.S.Mulliken, C.A.Rieke, D.Orloff, and H.Orloff. *J. Chem. Phys.*, 17(12):1248–1267, 1949.

[151] P.W.Atkins. *Molecular Quantum Mechanics*, pages 234–235. Oxford University Press, Oxford, 2nd edition, 1983.

[152] E.Clementi and D.L.Raimondi. *IBM Research Note*, (NJ-27), 1963.

[153] C.A.Coulson and F.P.Larkins. *J. Phys. Chem. Solids*, 32:2245–2257, 1971.

[154] A.H.Harker and F.P.Larkins. *J. Phys. C.*, 12:2497–2508, 1979.

[155] D.T.Edmonds, M.J.Hunt, and A.L.Mackay. *J. Magn. Reson.*, 9:66–74, 1973.

[156] Y.Mita, Y.Ohno, Y.Adachi, H.Kanehara, Y.Nisida, and T.Nakashima. *J. Phys. C.*, 2(43):8567–8574, 1990.

[157] G.K.Walters and T.L.Estle. *J. Appl. Phys.*, 32:1854, 1961.

[158] J.A.van Wyk. In *Diamond Conference, Bristol.* Unpublished, 1993. paper 22.

[159] G.Davies, S.C.Lawson, A.T.Collins, A.Mainwood, and S.J.Sharp. *Phys. Rev. B*, 46(20):13157–13170, 1992.

[160] W.J.P. van Enckevort and E.H.Versteegen. *J. Phys. C.*, 4:2361–2373, 1992.

[161] C.D.Clark, R.W.Ditchburn, and H.B.Dyer. *Proc. R. Soc. (London) Series A*, 234:363–381, 1956.

[162] R.G.Farrer and L.A.Vermeulen. *J. Phys. C.*, 5:2762–2768, 1972.

[163] J.A.Baldwin. *Phys. Rev. Lett.*, 10(6):220–222, 1963.

[164] J.Isoya, H.Kanda, Y.Uchida, S.C.Lawson, S.Yamasaki, H.Itoh, and Y.Morita. *Phys. Rev. B*, 45:1436–1439, 1992.

[165] J.Bernholc, A.Antonelli, and T.M.Del Sole. *Phys. Rev. Lett.*, 61(23):2689–2692, 1988.

[166] A.T.Collins. In R.R.Hashiguchi, editor, *Defects and Radiation effects in Semiconductors:IOP Conf. Proc. No.59*, pages 247–252. Institute of Physics, London, 1981.

[167] C.D.Clark, P.J.Kemmey, and E.W.Mitchell. *Discuss. Faraday Soc.*, 31:96–106, 1961.

[168] J.C.Bourgoin and B.Massarani. *Phys. Rev. B*, 14:3690–3694, 1976.

[169] J.F.Prins, T.E.Derry, and J.P.F.Sellschop. *Phys. Rev. B*, 33:8870–8874, 1986.

[170] W.Wu and S.Fahy. *Phys. Rev. B*, 49(5):3030–3035, 1994.

[171] C.D.Clark and E.W.J.Mitchell. In N.B.Urli and J.W.Corbett, editors, *Radiation Effects in Semiconductors, 1976:IOP Conf. Proc. No.31*, page 45ff. Institute of Physics, London, 1977.

[172] A.Mainwood, F.Larkins, and A.M.Stoneham. *Solid State Electron.*, 21:1431–1433, 1978.

[173] Y.M.Kim, Y.H.Lee, P.Brosius, and J.W.Corbett. In J.E.Whitehouse, editor, *Radiation Damage and Defects in Semiconductors (1972):IOP Conf. Proc. No.16*, pages 202–209. Institute of Physics, London, 1973.

[174] J.N.Lomer and C.M.Welbourn. In N.B.Urli and J.W.Corbett, editors, *Radiation Effects in Semiconductors, 1976:IOP Conf. Proc. No.31*, pages 339–345. Institute of Physics, London, 1977.

[175] W.Crookes. *Diamonds*, page 108. Harper, London, 1909.

[176] C.D.Clark and J.Walker. *Proc. R. Soc. (London) Series A*, 334:241–257, 1973.

[177] C.A.Coulson. In J.E.Whitehouse, editor, *Radiation Damage and Defects in Semiconductors (1972):IOP Conf. Proc. No.16*, pages 249–254. Institute of Physics, London, 1973.

[178] R.P.Messmer and G.D.Watkins. *Phys. Rev. B*, 7(6):2568–2590, 1972.

[179] A.Mainwood, J.E.Lowther, and J.A. van Wyk. *J. Phys. C.*, 5:7929–7934, 1993.

[180] C.Petrillo and F.Sacchetti. *Phys. Rev. B*, 51(8):4755–4762, 1995.

[181] N.B.Manson, J.Pörsch, and A.Runciman. *J. Phys. C.*, 13:L1005–9, 1980.

[182] J.E.Lowther. *Phil. Mag*, 36(2):483–93, 1977.

[183] J.E.Lowther. *Phys. Rev. B*, 48(16):11592–11601, 1993.

[184] J.E.Lowther. *J. Lumin.*, 60 & 61:531–534, 1994.

[185] A.Mainwood. *J. Phys. C.*, 11:L449–52, 1978.

[186] M.Stoneham. In *Diamond Conference, Reading.* Unpublished, 1977. paper 16.

[187] H.B.Dyer and L.du Preez. *J. Chem. Phys.*, 42(6):1898–1906, 1965.

[188] G.Davies. *Nature*, 269:498–500, 1977.

[189] I.N.Douglas and W.A.Runciman. *J. Phys. C.*, 10:2253–2259, 1977.

[190] J.H.N.Loubser and J.A.van Wyk. *Rep. Prog. Phys.*, 41:1201–1248, 1978.

[191] D.G.McGavin. *J. Magn. Reson.*, 74:19–55, 1987.

[192] G.Davies. In P.A.Thrower, editor, *Chemistry and Physics of Carbon*, volume 13, page 1ff. Marcel Dekker, New York, 1977.

[193] J.Hyde, M.Pasenkiewicz-Gierula, A.Jesmanowicz, and W.Antholine. *Appl. Magn. Reson.*, 1:483ff, 1990.

[194] J.Hyde, A.Jesmanowicz, J.J.Ratke, and W.Antholine. *J. Magn. Reson.*, 96(1):1–13, 1992.

[195] D.H.Tanimoto, W.M.Ziniker, and J.O.Kemp. *Phys. Rev. Lett.*, 14(16):645–647, 1965.

[196] G.D.Watkins. *Phys. Rev.*, 155:802–815, 1967.

[197] K.L.Brower. *Phys. Rev. B*, 4(6):1968–1982, 1970.

[198] J.E.Lowther and J.A.van Wyk. *Phys. Rev. B*, 49(16):11010–11015, 1994.

[199] B.A.Goodman and J.B.Raynor. In H.J.Emeleus and A.G.Sharpe, editors, *Advances in Inorganic and Radiochemistry*, pages 135–362. Academic Press, London, 1970.

[200] E.Pereira and L.Santos. *J. Lumin.*, 45:454–457, 1990.

[201] L.Santos and E.Pereira. *J. Lumin.*, 60 & 61:614–617, 1994.

[202] P.Omling, V.Kveder, B.K.Meyer, K.Oettinger, U.Kaufmann, and O.Kordina. *Phys. Rev. B*, 47(19):12527–12531, 1993.

[203] J.A.van Wyk and G.S.Woods. In *Diamond Conference, Oxford.* Unpublished, 1987. paper 10.

[204] J.A.van Wyk. In *Diamond Conference, Bristol.* Unpublished, 1989. poster 5.

[205] J.A.van Wyk. In *Diamond Conference, Oxford.* Unpublished, 1991. paper 43.

[206] O.D.Tucker, M.E.Newton, J.M.Baker, and J.A.van Wyk. In *Diamond Conference, Bristol.* Unpublished, 1993. paper 20.

[207] O.D.Tucker, M.E.Newton, and J.M.Baker. In *26th International ESR conference, Sheffield.* Unpublished, 1993. poster 37.

[208] J.A. van Wyk. *J. Phys. C.*, 6(3):801–810, 1994.

[209] J.N.Lomer and A.M.A.Wild. *Radiat. Effects*, 17:37–44, 1973.

[210] J.A.vanWyk, 1995. Private communication.

[211] J.M.Baker and T.Christidis. *J. Phys. C.*, 9:3813–3817, 1976.

[212] E.A.Faulkner and J.N.Lomer. *Phil. Mag*, 7:1995–2002, 1962.

[213] R.C.Burns and G.J.Davies. Growth of synthetic diamond. In J.E.Field, editor, *The Properties of Natural and Synthetic Diamond*, chapter 10, pages 395–422. Academic Press, London, 1992.

[214] H.Kanda and T.Sekine. High temperature, high pressure synthesis of diamond. In G.Davies, editor, *Properties and Growth of Diamond*, chapter 12, pages 401–426. INSPEC, London, 1994.

[215] M.N.Yoder. *Diamond and Related Mat.*, 2:59–64, 1993.

[216] A.T.Collins, G.Davies, H.Kanda, and G.S.Woods. *J. Phys. C.*, 21:1363–1376, 1988.

[217] J.W.Bray and T.R.Anthony. *Z. Phys. B*, 84:51–57, 1991.

[218] T.R.Anthony, W.F.Banholzer, J.F.Fleischer, L.Wei, P.K.Kuo, R.L.Thomas, and R.W.Pryor. *Phys. Rev. B*, 42(2):1104–1111, 1990.

[219] R.Berman. *Phys. Rev. B*, 45(10):5726–5728, 1992.

[220] J.W.Vandersande. Thermal conductivity of isotopically pure diamond. In G.Davies, editor, *Properties and Growth of Diamond*, chapter 8.4, pages 258–259. INSPEC, London, 1994.

[221] A.K.Ramdas. Phonon properties in $^{13}C$ diamond. In G.Davies, editor, *Properties and Growth of Diamond*, chapter 8.3, pages 255–257. INSPEC, London, 1994.

[222] G.Davies. Lattice spacing in $^{13}C$ diamond. In G.Davies, editor, *Properties and Growth of Diamond*, chapter 8.1, pages 243–247. INSPEC, London, 1994.

[223] G.Davies. Optical absorption and luminescence in $^{13}C$ diamond. In G.Davies, editor, *Properties and Growth of Diamond*, chapter 8.2, pages 248–254. INSPEC, London, 1994.

[224] M.E.Newton. Electron paramagnetic resonance of radiation damage centres in diamond. In G.Davies, editor, *Properties and Growth of Diamond*, chapter 5.2, pages 153–158. INSPEC, London, 1994.

[225] M.A.Lea-Wilson and J.N.Lomer. In *Diamond Conference, Cambridge.* Unpublished, 1983. poster 4.

[226] M.A.Lea-Wilson and J.N.Lomer. In *Diamond Conference, Reading.* Unpublished, 1985. poster 5.

[227] J.Walker. In *Diamond Conference, Cambridge*. Unpublished, 1975. paper 8.

[228] P.W.Whippey. *Canadian J. Phys.*, 50:803–12, 1972.

[229] J.Walker. *J. Phys. C.*, 10:3867–3876, 1977.

[230] R.H.Wentorf. *J. Phys. Chem.*, 75:1833–1837, 1971.

[231] G.S.Woods and A.R.Lang. *J. Cryst. Growth*, 28:215ff, 1975.

[232] P.Bowmar. D.Phil thesis, University of Oxford, 1994.

[233] J.J.van Vleck. *Phys. Rev.*, 74(9):1168–1183, 1948.

[234] D.F.Talbot-Ponsonby, 1995. Private communication.

Table 1.1: Names of the major defects discussed in this work, giving the structural, EPR, and optical notation. A full tabulation of diamond defects, and the known relations between optical and EPR defects, is given by Bridges *et al.* [16].

| Structural | EPR | Optical | Comments |
|---|---|---|---|
| $[N\text{–}C]^0$ | P1 | — | Single substitutional nitrogen. |
| $[N_3V]^0$ | P2 | N3 | Three nitrogen atoms surrounding a vacancy. |
| $[N\text{–}N]^0$ | — | A-centre | Two adjacent substitutional nitrogen atoms. |
| $[N\text{–}N]^+$ | W24 | — | Ionized di-nitrogen centre, also $[N\text{–}N]^-$, $[N\text{–}N]^{2+}$. |
| $[V]^0$ | — | GR1 | Neutral vacancy. |
| $[V]^-$ | ND1 | ND1 | Also Baldwin S1 EPR centre, negative vacancy. |
| $[V]^*$ | *none* | — | Only structurally derived EPR notation, excited state of the vacancy. Disregards ligand hyperfine interactions (see next entry). |
| $[V]^*_{10}$ | *none* | — | The subscripts denote 1 nearest neighbour $^{13}C$ atom, and 0 next-nearest neighbour $^{13}C$ atoms in this case. |
| ? | R1 | — | Radiation damage induced EPR centre, no structure known. |
| ? | R2 | 1.685 eV | Radiation damage induced EPR centre, associated with 1.68 eV ZPL seen in optical absorption. |
| ? | O1 | — | Modelled as ⟨100⟩ Frenkel pair ($C_i$+V), in neutral charge state. Possible correlation with cathodoluminescence ZPL's at 511.5 nm and 509 nm. |

| | |
|---|---|
| — | indicates the absence of an identified EPR or optical defect |
| ? | indicates that the structure is unknown |
| *none* | indicates that there is no EPR notation for the defect |